# CdSe AND ITS HYBRID MATERIALS
# FOR
# ENERGY APPLICATIONS

A THESIS
SUBMITTED TO THE
**UNIVERSITY OF PUNE**
FOR THE DEGREE OF
**DOCTOR OF PHILOSOPHY**
IN
**CHEMISTRY**

BY
**JOYASHISH DEBGUPTA**
UNDER THE GUIDANCE OF
**Dr. K. VIJAYAMOHANAN**

PHYSICAL AND MATERIALS CHEMISTRY DIVISION
NATIONAL CHEMICAL LABORATORY
PUNE-411008
INDIA

JUNE 2014

*Dedicated to My Beloved*
*Late Kakumoni,*
*Phoolpisimoni and Baba*

# DECLARATION

I, hereby declare that all the experiments embodied in this thesis entitled, “**CdSe AND ITS HYBRID MATERIALS FOR ENERGY APPLICATIONS**”, submitted for the degree of Doctor of Philosophy in Chemistry, to the University of Pune have been carried out by me at the Physical and Materials Chemistry Division, National Chemical Laboratory, Pune-411008, India, under the supervision of Dr. K. Vijayamohanan. The work is original and has not been submitted in part or full by me, for any degree or diploma to this or to any other University.

Date: **Joyashish Debgupta**
Physical and Materials Chemistry Division
National Chemical laboratory
Pune-411008

**Dr. K. Vijayamohanan**
**Scientist**

Physical and Materials
Chemistry Division
National Chemical Laboratory
Pune-411008
INDIA

Tel: +91-020-2590-2588
Res: +91-020-2587-0307
Fax: +91-020-2590-2636
Email: vk.pillai@ncl.res.in

# CERTIFICATE

This is to certify that the work incorporated in the thesis entitled, "**CdSe AND ITS HYBRID MATERIALS FOR ENERGY APPLICATIONS"** submitted by **Mr. JOYASHISH DEBGUPTA**, has been carried out by him under my supervision at the Physical and Materials Chemistry Division, National Chemical Laboratory, Pune-411008, India. All the materials from other sources have been duly acknowledged in the thesis.

Date:
Place: Pune

**Dr. K. Vijayamohanan**
(Research Guide)

# Acknowledgements

The PhD research period sustained the most difficult part of my life, not because of the unsolvable research problems, but due to several personal moments of difficulties. Naturally there are so many people involved in inspiring me at those moments of depressions, whose constant support and encouragement were so crucial to achieve what I am today. It was specially a cherished dream of my phoolpisimoni (aunt), kakumoni (uncle) and baba (father) that they would see me becoming a Doctor one day, although they left me in the half way of the journey! However, they will always remain in every part of my heart and will be the guiding spirit of all my future activities!

A mere word of sincere appreciation is insufficient to express my gratitude to my research supervisor Dr. K. Vijayamohanan. It does not really suite me to praise the qualities of him, since I am nowhere around him. I am really grateful to him for his guidance, fruitful discussions, technical critiques, valuable advice, constant support and encouragement throughout the course of this work. He is also a very good teacher and a wonderful research guide with vast knowledge and insight. But above all, he is a very good human being. He will always be an ideal and inspiring figure in my mind. I would be happy if I could acquire a few tips of his huge personality and knowledge. I also extend my sincere appreciation to Mrs. Manju madam for her motherly care, blessing and constant support.

I would also like to offer my sincere admiration to my co-guide Dr. K. Sreekumar, as he is so kind to me, always enquiring the progress of my work. I am really thankful to him for supporting me in every possible ways, especially in absence of my supervisor.

I would also like to sincerely thank Dr. (Mrs.) Manjusha V. Shelke for her constant help, support and suggestions.

I wish to thank Dr. S. Pal, Director, NCL for providing me all infrastructural facilities. I also thank Dr. Anil Kumar, Head of Physical & Materials Chemistry Division for allowing me to use all available facilities in the Division.

I am also grateful to my former and present teachers, Profs. A. M. Roychoudhury, A. K. Bhothra, D. Bhattacharya, P. Ghosh, R. Mukherjee, D. Debnath, P. Bandyopadhyay, A. Roy, P. S. Roy, A. Ghosh for their love and belief, as they had *built the foundation for this achievement. I would also thank Prof. Amitava Patra, IACS, Kolkata and his students Sadananda for active collaboration.*

*I am also thankful to Drs. Rahul Banerjee, Sayam Sengupta, B. L. V. Prasad, P. A. Joy, Pankaj Poddar, H. Kalkote, Suresh Bhat, Satish Ogale, S. K. Asha, K. Krishnamurthy, S. P. Gokhale, C. S. Gopinath to kindly allow me to use the instrumental facility in their lab.*

*I would also like to thank Mr. Dipak Jori & Mr. Puneikar in Physical Chemistry office for their timely help. I also thank the stuffs from Glass Blowing, Engineering Section, CMS, DIRC, Stores and Purchase for providing excellent facility.*

*I can never forget the help, love and constant encouragement from my lab seniors Drs. Bhalchandra, Meera, Bhaskar, Mahima Chechi, Kannan and Deepali. I would also like to thank all my past and present labmates Dhanraj, Vinayak, Beena, Vinisha, Sreekuttan, Vishal, Palani, Ranjith, Nilesh, Ashwini, Rami, Chaitanya, Indrapal, Sandeep, Rupali, Rajaperumal, Sidhhu, Pandiaraj, Sachin, Ajinkya, Pritish, Neeta, Hussain, Rajith, Bihaag, Harshitha, Robi, Kashyap and Praveen, for creating a wonderful and friendly atmosphere for research in the lab during my stay. I am especially thankful to Rami, Chaitanya, Shakeel, Vishal, Beena, Sreekuttan and Dhanraj for teaching me many experimental techniques and fruitful discussions. I also thank my summer students, Krishnadas, Raman, Abhishek and Sukant for their helpful contributions and teaching me so many things. I am also grateful to CMC Division for providing excellent instrumental facility and especially to Rupali Madam (for Raman), Ketan (for SEM), Pandiaraj, Anuj, Naren, Shrabani, Shravya (for TEM), Dr. K. R. Patil (for XPS), Deo sir for their help and support without which this work would not have been possible.*

*I would also like to express my sincere thanks to all my institute collegues and friends Pankaj, Mangesh, Ramsundar, Govind, Jaya, Lenin, Anjali, Bhindu, Srikanth, Raja, Chaka, Jeetu, Mohan, Sashi, Saritha, Shankar, Gopi, Shanti, Ashoke, Manisha, Drs. Nagesh, Geetanjali, Khaja, Vijay (Anna), Sreeja, Sahooji, Vilas, Deepti, Rupesh, Brijesh, Ravi, Pradeep, Jayashree madam, Kaushal, Chinmay, Nagesh, Edwin, Digambar, Vishal Thackare, Late Shubhro, Shruti, Meenal, Omkar, Datta, Mandakini and Mansi. My special thanks to Ramsundar and Indrapal to help me lot in finishing the thesis and so many other things. A special acknowledgement is also to all my Bong* *friends Krishanu, Shyam, Jhumur, Tanaya, Prasenjit, Soumen, Saibal, Arijit, DOS, Shubhadip, Debasish, Arpan, Kanak, Achintya, Tamas, Animesh, Aryya, Subha, Munmun, Chini, Himadri, Shankha, Prithvi, Santu, Manoj, Atreyee, Chayanika, Chandan, Sujit, Ramkrishna, Jaga, Pradip, Akash, Sujitda, Debasishda, Analda, Sumantada, Arijitda, Anup, Santigopal, Sanjeev, Bikash, Soumen (Dey), Binoy, Sumantrada, Abhik, Anirudhha, Pranab, Basabda, Patida, Anupam, Susanta, Saikat, Suman, Lili, Debanjanda, Sumona, Arunava, Hridesh, Atanu, Shantanu, Biplab, Abhigyan, Debarati, Gobindoda and many more for creating a joyful and enthusiastic atmosphere all the time.*

*I am also indebted to my uncle and local guardian Mr. Tarun Kr. Saha and his family for their unparallel love and encouragement.*

*I do not have words to express my feelings for my family members and all relatives for their blessings, constant encouragement, love, inspiration and support which make possible this achievement. I am especially indebted to my Didi, Tanmoyda, Dada who always supported in every possible ways and gave strength to me to fulfill my dream. I would also like to thank my father & mother-in-laws and Nini for their support and love.*

*Last but not least, my heartfelt thank to my beloved wife and friend Suranjana for understanding, supporting and guiding me always. It might not have been possible to achieve this goal without her constant support and inspiration.*

*As always, it is impossible to mention everybody who had an impact on this work. I apologize if I have forgotten to mention anyone.*

*Finally, I would like to thank the Almighty God for all his blessings which have provided guiding spirit, even at my saddest moments.*

*Joyashish Debgupta*

“Success is a not a destination, it’s a journey.”

# List of Abbreviations

| **Abbreviation** | **Expansion** |
|---|---|
| **1-D** | One-Dimensional |
| **2-D** | Two-Dimensional |
| **3-D** | Three-Dimensional |
| **0-D** | Zero-Dimensional |
| **QD** | Quantum Dot |
| **CdSe** | Cadmium Selenide |
| **UV** | Ultraviolet |
| **PL** | Photoluminescence |
| **ZnS** | Zinc Sulphide |
| **FWHM** | Full Width At Half Maximum |
| **GM** | Gopert-Mayer |
| **nm** | Nanometer |
| **FET** | Field Effect Transistor |
| **PEDOT** | Poly(Ethylene Dioxy Thiophene) |
| **PSS** | Poly Styrene Sulphonate |
| **P3HT** | Poly Hexylthiophene |
| **STM** | Scanning Tunneling Microscopy |
| **TEM** | Transmission Electron Microscopy |
| **SEM** | Scanning Electron Microscopy |
| **DMF** | Dimethyl Formamide |
| **MBE** | Molecular Beam Epitaxy |
| **ALD** | Atomic Layer Deposition |
| **CVD** | Chemical Vapor Deposition |
| **LED** | Light Emitting Diode |

| | |
|---|---|
| **PXRD** | Powder X-ray Diffraction |
| **CV** | Cyclic Voltammetry |
| **DPV** | Differential Pulse Voltammetry |
| **FTIR** | Fourier Transformed Infrared |
| **TGA** | Thermogravimetric Analysis |
| **EDAX** | Energy Dispersive X-ray Analysis |
| **FFT** | Fast Fourier Transform |
| **FRA** | Frequency Response Analyzer |
| **HOMO** | Highest Occupied Molecular Orbital |
| **MWCNT** | Multi Walled Carbon Nanotube |
| **SWCNT** | Single Walled Carbon Nanotube |
| **PTFE** | Polytetrafluoroethylene |
| **RBM** | Radial Breathing Mode |
| **SAED** | Selected Area Electron Diffraction |
| **SDS** | Sodium Dodecyl Sulphonate |
| **TBAHP$_6$** | Tetrabutylammonium Hexafluorophosphate |
| **TCSPC** | Time Correlated Single Photon Counting |
| **QY** | Quantum Yield |
| **NT** | Nanotube |
| **NW** | Nanowire |
| **4-ATP** | 4-Aminothiophenol |
| **RGO** | Reduced Graphene Oxide |

# Table of Contents

## Chapter 1

## CdSe Quantum Dots-A Critical Survey 1-32

## Chapter 2

## Electrochemistry of CdSe QDs-Investigation of Band Structure Parameters and Size Dependent Single Electron Transfer 33-56

## Chapter 3

## Behavior of CdSe QDs attached to Carbon Nanostructures

## Chapter4

## Anchoring of CdSe QDs on Graphene through Molecular Linkers

93-122

## Chapter5

## Vertically aligned CdSe Nanotubes and Its p-n Hetero-junction Diodes

124-156

**Chapter 6**

# CHAPTER 1

# CdSe Quantum Dots-A Critical Survey

This chapter presents a critical survey of the synthesis, properties and applications of CdSe quantum dots with special emphasis on the generation their hybrids. The variation of their optical as well as electronic properties with size and shape has been discussed with relevant theoretical background. This chapter also discusses various characterization techniques from spectroscopic, to microscopic to electrochemical methods in order to unravel their fascinating behavior considering fewer presentative mono-dispersed size distribution. Finally, the potential applications of these QDs for solar cells, photo-detectors, and water electrolyzers have been illustrated with specific details. The chapter also concludes by explaining the specific objectives of the present study, future prospects finally mentioning some of the existing limitations of these QDs and QD based hybrid nanomaterials.

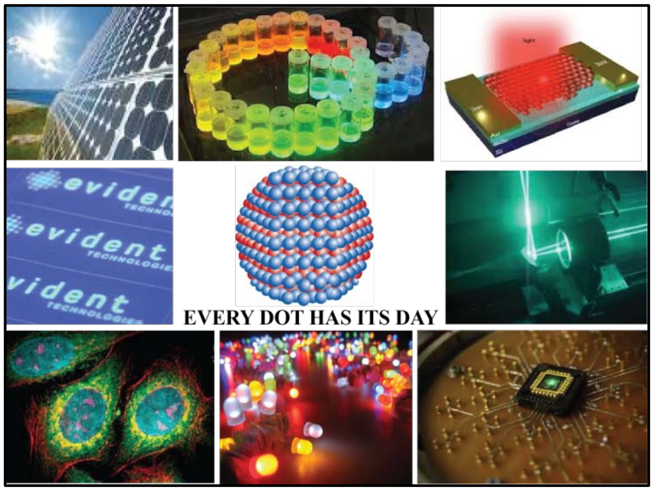

## 1.1. Introduction

Nanoscience and nanotechnology has played an important role in opening up many inter disciplinary fields of frontier research with commercial applications. The scope of research as well as the range of applications are very wide and extend from medicine, electronics, biomaterials, and metamaterials to energy production. An important feature of nanoscience and technology is the precise and purposeful manipulation of matter at the atomic or molecular level and also the assembly of the nanomaterials at meso-micro level to have some functionality that can be employed for various applications in day-to-day life.For example, the use of $TiO_2$ nanoparticles in sunscreen, cosmetics, surface coatings and food products; carbon allotropes (CNT, fullerenes etc) in making Gecko tape; silver nanoparticles in food packaging, clothing, disinfectant and in bandage for the fast recovery of wounds; cerium oxide nanoparticles as fuel catalyst; silica carbide nanoparticles in tyres to reduce abrasion; carbon nanotubes in making faster computers; gold nanoparticles in cancer therapy (photodynamic therapy), electronic chips as conductors, optical sensors for quality control and so on.[1a-1g]

In recent years, various synthetic routes are available for the preparation of a variety of nanostructures with reasonable size and shape selectivity using methods like laser or plasma deposition, chemical/physical vapor deposition, sol-gel or other wet chemical routes and electrodeposition.[1h-1y] However, these methods generally result in very tiny(2-10 nm) particles with different sizes and shapes, often in a metastable phase and due to the small sizes and shapes, many of the properties are influenced to a greater extent by quantum size effects. Experimental evidence of the quantum size effects for small particles has been provided by different methods, while the surface induced effect could be verified by the measurement of thermodynamic properties like vapor pressure, specific heat, thermal conductivity and melting point of small metallic particles.[2] Generally, smaller the size, larger is the band gap, since greater is the difference in energy between the valence band and conduction band edges as more energy is needed to excite the electrons and concurrently, more energy is released when they return to their original state.[3] The electronic structure of a nanomaterial and hence its properties (both physical and chemical) critically depends on its size and is drastically different from their bulk or atomic/molecular analogues as shown schematically in fig.1.1. This change in electronic structure due to their lower dimensionality can be generally defined by the electron transport t in a restricted environment such that the particle size is of the order of mean free path (i.e. phase coherence length of the electrons at least in one dimension, - commonly known as quantum confinement) resulting into a dramatic change in all properties.

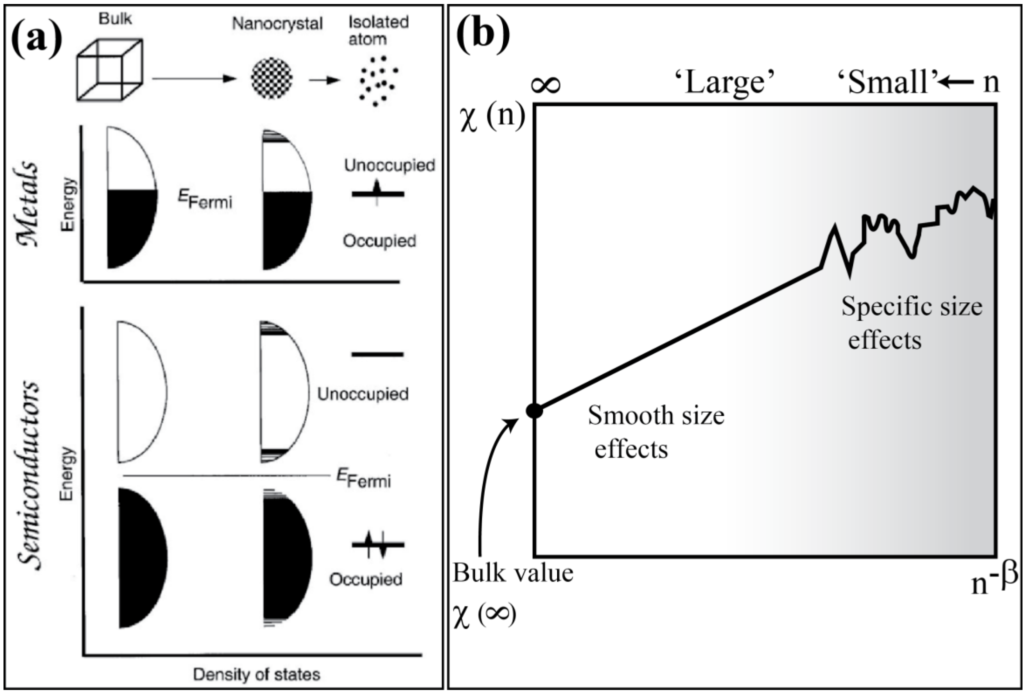

**Figure 1.1.** (a) Variation of electronic structure with particle size for metals and semiconductors;[4b-4c] (b) The size dependence of a property $\chi(n)$ on the number of atoms ($n$) in a nanoparticle. The data are plotted against $n^{-\beta}$ where $\beta \geq 0$; nanomaterials having size below a certain threshold, shows specific size effects; whereas larger particles are expected to have a smooth size dependence.[4a]

Specifically interesting and technologically important are the semiconductor nanoparticles (specially, the inorganic quantum dot semiconductors) in this regard. Because, semiconductors have intrinsic energy gaps which gets modulated when the size of the particles reaches below ~10 nm. This has direct impact on the optical properties (UV-Vis and photoluminescence) of the semiconductors. Decreasing the size also influences the intrinsic properties of semiconductors.[5] For example, the case of CdS which is a prototypical semiconductor, can be considered. The band-gap of CdS changes from 2.5 to 4 eV,[6] the energy required above band-gap to add an extra charge increases by 0.5 eV,[7] the melting temperature drops from 1600 to 400°C,[8] the pressure required for the transformation from 4- to 6-coordinate phase increases from 2 to 9 GPa[9] as the macroscopic crystal diminishes in size to join the molecular regime of CdS. Due to such exotic properties, studies in the field of semiconducting nanostructures have become popular in last few years and is expected to flourish without any sign of abatement.

### 1.2. Quantum Dots (QDs)

A representative class of semiconductor nanostructures is the "Quantum Dots (QDs)". From the perspective of a physicist, a Quantum Dot (Q-dot or simply QD) is a semiconductor nano-crystal exhibiting quantum confinement of both electron and hole in all three spatial dimensions. This happens when the diameter of a nanocrystal becomes smaller than a critical value which is known as the bulk exciton Bohr radius [10] for the material. Below this critical size the nanocrystals have only fewer charge carriers which are confined three dimensionally by high potential barriers. This eventually causes the bulk band structure of the semiconductor material to collapse into discrete energy levels just like that observed in case of atoms. The properties of such man-made finite fermion systems are, therefore, very similar to that of atoms in many aspects and so they are often termed as "artificial atoms" or "designer atoms". [11]

The most interesting property of QDs is the substantial changes in optical properties as a function of particle size.[12-13] The electronic excitation generally blue shifts as the QD size decreases and the oscillator strength becomes limited to only few transitions, although the basic crystal structure (bond length, unit cell dimension etc.) remains unaltered. It is important to note here that the absorption of QDs in the visible region is due to the generation of excitons, which are electrostatically bound electron-hole pair.[13] Variation of the absorption spectra of QDs having different size has been correlated to the bulk exciton diameter ($\alpha_b$) which is given by,

$$\alpha_b = \frac{h^2\varepsilon}{e^2}\left[\frac{1}{m_e^*} + \frac{1}{m_h^*}\right]\ldots\ldots\ldots\ldots\ldots\ldots\ldots\ldots\ldots(1)$$

where, $\varepsilon$ = size dependent dielectric constant, $m_e^*$ and $m_h^*$ are the electron and hole effective masses respectively. Fig. 1.2 shows the variation of absorption onset of QDs with particle size.

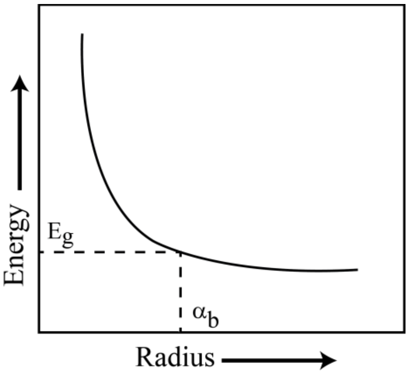

**Figure 1.2.** A schematic representation of the variation of absorption onset with the change in particle size of QDs; onset of absorption generally moves to higher energy as the particle size decreases.[4a]

It is clear from the fig. 1.2 that the absorption onset of QDs is inversely proportional to the particle size. There is a sharp increase in absorption onset (exponential increase) below $\alpha_b$, but shows a monotonous change above $\alpha_b$. In fact, QDs fall into three distinct regime based on the strength of “quantum confinement”, which is further related to $\alpha_b$, as follows,[14]

(i) Strong Confinement Regime: when $R \ll \alpha_b$

(ii) Weak Confiment Regime: when $R \gg \alpha_b$

(iii) Intermediate Confinement Regime: when $(\alpha_b)_e > R > (\alpha_b)_h$, where $(\alpha_b)_e$ and $(\alpha_b)_h$ are the Bohr radii of electron and hole respectively. Here, R is the nanocrystal radius.

Many different approaches have been proposed to quantitatively relate the electronic structure and size of QDs. The first approach towards this direction was offered by Efros and Efros based on the effective mass approximation of electron and hole.[15]Later, Brus[16-17] proposed the following relation for the electronic structure of QDs in the strong confinement regime:

$$E(R) = E_g + \frac{\hbar^2\pi^2}{2R^2}\left[\frac{1}{m_e^*} + \frac{1}{m_h^*}\right] - \frac{1.8e^2}{\varepsilon R} - 0.248\, E_{R_y}^* \text{…………(2)}$$

where, $E_g$ = bulk band-gap energy of the semiconducor, $m_e^*$ = effective mass of electron, $m_h^*$ = effective mass of hole and $\varepsilon$ = size dependent dielectric constant of the material. The third term accounts for the Coulomb interaction between the electron and the hole, whereas the fourth term arises due to the spatial correlation of the electron and the hole. The last term is generally very small as compared to other terms and is, therefore, often ignored. This is the well-known Brus correlation for the electronic structure of QDs.

In addition to such tunable absorption property, QDs also possess another intriguing and perhaps one of the most exploited properties which is their band edge photoluminescence (PL). The PL of QDs is generally affected by the particle size and surface structure.[18] For example, Fig.1.3 shows the variation of the emission wavelength as a function of size where a single material, like CdSe, can emit PL that can cover the entire visible range (from blue to red). Even, in the case of ZnS@CdSe QD, the PL is very narrow (FWHM ≤ 40 nm) with a high level of brightness (quantum yield 30-50%).[18]

**Figure 1.3.** Emission from CdSe QDs of varying size (size increases from left to right).[19]

Another interesting optical phenomenon observed for QDs is the “Blinking”, i.e., intermittent PL.[20] This blinking behavior has been attributed to the QDs becoming charged which causes its PL to be turned off due to a three body Auger recombination process.[21] For this behavior, QDs have been used in single molecule PL spectroscopy.

Due to these exotic properties, QDs are an important class of material which are continuously being used in sensitized solar cells for converting photon to electricity because of the high extinction coefficient and multi-exciton generation,[22-23] and in light emitting diodes,[24] diode lasers,[25] photodetectors,[26] single electron transistors[27] and so on. They are also interesting to physicist as they represent a model system to study confined charges. Apart from chemist and physicist, biologists are also interested in QDs as fluorescent tags which stems from their high quantum yield, tunable and narrow PL, customizable functionality and high resistance to photo-bleaching or photochemical degradation.[28] PL lifetime of QDs is also higher (at least an order in magnitude) than that of conventional fluorescent organic dye molecules used as labels. For example, sentinel lymph node mapping[29-30] and *in vivo* imaging[31] are some of the areas in biology where QDs have been used. Finally, for almost all these applications, colloidal QDs are mostly used, because these can be easily synthesized, manipulated and incorporated in the device structure. The present thesis, therefore, deals exclusively with only chemically synthesized colloidal QDs rather than lithographically patterned [32] or self-assembled (Stransky-Krastanov mode of growth) QDs[33-34]).

### 1.3. Importance of CdSe and Its Hybrids

Cadmium Selenide (CdSe) is a yellow-orange inorganic solid compound.[35] It falls in the subcategory of II-VI semiconductors due to the positions of Cd and Se in the periodic table. It is an n-type semiconductor with three known different polymorphs namely, wurtzite (hexagonal), sphalerite (cubic) and rock-salt (cubic). The sphalerite structure is unstable and converts to the wurtzite form upon moderate heating. The onset of transition is at about 130°C and at elevated temperature (700°C), the transformation completes within one day. The rock salt structure, however, is realized only at high pressure.[36]

There are few salient features of CdSe. For example:

(i) It is a direct band-gap semiconductor[37] and so no extra energy or phonon is required for the excitation. Similarly, no energy dissipates as heat during the relaxation from the excited to ground state.

(ii) CdSe has a band-gap of ~1.797 eV in the wurtzite phase and ~1.712 eV in the zinc blende phase.[38] Such a wide band-gap favors absorption over a large range of the visible spectrum.

(iii) Two photon absorption (TPA) cross section is as high as ~$10^4$ GM (Göpert-Mayer units, 1GM = $10^{-50}$ $cm^4.s.photon^{-1}$) for CdSe QDs.[39] The value is highest among other II-VI semiconductors and is also higher than most of the semiconductor QDs.

(iv) Considering Bohr exciton radius for bulk CdSe (~6 nm, i.e., an exciton delocalizes over ~12 nm),[40] the emission of CdSe QDs can be tuned precisely from deep red to blue by reducing the size from 5 nm to 0.7 nm under UV radiation.[41]

All the above properties make CdSe as a promising material for numerous applications such as photodetectors, field effect transistors (FETs), field emitters, solar cells, light emitting diodes, memory devices, biosensors and biomedical imaging.

The scope of utilizing the intrinsic properties of CdSe QDs can be further widened by combining them with appropriate systems. For example, hybrids of CdSe QDs with various other materials have been prepared and used for various applications. Accordingly, CdSe QDs can be protected from recombination losses and photo-degradation by coating with a conducting polymer like PEDOT:PSS,[42] efficiency of bulk hetero-junction solar cell can be enhanced by a combination of poly (3-hexylthiophene) (P3HT)-single walled carbon nanotubes,[43] composite of P3HT-CdSe QD has been used for selective sensing of chloroform vapor.[44] Again, a combination of $TiO_2$-Au nanoparticles and CdSe QDs have been shown to enhance the photovoltaic conversion efficiency,[45] PL of (CdSe) ZnS core-shell QDs has been found to increase in contact with gold colloid.[46] Due to their unique optical properties, CdSe QDs bio-conjugates have also been exploited in *in vitro* and *in vivo* imaging.[47] Hybrids of CdSe QDs with carbon nanostructures such as fullerene, graphene or carbon nanotubes are another type of materials which find many applications starting from photovoltaic devices, sensors and even removal of pollutants.[48] CdSe QDs and its hybrids are, therefore, very important in the emerging area of nanoscience and technology.

## 1.4. Properties of CdSe Quantum Dots (CdSe QDs)

### 1.4.1. Electronic Structure of Cadmium Selenide (CdSe) - Bulk *vs* Nano

The electronic as well as excitonic structure of CdSe QDs can be understood in either of two ways-

(i) What happens when the bulk CdSe shrinks till it reaches the limit when quantum confinement starts to predominate (top down approach).

(ii) What happens when cluster of atoms grows to form CdSe QDs (bottom up approach).

However, the present discussion will be qualitative and will be limited to the first category where the fate of bulk band structure of CdSe will be discussed when it reaches to the quantum confinement limit. Quantitative treatment can be found elsewhere [15], [16], [49] In bulk CdSe, Se 4p states form the valence band (because Se is more electronegative than Cd), whereas the conduction band consists of Cd 5s states. The quantum number for the conduction band is $J_z = 1/2$. On the other hand, the valence band has three sub-bands with quantum numbers $J_z = 3/2, 1/2, 1/2$ with $J_z = 3/2$ being the highest energy band. Fig. 1.4 shows the band diagram of bulk CdSe. Top of the valence band is separated from the bottom of the conduction band by the bulk band-gap energy ~1.75 eV at room temperature (~708 eV). Effective mass of the highest energy valence band is ~1 which is heavier than the effective mass of the conduction band (~0.1 eV). It is, therefore, said that CdSe has a “heavy hole”. A “light hole” band also exists just below the “heavy hole”.[50]

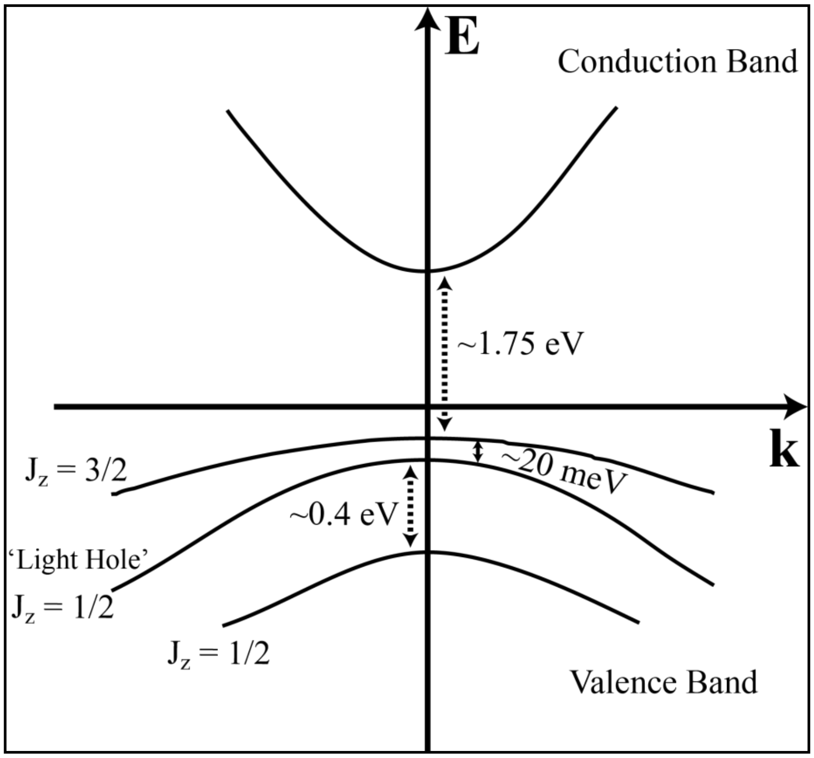

**Figure 1.4.** Band structure of bulk CdSe showing valence and conduction bands separated by a bulk band-gap of ~1.75 eV.[50]

The situation is, however, different when the bulk CdSe shrinks to a size that is less than ~6 nm (excitonic Bohr radius of bulk CdSe, i.e., photogenerated exciton travels ~12 nm in the CdSe crystal). Size reduction theoretically implies the removal of the contributing atomic states from the valence and conduction states so that in the quantum confinement regime (<~6 nm), the valence and conduction states (VB and CB) no longer remain bands, rather they turn into discrete atom like states. But, the VB and CB still consist of Se 4p and Cd 5s atomic states. The immediate effect of quantum confinement is seen in the blue shifting of the first absorbance feature as the QD size decreases (fig. 1.5). This is analogous to the system "particle in a spherical box" where the energy E of the particle is directly proportional to $1/a^2$, where "a" is the radius of the box. Energy of the particle increases as the radius of the box decreases.

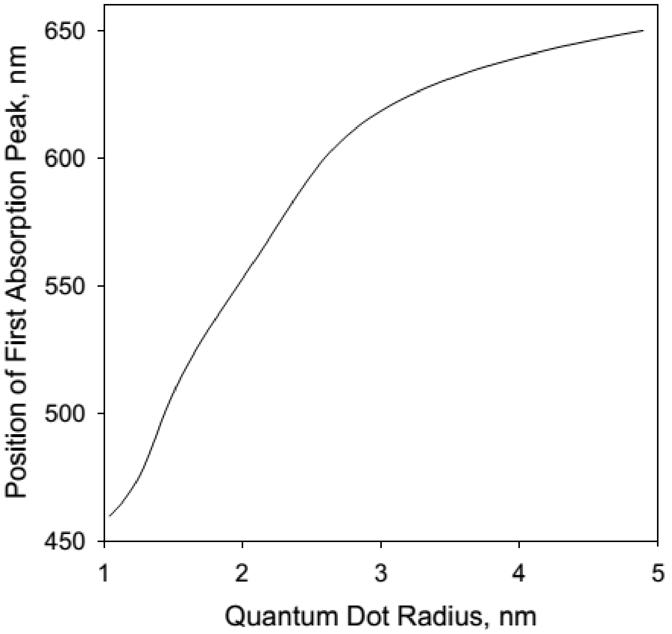

**Figure 1.5.** Variation of first absorption peak with the particle size of CdSe QDs.[57]

### 1.4.2. Optical Properties of CdSe QDs

Optical properties of CdSe QDs are very much dependent on the band structure. Bulk CdSe shows a broad and mostly featureless absorption starting at ~716 nm corresponding to excitation of electron from top of the VB to the bottom of the CB. Since CdSe QDs possess atom like discrete electronic states rather than energy bands observed in the bulk form, the absorption spectra no longer remain featureless and shows a blue shift of the first absorption peak. As can be seen in fig. 1.5(a), a 15 nm CdSe particle shows features like bulk because quantum confinement is not much dominant in this size. But the particles, less than 15 nm, have a clear sign of quantum confinement effect. To understand the optical transitions, the electronic structure of CdSe QD should be considered. Accordingly, fig. 1.5(b) shows the simplified electronic structure of CdSe

QD without the electronic or excitonic fine structure. Allowed transitions between valence and conduction states are also indicated along with a model spectrum where the features arising from these transitions are shown.

However, the valence and conduction states bear some of the basic features of the VB and CB, even if they no longer exist as distinct bands. Hence, the highest energy valence state has still higher effective mass than the lowest energy conduction state. The consequence is that when an exciton is generated, the population of hole states is much higher than that of the electron states.[49-57]

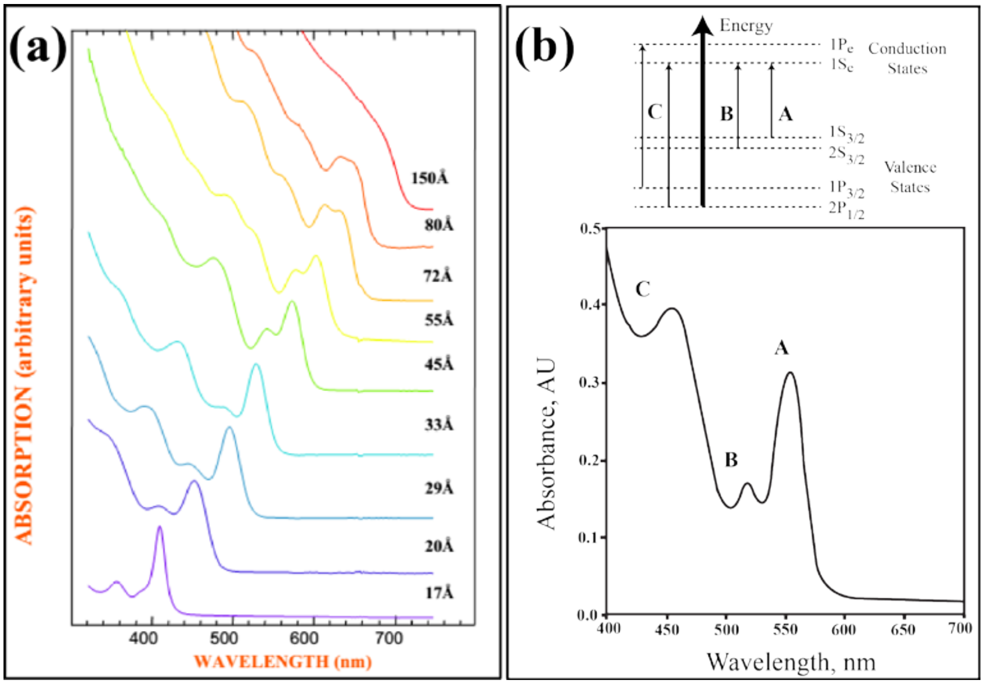

**Figure 1.5.** (a) Size dependence of the absorption spectrum of CdSe quantum dots[58a] (The numbers on the right of each spectrum represent the quantum dot diameter); (b) Simplified energy levels of CdSe QDs (fine structure is not shown; not to scale) and corresponding excitations (indicated by A, B, C).[58b]

Similar trend has been observed in the case of emission from these QDs, i.e., PL emission blue shifts as the QD size decreases.

### 1.4.3. Electronic Properties

Quantum confinement also changes the electronic properties of CdSe QDs apart from changing the optical properties as compared to that of bulk. Self- charging energy, i.e., energy required to add a charge to a neutral QD, Coulomb charging energy, i.e., energy required to add a charge of same sign to a QD which is already charged and exciton ionization energy are three properties which show variation with QD size.[16]These energies are important because they are responsible for charge transport through the QD films. Self and Coulomb charging energies are found to increase with decrease in CdSe QD size just like the blue shift in the absorption. Estimated Coulomb charging energy for CdSe QD having size <~10 nm, is >100 meV.[59] The available thermal energy at room temperature (298 K) is ~25 meV which is very less compared to the Coulomb charging energy of CdSe QDs and so cannot cause conductivity at room temperature. Consequently, high electric field is required to cause any conduction in a film of CdSe QDs. Similarly, high electric field is also required to ionize an exciton in CdSe QDs where exciton ionization energy has been found to be ~100-600 meV.[26]

### 1.4.4. Coulomb Blockade/Single Electron Transfer

Another interesting consequence of quantum confinement (and discrete atom like states) is the peculiar "single electron transfer" behavior.[60] Single electron transfer, also known as "Coulomb blockade", phenomenon is the addition or subtraction of one electron at a time to a nanoparticle for charging. In the I-V plot, this behavior is observed as staircase and so it is also known as "Coulomb staircase" behavior. Klein *et al* studied single electron behavior of CdSe QDs by fabricating a single electron transistor.[60]Alperson *et al* first showed single electron transport behavior in the electrodeposited film of CdSe QDs using scanning tunneling spectroscopy (STS) at very low temperature (4.2 K).[61]In their case, the charging energy ($E_C$) as well as inter-peak spacing have been found to increase as the dot size decreases. Fig. 1.6 shows the STS plots for the three different sizes of CdSe QDs showing Coulomb blockade behavior.

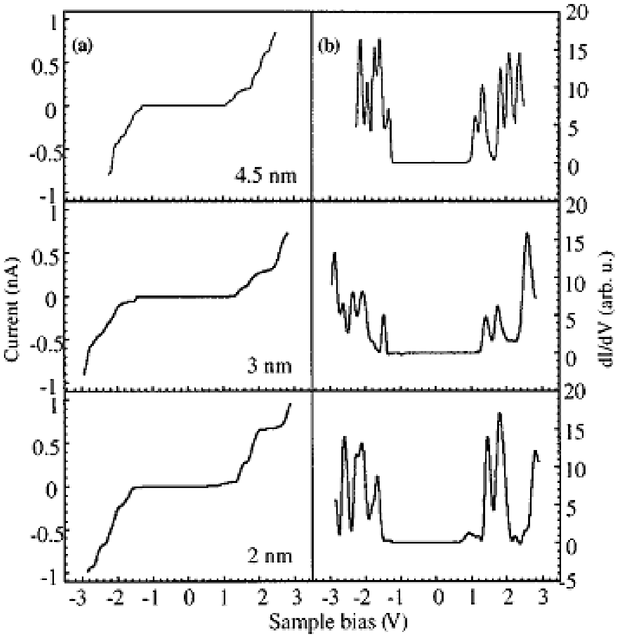

**Figure 1.6.** (a) Tunneling current *vs* applied voltage (bias) and (b) corresponding conductance spectra of CdSe QDs (2 nm, 3 nm and 4.5 nm) having three different sizes obtained at 4.2 K.[61]

## 1.5. Synthesis of CdSe Quantum Dots (CdSe QDs)

Numerous synthetic methodologies and processes have been developed during the last decade for the synthesis of CdSe QDs and various nanostructures of CdSe in general.[62-64] Of course, the synthetic method to be adopted is highly dependent on the end use of the QDs. Some of the well-known methods for growing CdSe QDs are discussed in the following sections.

### 1.5.1. Solution Synthesis

### 1.5.1.1. Hot Injection Method (Nonaqueous method)/Colloidal Synthesis

The most successful method of preparing CdSe QDs till to date is the so called “hot injection synthesis”. Alivisatos, Peng and co-workers successfully synthesized nearly monodispersed II-VI semiconductor nanoparticles by employing different cadmium (Cd) precursors in trioctylphosphine oxide (TOPO).[65-66]Various other Cd-precursors have been for this type of synthesis. Briefly, in this method Cd-precursor (CdO, $Cd(OAc)_2$, $Cd(CH_3)_2$) is allowed form a complex with the capping agents (TOPO, oleic acid, stearic acid etc.) at temperatures ranging from 250 to 350°C. When proper temperature is reached, certain amount of Se precursor (made by dissolving Se powder in either TOP or

TBP by slight warming) is injected while the solution is still hot. Immediate drop in temperature occurs and nucleation sets in. On keeping at this temperature for sometime, the solution changes color from light yellow to deep red indicating the formation of CdSe QDs. The color change is generally due to the gradual increase in particle size. This method gives highly mono-dispersed, crystalline QDs. By choosing appropriate precursor concentration, solvent, temperature and growth time, QDs of particular size, shape and concentration can be obtained. Fig. 1.7 is the schematic representation of the overall process.

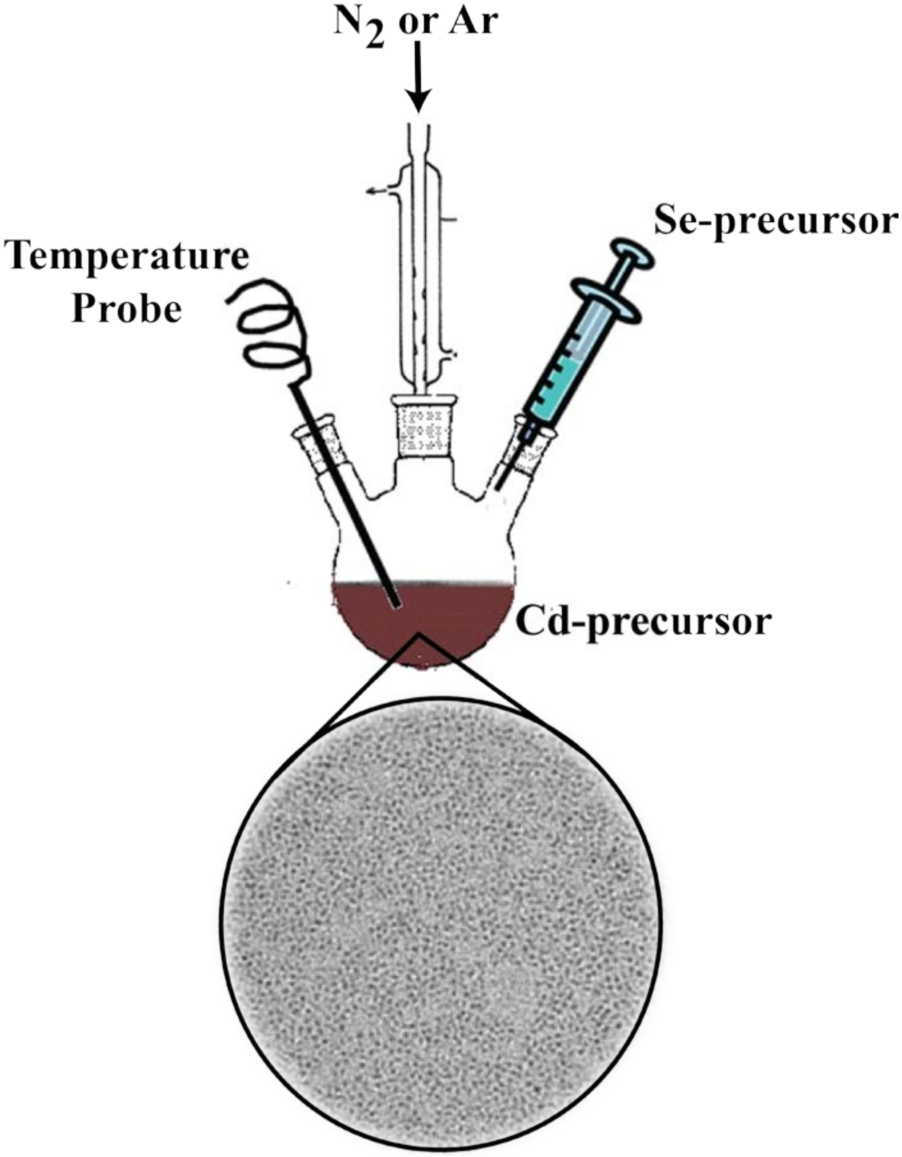

**Figure 1.7.** A schematic representation of the hot-injection method, with the low resolution TEM image of the so formed monodispersed CdSe QDs below. (present work)

### 1.5.1.2. Low Temperature Aqueous Method

This can be regarded as the aqueous version of the hot-injection method. This works at relatively low temperature. Cd-precursors used are water soluble Cd-salts such as $CdCl_2$, $Cd(OAc)_2$, $Cd(NO_3)_2$, $Cd(ClO_4)_2$ etc; whereas Se-precursor used are $Na_2SeO_3$, NaHSe, $Na_2SeSO_3$ etc. Common capping agents are 3-mercaptopropionic acid, 2-mercaptoethanol, thioglycolic acid etc. which are also water soluble. The process is highly pH sensitive. The only limitation of this method is that the CdSe QDs obtained are of slightly inferior optical quality than those obtained in the hot injection method.

### 1.5.1.3. Electrochemical Method

Electrodeposition is perhaps one of the easiest and more controllable method of CdSe QD synthesis, because the quality, phase and particle size of the deposit can be controlled by changing merely the deposition potential or the current density using modern potentiostats or galvanostats. Different groups have used different composition of solute and solvent for electrodeposition of CdSe. For example, Fawcett and Baranski have employed a composition of 100 mL DMF, 1 g $CdCl_2$, 1 g KI and saturated Se solution to deposit CdSe while [67]KI is used to make the electrodeposited film smooth and coherent. CdSe deposition has also been carried out from acidic solution which contains $CdSO_4$ as Cd and $SeO_2$ as Se source.[68-72]CdSe has also been deposited from alkaline bath containing CdO, NaOH, NaCN, $SeO_2$ and Triton X-100 surfactant for better adhesion and quality of the deposit.[68],[73] Again, Golan *et al* have electrodeposited epitaxial CdSe QDs of 5 nm size on evaporated Au (111) film from DMSO.[74] They have also shown the formation of rock-salt CdSe structure (8-coordinated) which otherwise is known to be a metastable phase and occurs at high pressure only.[75] In an another interesting approach, Mastai *et al* prepared CdSe QDs by sono-electrochemical method where simultaneous application of ultrasonication and electrochemical potential led to almost uniform size distribution of CdSe QDs.[76] However, the major limitation of this method is that it requires conducting substrate for deposition and so is of limited use in electronics.

### 1.5.1.4. Hydrothermal/Solvothermal Method

This process generally involves reactions in a closed system in the presence of a solvent (aqueous or non-aqueous) at its supercritical temperature (i.e., temperature higher than the boiling point of the solvent).[77] In 1990s, Qian, Li and co-workers developed this milder, more convenient route of 1D nanostructures of metal chalcogenide of formula, ME (M = Zn/Cd, E = S/Se) at relatively low temperature.[78-79] They studied several solvent systems including water for the reaction but CdE (E = S/Se) could only form in coordinating amine solvents (such as diethylamine, ethylenediamine, pyridine and 1,6-diaminohexane) by the elemental reaction between Cd and chalcogen at relatively low temperature.[80] Moreover, it is found that CdSe nanoparticles are only obtained when pyridine or diethylamine are used as solvents, whereas ethylenediamine leads to nanorod morphology.[81] Peng and co-workers successfully synthesized wurtzite CdSe QDs using $Cd(NO_3)_2.4H_2O$, $Na_2SeO_3$ and $N_2H_4.H_2O$ as reactants in $NH_3.H_2O$ complexation system and found that the phase of CdSe could be tuned from wurtzite to zinc blende by simply changing the complexation system from $NH_3.H_2O$ to EDTA.[82] Even more interesting is the solvothermal preparation of dodecanethiol capped, nearly monodispersed, large scale synthesis of 3 nm CdSe QDs by Gautam *et al*. Cd-stearate and $H_2Se$ were the source of Cd and Se respectively. $H_2Se$ was generated *in situ* by the reaction of elemental Se with tetralene which in turn becomes aromatic by losing a proton.[83]

### 1.5.2. Solid State Synthesis

This type of synthesis does not involve any chemical reaction in solution phase; rather all the reactions do take place in solid state and by physical forces such as heat, mechanical energy, pressure etc.

#### 1.5.2.1. Mechano-chemical Method

CdSe QDs have been prepared by ball milling elemental Cd and Se under Ar-atmosphere to protect the CdSe.[84]This type of CdSe QDs have an average particle size of 35 nm.

#### 1.5.2.2. Vapor Deposition Method

Vapor deposition methods are of two types-physical vapor deposition (PVD) and chemical vapor deposition (CVD). Although very few reports are there on PVD and CVD for CdSe synthesis, these techniques often lead to different nanostructure other than spherical CdSe. For example, CdSe nanobelts and nanosaws have been prepared by PVD method employing CdSe powder which was sublimed at 750°C and subsequently deposited on gold nanoparticles (3-5 nm) decorated single crystalline Si-substrate.[85]

On the other hand, single crystalline CdSe nanobelts have been prepared by Venugopal *et al* by a CVD method assisted by laser ablation by employing CdSe powder as source.[86] Similarly, various nanostructures of CdSe have been prepared by Zhang *et al* using Si-assisted CVD process.[87]Although the processes give good yield of the nanostructured products, they suffer from limitations of employing high temperature and/or costly apparatus which automatically increase the cost of production in large scale as is required for the industry. Maintaining proper gas flow rate, type of precursors, rate of heating and cooling can also affect the selectivity and yield of these processes significantly.

### 1.5.2.3. Molecular Beam Epitaxy (MBE) and Gas Phase Methods

Molecular beam epitaxy (MBE) is one of the several methods of depositing single crystals. MBE is widely used in the manufacture of semiconductor devices, including transistors for cellular phones and WiFi. Self assembling growth of CdSe QDs has been reported by Xin *et al* during MBE on ZnSe and ZnMnSe. The so formed CdSe QDs are uniform in size with an average diameter of 40±5 nm.[88]

Some reports are also there for the gas phase synthesis of CdSe QDs by decomposing some volatile precursors. For example, volatile chalcogenolato complexes of cadmium with stertically demanding thio- and selenophenolato ligands have been synthesized by Bochmann *et al*. These complexes decompose at temperature >350°C to form thin film of CdSe QDs.[89] Organic vapor phase epitaxy has also been used to make CdSe QD film by employing dimethylcadmium and $H_2Se$ as the precursors for Cd and Se respectively.[90]Atomic Layer Deposition (ALD) is another gas phase technique for the deposition of conformal film of CdSe. This consists of sending the Cd and Se from their respective elemental source consecutively with a dead time between the vapor pulses to stabilize the surface and to re-evaporate the possible excess material. The sequence of steps forms one complete ALD cycle. ALD differs from MBE in the fact that the constitutive elements are brought onto the surface together (at the same time) in case of MBE. ALD gives much better control on the morphology of the deposited film as compared to MBE.

Table 1.1 lists merits and demerits of all the synthetic procedures described.

**Table 1.1.** Comparison of the synthesis methods used for the synthesis of CdSe QDs

| Method | Advantage | Limitation | Reference |
|---|---|---|---|
| **Colloidal Synthesis** | Uniform particle size, good quantum yield | Poor yield per batch | [64-66] |
| **Electrochemical Synthesis** | Very easy, can be performed in ambient condition | Difficult for very small QDs (~1-3 nm), often results in dendritic growth | [67-72] |
| **Hydrothermal Synthesis** | Yield is good, easy process, common precursors | Non-uniform particle size distribution, higher surface defects | [77-79] |
| **Mechano Chemical Synthesis** | Room temperature synthesis | Bigger particle size (~35 nm), poor optical properties | [84] |
| **Vapor Deposition Methods (ALD, MBE, CVD)** | Very good control over product and/or film | High temperature process, costly accessories in some methods (MBE, ALD), slow process | [85-87] |

## 1.6. Applications of CdSe Quantum Dots

Due to its unique features like direct band-gap and excellent photoelectrical properties, CdSe finds many applications starting from optoelectronic devices to transistors, sensors and even biological labelling.

### 1.6.1. Solar Cells

CdSe is an important material for solar photovoltaic applications because of its low band-gap and good transport properties. Consequently, CdSe QDs are used in following three different ways in solar cells:

(i) It can be used as a carrier transport material because it covers almost the entire solar spectrum. For example, colloidal CdSe nanorods have been used in bilayer nanocrystal solar cells which shows power conversion efficiency of 3%.[91]Again, Kuno *et al* have found that the addition of CdSe QDs to CdSe nanowires solar cell enhances the power conversion efficiency from 13% to 25% at 500 nm.[92] Recently, Cao *et al* have developed solar cell based on CdSe nanobelt and CNT which act as both transparent medium to allow passage of light as well as provides a conducting pathway for transporting the photo-generated electrons to the current collectors.[93] A similar strategy has been also adopted to make solar cell employing CdSe nanobelt and graphene.[94]

(ii) CdSe QDs can be decorated on inorganic nanostructures such as $TiO_2$ or ZnO nanoparticles for quantum dot sensitized solar cells (QDSSCs). Due to its tunable optical properties, CdSe QDs or nanostructures in general can function as efficient sensitizer through the entire visible region.[95] For example, CdSe QD decorated $TiO_2$ nanotube arrays has been shown to give an efficiency as high as 4.15%.[96]

(iii) Hybrids of CdSe QDs and conjugate polymers are also an interesting materials for solar cells because they allow the unique optoelecronic properties of organic semiconductors to be coupled with the intriguing properties of CdSe QDs. Accordingly, CdSe nanorods with good hole transporting polymer P3HT have been utilized in fabricating nanorod-polymer blend solar cell with external quantum efficiency as high as 59% under 0.1 $mWcm^{-2}$ illumination at 450 nm.[97]

### 1.6.2. Photodetectors

Photodetectors are a class of important optoelectronic device which are used for photon detection in the UV or IR region. This has so many practical applications such as biological diagnostics, chemical sensors, missile launch and light-wave communications. The heart of a photodetector is a semiconductor which absorbs light with higher energy than the band-gap energy of the semiconductor.[98] CdSe, being a direct and low band-gap semiconductor material, is an ideal candidate for photodetectors. For example, a photodetector has been successfully prepared using CVD grown CdSe nanoribbons. The device shows photoconductance of the CdSe nanoribbons to be 2816 nS at 650 nm and 0.095 nS in the dark condition.[99]

### 1.6.3. Light Emitting Diodes (LEDs)

Light emitting diodes (LEDs) are solid state devices. Much attention is now being focused for the development of low cost, highly efficient LEDs of different color, especially a need exists for white light LEDs in order to replace the conventional light source. High quality CdSe QDs has high quantum efficiency and the size can be tuned so as to control their emission within 500 and 650 nm. So CdSe QDs are interesting as LED material. For example, Rosenthal *et al* demonstrated white light emission from ultra small CdSe QDs.[100-101]These ultra-small CdSe QDs show emissions from 420-710 nm (broadband emission) without suffering the problem of self-absorption. CdSe QDs have also been utilized as the red emitting counterpart in LEDs. For example, Jeon *et al* have recently synthesized greenish-yellow emitting $Sr_3SiO_5:Ce^{3+}$, $Li^+$ and high quality TOP/TOPO/HAD-capped CdSe QDs. They fabricated a LED which can render good colors, by coating the two luminescent materials on a blue LED chip.[102]

### 1.6.4. Biological Applications

Long lived, stable, narrow PL is the key feature which makes CdSe QDs attractive for biologists. Its intrinsic PL has been widely exploited for bio-imaging. CdSe QDs have also been used for biosensors. Nocera *et al* systematically reviewed the applications of CdSe QDs as biosensors.[103-105]

Moreover, CdSe QDs have also been employed in other applications such as emitters for color displays,[106]optical fiber amplifiers,[107] low threshold lasers, self assembled photonic sphere arrays, optical temperature probes, chemical sensors,[108] etc.

## 1.7. Conclusions and Perspectives

Some of the most interesting developments of CdSe QDs and its hybrid nano-structures are reviewed in this chapter with special emphasis on the synthesis, properties and various applications. Theory along with experimental evidence suggests intriguing structure and size as well as shape dependent optical and electronic properties of these semiconductor nanoparticles. Presence of discrete, atom like states in QDs has profound impact on nanoelectronics, especially for designing single electron transistors, single photon counting devices etc. Also, having vast tunability with respect to their structure and property, these applications are expected to lead the prospect of this field for continuing decades perhaps, with immense benefits in many areas like energy, healthcare and environmental monitoring. More precisely, they act as the building blocks for hierarchical, multifunctional, tailor-made materials with potential applications in our day-to-day life. However, although there are so many methods available for the synthesis and applications of CdSe QDs and the hybrids, several daunting challenges of these materials such as development of low cost, synthetic methods, scale up synthesis as well as ease of fabrication of devices requires breakthrough results for the sake of technology.

### 1.8. Motivation, Scope and Organization of the Thesis

The genesis of the present thesis is inspired by many of the interesting issues unraveled during the preparation of the above critical review related to both fundamental and applied aspects of CdSe QDs and its hybrids. This includes the development of novel approaches to synthesize CdSe QDs directly on graphene or graphene nanoribbons (GNRs), followed by their detailed characterizations. If processed properly, these QDs and also their hybrids can open up new avenues for various unprecedented applications. As a consequence, it is imperative to study different properties such as optical, electrochemical, wetting for the pursuit of various applications.

### 1.9. Objectives of the Present Investigation

The present thesis attempts to address some of the above challenges by designing new synthetic methodologies followed by chemical and electrochemical characterization. More specifically, the objectives of the thesis are set as follows:

(i) To study the band structure parameters (HOMO-LUMO positions) of CdSe QDs of different sizes by various electrochemical techniques starting from cyclic voltammetry (CV), differential pulse voltammetry (DPV), chronoamperometry and electrochemical impedance spectroscopy.

(ii) To study the wetting properties of CNTs with various liquids including water.

(iii) To generate CdSe QDs electrochemically directly on graphene nanoribbons obtained from unzipping of CNTs and characterization of the hybrids.

(iv) To develop new methodology to make thiol terminated graphene using diazonium salt chemistry and using it to anchor CdSe QDs.

(v) To study the excited state charge transfer dynamics of CdSe QDs and those attached to thiol modified graphene.

(vi) To study the photovoltaic properties of the CdSe QD-thiolated graphene hybrids.

(vii) To synthesize CdSe nanotubes by ZnO template assisted electrodeposition for the fabrication of a n-p heterojunction diode for optoelectronic applications.

The present thesis consists of six chapters which discuss few novel methods of preparing CdSe and its hybrids with carbon based materials, namely CNTs and graphene as well as with p-type $Cu_2O$, their detail characterizations using various techniques followed by potential applications in case of energy generation. **Chapter 1** is a critical survey of Quantum dots and CdSe QDs in particular. Variation in optical as well as electronic properties with variation in size and shape has been discussed with little theoretical discussion. The chapter also discusses various synthetic methods available so far for the synthesis of CdSe QDs along with special emphasis on various characterization techniques starting from spectroscopic and microscopic to electrochemical techniques. Finally, the potential applications of these QDs for solar cells, photodetectors, water splitting etc. have been introduced. The chapter concludes by setting up the specific objectives for the present study, future prospects and finally mentioning some of the existing limitations of these QDs and QD based hybrid nanomaterials.

**Chapter 2** illustrates the electrochemical properties of CdSe QDs of varying size. The prepared QDs have been characterized by various techniques starting from UV-Vis, PL, powder X-ray diffraction (PXRD) to light scattering techniques. Absolute band positions of these QDs along with their electrochemical bandgap variation have been studied in detail by various electrochemical techniques starting from cyclic voltammetry, differential pulse voltammetry and impedance techniques.

**Chapter 3** is about the exploratory behavior of QDs attached to carbon nanostructures, especially carbon nanotubes and graphene nanoribbons. More specifically, single walled carbon nanotube (SWCNT) surface is modified with –PhSH group with the help of diazonium functionalization in order to anchor oleic acid capped CdSe QDs *via*a simple solution exchange methodology. Wetting behavior of pristine as well as functionalized CNTs is studied with water and various organic liquids. Electrochemical properties of the QD-CNT/GNR hybrids are studied with DPV, CV and impedance. In the next part of the chapter CdSe QDs have been decorated on graphene nanoribbons (GNRs) obtained from the electrochemical unzipping of SWCNTs to understand the properties of CdSe QDs in presence of quasi 2-D carbon sheet. GNR is chosen because it's band structure and properties are different as compared to that of CNT or graphene (2-D). More interestingly, the width of the GNR has a profound effect on its band structure in controlling the edge-states. The resulting hybrid has been characterized using various techniques starting from PXRD, UV-Vis, PL to electrochemical techniques. Micro Raman has been used extensively to study the unzipping process of SWCNT and subsequent CdSe QD attachment *via* electrochemical technique. Photoconductivity study has been carried out to explore these materials as potential candidates for 3rd generation solar cells, photodetectors and other optoelectronic devices.

**Chapter 4** illustrates the study of the hybrid consisting of CdSe QDs attached to Graphene (a real 2-D system) *via* –PhSH linker group. This chapter is divided into two parts. In the first part of the chapter, Graphene, derived from the reduction of graphene oxide with $NaBH_4$, surface is modified with –PhSH group with the help of diazonium functionalization followed by the attachment of oleic acid capped CdSe QDs *via*a simple solution exchange methodology. The resulting hybrid has been studied with various characterization techniques such as FTIR, elemental mapping, cyclic voltammetry, impedance technique, contact angle measurement, micro Raman, UV-Vis, steady state PL, TEM and XPS. The strategy has been unique in facilitating monodisperse, predefined size CdSe QDs to be arranged on 2-D plane of graphene with the help of very simple solution chemistry. XPS result confirms the binding of CdSe to the –SH group on graphene surface. In the second part, ultrafast charge carrier dynamics study has been carried out in order to understand charge transfer from excited CdSe QDs to –PhSH functionalized graphene. Time resolved photoluminescence measurement has been carried out along with steady state PL for this purpose. Charge transfer has been found to be the major pathway for the deactivation of excited QDs in presence of –SH functionalized graphene and the rate of electron transfer has been estimated as high as $\sim 13 \times 10^{8}\ s^{-1}$. Moreover, a prototype bulk hetero-junction has been made out of this hybrid employing PEDOT:PSS as a hole-conducting layer and it is found to show good photoconductivity in presence of AM 1.5 solar simulated light. This again proves the use of this hybrid-material for solar cells and other optoelectronic devices. The chapter ends with the conclusion of developing a new hybrid system for potential solar applications.

**Chapter 5** describes the electrochemical synthesis of vertically aligned CdSe nanotubes on conducting glass substrates (FTO). In order to facilitate this ZnO NWs have been grown first on FTO plates using hydrothermal method followed by electrodeposition of

CdSe on ZnO NWs. Removal of the ZnO core results in hollow, vertically aligned CdSe nanotubes which retain the morphology of ZnO NW templates. SEM, TEM, electrochemical techniques, micro Raman, UV-Vis, PL are used to characterized the materials. Next, p-type $Cu_2O$ film has been electrodeposited on FTO plates from a copper-lactate bath. The two FTO plates-one containing CdSe nanotubes and another containing $Cu_2O$, are then brought in intimate contact with each other in a flip-chip geometry. I-V measurement shows the formation n-p type hetero-junction at the interface. The resulting hetero-junction shows good photoconductivity in presence of AM 1.5 solar simulated light. Further, a threefold increment in conductivity has been observed for this system in presence of light, thereby proving the system to be a good photon harvesting device. The role of individual interface and shape and size dependant performance parameters are discussed on the basis of I-V plots.

**Chapter 6** is a summary of all the major conclusions of the present study with respect to the preparation, characterization, properties and potential applications of these hybrid nanomaterials. It also indicates the possible advantage of CdSe and CdSe based hybrid nanostructures for the fabrication of next generation optoelectronic devices with the much sought flexibility in the resulting devices. This chapter also outlines some of the limitations of this electrochemical synthesis along with ample scope of further work in this area and its bright future prospects.

The results presented in the thesis clearly suggest the usefulness of CdSe QDs and its hybrid nanostructures as multifunctional materials for many industrial applications like solar cells, nanoelectronics and biological imaging. The possibility of manipulating the optical properties as well as electron transfer characterisics of CdSe QDsby combining with different materials (particularly carbonaceous nanomaterials) has also been demonstrated which is expected to resolve several important issues related to fundamental properties of CdSe QDs and their interactions with hybrids. The insights obtained from these are valid for all types of quantum dots, which could be of immense utility in designing new materials with improved performance attributes.

## 1.10. References

1. (a) Kurtoglu, M. E.; Longenbach, T.; Reddington, P.; Gogotsi, Y. *J. Am. Ceram. Soc.* **2011**, *94 (4)*, 1101. (b) Ge, L.; Sethi, S.; Ci, L.; Ajayan, P. M.; Dhinojwala, A. *Proc. National Acad. Sciences* **2007**, *104*, 10792. (c) "Nanotechnology Consumer Products". *nnin.org*. **2010,** Retrieved April 21, **2014**. (d) "Nanotechnology Information Center: Properties, Applications, Research, and Safety Guidelines". American Elements. Retrieved April 21, **2014**. (e) http://www.azonano.com/article.aspx?ArticleID=3396, Retrived April 21, **2014**. (f) Shulaker, M. M.; Hills, G.; Patil, N.; Wei, H.; Chen, H.-Y.; Wong, H.-S. P.; Mitra, S. *Nature* **2013**, *501*, 526. (g) http://www.sigmaaldrich.com/materials-science/nanomaterials/gold-nanoparticles.html, Retrived April 21, **2014**. (h) Wang, S.; Jiang, L. *Adv. Mater.* **2007**, *19*, 3423. (i) Young, T. *Phil. Trans. R. Soc. Lond.* **1805**, *95*, 65. (j) Wenzel, R. N. *Ind. Eng. Chem.* **1936**, *28*, 988. (d) Extrand, C. *Langmuir* **2005**, *68*, 2495. (k) Johnson, R E.; Dettre, R. H. *J. Phys. Chem.* **1964**, *68*, 1744. (l) Onda, T.; Shibuichi, S.; Satoh, N.; Tsujii, K. *Langmuir* **1996**, *12*, 2125. (m) Miwa, M.; Nakajima, A.; Fujishima, A.; Hashimoto, K.; Watanabe, T. *Langmuir* **2000**, *16*, 5754. (n) Shirtcliffe, N. J.; McHale, G.; Newton, M. I.; Perry, C. C. *Langmuir* **2003**, *19*, 5626. (o) Teare, D.; Spanos, C. G.; Ridley, P.; Kinmond, E. J.; Roucoules, V.; Badyal, J. P. S.; Brewer, S. A.; Coulson, S. *Chem. Mater.* **2002**, *14*, 4566. (p) Bico, J.; Marzolin, C.; Quere, D. *Europhys. Lett.***1999**, *47*, 743. (q) Extrand, C. *MRS Bulletin* **2008**, 733. (r) Gao, L. C.; McCarthy, T. J. *Langmuir* **2007**, *23*, 3762. (s) Chen, W.; Fadeev, A. Y.; Hsieh, M. C.; Oner, D.; Youngblood, J.; McCarthy, T. J. *Langmuir* **1999**, *15*, 3395. (t) Wang, S. T.; Liu, H.; Jiang, L. *Ann. Rev. Nano Res.* **2006**, *1*, 573. (u) Lim, H. S.; Kwak, D.; Lee, D. Y.; Lee, S. G.; Cho, K. *J. Am. Chem. Soc.* **2007**, *129*, 4128. (v) Xue, C. H. *Sci. Technol. Adv. Mater.* **2008**, *9*, 035008. (w) Xue, C. H. *Sci. Technol. Adv. Mater.* **2008**, *9*, 035001. (x) Yuan, Z. *Sci. Technol. Adv. Mater.* **2008**, *9*, 045007. (y) Ressine, A.; Marko-Varga, G.; Laurell, T. *Biotechnol. Ann. Rev.* **2007**, *13*, 149.

2. (a) Zhen, H. L.; Donald G. T. *J. Am. Chem. Soc.* **2008**, *130*, 12698. (b) Nagarajan, R. *ACS Symposium Series* **2008**, *996*, 2**.** (c) Drexler, E. *Enginesof Creation: The Coming Era of Nanotechnology;* Anchor Press/ Doubleday: New York, **1986**. (d) Drexler, K.

E. *Nanosystems: molecular machinery, manufacturing and computation;* John Wiley & Sons: New York, **1992**. (e) Kohler, M.; Fritzsche, W. *Nanotechnology, An Introduction to Nanostructuring Techniques*, Wiley-VCH Verlag GmbH and Co. KgaA, **2004**.

3. (a) West, A. R. *Solid State Chemistry and Its Applications.* **ISBN: 978-0-471-90874-6.** (b) Cottey A. A. *J. Phys. C: Solid State Phys.***1971**, *4*, 1734**.**
4. (a) Rao, C. N. R.; Thomas, P. J.; Kulkarni, G. *Nanocrystals:: Synthesis, Properties and Applications, Vol. 95*, Springer **2007**. (b) Leutwyler, W. K.; Bürgi, S. L.; Burgl, H. *Science* **1996**, *271*, 933. (c) Alvisatos, A.P. *Science* **1996**, *271*, 933.
5. Alivisatos, A. P. *J. Phys. Chem.* **1996**, *100*, 13226.
6. Vossmeyer, T.; Katsikas, L.; Giersig, M.; Popovic, I.; Diesner, K.; Chemseddine, A.; Eychmüller, A.; Weller, H. *J. Phys. Chem.* **1994**, *98*, 7665.
7. Leutwyler, W. K.; Bürgi, S. L.; Burgl, H. *Science* **1996**, *271*, 933.
8. Goldstein, A.; Echer, C.; Alivisatos, A. *Science* **1992**, *256*, 1425.
9. Tolbert, S. H.; Alivisatos, A. *Annu. Rev. Phys. Chem.***1995**, *46*, 595.
10. Buhro, W. E.; Colvin, V. L. *Nature materials* **2003**, *2*, 138.
11. (a) Maksym, P.; Chakraborty, T. *Phys. Rev. Lett.***1990**, *65*, 108. (b) Chakraborty, T. *Matter Phys.* **1992,**16, 35; Maksym, P. A.; Chakraborty T. *Phys. Rev. Lett.* **1990**, *65*, 108. (c) Chakraborty, T.: *Quantum Dots: A survey of the properties of artificial atoms*; Elsevier, **1999**. (d) Kasfner, M. A.: Artificial atoms. *Physics today* **1993**, 25. (e) Reed, M. A. *Scientific American* **1993**, *268*, 118. (f) Leutwyler, W. K.; Bürgi, S. L.; Burgl, H. *Science* **1996**, *271*, 933. (g)Ashoori, R. *Nature* **1996**, *379*, 413. (h) McEuen, P. L. *Science* **1997**, *278*, 1729. (i) Gammon, D. *Nature* **2000**, *405*, 899.
12. (a) Ekimov, A. I.; Onushchenko, A. A.Fiz. Tekh. PoluproVodn.**1982**, *16*, 1215 (Translation: SoV. Phys. Semicond. ***1982****, 16, 775).* (b) Rossetti, R.; Nakahara, S.; Brus, L. *J. Chem. Phys.* **1983**, *79*, 1086.
13. Kittel, C.; McEuen, P.: *Introduction to solid state physics*; Wiley New York, **1986***; Vol. 8***.**
14. Efros, A. L.; Rosen, M. *Annu. Rev. Mater. Sci.* **2000**, *30*, 475.
15. Efros, A. L.; Efros, A. L. *Soviet Physics Semiconductors-Ussr* **1982**, *16*, 772.
16. Brus**,** L. *J. Chem. Phys.* **1983**, *79*, 5566.

17. Brus, *L.* E. *J. Chem. Phys.* **1984**, *80*, 4403.
18. Dabbousi, B. O.; Rodriguez-Viejo, J.; Mikulec, F. V.; Heine, J. R.; Mattoussi, H.; Ober, R.; Jensen, K. *F.; Bawendi, M. G. J. Phys. Chem. B* **1997**, *101*, 9463.
19. http://www.nanocrystals.nl/Photos.HTML (last retrieved on 29th March, **2014**).
20. Nirmal, M.; Dabbousi, B.; Bawendi, M.; Macklin, J.; Trautman, J.; Harris, T.; Brus, L. *Nature* **1996**, *383*, 802.
21. Fisher, B. R.; Eisler, H.-J.; Stott, N. E.; Bawendi, M. G. *J. Phys. Chem. B* **2004**, *108*, 143.
22. Leatherdale, C. A.; Woo, W. -K.; Mikulec, F. V.; Bawendi, M. G. *J. Phys. Chem. B* **2002,** *106* (31), 7619.
23. Nozik, A. *J. Chem. Phys. Lett.* **2008**, *457*, 3.
24. (a) Coe-Sullivan, S.; Woo, W.-K.; Steckel, J. S.; Bawendi, M.; Bulović, V. *Org. Electron.***2003**, *4*, 123. (b) Coe, S.; Woo, W.-K.; Bawendi, M.; Bulović, V. *Nature* **2002**, *420*, 800. (c) Colvin, V.; Schlamp, M.; Alivisatos, A. *Nature* **1994**, *370*, 354. (d) Dabbousi, B.; Bawendi, M.; Onitsuka, O.; Rubner, M. *Appl. Phys. Lett.***1995**, *66*, 1316.
25. (a) Eisler, H.-J.; Sundar, V. C.; Bawendi, M. G.; Walsh, M.; Smith, H. I.; Klimov, V. *Appl. Phys. Lett.***2002**, *80*, 4614. (b) Sundar, V. C.; Eisler, H. J.; Bawendi, M. G. *Adv. Mater.***2002**, *14*, 739.
26. (a) Bawendi, M. G.: The electronic and optical properties of close packed cadmium selenide quantum dot solids. Massachusetts Institute of Technology, **1996**. (b) Leatherdale, C.; Kagan, C.; Morgan, N.; Empedocles, S.; Kastner, M.; Bawendi, M. *Phys. Rev. B* **2000**, *62*, 2669. (c) Jarosz, M.; Stott, N.; Drndic, M.; Morgan, N.; Kastner, M.; Bawendi, M. *J. Phys. Chem. B* **2003**, *107*, 12585. (d) Drndić, M.; Jarosz, M.; Morgan, N.; Kastner, M.; Bawendi, M. *J. Appl. Phys.* **2002**, *92*, 7498. (e) Ting, D. Z.; Soibel, A.; Keo, S. A.; Rafol, S. B.; Mumolo, J. M.; Liu, J. K.; Hill, C. J.; Khoshakhlagh, A.; Hoeglund, L.; Luong, E. M.; Gunapala, S. D. *J. Appl. Remote Sens.* **2014**, *8*. (f) Chen, M.; Yu, H.; Kershaw, S. V.; Xu, H.; Gupta, S.; Hetsch, F.; Rogach, A. L.; Zhao, N. *Adv. Funct. Mater.* **2014**, *24*, 53. (g) Gustafsson, O.; Karim, A.; Asplund, C.; Wang, Q.; Zabel, T.; Almqvist, S.; Savage, S.; Andersson, J. Y.; Hammar, M. *Infrared Phys. Technol.* **2013**, *61*, 319. (h) Lao, Y.-F.; Wolde, S.;

Perera, A. G. U.; Zhang, Y. H.; Wang, T. M.; Liu, H. C.; Kim, J. O.; Schuler-Sandy, T.; Tian, Z.-B.; Krishna, S. S. *Appl. Phys. Lett.* **2013**, *103*. (i) Lao, Y.-F.; Wolde, S.; Perera, A. G. U.; Zhang, Y. H.; Wang, T. M.; Liu, H. C.; Kim, J. O.; Schuler-Sandy, T.; Tian, Z.-B.; Krishna, S. S. *Appl. Phys. Lett.* **2013**, *103*.

27. (a) Miralaie, M.; Leilaeioun, M.; Abbasian, K.; Hasani, M. *J. Comput. Theor. Nanos.* **2014**, *11*, 15. (b) See, A. M.; Klochan, O.; Micolich, P.; Aagesen, M.; Lindelof, P. E.; Hamilton, A. R. *J. Phys. Cond. Mat.* **2013**, *25*.
28. Bruchez, M.; Moronne, M.; Gin, P.; Weiss, S.; Alivisatos, A. P. *Science* **1998**, *281*, 2013.
29. Taik Lim, Y.; Kim, S.; Nakayama, A.; Stott, N. E.; Bawendi, M. G.; Frangioni, J. V. *Mol. Imaging* **2003**, *2*.
30. Kim, S.; Lim, Y. T.; Soltesz, E. G.; De Grand, A. M.; Lee, J.; Nakayama, A.; Parker, J. A.; Mihaljevic, T.; Laurence, R. G.; Dor, D. M. *Nat. Biotechnol.* **2004**, *22*, 93.
31. Dahan, M.; Laurence, T.; Pinaud, F.; Chemla, D.; Alivisatos, A.; Sauer, M.; Weiss, S. *Opt. Lett.* **2001**, *26*, 825.
32. Kastner, M. A. *Physics Today* **1993,** *46 (24)*, 24.
33. Moison, J. M.; Houzay, F.; Barthe, F.; Leprince, L.; Andre, E.; Vatel, O. *Appl. Phys. Lett.* **1994**, *64 (2)*, 196.
34. Leonard, D.; Krishnamurthy, M.; Reaves, C. M.; Denbaars, S. P.; Petroff, P. M. *Appl. Phys. Lett.* **1993** *63 (23)*, 3203.
35. http://en.wikipedia.org/wiki/Cadmium_selenide (last retrieved on 29th March, **2014**).
36. Lev Isaakovich Berger (**1996**). *Semiconductor materials*. CRC Press. p. 202. ISBN 0-8493-8912-7.O. Madelung, ed., Crystal and Solid State Physics, Landolt Bornstein Numerical
37. Data and Functional Relationships in Science and Technology (Springer-Verlag, Berlin, **1982**), Vol. 17b: Physics of II-VI and I-VII Compounds, Semimagnetic Semiconductors.
38. Peng , Q.; Dong , Y. J.; Demng , Z. X.; Li , Y. D. *Inorg. Chem.* **2002**, *41*, 5249.
39. Blanton, S. A.; Dehestani, A.; Guyot-Sionnest, P.; Lin, P. C. *Chem. Phys. Lett.***1994**, *229*, 317.

40. Murray, C. B.: Synthesis and characterization of II-IV quantum dots and their assembly into 3D quantum dot superlattices. Massachusetts Institute of Technology, **1995**.
41. Klimov, V. I. *Los Alamos Science* **2003**, *28*, 214.
42. Min, S.-K.; Lee, W.; Cai, G.; Lee, M.; Cho, B. W.; Lee, S.-H.; Han, S.-H. *J. Nanosci. Nanotechno.* **2009**, *9*, 7123.
43. Dixit, S. K.; Madan, S.; Kaur, A.; Madhwal, D.; Singh, I.; Bhatnagar, P. K.; Mathur, P. C.; Bhatia, C. S. *J. Renew. Sus. Energy* **2013**, *5*.
44. Mondal, S. P.; Bera, S.; Narender, G.; Ray, S. K. *Appl. Phys. Lett.* **2012**, *101*, 173108.
45. Zarazua, I.; De la Rosa, E.; Lopez-Luke, T.; Reyes-Gomez, J.; Ruiz, S.; Angeles Chavez, C.; Zhang, J. Z. *J. Phys. Chem. C* **2011**, *115*, 23209.
46. Kulakovich, O.; Strekal, N.; Yaroshevich, A.; Maskevich, S.; Gaponenko, S.; Nabiev, I.; Woggon, U.; Artemyev, M. *Nano Lett.* **2002**, *2*, 1449.
47. Medintz, I. L.; Uyeda, H. T.; Goldman, E. R.; Mattoussi, H. *Nature materials* **2005**, *4*, 435.
48. Ghosh, T.; Cho, K. Y.; Ullah, K.; Nikam, V.; Park, C. Y.; Meng, Z. D.; Oh, W. C. *J. Ind. Eng. Chem.* **2013,** *19(3)*, 797.
49. Efros, A. L.; Rosen, M. *Phys. Rev. B* **1998**, *58*, 7120. (b)
50. Madelung, O. ed., Crystal and Solid State Physics, Landolt Bornstein Numerical Data and Functional Relationships in Science and Technology (Springer-Verlag, Berlin, 1982), Vol. 17b: Physics of II-VI and I-VII Compounds, Semimagnetic Semiconductors.
51. Guyot-Sionnest, P.; Shim, M.; Matranga, C.; Hines, M. *Phys. Rev. B***1999**, *60*, R2181.
52. Guyot-Sionnest, P.; Hines, M. A. *Appl. Phys. Lett.***1998**, *72*, 686.
53. Shim, M.; Shilov, S. V.; Braiman, M. S.; Guyot-Sionnest, P. *J. Phys. Chem. B* **2000**, *104*, 1494.
54. Shim, M.; Guyot-Sionnest, P. *Nature* **2000**, *407*, 981-983.
55. Shim, M.; Wang, C.; Guyot-Sionnest, P. *J. Phys. Chem. B* **2001**, *105*, 2369.
56. Wang, C.; Shim, M.; Guyot-Sionnest, P. *Appl. Phys. Lett.* **2002**, *80*, 4.
57. Kuno, M. K. "Band Edge Spectroscopy of CdSe QuantumDots," (Massachusetts Institute of Technology, Cambridge, **1998**)

58. (a) Leatherdale, C. A. "Photophysics of CadmiumSelenide QuantumDot Solids," (Ph.D. Thesis, Massachusetts Institute of Technology, Cambridge, MA, **2000**). (b) Jarosz, M.: The physics and chemistry of transport in CdSe quantum dot solids. Massachusetts Institute of Technology, **2004**.
59. (a) Romero, H. E.; Drndic, M. *Phys. Rev. Lett.* **2005**, *95*, 156801. (b) Shinde, D. B.; Pillai, V. K. *Angew. Chem. Int. Ed.* **2013**, *52*, 2482.
60. Klein, D. L.; Roth, R.; Lim, A. K.; Alivisatos, A. P.; McEuen, P. L. *Nature* **1997**, *389*, 699.
61. Alperson, B.; Rubinstein, I.; Hodes, G.; Porath, D.; Millo, O. *Appl. Phys. Lett.* **1999**, *75*, 1751.
62. Yu, S.-H.; Yang, J.; Han, Z.-H.; Yang, R.-Y.; Qian, Y.-T.; Zhang, Y.-H. *J. Solid State Chem.* **1999**, *147*, 637.
63. Zhao, L.; Hu, L.; Fang, X. *Adv. Funct. Mater.***2012**, *22*, 1551.
64. Manna , L.; Scher , E. C.; Li , L. S.; Alivisatos , A. P. *J. Am. Chem. Soc.* **2002**, *124*, 7136.
65. Peng, Z. A.; Peng, X. G. *J. Am. Chem. Soc.* **2002**, *124*, 3343.
66. Fawcett, W. R.; Baranski, A. S. **1983**. U.S. Pat. No. 4, 376, 682.
67. Hodes, G.; Manassen, J.; Neagu, S.*Thin Solid Films* 1**982,** *90* 433.
68. Hodes, G.; Manassen, J.; Cahen, D. *Nature* 1**976**, *261*, 403.
69. Tomkiewicz, M.; Ling, I.; Parsons, S. *J. Electrochem. Soc.* **1982**, *129*, 2016.
70. Boudreau, R A.; Rauh, R D. *Sol. Energy Mater.* **1982** *7* 385.
71. Vas'ko, A. T.; Tsikovkin, E. M.; Kovach, S. K. *U kr. Khim. Zh.* **1983,** 49, 1074.
72. Skyllas Kazacos, M. *J. Electroanal. Chem.* **1983**, *148*, 233.
73. Golan, Y.; Hodes, G.; Rubinstein, I. *J. Phys. Chem.* **1996**, *100*, 2220.
74. Zhang, Y.; Hodes, G.; Rubinstein, I.; Gruenbaum, E.; Nayak, R. R.; Hutchison, J. L. *Adv. Mater.***1999**, *11*, 1437.
75. Mastai, Y.; Polsky, R.; Koltypin, Y.; Gedanken, A.; Hodes, G. *J. Am. Chem. Soc.* **1999**, *121*, 10047.
76. Demazeau, G. *J. Mater. Sci.* **2008**, *43*, 2104.
77. Li , Y. D.; Liao, H. W.; Fan, Y.; Li, L. Q.; Qian, Y. T. *Mater. Chem. Phys.* **1999**, *58*, 87.

78. Wang, W. Z; Geng, Y.; Yan , P.; Liu , F. Y.; Xie , Y.; Qian, Y. T. *Inorg. Chem. Commun.* **1999**, *2*, 83.
79. Peng, Q.; Dong , Y. J.; Demg , Z. X.; Sun , X. M.; Li , Y. D. *Inorg. Chem.* **2001**, *40*, 3840.
80. Li, Y. D.; Liao, H. W.; Ding , Y.; Fan , Y.; Zhang , Y.; Qian, Y. T. *Inorg. Chem.* **1999**, *38*, 1382 .
81. Peng , Q.; Dong , Y. J.; Demng , Z. X.; Li , Y. D. I*norg. Chem*. **2002**, *41*, 5249.
82. Gautam, U. K.; Rajamathi, M.; Meldrum, F.; Morgan, P.; Seshadri, R. *Chem. Commun.***2001**, 629.
83. Baláž, P.; Jardin, R.; Dutková, E.; Sayagués, M.; Baláž, M.; Mojžušová, G.; Mojžiš, J.; Turianicová, E.; Fabián, M. *Acta Phys. Pol. A.***2012**, *122.*
84. Ma , C.; Ding , Y.; Moore , D.; Wang, X. D.; Wang , Z. L. *J. Am. Chem. Soc.* **2004**, *126*, 708.
85. Venugopal , R.; Lin, P. I.; Liu, C. C.; Chen, Y. T. *J. Am. Chem. Soc.* **2005**, *127*, 11262.
86. Wang , Z. Y. Q. F. Lu , X. S. Fang , X. K. Tian , L. D. Zhang , *Adv. Funct. Mater.* 2006, 16, 661.
87. (a) Xin, S.; Wang, P.; Yin, A.; Kim, C.; Dobrowolska, M.; Merz, J.; Furdyna, J. *Appl. Phys. Lett.***1996**, *69*, 3884. (b) Kany, F.; Hartmann, J.; Ulmer-Tuffigo, H.; Mariette, H. *Superlattices Microstruct.***1998**, *23*, 1359.
88. Bochmann, M.; Webb, K.; Harman, M.; Hursthouse, M. B. *Angew. Chem. Int. Ed. English* **1990**, *29*, 638.
89. Fryer, J. *J. Mater. Chem.***1997**, *7*, 1855.
90. Gur, I.; Fromer , N. A.; Geier, M. L.; Alivisatos, A. P. *Science* **2005**, *310*, 462.
91. Yu , Y. H.; Prashant, V. K.; Masaru, K. *Adv. Funct. Mater.* **2010**, *20*, 1464.
92. Zhang, L. H.; Jia , Y.; Wang , S. S.; Li , Z.; Ji , C. Y.; Wei , J. Q; Zhu , H. W.; Wang, K. L.; Wu, D. H.; Shi, E. Z.; Fang , Y.; Cao , A. Y. *Nano Lett*. **2010**, *10*, 3583.
93. Zhang , L. H.; Fan, L. L.; Li, Z.; Shi, E. Z.; Li, X. M.; Li, H. B.; Ji, C. Y.; Jia, Y.; Wei , J. Q.; Wang , K. L.; Zhu , H. W.; Wu , D. H.; Cao, A. Y. *Nano Res.* **2011**, *4*, 891.

94. Zhang, L. H.; Fan, L. L.; Li , Z.; Shi, E. Z.; Li , X. M.; Li , H. B.; Ji , C. Y.; Jia , Y.; Wei , J. Q.; Wang , K. L.; Zhu , H. W.; Wu , D. H.; Cao , A. Y. *Nano Res.* **2011,** *4*, 891.
95. Sun, W. T.; Yu , Y.; Pan, H. Y.; Gao, X. F.; Chen, Q.; Peng, L. M. *J. Am. Chem. Soc.* **2008**, *130*, 1124 .
96. Huynh, W. U.; Dittmer, J. J.; Libby, W. C.; Whiting, G. L.; Alivisatos, A. P. *Adv. Funct. Mater.* **2003**, *13*, 73.
97. a) Li , L.; Wu, P.; Fang, X. S.; Zhai, T. Y.; Dai, L.; Liao, M. Y.; Koide, Y.; Wang , H. Q.; Bando , Y.; Golberg, D.; *Adv. Mater.* **2010**, *22*, 3161 ; b) Zhai, T. Y.; Li , L.; Wang , X.; Fang , X. S.; Bando , Y.; Golberg , D. *Adv. Funct. Mater.* **2010**, *20*, 4233 .
98. Jiang, Y.; Zhang, W. J.; Jie , J. S.; Meng, X. M.; Fan, X.; Lee , S. T.; *Adv. Funct. Mater.* **2007**, *17*, 1795.
99. Bowers II , M. J.; McBride, J. R.; Rosenthal, S. J. *J. Am. Chem. Soc.* **2005**, *127*, 15378.
100. Schreuder, M. A.; Xiao , K.; Ivanov, I. N.; Weiss, S. M.; Rosenthal, S. J. *Nano Lett.* **2010**, *10*, 573.
101. Jang , H. S. ; Yang , H.; Kim , S. W.; Han , J. Y.; Lee , S. G.; Jeon , D. Y. *Adv. Mater.* **2008**, *20*, 2696 .
102. Somers, R. C.; Bawendi , M. G.; Nocera , D. G. *Chem. Soc. Rev.* **2007**, *36*, 579.
103. Kim, T. H.; Cho, K. S.; Lee, E. K.; Lee, S. J.; Chae, J.; Kim, J. W.; Kim, K. *Nat. Photonics* **2011,** *5*(3), 176.
104. Burt, M. G.: Optical fibre with quantum dots. Google Patents, **1999**.
105. Bawendi, M. G.; Haavisto, J. R.; Hakimi, F.; Tumminelli, R.: Quantum dot Laser. Google Patents, 1993.
106. Vlasov, Y. A.; Deutsch, M.; Norris, D. *Appl. Phys. Lett.* **2000**, *76*, 1627.
107. Walker, G. W.; Sundar, V. C.; Rudzinski, C. M.; Wun, A. W.; Bawendi, M. G.; Nocera, D. G. *Appl. Phys. Lett.* **2003**, *83*, 3555.
108. Frasco, M. F.; Chaniotakis, N. *Sensors* **2009**, *9*, 7266.

# CHAPTER 2

## Electrochemistry of CdSe QDs-Investigation of Band Structure Parameters and Size Dependent Single Electron Transfer

---

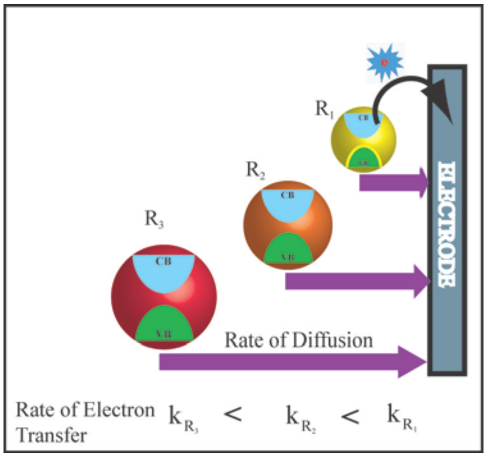

This chapter deals with size dependent electron transfer kinetics of oleic acid capped CdSe Quantum dots (QDs), where heterogeneous electron transfer from QDs to the metal electrode has been studied using different electrochemical techniques. Five different sizes of CdSe nanoparticles (3, 3.8, 4, 4.7, 4.9 nm) are prepared and their photophysical properties as well as redox properties are probed using various optical and electrochemical methods. Band structure parameters are determined using differential pulse and cyclic voltammetry and kinetic parameters are gauged using electrochemical impedance spectroscopy. The optical bandgap of the particle matches well with that obtained using electrochemistry (i.e., electrochemical band gap) revealing insignificant contributions from the solvent. Impedance analysis gives interesting size dependent electron transfer rate constants and diffusion coefficient of the particles.

---

## 2.1. Introduction

Cadmium selenide (CdSe) nanoparticles (QDs), especially within few nanometer size range, are extensively used for various applications like fluorescent probes in biological imaging,[1-2] tunable absorbers and emitters in nanoscale electronics,[3] and quantum dot lasers.[4] Consequently many groups have focused their attempts in controlling their size and shape to modulate electronic properties after remarkable advances in their synthetic strategies, including specially controlled colloidal techniques.[5-6] Previous chapter has discussed these elaborately. One of the most interesting features of such semiconducting nanocrystals (Quantum dots or QDs) is the nonlinear variation of optical properties as a function of size and shape which is actually the manifestation of the well-known quantum confinement effect.[7-8] However, their properties also are very sensitive to the surface structure because of high surface to bulk ratio of NPs compared to that of bulk materials, thus adversely affecting their stability. The size as well as shape variation gives rise to different distribution of electronic energy levels and one important way to unravel the size and shape dependent properties is by employing various spectroscopic methods, especially UV-VIS absorption and photoluminescence. However, these techniques neither directly nor coupled with other complementary techniques can provide adequate information on band positions (analogous to HOMO-LUMO gap) and hence are of limited use for correlating size with applications. Electrochemical techniques, on the other hand, can serve as an inexpensive and easy tool for determining the band structural parameters, especially when size and shape cause subtle variations in Fermi energy and solvation parameters. In fact, electrochemistry in combination with the spectroscopic techniques can provide useful information about the electronic structure of these nano-particles facilitating better insights into the variation of charge transfer kinetics.

The electrochemical behavior of semiconductor QDs varies from material to material although it is possible to understand this variation with respect to size, shape, nature of capping agent and dependence on solvent and counter ions.[9] The information obtained also depends on the technique to be used and its time scale so that a judicious choice of techniques can afford adequate information. For example, when the size is extremely small, these NPs can show quantized double layer charging (QDL)[10-12] on electron transfer and sometimes even undergo rapid disproportionation due to subtle changes of oxidation and reduction. However, for many semiconductor QDs, such a QDL charging effect has not been observed unambiguously, although Si NPs have been found to show multiple cathodic peaks in voltammetry as a result of QDL charging.[13] Similarly, size dependent cyclic voltammetric behavior of CdS QDs has been reported recently and more importantly, a correlation between the optical band gap and the electrochemical gap has been estimated in toluene-DMSO mixture.[14-15] However, no attention has been paid to date to the mechanism of charge transfer of these ultra-small semiconducting clusters in order to substantiate any relation between the particle size and the ease of electron transfer. The major problem of QDs electrochemistry lies in their poor dispersion in water and many polar solvents, where, the particles tend to degrade faster upon electron transfer and the accessible electrochemical window is also small (-1 to +1 V). Furthermore this very small concentration (~µM) often leads to poor sensitivity for detection over the background signal. Differential pulse voltammetry (DPV) can thus be used to estimate the band structure parameters of QDs (HOMO-LUMO gap) in solution assuming negligible solvation. Bard *et al* recently used differential pulse voltammetry (DPV) on TOPO-capped CdTe QDs[16] to reveal the usefulness of DPV for successfully investigating the electrochemical HOMO-LUMO gap of such small semiconductor particles. Another limitation of all these studies is that no kinetic information is provided during the charge transfer processes between the nanoparticles and electrodes.

Here we describe the estimation of the quasiparticle gap of various sizes of CdSe QDs in order to correlate the electrochemical HOMO-LUMO gap with that obtained from the UV-VIS spectroscopy, with special attention to understand the charge transfer process for CdSe nanoparticles of different size (3, 3.8, 4, 4.7 and 4.9 nm). Electrochemical Impedance method has been employed to understand the kinetics of charge transfer during electron ejection or injection (oxidation or reduction respectively) from/into the nanoparticles.

## 2.2. Experimental Section

### 2.2.1. Materials

Cadmium oxide (CdO), trioctyl phosphine (TOP) and 1-octadecene were purchased from Aldrich and used as received. Selenium powder, hexane and ethanol (99.9%) of analytical reagent grade were purchased from Thomas Baker. Oleic acid was purchased from Rankem and used without further purification. Dichloromethane (DCM) was from Rankem and was used after distillation from $CaH_2$ and stored over 4Å molecular sieve (from Aldrich). Tetrabutyl ammonium hexafluorophosphate ($TBAPF_6$) was purchased from Aldrich and used as received as electrolyte in nonaqueous media.

### 2.2.2. Synthesis of oleic acid capped CdSe QDs of varying sizes

Typically, 18 mg of CdO was taken in a four-neck RB flask along with 0.6 ml oleic acid and 10 ml 1-octadecene (ODE). A Se-precursor (Se-TOP) was prepared by dissolving 32 mg Se powder in 5 ml ODE containing 0.6 mL trioctylphosphine (TOP) by slight warming at 60°C. The RB containing CdO was then heated at 190°C when red CdO dissolved to give a colorless solution (Cd-oleate). The heating was continued until it reached to 230°C, when 1 ml Se-TOP was quickly injected into the reaction mixture. The solution immediately turned light yellow due to the formation of very small CdSe QDs. The heating was subsequently stopped and the particles were allowed to grow at that temperature. Aliquotes were collected at different time interval (30 sec, 1, 3, 5, and 10 min) to get different particle sizes. The nanoparticles (NPs, i.e., QDs) were then precipitated out from the solution by using small amount of hexane followed by copious amount of ethanol. These samples were then centrifuged and washed and the procedure was repeated 5-6 times to get pure nanocrystals. The precipitate was subsequently vacuum dried to obtain dry powder of CdSe nanoparticles.

## 2.3. Structural and Morphological Characterization

### 2.3.1. Powder X-ray Diffraction (PXRD)

Powder X-ray diffraction was carried out using CuKα ($\lambda$ = 1.54 Å) radiation on a Philips PW1830 instrument operating at 40 kV and a current of 30 mA at room temperature. Diffraction patterns were collected at a step of 0.02°(2θ) after background subtraction with the help of a linear interpolation method.[17] Samples were prepared as thin films on glass substrates.

### 2.3.2. UV-Vis Spectroscopy

UV-VIS absorbance studies were carried out with Varian Carry 50 instrument equipped with a single beam facility (with a spectral resolution of 0.5 nm). For the absorbance measurements, samples were diluted with toluene.

### 2.3.3. Transmission Electron Microscopy

A small amount of sample was dispersed in ethanol by sonication to prepare a very dilute suspension. Proper care was taken not to sonicate for long time to prevent possible damage of the sample. A drop of this suspension was put on carbon film-coated copper micro-grids. After drying, these grids were then used for structural investigation using a high resolution transmission electron microscope (HRTEM) of TECHNAI $G^2$ F30), equipped with a high resolution objective stage, operating at 300 kV, and providing a point resolution better than 0.3 nm, the coefficient of spherical aberration being 1.35 mm. The images were digitized in the size of 256 × 256 pixels with a pixel size of 0.03994 nm and thus atomically resolved images were possible. These images were analyzed using Gatan Digital Micrograph Software to enable detailed structural analysis in terms of inter-planar distances, angle between planes etc.

### 2.3.4. Electrochemical Measurements

All the electrochemical measurements were carried out using CHI 900b (for differential pulse voltammetry) and BioLogic (Model SP300) potentiostats employing a three electrode set up containing a 0.3 mm diameter Pt disk as working and two Pt-wires as reference and counter electrodes respectively in 0.1 M tetrabutylammonium hexafluorophosphate ($TBAPF_6$) dissolved in freshly distilled dichloromethane ($CH_2Cl_2$).

## 2.4. Results and Discussion

### 2.4.1. UV-Vis and Photoluminescence (PL)

Fig. 2.1. shows superimposed absorption spectra (fig. 2.1.(a)) and Photoluminescence (PL) emission spectra (fig. 2.1.(b)) of the purified colloidal CdSe nanoparticles of different sizes capped with oleic acid. The first excitonic peak (due to $1S_{(h)}$-$1S_{(e)}$ transition) [18-19] is observed in all the absorption spectra. As expected for quantum-sized particles, the position of the first electronic transition is shifted to higher photon energies and become more pronounced with decreasing particle size according to the size quantization effect. The optical band-gap of the particles is obtained from the onset of the absorption of the nanoparticles.

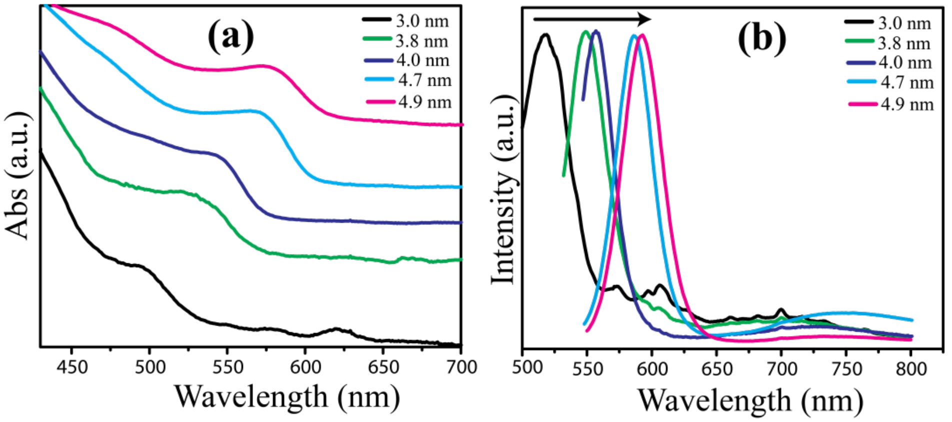

**Figure 2.1.** (a) Absorption and (b) Photoluminescence spectra of the CdSe nanoparticles capped with oleic acid in toluene; The sizes of the nanoparticles (obtained from the first excitonic peak positions) have been shown in the inset.

Average particle size of all the CdSe QDs have been obtained by using the following empirical formula suggested by Yu *et al*.[20]

$$D = (1.16122 \times 10^{-9})\lambda^4 - (2.6575 \times 10^{-6})\lambda^3 + (1.6242 \times 10^{-3})\lambda^2 - (0.4277)\lambda + (41.57) \ldots\ldots (1)$$

where, D is the diameter of the QDs and λ is the corresponding wavelength of the first absorption maximum in the absorption (i.e., lowest energy maximum) plot of the QDs. The formula is based on the following assumptions,[20]

(i) All the monomers added for the growth of QDs are all converted to nanocrystals.

(ii) All the QDs are almost spherical in shape.

(iii) It is independent of the nature of surface capping agents, refractive index of the solvent, quantum yield of each QD size and the method employed for the determination of the extinction coefficient of QDs.

On the other hand, all the QDs show interesting PL behavior (fig.2.1.(b)). The band edge PL emission maximum shows red shift as the particle size increases. All the PL peaks are narrow (FWHM≤ 34) and sharp indicating narrow size distribution of the QDs in the solution.[21] Some of the PL also show a broad emission at higher wavelength

(>650 nm). This has been attributed to the defect state emission (i.e., non-coordinated surface sites).[22]

### 2.4.2. Transmission Electron Microscopy (TEM)

Fig. 2.2 shows the TEM images of three different sizes of CdSe QDs used for the present study. All of the images suggest the formation of mono-disperse CdSe QDs. Sizes of QDs match closely with the size obtained from UV-Vis spectra.

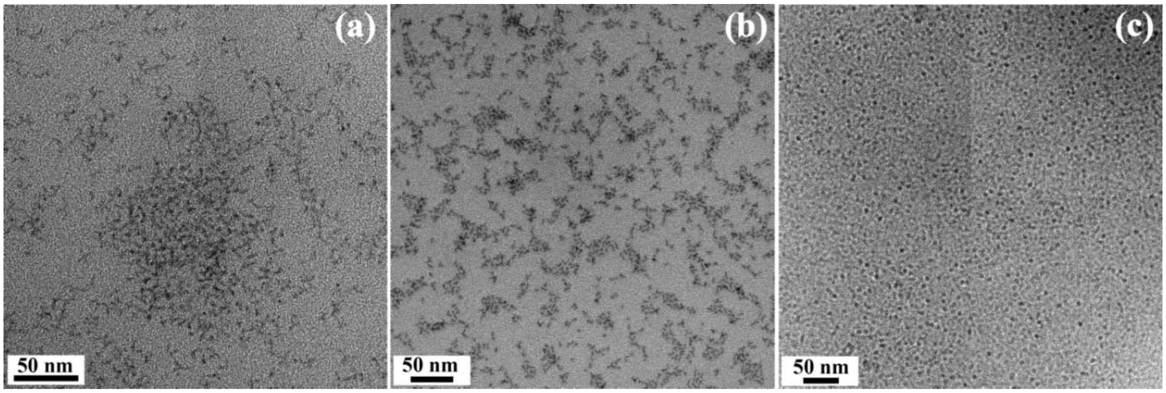

**Figure 2.2.** Low resolution transmission electron micrographs of oleic acid capped CdSe QDs at different time intervals from the reaction mixture-(a) 30 s (~3 nm), (b) 1 min (~3.8 nm) and (c) 2 min (~4 nm)

### 2.4.3. Fourier transformed Infrared Spectroscopy (FTIR) and Powder X-ray Diffraction (PXRD)

Fig. 2.3(a) shows the X-ray diffraction patterns of oleic acid capped CdSe nanoparticles. The diffractogram confirms the crystallinity of the CdSe nanoparticles. Three main diffraction peaks could be identified in the pattern and those peaks match well with the reflections from (111), (220) and (311) planes indicating a cubic phase formation (zinc blende phase, JCPDS card no.19-0191). In all the diffractograms, the peak corresponding to (111) plane is the highest intense peak. The broadness of the diffraction peaks of CdSe QDs increases gradually with a decrease in particle size (fig. 2.3(b)) as is expected for any other nanomaterial.

Fig. 2.3.(c) is the comparative FTIR spectra of pure oleic acid and oleic acid capped CdSe QDs. Fig. 2.3(b) is the enlarged portion (600-2000 cm$^{-1}$) of fig. 2.3(c) showing the presence of oleic acid on CdSe QDs. The spectra show three major well defined triplet peaks at 2853, 2923 and 2958 cm$^{-1}$ in case of CdSe QDs corresponding

respectively to symmetric and asymmetric $CH_2(sp^3)$ stretching of the aliphatic chain of oleic acid, also confirming the presence of oleic acid on the surface. The peak at 706 cm$^{-1}$ in CdSe QDs is due to C-H stretching of C=C bond of oleic acid. Similarly, other peaks in CdSe QDs can also be assigned such as C-O stretching at 1094 cm$^{-1}$and C-O scissoring at 800 cm$^{-1}$(from –COO$^-$ group),$CH_2$-$CH_3$ stretching at 1458 cm$^{-1}$, C=O stretching at 1729 cm$^{-1}$. Moreover, the peak at 1259 cm$^{-1}$ is due to the stretching of –COO bond in $COO^-M^+$ and thereby confirms the binding of –COO$^-$ group to CdSe QD surface. Hence, comparative analysis of FTIR spectra of oleic acid and CdSe QDs ostensibly suggests the capping by oleic acid molecule.[23]

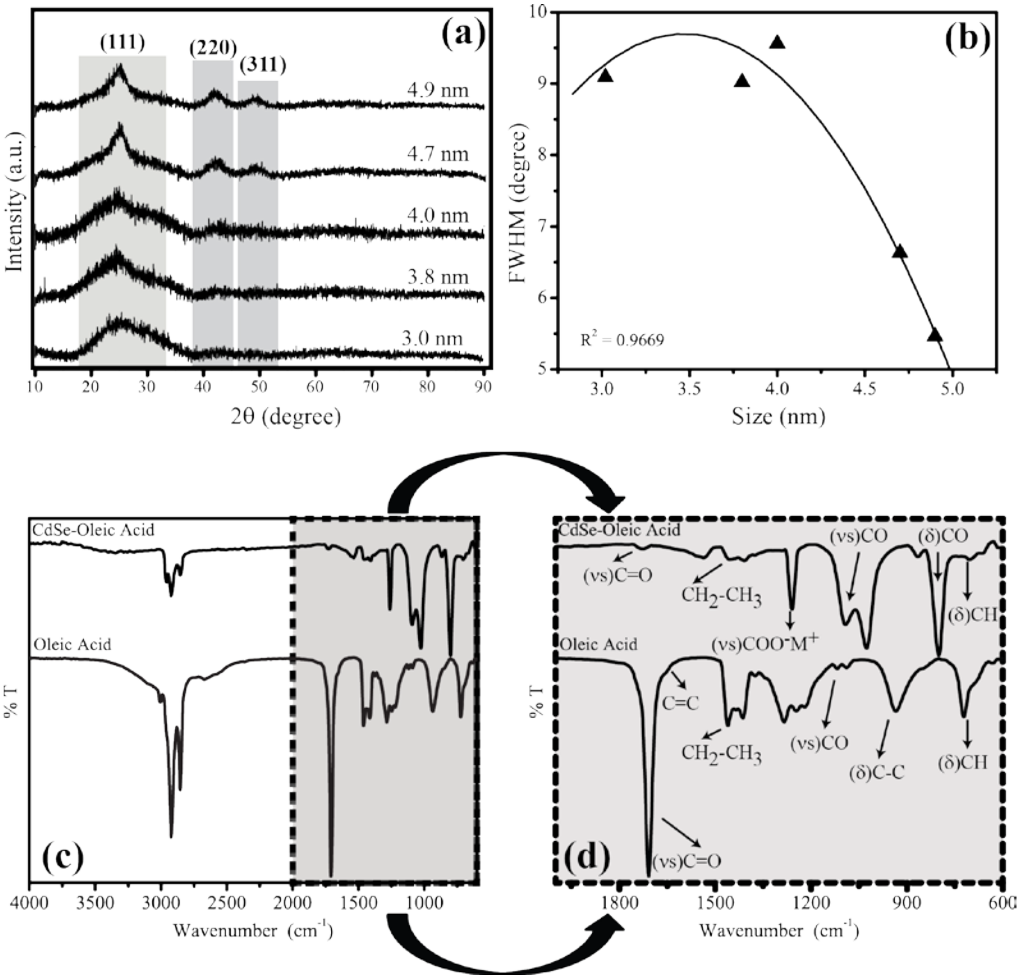

**Figure 2.3.** (a) A comparison of the powder X-ray diffraction patterns of oleic acid capped CdSe QDs of various sizes, (b) variation of FWHM of PXRD peak (111) of CdSe QDs with particle size, (c) comparative FTIR spectra of oleic acid and oleic acid capped CdSe QDs and (d) enlarged portion of (c) (600-2000 cm$^{-1}$) showing adsorption of oleic acid on CdSe surface.

### 2.4.4. Electrochemical Characterization

Mono-dispersed CdSe QDs capped with organic capping agents like oleic acid (OA), dispersed in a solution of electrolyte, can be considered as a QD of a core with dielectric constant $\varepsilon_{in}$ surrounded by another dielectric medium (capping layer) of dielectric constant $\varepsilon_{out}$.[24] The outer dielectric medium separates one CdSe QD to another. These QDs are otherwise neutral without any external perturbation in terms of heat, photon, electricity etc. However, QDs undergo excitation (i.e., charge transfer) when subjected to any kind of external perturbation. Generally, four kinds of charge transfer processes can be considered as has been shown in fig. 2.4. [25]

(i) Electron injection from an electrode to a neutral QD (reduction) (fig. 2.4.(a))

(ii) Electron extraction from a neutral QD (oxidation) (fig. 2.4.(b))

(iii) Creation of a non-interacting electron-hole pair by simultaneous electron injection and extraction from two identical neutral QDs (fig. 2.4.(c)). This literally means taking electron from one QD (oxidation of one QD) and putting the same electron in another identical neutral QD (reduction of the other QD) situated at infinite distance. The energy required to create such non-interacting electron-hole pair, is termed as the quasi- particle gap or electrochemical band-gap ($E_g^{el}$), especially if this is in solution, which corresponds to the difference between the first oxidation and first reduction peaks in voltammetric measurements. Electrochemical band-gap is given by the following equation,[26]

$$E_g^{el} = E_g^0 + \Sigma_e^{pol} + \Sigma_h^{pol} \ldots\ldots\ldots\ldots(2)$$

where, $E_g^0 = E_e^0 - E_h^0$ is the single particle gap of the QD and considers only size quantization effect, $\Sigma_e^{pol}$ and $\Sigma_h^{pol}$ are terms arising due to individual confinement of electron and hole respectively.[15]

(iv) Creation of exciton, i.e., interacting electron-hole pair within the same QD by optical excitation (fig. 2.4.(d)). Light energy causes valence band (VB) electron to get excited to conduction band (CB) and the minimum energy required for this transition is called optical band-gap ($E_g^{op}$) of the QD. Minimum energy refers to the energy for electronic transition from top of the VB (VB edge) to the minimum of CB (CB edge). $E_g^{op}$ is related to the $E_g^{el}$ by the following equation,[27]

$$E_g^{op} = E_g^{el} - J_{e,h} - E_{ligand}^{bar} \ldots\ldots\ldots\ldots\ldots(3)$$

where, $J_{e,h}$ is the total electron-hole Coulomb interaction energy which originates due to the electrostatic interaction of electrons and holes of the QD with the incoming electron or hole (this term accounts for both direct and dielectric polarization-induced Coulomb interactions on the electrons and holes of the QD) and $E_{ligand}^{bar}$ is the additional energy barrier to be overcome in order to add electron or hole into the QD. Due to these additional contributions, electrochemical band-gap is generally greater than optical band-gap. However, electrochemical band-gap is often affected by the surface states or surface traps (inter band-gap states) because surface of the QDs mostly takes part in electrochemical experiments, whereas optical excitation mostly involves the core of the QDs. The solvent contribution is assumed to be negligible in all the above cases[25]

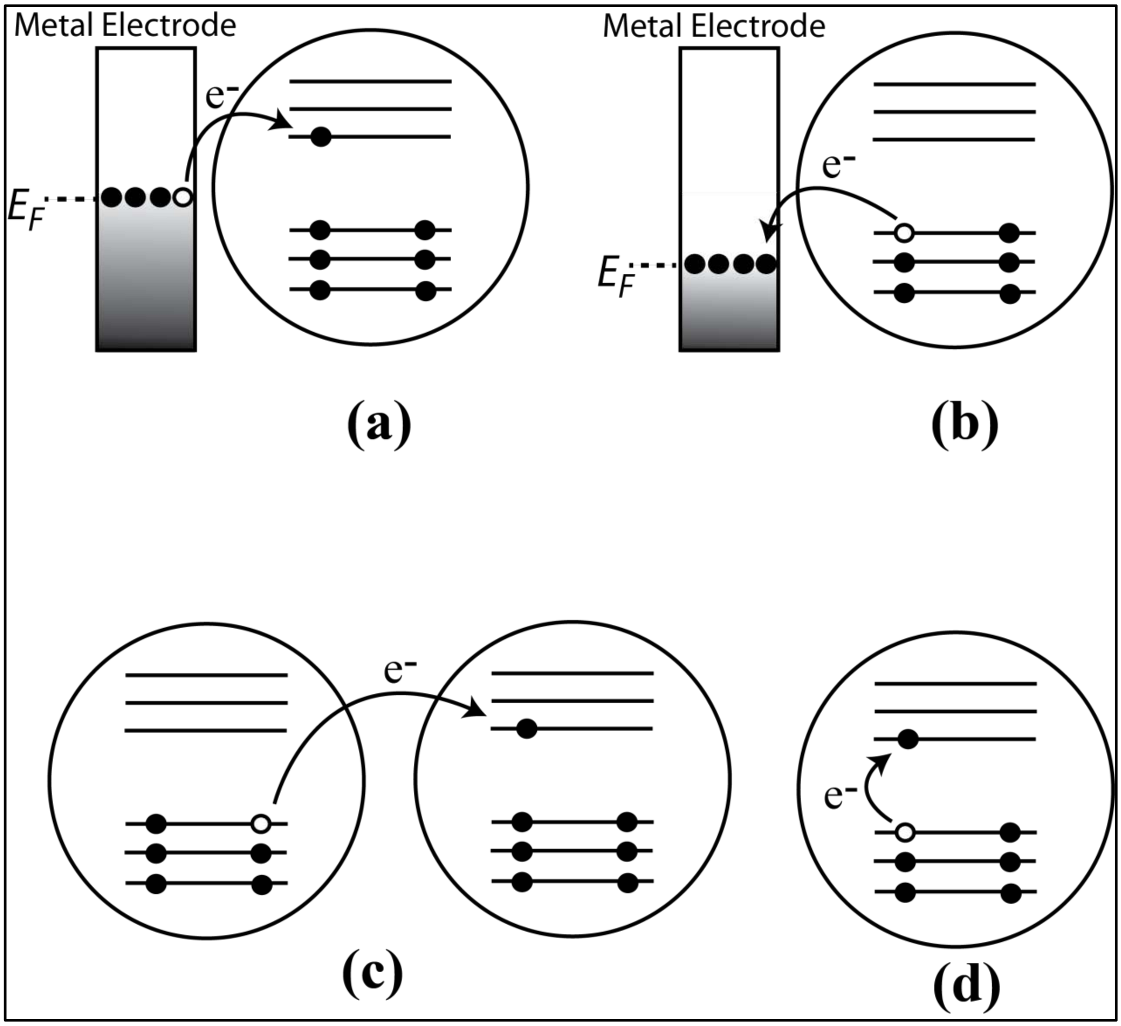

**Figure 2.4.** Different processes of charging QDs-(a) electron addition to a neutral QD, (b) electron removal from a QD, (c) creation of non-interacting electron-hole pair by mutual charge transfer and (d) optical excitation.[15], [25]

### 2.4.4.1. Differential Pulse Voltammetry (DPV) of oleic acid capped CdSe QDs

Differential pulse voltammetry is a very important voltammetric technique which employs short, gradually increasing potential pulses for measurements. Current sampling is done twice-one just before applying pulse and another just before ending the pulse. The difference in the two currents is plotted against the applied potential. The y-axis in the resultant voltammogram then becomes differential current rather than normal current (which is generally used in normal voltammetry).[28] This effectively removes the contribution due to background current (charging current) and so the peak obtained is solely due to the redox process occurring in the system under study. Accordingly, fig. 2.5 shows a comparison of differential pulse voltammograms (DPVs) of five distinct sizes of CdSe QDs in a typical non-aqueous electrolyte.

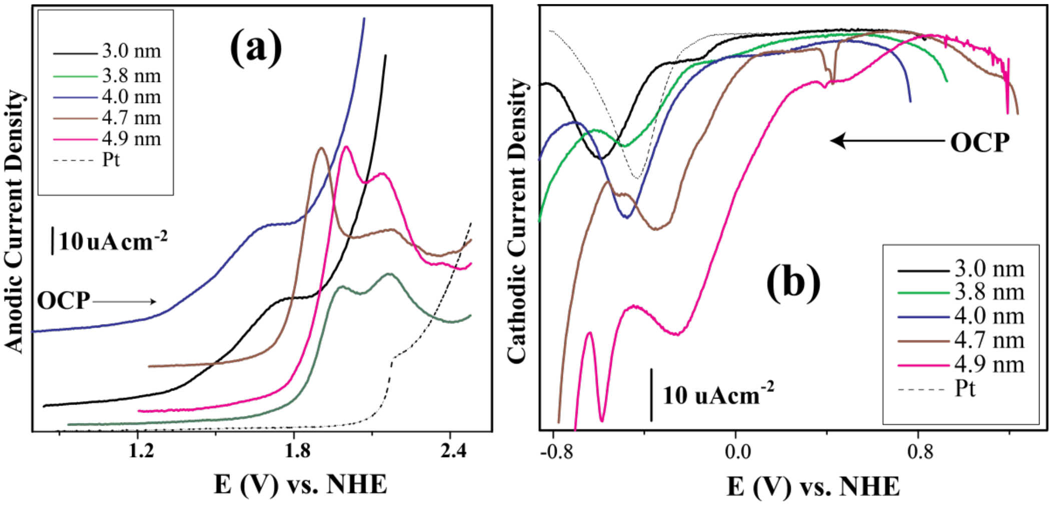

**Figure 2.5.** (a) Anodic and (b) Cathodic Differential pulse voltammograms of CdSe QDs capped by oleic acid; 0.2 cm diameter Pt-disk was used as working electrode, Pt wire as quasi reference and Counter electrodes; Scan rate was 10 mV/s and pulse amplitude was 50 mV; Dry dichloromethane was used for the study and $TBAPF_6$ was used as supporting electrolyte; Dotted line shows the blank; in all cases concentration of QDs was kept in the μM ($10^{-6}$ M) range.

The potential is swept cathodically from open circuit potential (OCP) to -1.5 V (fig. 2.5.(b)) and subsequently anodically from OCP to 1.5 V (fig. 2.5.(a)) with respect to a Pt quasi-reference electrode. Each sample of CdSe QDs gives two distinct peaks – one corresponds to reduction and the other corresponding to oxidation respectively. The

HOMO and LUMO correspond to the first oxidation and first reduction peaks respectively assuming one electron oxidation and reduction of CdSe QDs. The difference between these two peaks thus represents the electrochemical bandgap ($E_g^{el}$). Interestingly, these two peaks shift towards each other systematically as we move from smaller to larger sized particles as is expected due to quantum confinement effect (difference between VB and CB decreases as the particle size increases). Absolute value of the band (HOMO/LUMO) position is calculated according to the following equations:[29]

$$E_{HOMO} = -\left(E_{[ox\ vs\ NHE]} + 4.75\right)eV \ldots\ldots\ldots\ldots\ldots\ldots(4)$$

$$E_{LUMO} = -\left(E_{[red\ vs\ NHE]} + 4.75\right)eV \ldots\ldots\ldots\ldots\ldots..(5)$$

where, $E_{ox}$ and $E_{red}$ are the peak potentials for oxidation and reduction respectively and 4.75 eV is the absolute potential of normal hydrogen electrode (NHE).

There are also some interesting additional peaks observed in these voltammograms. The extra oxidation peaks revealed for some particles before the oxidation from the HOMO level can be attributed to the surface traps present at the mid-gap region (as is revealed from photoluminescence). During potential sweep the traps (either Cd or Se sites) get oxidized/reduced preferentially as compared to the HOMO level. This is consistent with the literature and also supports the surface mediated electron transfer as has been observed previously.[15] Table 2.1 represents absolute band positions for each batch of the CdSe QDs. It also shows the values of optical bandgap for the corresponding CdSe QD along with that of electrochemical HOMO-LUMO gap for differently sized particles and a good correlation is observed between the two. Interestingly, the bandgap value of particles changes as the particle size increases and follows an inverse $r^2$ (r = radius of the particle) relationship as has been predicted by Brus for semiconductor nanoparticles.[30] However, in the present study, the electrochemical HOMO-LUMO gap, obtained from DPV, is found to be less than the optical band-gap for all the particles and this can be attributed to the presence of multiple surface traps in the QDs as well as to the possible degradation of the QDs into Cd and Se upon multiple electron transfer.[31] Presence of surface traps has already been confirmed from photoluminescence (fig. 2.1(b)) (broad humps ranging between 650 and 800 nm). Solvent contribution could also be significant in some cases.[32]

**Table 2.1.**Band positions of CdSe QDs of different size

| Particle size (nm) | HOMO (eV) *vs* vacuum | LUMO (eV) *vs* vacuum | Electrochemical Bandgap ($E_g^{el}$) eV | Optical Bandgap ($E_g^{op}$) eV |
|---|---|---|---|---|
| 3 | -5.57 | -3.23 | 2.34 | 2.39 |
| 3.8 | -5.8 | -3.72 | 2.08 | 2.26 |
| 4.0 | -5.51 | -3.33 | 2.18 | 2.23 |
| 4.7 | -5.72 | -3.5 | 2.22 | 2.12 |
| 4.9 | -5.81 | -3.57 | 2.24 | 2.09 |
| Bulk | -5.96 | -4.08 | 1.8 | 1.74 |

Fig.2.6 shows the comparative band structures of different sized CdSe QDs obtained by various groups.[15], [24], [33-35] The values obtained from this study matches well with the theoretical values (Zunger[24] et al., sky blue diamonds in fig. 2.6.) as well as experimental values from literature. However, a little divergence has been observed, perhaps due to the effect of solvent (dichloromethane in our case).[32]

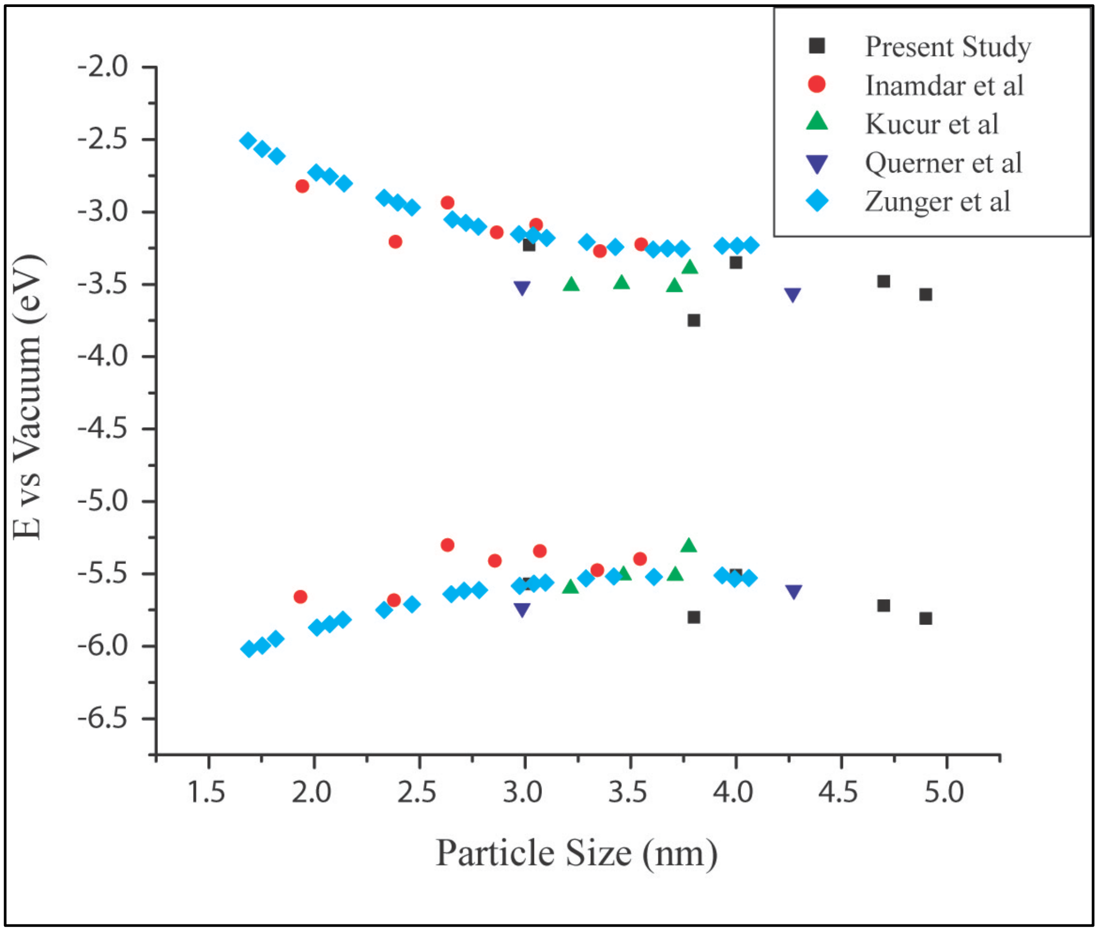

**Figure 2.6.** Comparative analysis of band structure of CdSe nanoparticles having different sizes with the data available in the literature; in all the cases the core CdSe remains same but the outer capping layer varies in different studies.[15], [24], [33-34]

### 2.4.4.2. Cyclic Voltammetry of oleic acid capped CdSe QDs

In order to ensure the reliability of the DPV data, cyclic voltammetry was performed in the same electrochemical cell. Accordingly, fig. 2.7(a) shows the cyclic voltammogram of CdSe QD having 4 nm size. Clear oxidation (A1) and reduction (C1) peaks are observed corresponding to the oxidation of HOMO and reduction or electron addition or charge injection into the LUMO levels of the QDs. The positions of the peaks are in good agreement with that observed in DPV. The difference between those two peaks also matches well with the difference obtained from DPV. There are also other small, irreversible peaks in the voltammograms. But these peaks do not have complementary oxidation/reduction peaks and they do not appear regularly when the scan is repeated several times. Hence, these peaks are perhaps due to the degradation products of QDs obtained during redox processes of QDs.[25]

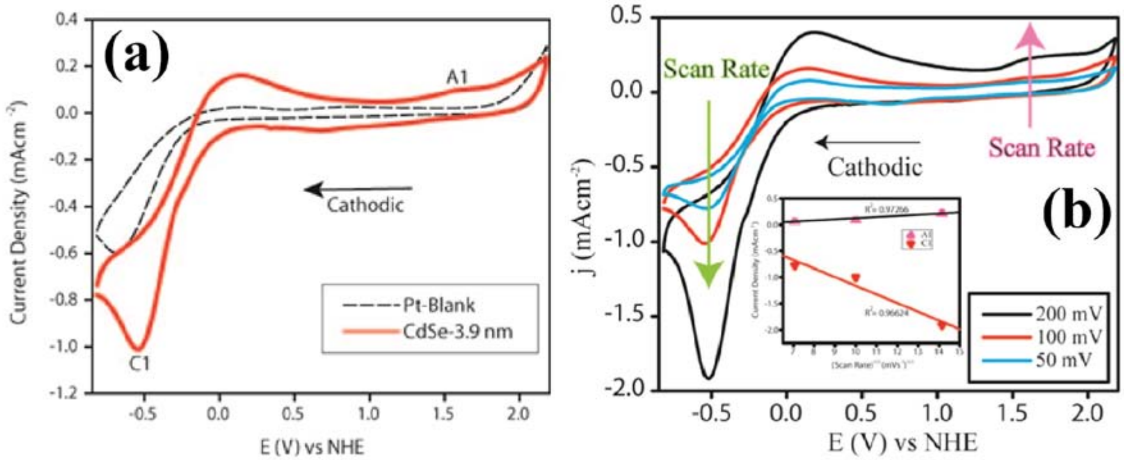

**Figure 2.7.** (a) Cyclic voltammogram of CdSe QDs (4 nm) in dichloromethane containing 0.1 M $TBAPF_6$ (supporting electrolyte), Pt-foil was used as counter and a Pt-wire was used as quasi-reference electrode; The potential values were then calibrated independently with standard $Fc/Fc^+$ couple; (b) Cyclic voltammogram of CdSe QD (Size 4 nm) with varying scan rate, inset shows the linear fit of peak current vs. square root of scan rates.

Fig. 2.7(b) shows the variation of the peaks A1 and C1 with different scan rates and the inset plot shows that the peak current varies linearly with the square root of scan rate. This, therefore, provides evidence that the two peaks (A1 and C1) originate due to diffusion controlled electron transfer according to Randles-Sevick and so the adsorption induced charge transfer (i.e., adsorption followed by charge transfer) can be ruled out. However, the two peaks are separated by 2.18 V, which is far beyond the reversible domain of 60 mV according to Nernstian behavior, suggesting that A1 and C1 form adiffusion controlled non-interacting pair, which is a prerequisite for determining electrochemical band-gap. Therefore, the difference between these two peaks (2.18 V) has been taken as the electrochemical bandgap ($E_g^{el}$) and has been found to be very close to its optical band-gap (2.23 eV). Fig. 2.8 shows the cyclic voltammograms for different sizes of CdSe particles. Like DPV, in this case also, the peaks due to oxidation and reduction shift toward each other systematically and thereby complementing the data obtained using DPV. However, the peaks are poorly resolved in this case unlike the case for DPV for the same molar concentration (~$10^{-6}$ M) because contribution of charging current is more in case of CV, which often makes it difficult to observe the expected peak over background. This, therefore, implies the advantage of DPV over CV for determining band structure parameters.

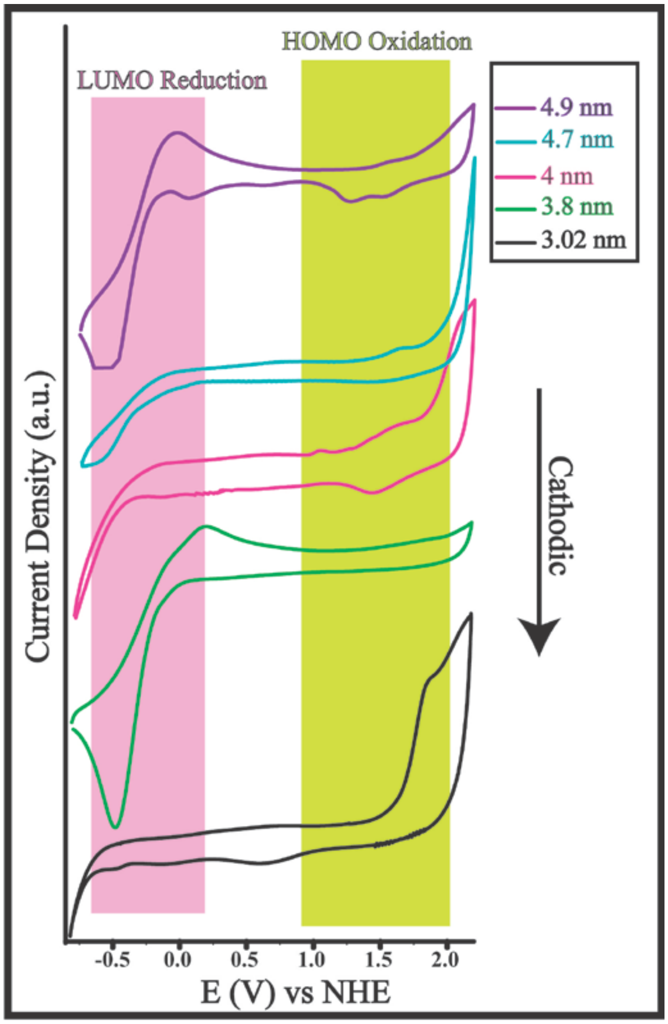

**Figure 2.8.** Cyclic voltammograms of CdSe QDs of varying sizes in dichloromethane containing 0.1 M TBAPF$_6$ as supporting electrolyte under identical condition. Concentrations are maintained in the micromolar range in order to compare DPV and CV. However, negligible variation in concentration is possible during experiment. Some peaks do not appear all the time and so they perhaps represent degradation of QDs upon electron transfer.[15]

### 2.4.4.3. Impedance measurements of the CdSe QDs solutions

Fig. 2.9(a) is the representative Nyquist plot of CdSe QD (3 nm) capped with oleic acid in dichloromethane ($CH_2Cl_2$) on a pt-disk (0.2 cm diameter) working electrode at OCP and at 1.75 V (*vs* NHE), i.e., at potential where oxidation of CdSe QD (3 nm) occurs (HOMO oxidation). The impedance data (at OCP) has been divided into high frequency where a depressed semicircle is observed and low frequency domain which shows a straight line with more than 45° angle, for the convenience of interpretation. The high frequency semicircle does not show significant change on application of potential, but the low frequency side shows one more depressed semicircle followed by straight line. The second semicircle perhaps indicates electron transfer. Similarly, fig. 2.9 (b) shows the complex plane impedance plots for CdSe QDs at different DC bias. The bias for each QD has been chosen depending on the oxidation potential of that QD (obtained from DPV), i.e., potential corresponding to its HOMO level in 0.1 M tetrabutylammonium hexafluorophosphate ($TBAPF_6$) as the supporting electrolyte. The plots show a semicircle at high frequency domain followed by a straight line with less than 45° angle with the real axis at the low frequency region for every particle size. Here, bias potentials are potentials where QDs get oxidized, i.e., corresponding to HOMO position.

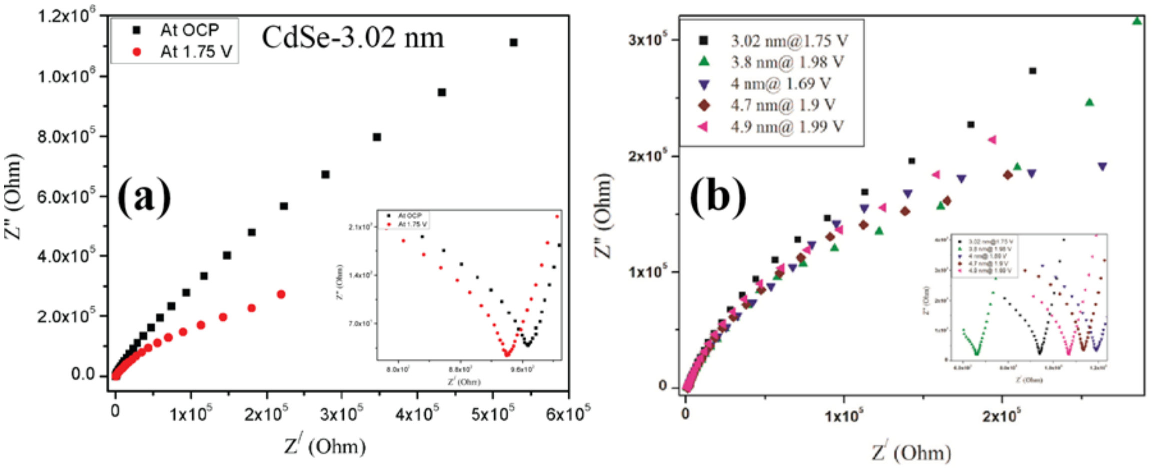

**Figure 2.9.** (a) Nyquist plot of CdSe QD (3 nm) at open circuit potential (OCP) and at 1.75 V (*vs* NHE) where oxidation of CdSe occurs; (b) Complex plane impedance plots (Nyquist plots) of CdSe nanoparticles of varying sizes in $CH_2Cl_2$ on a Pt disk (0.2 cm diameter) under DC bias corresponding to the anodic peak potential of the respective QDs in DPV; inset highlights the enlarged portion of the high frequency part.

All the impedance data are analyzed using the Randles equivalent circuit (fig. 2.10), assuming the electron transfer process at the electrode surface to be a single-step, one electron process.[28]

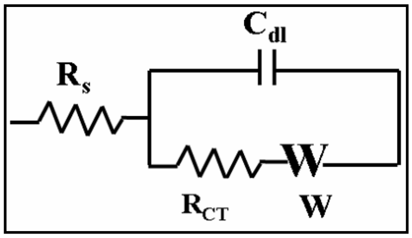

**Figure 2.10.** Schematic representation of Randles equivalent circuit used for analyzing the complex plane impedance plots, where $R_s$ is solution resistance, $R_{CT}$ is charge transfer resistance, $C_{dl}$ is the double layer capacitance and W is the Warburg impedance.

The high frequency part of these plots has been fitted to a semicircle using complex non-linear least square (CNLS) procedure. From the fitted semicircle the standard rate constant for heterogeneous electron transfer during the band edge oxidation, has been calculated for different sizes of the CdSe nanoparticles using the following equation.[28]

$$k_0 = \frac{RT}{n^2 F^2 R_{CT} C_n} \ldots\ldots\ldots\ldots\ldots(6)$$

where, $k_0$ = standard rate constant for the charge injection, $R$= absolute gas constant, $T$= 298 K, $n$= no. of electron or hole transferred, $F$= 96500 C, $R_{CT}$ = charge transfer resistance, $C_n$ = concentration of the CdSe nanoparticles (in $gL^{-1}$). Table 2.2 shows the variation of charge transfer resistance and standard heterogeneous rate constant for electron transfer ($k_0$) with the particle size.

**Table 2.2.**Variation of $R_{CT}$ and $k_0$ with size as obtained from the fitting of the high frequency region of the impedance plots with semicircle

| Particle size (nm) | $R_{CT}$ ($\Omega cm^{-2}$) | $k_0$ ($cms^{-1}$) | Bias (V) *vs.* NHE |
|---|---|---|---|
| 3 | 486.2 | $87.16 \times 10^{-5}$ | 1.75 V |
| 3.8 | 373.2 | $22.71 \times 10^{-5}$ | 1.98 V |
| 4.0 | 929.2 | $3.80 \times 10^{-5}$ | 1.69 V |
| 4.7 | 659.5 | $9.17 \times 10^{-5}$ | 1.9 V |
| 4.9 | 647.7 | $7.26 \times 10^{-5}$ | 1.99 V |

Fig. 2.11 graphically shows the variation of charge transfer kinetics with varying sizes of CdSe QDs with the Pt-electrode. From the plot it is clear that charge transport is rather facile in case of smaller QDs as compared to the larger one.

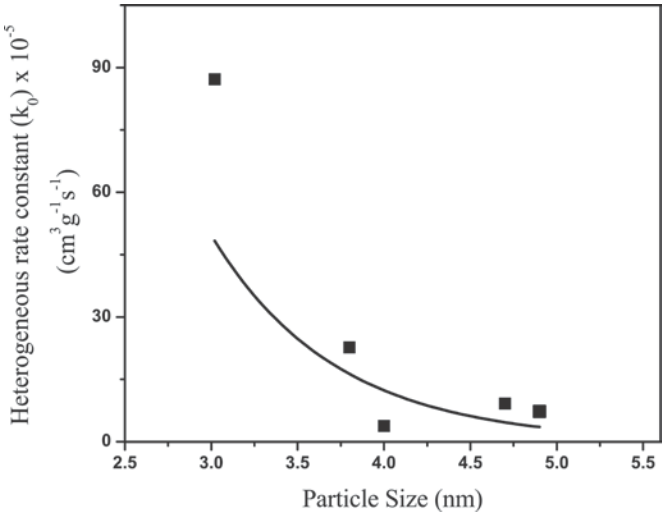

**Figure 2.11.** (a) Particle size *vs* heterogeneous electron transfer rate constants obtained from impedance measurements, it follows apparently an exponential decay with increment in particle size.

The size dependency can be explained using Marcus's theory for nonadiabatic electron transfer in the classical activation limit.[35-36] Theoretical calculation gives the following equation for rate constant for any electrochemical reaction,

$$k = K_{P,O} \nu_n \kappa_{el} \exp\left(\frac{-\Delta G^{\neq}}{RT}\right) \dots\dots\dots\dots\dots\dots\dots\dots\dots. (7)$$

where, $\Delta G^{\neq}$is the activation energy for oxidation/reduction, $K_{P,O}$ is a precursor equilibrium constant, $\nu_n$ is the nuclear frequency factor ($s^{-1}$) and $\kappa_{el}$ is the electronic transmission coefficient which is related to the tunneling probability of electron. According to Marcus theory, $\Delta G^{\neq}$ is given by,

$$\Delta G^{\neq} = \frac{\lambda}{4}(1 + \frac{F(E-E^0)}{\lambda})^2 \dots\dots\dots\dots\dots\dots\dots\dots (8)$$

where, $E$ and $E^0$ are the formal and standard redox potentials respectively for the redox process, $F$ is the Faraday constant and $\lambda$ is the reorganization energy. It is clear from the above equations (7 & 8) that $k$ has an inverse exponential relationship with activation enrgy or applied potential in particular (driving force).

In the present case, the driving force for electron transfer between Pt-electrode and CdSe QD has been taken as the formal redox potential of the QDs of varying size. As is seen from the previous section that the potential for oxidation increases with the increase in particle size (fig. 2.9(b)). Driving force thus increases proportionally with increase in

QD size as per equation 8. Hence, the electron transfer rate increases with decrease in particle size.

The size dependent electron transfer rate can also be explained by considering their size dependent diffusion coefficient. The variation of heterogeneous electron transfer rate constant against particle size interestingly gives an exponential decay behavior, which coincides with the Brus correlation. The fact that the charge transfer kinetics is rather fast for small size particles, is in line with the fact that smaller size particle diffuses faster than the larger ones due to less visco-elastic drag in the same medium and hence the rate of electron transfer is also higher. We have used the Modified Stokes-Einstein equation (eqn.8)[37] to calculate the hydrodynamic radii of different size QDs in dichloromethane as summarized in Table 2.3.

$$D = \frac{kT}{6\pi\eta r}\text{…………….(9)}$$

where, D is the diffusion coefficient, k is the Boltzmann const., η is viscosity and r is the hydrodynamic diameter of the particles (taken as the sum of nanocrystal diameter and twice the length of oleic acid chain length (1.97 nm). The values obtained are very much similar to that obtained previously for CdTe nanoparticles.[16]

However, the role of surface state, effect of migration of the QDs upon charge transfer, electrical as well as electrochemical nature of the capping molecules (here oleic acid), effect of specific adsorption of ions (from supporting electrolyte), reorganization of surface dipoles etc. are neglected while explaining the trend in heterogeneous electron transfer kinetics of these QDs. But all the above parameters are important for the proper understanding of the electron transfer rate in QDs.

**Table 2.3.**Diffusion coefficient calculated from Stokes-Einstein theory (viscosity of the dichloromethane is taken as 0.393 cP)

| **Particle size/Core diameter (nm) (From UV-VIS)** | **Hydrodynamic Diameter (nm)** | **Diffusion Coeff. (cm.s$^{-1}$)** |
|---|---|---|
| 3 | 6.96 | 2.43 x $10^{-6}$ |
| 3.8 | 7.74 | 2.18 x $10^{-6}$ |
| 4 | 7.94 | 2.13 x $10^{-6}$ |

| | | |
|---|---|---|
| 4.7 | 8.64 | $1.96 \times 10^{-6}$ |
| 4.9 | 8.84 | $1.91 \times 10^{-6}$ |

It is, therefore, observed from all the above discussions that band structure parameters can be easily obtained using electrochemistry such as differential pulse voltammetry or cyclic voltammetry, but of course, with some limitations. In particular, DPV gives more reliable information when the concentration of the QDs is too low to get appreciable signal over the background. Again, as the capacitance increases with decrease in particle size (according to the Concentric Sphere Capacitance Model), cyclic voltammetry becomes less effective in resolving the redox peaks over the background charging current. DPV, thus, becomes extremely useful to distinguish and identify the redox peaks over the background, because it uses differential currents before and after the application of voltage pulse. Moreover, electrochemical impedance technique provides valuable information about the kinetics of charge transfer often inextricable by fitting the experimental data using suitable equivalent circuit despite its model-dependence. A rough estimate of the thermodynamic information (free energy change for example) is possible for CdSe QDs of varying size. For instance, our preliminary data unambiguously suggest that the change in free energy decreases as the particle size increases especially below a critical threshold. All the above studies suggest a systematic trend in charge transfer kinetics for different size QDs illustrating that smaller sized QDs react faster than the larger ones arising perhaps from fact that the rate of diffusion is faster in case of smaller QDs assuming same solvation parameters.

## 2.5. Conclusion

We have synthesized five different sizes of oleic acid capped CdSe QDs (sizes below 5 nm, i.e., below the excitonic Bohr radius of CdSe QDs) and have investigated their electron transfer kinetics using various optical and electrochemical methods. The DPV of oleic acid capped CdSe QDs reveals a band gap that varies with the particle size, despite being reasonably close to the corresponding optical band gap value. The possibility of existence of surface traps, which might interfere with the voltammetric measurements, cannot be ignored. Thus, DPV has been found to be a very useful technique in determining band structure parameters (such HOMO-LUMO gap of the QDs especially at very low concentrations to 0.1 μM) assuming negligible solvation effects. Cyclic voltammetry has also been carried out to supplement the DPV outcome and the results obtained are in excellent agreement to the DPV observations. Moreover, electrochemical impedance analysis of the CdSe QD solutions shows that the kinetics of charge transfer to or from the particles from or to the electrode becomes more facile with the decrease in core diameter of the particles, which indeed manifests varying diffusion coefficients of the differently sized particles. In fact, the smallest particles (3.nm) can transfer charge ~12 times faster than that of the largest particles (4.9 nm) although the diffusion coefficient for the smallest particles varies only ~1.2 times than that for largest particles. All methods are experimentally simple and do not require complicated instrumental infra-structure or complex hardware However, the charge transfer kinetics is also likely to be influenced by several other factors including the surrounding dielectric medium (solvent, supporting electrolyte etc.) and many of these are not considered in this study. Almost identical conditions have been maintained during the experiments to avoid complications arising from such factors and we hope these results would be useful to understand the mechanism of charge transfer of QDs.

## 2.6. References

1. Michalet, X.; Pinaud, F.; Lacoste, T. D.; Dahan, M.; Bruchez, M.P.; Alvisatos, A.P.; Weiss, S. *Single Mol.***2001**, *2* (4), 261.
2. Bakalova, R.; Ohba, H.; Zhelev, Z.; Nagase, T.; Jose, R.; Ishikawa, M.; Baba, Y. *Nano Lett.* **2004**, *4* (9), 1567.
3. Schlamp, M.C.; Peng, X.; Alvisatos, A.P. *J. Appl. Phys.***1997**, *82* (11), 5837.
4. Klimov, V. I.; Mikhailovsky, A. A.; Xu, S.; Malko, A.; Hollingsworth, J. A.; Leatherdale, C. A.; Eisler, H. J.; Bawendi, M.G. *Science* **2000**, *290* (5490), 314.
5. Murray, C.B.; Kagan, C.R.; Bawendi, M.G. *Annu. Rev. Mater. Sci.* **2000**, *30* (1), 545.
6. Qu, L.; Peng, Z. A.; Peng, X. *Nano Lett.* **2001**, *1* (6), 333.
7. Brus, L. *J. Phys. Chem.***1986**, *90* (12), 2555.
8. Alvisatos, A.P. *Science* **1996**, *271*, 933.
9. Bouroushian, M.: *Electrochemistry of metal chalcogenides*; Springer, **2010**.

10. Ingram, R. S.; Hostetler, M. J.; Murray, R.W.; Schaaff, T. G.; Khoury, J. T.; Whetten, R. L.; Bigioni, T. P.; Guthrie, D. K.; First, P. N. *J. Am. Chem. Soc.* **1997**, *119*, 9279.
11. Chen, S.; Murray, R.W.; Feldberg, S.W. *J. Phys. Chem. B* **1998**, *102*, 9898.
12. Chen, S.; Ingram, R. S.; Hostetler, M. J.; Pietron, J. J.; Murray, R.W.; Schaaff, T. G.; Khoury, J.T.; Alvarez, M.M.; Whetten, R. L. *Science* **1998**, *280,* 2098.
13. Templeton, A. C.; Wuelfing, W. P.; Murray, R.W. *Acc. Chem. Res.* **2000**, *33*, 27.
14. Ding, Z.; Quinn, B. M.; Haram, S. K.; Pell, L. F.; Korgel, B. A.; Bard, A. J. *Science* **2002**, *296*, 1293.
15. Haram, S. K.; Quinn, B. M.; Bard, A. J. *J. Am. Chem. Soc.* **2001**, *123*, 8860.
16. Inamdar, S. N.; Ingole, P. P.; Haram, S. K. *Chem. Phys. Chem.* **2008**, *9*, 2574.
17. Bae, Y.; Myung, N.; Bard, A.J. *Nano Lett.* **2004**, *4*, 1153.
18. Motl, N. E.; Ewusiannan, E.; Sines, I.T.; Jensen, L.; Schaak, R. E. *J. Phy. Chem. C* **2010**, *114*, 19263.
19. Reimann, S. M.; Manninen, M. *Rev. of Mod. Phys*. **2002**, *74*, 1283.
20. Sapra, S.; Shanthi, N.; Sarma, D. D. *Phys. Rev. B* **2002**, *66*, 205202.
21. Yu, W. W.; Qu, L.; Guo, W.; Peng, X. *Chem. Mater.* **2003**, *15*, 2854.
22. Murray, C. B.; Norris, D. J.; Bawendi, M. G. *J. Am. Chem. Soc.* **1993**, *115*, 8706.
23. Qu, L.; Yu, W. W.; Peng, X.; *Nano Lett.* **2004**, *4*, 465–469.
24. (a) Hamizi, N. A.; Johan, M. R. *Mater. Chem. Phys.* **2010**, *124*, 395. (b) Silverstein, R. M.; Webster, F. X.; Kiemle, D. J., *Spectrometric Identification of Organic Compounds*, 7th Ed., John Wiley & Sons.
25. Franceschetti, A.; Zunger, A. *Phys. Rev. B* **2000**, 62, 2614.
26. Amelia, M.; Lincheneau, C.; Silvi, S.; Credi, A.: Electrochemical properties of CdSe and CdTe quantum dots. *Chem. Soc. Rev.* **2012**, *41*, 5728.
27. (a) Jasieniak, J.; Califano, M.; Watkins, S. E. *ACS nano* **2011**, *5*, 5888. (b) Liu, J.; Yang, W.; Li, Y.; Fan, L.; Li, Y. *Phys. Chem. Chem. Phys.* **2014**, *16*, 4778.
28. Bard, A. J.; Faulkner, L. R. *Electrochemical Methods, Fundamentals and Applications; 2nd ed.* John Wiley & Sons: New York, 2001.
29. Cardona, C. M.; Li, W.; Kaifer, A. E.; Stockdale, D.; Bazan, G. C. *Adv. Mater.* **2011**, *23*, 2367.
30. Bawendi, M.G.; Steigerwald, M.L.; Brus, L. E. *Annu. Rev. Phys. Chem.***1990**, *41*, 477.

31. (a) Impellizzeri, S.; Monaco, S.; Yildiz, I.; Amelia, M.; Credi, A.; Raymo, F. M. *J. Phys. Chem. C* **2010**, *114 (15)*, 7007. (b) Amelia, M.; Impellizzeri, S.; Monaco, S.; Yildiz, I.; Silvi, S.; Raymo, F. M.; Credi, A. *Chem. Phys. Chem.* **2011**, *12* (12), 2280.
32. Kucur, E.; Bücking, W.; Giernoth, R.; Nann, T. *J. Phys. Chem. B* **2005**, *109*, 20355.
33. Querner, C.; Reiss, P.; Sadki, S.; Zagorska, M.; Pron, A. *Phys. Chem. Chem. Phys.* **2005**, *7*, 3204.
34. Leatherdale, C. A.; Bawendi, M. G. *Phys. Rev. B* **2001**, *63* (16), 1653151.
35. Marcus, R. A. *J. Chem. Phys.* **1965,** *43***,** 679.
36. (a) Sutin, N. *Prog. Inorg. Chem*. **1983,** *30*, 441. (b) Bhat, M. A. *New J. Chem.* **2009**, *33* (1), 207.
37. (a) Edward, J. T. *J. Chem. Educ.***1970**, *47*, 261. (b) Zwanzig, R.; Harrison, A. K. *J. Chem. Phys.***1985**, *83*, 5861.

# CHAPTER 3

# Behavior of CdSe Quantum Dots attached to Carbon Nanostructures

This chapter deals with the synthesis, characterization and applications of hybrid nanostructures of CdSe (3-5 nm) QDs with two different, yet interconnected carbon nanostructures single walled carbon nanotubes (SWCNT) and graphene nanoribbons (GNRs). For example, diazonium salt chemistry has been used to functionalize SWCNT surface while GNRs have been synthesized by unzipping SWCNT by a recently reported electrochemical method. In comparison, CdSe QDs have been attached to SWCNTs via ligand exchange while in case of GNRs, CdSe QDs have been electrochemically generated *in situ* on GNRs during the unzipping of SWCNTs. All the materials are characterized using various physicochemical tools such as SEM, TEM, XPS, Raman, TGA, contact angle measurement and cyclic voltammetry. Photoluminescence quenching along with photoconductivity measurement suggests that these types of hybrid materials can be very useful for the next generation photovoltaics as well as optoelectronic devices.

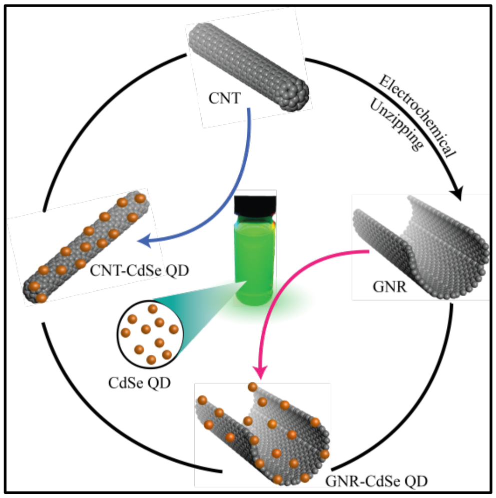

---

*Part of the works discussed in this chapter have been published in: (a) *Phys. Chem. Chem. Phys.*, **2011**, *13*, 14669-14675. (b) *Chem. Commun.* **2012**, *48*, 3088-3090.

## 3.1. Introduction

Semiconductor quantum dots (QDs), often termed as the giant artificial atoms, of varying size and shape possess unique properties like tunable absorption of light,[1] and generation of multiple excitons[2] which make them ideal candidate for solar cells and other optoelectronic devices. Consequentially, the exploration of the structure and properties of these QDs has strong implications on the development of high throughput optoelectronic devices.[3]Moreover, carbon-based materials such as diamond, carbon nanotubes (CNTs), carbon nanofibers (CNFs), carbon nanospheres (CNSs) and graphenes coupled with QDs are more favorable in terms of their better stability and mechanical strength.[4] Among these, CNTs and graphene do possess unique structural, electronic, mechanical and optical properties and hence they are actively sought as an effective component of a variety of devices including field-effect transistors (FETs), Li-ion batteries, light-emitting diodes (LEDs) and also as a catalyst support in fuel cells.[5] Additionally, higher surface area, mechanical strength and thermal stability of these materials suggest a host of wide-ranging, potential applications in heterogeneous catalysis, field emitters, high-strength engineering fibers, sensors, actuators, composites, tips for scanning probe microscopy, gas storage media and next generation molecular and electronic devices.[6] Blending of these two different materials, therefore, can give rise to important hybrid materials with improved characteristics than that of the individual materials.

However, several challenges lie ahead in finding suitable methods for successfully combining these two materials. For example, although there are several strategies for attaching CdSe QDs to different carbon nanostructures, a few have serious stability issues, Some of them rely on covalent functionalization of carbon nanostructures followed by chemical binding of QDs by means of suitable chemical reactions, or polymer wrapping of carbon structures for attachment of QDs or *in situ* synthesis. But almost all the methods suffer from common limitations of using high temperature, multistep reactions, low yield and size control of the QDs and above all difficulties of obtaining a uniform distribution of QDs on the carbon surface. Moreover, detailed characterization studies on the performance of such hybrids are rare.

In the previous chapter, we have discussed the hot injection synthesis of CdSe QDs of varying size and shape with possible mono-dispersed size distribution. It has also been demonstrated that their electronic properties/band structure parameters are very much dependent on their size and shape. But nothing has been discussed about their properties in presence of carbon nanostructures.

Present chapter, therefore, aims to develop a new simple methodology for synthesizing CdSe QD-carbon nanostructure hybrids in order to explore their properties and possible applications. Two different nanostructures of carbon, namely single walled carbon nanotubes (SWCNTs) and graphene nanoribbons (GNRs) have been chosen for the study mainly due to their topological relationship. GNRs have been synthesized by electrochemical unzipping of SWCNTs and CdSe QDs are generated on GNRs by means of *in situ* electro-deposition.[7] SWCNTs have been functionalized with diazonium salt of 4-aminothiophenol (4-ATP) to obtain –SH terminated SWCNTs and then oleic acid capped CdSe QDs have been exchanged with –SH group to get CdSe QD decorated SWCNT. The hybrids have been characterized with many techniques including SEM, EDAX, TEM, Raman, UV-Vis, Photoluminescence, Cyclic voltammetry, Thermogravimetry and Contact angle measurements.

## 3.2. Experimental Section

### 3.2.1. Materials

CNTs were obtained from Carbon Nanotechnologies Inc. and were purified according to the reported protocol.[7]Sodium dodecylsulphonate (SDS), and 4-aminothiophenol were purchased from Aldrich and used as received. $H_2SO_4$ (98%), HCl (38%), $NaNO_2$, $H_2O_2$ were received from Thomas Baker and used without any further purification. PTFE filter paper was obtained from Rankem. MilliQ water (DI water) was used for all purposes unless otherwise stated. Cadmium oxide (CdO), trioctyl phosphine (TOP) and 1-octadecene were purchased from Aldrich and used as received. Se powder, hexane and ethanol (99.9%) of analytical reagent grade were purchased from Thomas Baker. Oleic acid was purchased from Rankem and used without further purification. Acetonitrile ($CH_3CN$, HPLC grade) and Dichloromethane ($CH_2Cl_2$. AR grade) were purchased from

Rankem Co. and purified and dried according to the standard procedures before use for the wetting studies.

### 3.2.2. Preparation of thiol (-SH) functionalized SWCNTs (SWCNT-SH)

SWCNTs were dispersed in 0.1% SDS aqueous solution. A diazonium salt of 4-aminothiophenol (4-ATP) was prepared by mixing 70 mg 4-ATP with 200 mg $NaNO_2$ in 40 mL distilled water at 0-5°C followed by the addition of 3 mL 6 M HCl solution (ice cold) slowly to the above mixture. A gradual change of the solution color (transparent) to pale yellow indicated the formation of diazonium salt. The mixture was then slowly (and with constant stirring) added to the SWCNT suspension (at 0-5°C) and allowed to stir for another 4 h. Subsequently, the reaction mixture was filtered, washed with DI water and re-suspended in DMF to remove the SDS surfactant and excess of unreacted 4-ATP molecules. The suspension was finally filtered and washed to get –Ph-SH functionalized SWCNT (denoted as SWCNT-SH).

### 3.2.3. Unzipping of SWCNT to synthesize Graphene Nanoribbons (GNRs) and *in situ* CdSe QD anchoring

SWCNTs were unzipped according to a procedure reported recently by our group[8] Briefly, a thin coating of SWCNT was prepared on a Pt-electrode (2 mm diameter) using 0.05 wt% nafion. It was then unzipped to form graphene sheets in 0.5 M $H_2SO_4$ by first oxidizing at 0.8 V (*vs* mercury-mercurous sulphate reference electrodefor 6 h) followed by reduction at -0.7 V (for another 6 h). At the end of this reduction process, 10 mM $CdSO_4$ and 5 mM $Na_2SeO_3$ aqueous solution were added in the solution and the reduction was continued for 5 min, 15 min and 1 h for CdSe formation (Scheme 3.1). Samples were collected by sonication of the electrode in deionized water and washed several times before submitting for further characterization.

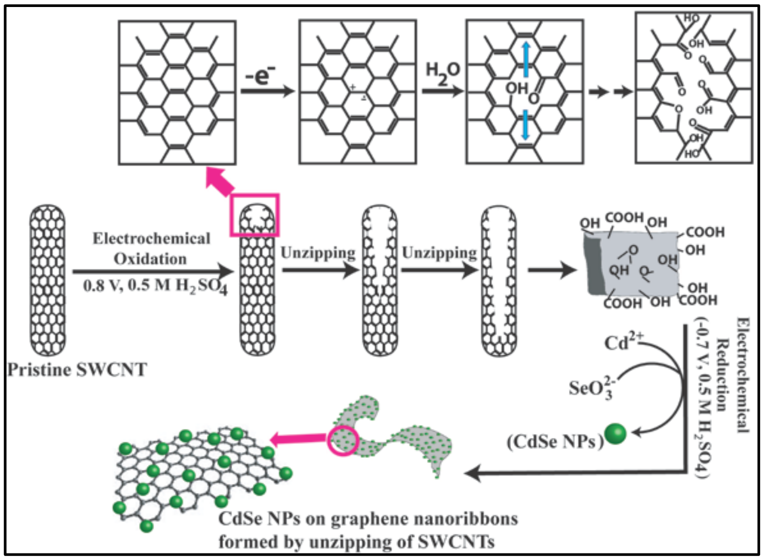

**Scheme 3.1.** Electrochemical unzipping of SWCNT and subsequent CdSe nanoparticle decoration on the so formed GNRs; pristine SWCNT coated on Pt foil is electrochemically unzipped in 0.5 M $H_2SO_4$ at room temperature; CdSe has been subsequently deposited on GNRs using $CdSO_4$ and $Na_2SeO_3$ as Cd and Se precursors respectively during the reduction of oxidized GNRs.

### 3.2.4. Exchange of oleic acid capped CdSe QDs with SWCNT-SH

18 mg of CdO was taken in a four-neck RB flask along with 0.6 ml oleic acid and 10 ml 1-octadecene (ODE). A Se-precursor (Se-TOP) solution was prepared by dissolving 32 mg Se powder in 5 ml ODE containing 0.6 mL trioctylphosphine (TOP) by slight warming at 60°C. The RB flask containing CdO was then heated at 190°C when red CdO dissolved completely to give a colorless solution (Cd-oleate). The heating was continued until it reached to 230°C, when 1 ml Se-TOP was quickly injected into the reaction mixture when the solution turned light yellow due to the formation of very small CdSe NPs. The heating was subsequently stopped and the particles were allowed to settle at that temperature. Aliquotes were collected at different time interval (30 s, 1 min, 3 min) to get different particle sizes. The nanoparticles (NPs) were then precipitated out from the solution by using a small amount of hexane followed by copious amount of ethanol. This was then centrifuged and washed and the procedure was repeated 5-6 times to get pure nanocrystals. The precipitate was then vacuum dried to obtain dry powder of CdSe nanoparticles.Oleic acid capped CdSe NPs (CdSe-OA) (concentration of CdSe suspension was maintained by fixing the first excitonic peak intensity at 0.1 optical

density throughout all our experiments) were then exchanged by mixing the DMF suspension of SWCNT-SH (12.7 mg $ml^{-1}$) with toluene soluble CdSe-OA.

### 3.2.5. Ozonolysis of MWCNTs

Multiwalled carbon nanotubes (MWCNTs) were prepared by a CVD method[9] using a ferrocene and xylene mixture at 700°C in a tubular furnace in Ar-flow. Ozonolized bucky papers for this study were prepared as described elsewhere.[10] In brief, MWCNTs (purity >90 %,diameter 20-30 nm and ~1% contains CNTs having diameter 100-150 nm as determined from TEM analysis; not shown), dispersed in dichloromethane (60 mg in 40 mL $CH_2Cl_2$), were subjected to ozonolysis in a suitable reactor (Fischer Ltd.) for about an hour, quenched with dimethyl sulphide(2 mL),washed with dichloromethane and subsequently filtered and dried at $80^0$ C under vacuum (this ozonized sample is denoted as oz-MWCNT while pristine sample is described as p-MWCNT). Finally, the dried material was pressed at 0.2 bar pressure to obtain bucky paper (60-80 μm thick).

## 3.3. Structural and Morphological Characterization

### 3.3.1. Scanning electron microscopy (SEM) and EDAX

The surface morphology of the samples was examined by using a Quanta 200 3D, FEI scanning electron microscope (SEM) operating at 30 kV.A small piece of FTO plate containing the sample was mounted on aluminium stubs and micrographs were recorded with a 30 kV tension and 20 pA current with the help of a camera attached on the high resolution recording unit. This SEM instrument was equipped with Phoenix energy dispersive spectral (EDS) analysis setup for the elemental analysis.

### 3.3.2. Thermogravimetric analysis (TGA)

Thermogravimetric analysis was carried out on a TGA Q5000 TA Instruments - Thermal analyzer from 50°C to 900°C at a rate of 10°C/ min in air as well as in nitrogen. Both p-MWCNT and oz-MWCNTs were soaked in dichloromethane and acetonitrile for 2 h prior to TGA measurements.

### 3.3.3. XPS analysis

X-ray photoelectron spectroscopic (XPS) measurements were carried out on a VG Micro Tech ESCA 3000 instrument at a pressure of > $1x10^{-9}$Torr (pass energy of 50 eV with an electron take off angle $60^o$ and an overall resolution of 1 eV) using Mg Kα (source, hν =

1253.6 eV) radiation. The alignment of binding energy (BE) was calibrated using Au 4f binding energy of 84 eV as the reference. The X-ray flux (power 70 W) was kept deliberately low in order to reduce the beam-induced damage. The spectra were fitted using a combined polynomial and Shirley type background function.[11]

### 3.3.4. Micro Raman

All Raman spectroscopy measurements were carried out at room temperature on an HR 800 Raman spectrophotometer (Jobin Yvon HORIBA, France) using monochromatic radiation emitted by a He–Ne laser (632.8nm), operating at 20 mW. The experiment was repeated several times to verify the consistency of the spectra.

### 3.3.5. Contact angle measurement

All contact angle measurements were performed by a sessile drop method on a GBX model (DIGIDROP contact angle instrument) using Windrop software. In case of MWCNTs and oz-MWCNTs, contact angle measurements were performed after fixing the bucky paper (thickness 0.5 mm) on a cleaned, dry glass slide with double side stick-tape with no effect due to the tape. Extreme care has been taken in carrying out these measurements to monitor contact angle values within 1-2 minutes to avoid the evaporation effects. All contact angle measurements were carried out at room temperature ($27^{o}$C) and constant humidity (40-50%) with a standard deviation of $\pm 2^{o}$.

### 3.3.6. Electrical Characterizations

Photoconductivity of the sample was measured by two probe method using KEITHLEY source metre and voltmeter in presence of 1.5 AM light source.

## 3.4. Results and Discussion

### 3.4.1. FTIR analysis

FTIR is very valuable technique to know the functional groups present on CNTs both before and after chemical modification. It also gives information about the possibility of functional groups being generated during electrochemical unzipping of CNTs. Accordingly, Fig. 3.1(a) and (b) display a superimposition of the representative FTIR spectra of p-SWCNT and un-SWCNT-CdSe composite showing interesting structural changes on SWCNT surface due to electrochemical oxidation. The peak originating at

1614 cm$^{-1}$ is attributed to the stretching frequency of –COO$^{-}$ from –COOH group upon the electrochemical oxidation. The bands at 1146, 1038 and 856.4 cm$^{-1}$ are due to the C=C backbone of p-SWCNT while the broad band between3000-4000 cm$^{-1}$ is indicative of adsorbed moisture and aerial oxidation on SWCNT surface. All peaks match well with that of the reported values for similar functional groups.[12] It is however, noteworthy that absorption peaks corresponding to other oxygen functionalities like epoxy and, carboxylic acids are either absent or present in a very insignificant amount. This may be attributed to the fact that during the electrochemical reduction cycle, most of the oxygenated functional groups get reduced leaving behind a very less number of such groups which further act as anchoring sites for the CdSe nanoparticles during their subsequent formation by electrochemical reduction (REF).

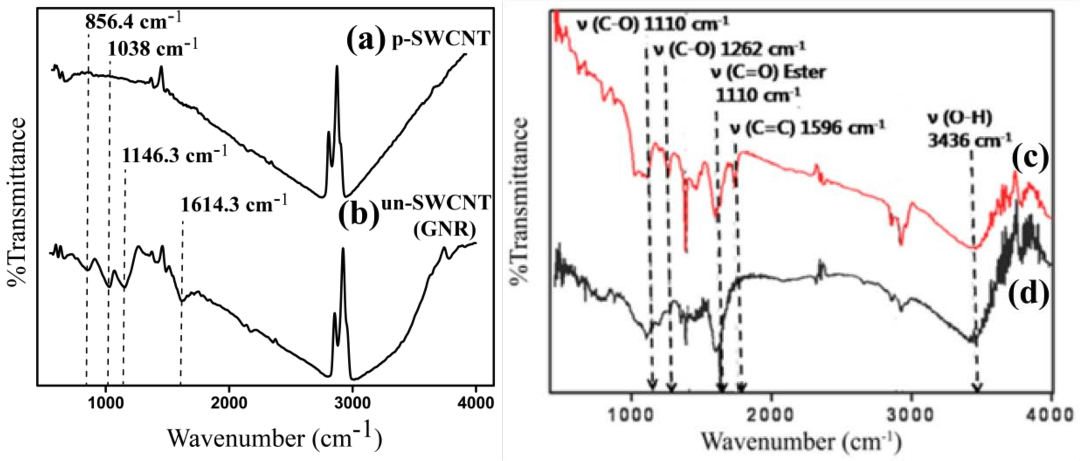

**Figure 3.1.** A comparison of the FTIR spectra of (a) SWCNT,(b) unzipped SWCNTs, (c) ozonized MWCNT (oz-MWCNT) and (d) pristine MWCNT (p-WCNT); Ozone exposure causes outer-wall functionalization which results in the formation of C-O, C=O groups; Frequencies of the vibrations for these groups are indicative of the formation of ester linkages on the outer-wall of CNTs.

Similarly, a comparison of fig. 3.1(c) and (d) presents interesting the FTIR spectral changes of MWCNT sample before and after ozonolysis. The spectral bands originating at frequencies 1736 cm$^{-1}$, 1262 cm$^{-1}$, 1110 cm$^{-1}$ are indicative of ester group formation. Band at 1736 cm$^{-1}$ is assigned to C=O group and that at 1110 and 1262 cm$^{-1}$ are due to the C-O stretching. Peak at 1596 cm$^{-1}$ is the stretching frequency of C=C group located near the newly formed oxygenated groups. Peak at 3436 cm$^{-1}$ is assigned to adsorbed moisture. All peaks are in accordance with that in previously reported works.[12]

### 3.4.2. Scanning Electron Microscopy and EDAX

fig. 3.2 presents a comparative analysis of the scanning electron micrographs of p-MWCNT and oz-MWCNT. Interesting change in the contrast for the image of Oz-MWCNTs indicates the formation of surface functionality on exposure to ozone. Also the images show more compactness of the bucky paper (i.e., assembly of CNTs pressed to make paper like stuff) as compared to that of p-MWCNTs. During ozonolysis the long CNTs break down into smaller fragments, but that is not clear from the SEM images which are limited due to its low resolution.

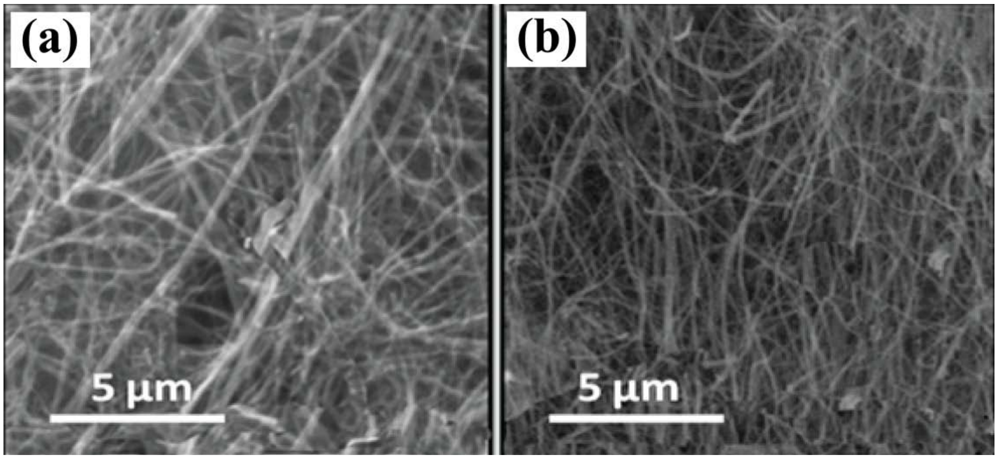

**Figure 3.2.** Scanning electron micrographs of (a) pristine MWCNT and (b) the bucky paper after subjecting the MWCNTs to ozonolysis.

EDAX analysis has been performed both to know the distribution of –SH group in case of thiol modified SWCNTs as well as to find out the Cd to Se ratio in case of *in situ* generated CdSe on unzipped SWCNTs (GNRs). Accordingly, fig.3.3 shows the EDAX analysis report of *in situ* generated CdSe on GNRs. It surprisingly, gives the Cd to Se ratio 1:2 instead of 1:1 (i.e., stoichiometric CdSe alloy). One of the intermediates during electrodeposition of CdSe is $H_2Se$ which further reacts with Cd to form CdSe. Once formed, some part of $H_2Se$ reacts with $H_2SeO_3$ to generate free Se according to the parasitic reaction,

$$2Se + 4H^+ + 4e = 2H_2Se\,, E^0 = -0.40\ V\ vs\ NHE$$

$$2H_2Se + Na_2SeO_3 + 2H^+ = 3Se + 3H_2O + 2Na^+$$

This free Se then gets deposited on the preformed CdSe and also on graphene. Hence, there is almost invariably some excess selenium during the electrodeposition of CdSe, especially in acidic medium (since the above reactions are pH dependent) as has been proposed in the previous studies.[13]However, this excess Se is amorphous in nature and can be removed later either by vacuum annealing or by etching in alkaline $Na_2S$ solution (1 M).[13] In fact, excess selenium formation can be avoided by changing the mode of electrodeposition from potentiostatic (in the present case) to potentiodynamic (i.e., using repeated cyclic voltammetric scans).In this case Se concentration is adjusted in such a low amount that submonolayer amount of Se can only get reduced in each cycle. More importantly, excess Cd formed in each cycle, is consumed during the subsequent cycle to form stoichiometric CdSe NPs (Cd:Se is 1:1).[14]However, in the present case we have mostly relied on potentiostatic deposition in order to effect simultaneous reduction of oxidized grapheme nanoribbons as well as CdSe co-deposition.

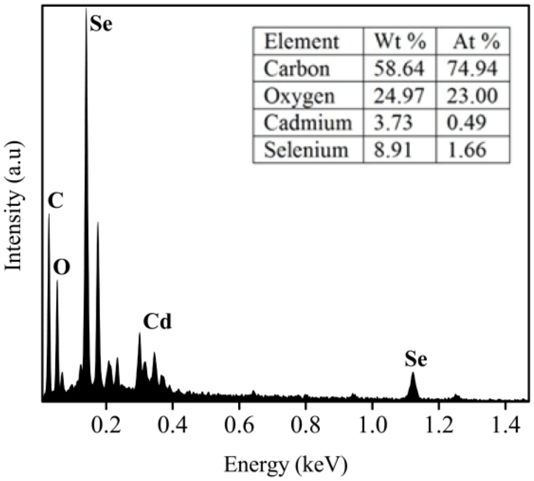

| Element | Wt % | At % |
|---|---|---|
| Carbon | 58.64 | 74.94 |
| Oxygen | 24.97 | 23.00 |
| Cadmium | 3.73 | 0.49 |
| Selenium | 8.91 | 1.66 |

**Figure 3.3.** Representative EDAX spectrum of the composite revealing the presence of Cd and Se in ~1:2 ratio.

Fig. 3.4 shows the EDAX analysis and elemental mapping of SWCNT-SH-CdSe (CdSe decorated SWCNT-SH) sample. Fig.3.4 (e) is the EDAX spectrum of SWCNT-SH, which shows the presence of about 3.6-4% S in the sample of SWCNT-SH-CdSe for the initial SWCNT to 4-ATP ratio of 1:1. This is equivalent to ~$10^{18}$ to $10^{20}$ number of –SH units per gram of SWCNTs. Moreover, a uniform distribution of S or –SH groups is also seen on SWCNT surface (fig. 3.4(a), (b)). This, therefore, suggests a homogeneous functionalization of SWCNTs. Fig. 3.4 (b) and (c) are the elemental maps of C, Cd and Se respectively for SWCNT-SH-CdSe samples. This homogeneous distribution of CdSe perhaps indicates a successful ligand exchange and subsequent decoration of CdSe QDs on SWCNT surface.

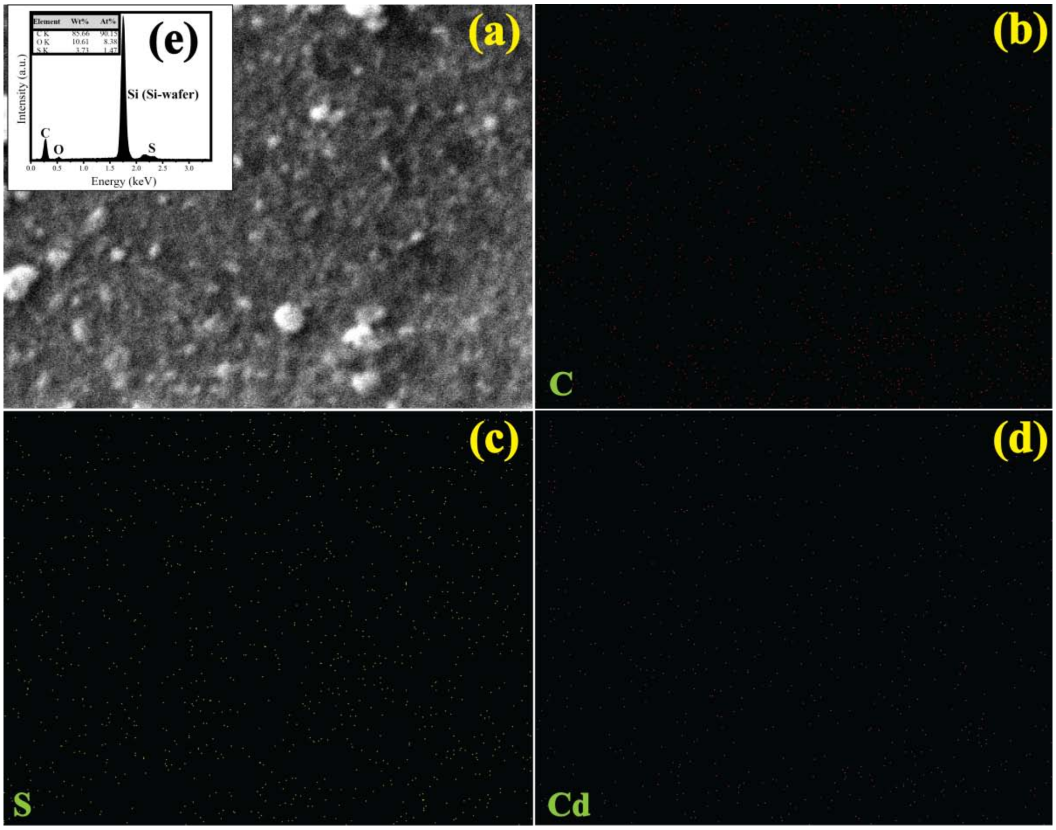

**Figure 3.4.** (a) SEM image and elemental mapping of (b) C (c) S and (d) Cd in SWCNT-SH-CdSe sample showing uniform distribution of the elements over SWCNT bundles, (e) EDAX spectrum of SWCNT-SH showing the percentage of the elements present.

### 3.4.3. TG analysis

In order to further confirm the chemical interaction between –PhSH group and SWCNT surface, thermogravimetric experiments have been carried out. Accordingly, fig.3.5 shows the thermograms of pristine SWCNT (p-SWCNT) and SWCNT-SH (chemically functionalized SWCNT) respectively. Interestingly, the decomposition profiles of p-SWCNT and SWCNT-SH are different. For example, at 900°C, SWCNT-SH shows a higher weight loss (~18%) than p-SWCNT (~10-12%) and thus provides conclusive evidence for the presence of functional groups other than oxygen functionalities in SWCNT-SH. This undoubtedly proves that chemical bonding occurs between 4-ATP and RGO during diazotization. FTIR, EDAX and TGA analysis thus ostensibly confirms the successful grafting of –SH group in SWCNT.

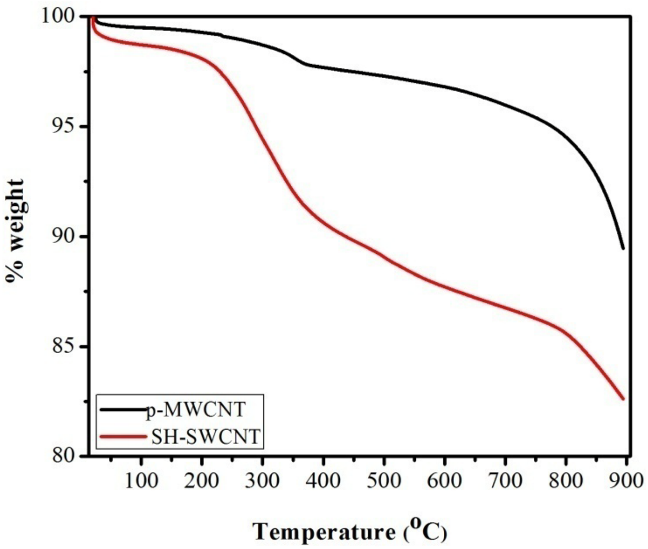

**Figure 3.5.** A comparison of the decompositon profiles of p-SWCNT (black) and SWCNT-SH (red) in nitrogen atmosphere; lower retention in case of SWCNT-SH confirms the chemical bonding between –PhSH moiety and SWCNT surface.

Thermogravimetric analysis has also been carried out in order to understand the adsorption-desorption behaviour of $CH_3CN$ and $CH_2Cl_2$ on p-MWCNTs and oz-MWCNTs respectively. Accordingly, fig.3.6 shows a comparison of thermograms of p-MWCNTs and oz-MWCNTs in nitrogen atmosphere after soaking in acetonitrile and dichloromethane respectively. Thermal profiles of p-MWCNT and oz-MWCNT (in $N_2$ as well as in air) have also been incorporated for comparison. Interestingly, the %weight of both p- as well as oz-MWCNT is found to increase after soaking in the respective solvents and the decrease in weight starts at much higher temperature as compared to that of the reference samples. However, the nature of the plot and the amount of the %weight loss are not the same for samples soaked in $CH_2Cl_2$ and $CH_3CN$ and the difference is more significant for p- and oz-MWCNTs. This clearly indicates different types of adsorption for the two liquids on CNTs and moreover the nature of adsorption seems to change with the ozone treatment. One probable reason could be the chopping of CNTs upon ozone treatment and thereby facilitating some liquids to get incorporated into the capillary of CNTs (other than the grooves and interstices of ozone treated CNT bucky paper) and those liquids may get desorbed at higher temperature or react with CNTs resulting in the initial weight increment in TGA (for p-MWCNTs it is mostly the liquids at the interstices of CNT bundles which might react with CNTs).

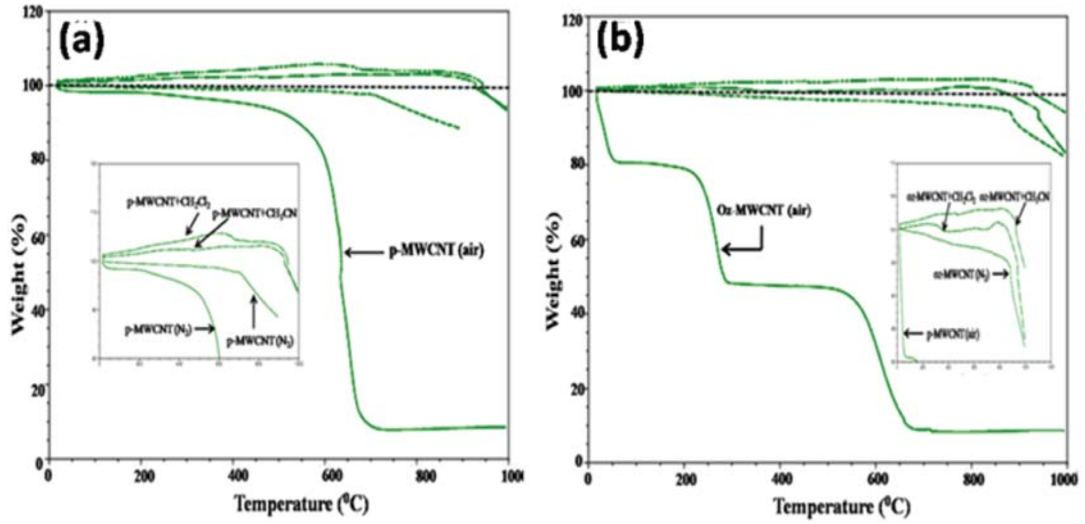

**Figure 3.6.** Thermograms of (a) pristine MWCNTs and (b) ozonized MWCNTs after soaking and heating in dichloromethane and acetonitrile respectively; All measurements were performed in nitrogen atmosphere; TGA of p-MWCNT and oz-MWCNT in air are incorporated in the figure for comparison; Inset shows the enlarged view of the thermograms after soaking in acetonitrile and dichloromethane.

### 3.4.4. XPS analysis

In order to get better insight into the nature of interaction between acetonitrile and CNTs,

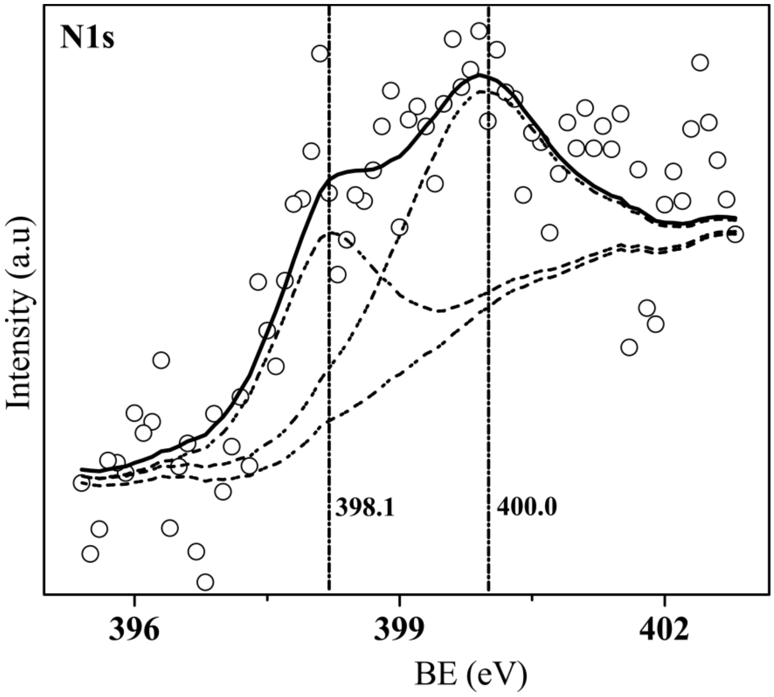

**Figure 3.7.** Core level N-1s spectrum showing the interaction of acetonitrile with CNT.

XPS study can be very useful to understand the nature of intercations of various molecules with CNT surface. Accordingly, fig.3.7 shows the N-1s core level spectrum after acetonitrile adsorption on CNTs. The spectrum suggests that the amount of nitrogen is extremely small especially when we consider the weak adsorption of acetonitrile molecules during the experiment (leaving behind non-interacted acetonitrile). Hence, the XP spectrum of N-1s apparently appears so noisy. However, deconvolution gives two peaks at 398.1 eV and 400.0 eV respectively. The nitrogen of $CH_3CN$ has a binding energy of 399.4 eV.[15] The first peak (398.1 eV) may be assigned to the N-atom of some loosely-adsorbed acetonitrile while the second peak at higher binding energy indicates electron donation from N-atom of $CH_3CN$ molecule to the CNT whereby the N-atom becomes electron deficient and hence there is an upshift of N-binding energy. However, it is difficult to conclude from these experiments whether acetonitrile interacts via π- π interaction or directly via the donation of unshared electron (or follows both the way). This interaction also supports the slow change of contact angle for p-MWCNT when a drop of acetonitrile is put on its surface. Dichloromethane, on the other hand, cannot interact in such a way because, it neitherhas π- electron to interact nor unshared electrons to donate to CNT. Further, it is less polar in nature so that it is incapable of inducing charge transfer to or from the CNTs. Thus dichloromethane gets very weakly adsorbed on CNT surface to cause physical dampening of the phonon modes of CNTs which is supported by the minor upshift (4 $cm^{-1}$) of D and G bands upon wetting. In sharp contrast, for oz-MWCNT, such an explanation no longer holds good, partly because of the opening of the tips of CNTs after ozonolysis and partly because of the fact that π-electron cloud on CNT gets reduced upon ozonolysis due to the formation of more $sp^3$ carbon atoms on its surface at the cost of $sp^2$ carbon atoms. The open tips allow easy percolation of the liquids inside the channels and therefore results in observed wetting dynamics.

### 3.4.5. Cyclic voltammetry (CV) Experiments

#### 3.4.5.1. CV before and after unzipping of SWCNTs

CV is extremely useful in understanding the unzipping process of SWCNT under controlled potential conditions. Accordingly, fig. 3.8 shows the cyclic voltammograms of SWCNTs (coated on a 2 mm Pt-disk electrode) before and after applying constant anodic bias (0.8 V *vs* MMS) for 10 h in 0.5 M $H_2SO_4$. The peaks A1/C1 is attributed to quinone-hydroquinone couple which is well known for CNT under similar conditions.[16]The suitable potential for unzipping has been selected on the basis of voltammograms of SWCNT in 0.5 M $H_2SO_4$ (the potential was marked by thick arrow in fig.3.8 where oxygen evolution just starts).The capacitive current increases significantly after applying a positive potential for 10 h (as is indicated by the increase in height of the quinone-hydroquinone peak), indicating the increase in overall surface area of the material due to unzipping to form oxidized GNRs.[17] CV of blank platinum electrode without CNT coating is also shown for comparison as this succinctly reveals the characteristic hydrogen desorption and oxygen reduction peaks for polycrystalline Pt.

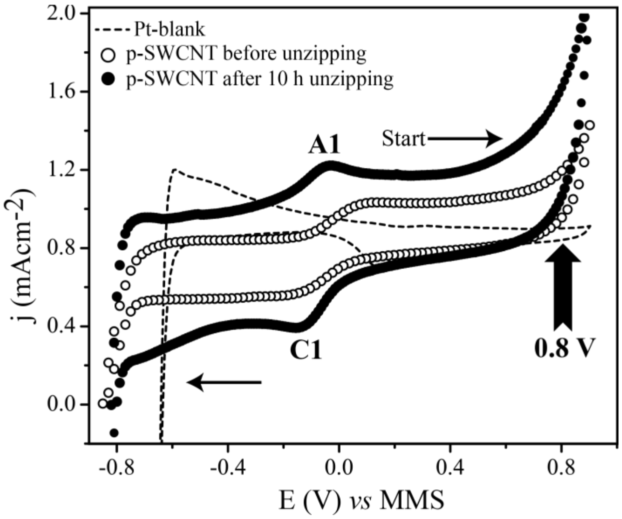

**Figure 3.8.** Cyclic voltammogram of SWCNTs on Pt-electrode in 0.5 M $H_2SO_4$ before and after oxidative unzipping at 0.8 V for 10 h; scan rate is 100 $mVs^{-1}$.

### 3.4.5.2. CV for the electrodeposition of CdSe

Again CV is employed to find out the suitable potential required for theco-deposition of CdSe along with the simultaneous reduction of oxidized GNRs. A solution containing 10 mM $CdSO_4$ and 5 mM $Na_2SeO_3$ in 0.5 M $H_2SO_4$ is used for *in situ*electro-deposition of CdSe. Accordingly, Fig.3.9 shows a comparison of CVs of only $Na_2SeO_3$, only $CdSO_4$ and a mixture of $CdSO_4$ and $Na_2SeO_3$ using GNR as a working electrode; indeed, $Na_2SeO_3$ alone shows multiple redox peaks.

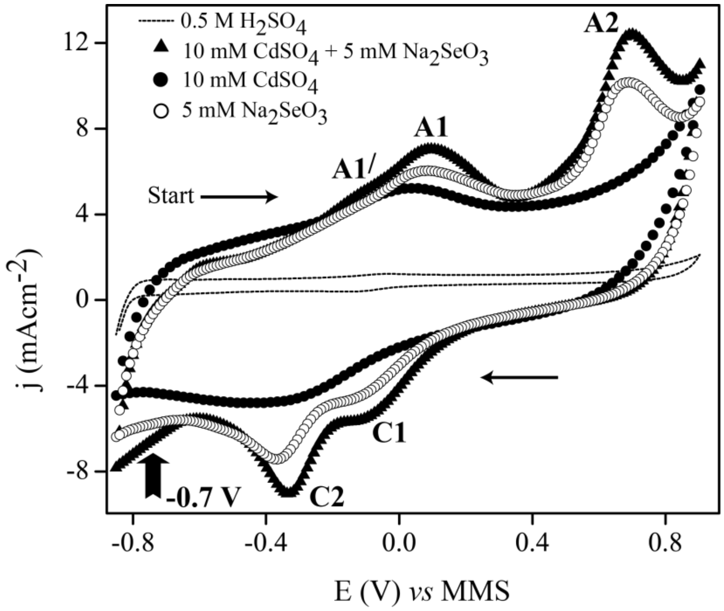

**Figure 3.9.** (a) Cyclic voltammogram of unzipped SWCNT during reduction at -0.7 V and in presence of 10 mM $CdSO_{4,}$ 5 mM $Na_2SeO_3$ and a mixture of both the species; CV of GNRs (unzipped CNTs) in 0.5 M $H_2SO_4$ has also been shown for comparison; All voltammograms are recorded at a scan rate of 100 mVs$^{-1}$ using Pt-foil as counter electrode and Pt-wire as quasi-reference electrode and potentials are corrected with respect to mercury-mercuroussulphate (MMS) reference electrode;. The thick arrow indicates the corresponding potentials used for potentiostatic oxidation of SWCNT and CdSe deposition during reduction cycle respectively.

The peaks can be identified as follows (according to the redox reactions of $SeO_3^{2-}$ in acidic pH):[18]

$A1' : H_2Se = Se + 2H^+ + 2e\,, E^0 = -0.40\ V\ vs\ NHE$……………………………….(1)

$A1 : H_2Se = Se + 2H^+ + 2e\,, E^0 = -0.115\ V\ vs\ NHE$……………………………….(2)

$A2 : Se + 3H_2O = H_2SeO_3 + 4H^+ + 4e\,, E^0 = 0.74\ V\ vs\ NHE$…………………….(3)

$C1 : H_2SeO_3 + 4H^+ + 4e = Se\ (grey) + 3H_2O$……………………………………….(4)

$C2 : 2Se\ (grey) + 4H^+ + 4e = 2H_2Se + 4H^+ + 2e$…………………………………(5)

$2H_2Se + Na_2SeO_3 + 2H^+ = 3Se\ (red) + 3H_2O + 2Na^+$……………………………(6)

Similarly, $CdSO_4$ shows two peaks corresponding to $Cd^{2+}$/Cd couple. This couple however, vanishes in the presence of $Na_2SeO_3$ and peaks due to $SeO_3^{2-}$ redox processes predominate. $Cd^{2+}$ reacts with $H_2Se$, according to equation (5), to form CdSe. Interestingly, no CdSe has been found to form in the solution. This suggests that $Cd^{2+}$ is initially bonded to the functional group present on the partially reduced GNRs and finally to form CdSe nanoparticles (QDs) on GNRs. However, reaction (6) often competes and results in slight excess Se deposition on so formed CdSe QDs. This agrees with EDAX and Raman observation of the hybrids. Reactions of $SeO_3^{2-}$ are highly pH sensitive as can be seen from equation (1) to (6). But, since unzipping has been done in 0.5 M $H_2SO_4$, no other pH has been tested for CdSe deposition. Temperature has been kept constant at 303 K. From the CV analysis it is clear that the $SeO_3^{2-}$ reduction is complete after -0.4 V (*vs* MMS) and that the oxidized GNRs are completely reduced at a constant potential of -0.7 V (*vs* MMS). Hence, at -0.7 V simultaneous reduction of oxidized GNRs and formation of CdSe is expected to occur.

### 3.4.6. Chronoamperometry

In order to determine the suitable potential for reduction and also to investigate the mechanism of deposition, chronoamperometry has been performed for 100 s at two different potentials (-0.33 V and -0.77 V *vs* MMS respectively), which are more negative than the open circuit potential (OCP) of the system (-0.21 V *vs* MMS). Accordingly, fig.3.10(a) shows the amperogram for the deposition. Both the plots show an initial sharp decrease (within ~2 s) in current density perhaps due to double layer charging and also due to parasitic (local) currents (not shown in the plot). The current transient then steadily increases to show a shoulder (or hump) followed by a minor decrease to a certain value, eventually reaching a plateau. The Peak maximum, however, increases and becomes more pronounced as the deposition potential becomes more negative (-0.33 V to -0.7 V) as has been predicted by classical nucleation theory.[19]Since the reduction of oxidized SWCNT is carried out at -0.7 V, electrodeposition has also been carried out subsequently at -0.7 V. In order to unravel the nucleation process, the current-time transient obtained at -0.7 V, has been subdivided into 3 zones (fig. 3.10(a)) - I, II and III. Linearity of current density *vs*$t^{-1/2}$ (fig.3.10(b)) for zone-I (i.e, before peak maximum) is indicative of instantaneous 3D nuclei formation with hemispherical growth. There are two models available to describe nucleation - instantaneous and progressive.[19-20]A plot of two dimensionless numbers namely $(i/i_m)^2$ and $t/t_m$ give information about either of the above mechanisms.

$$\left(\frac{i}{i_m}\right)^2 = \frac{1.9542}{\frac{t}{t_m}}\{1-\exp[-1.2564\left(\frac{t}{t_m}\right)]\}^2 \quad \text{……………………………………………….(7)}$$

$$(\frac{i}{i_m})^2 = \frac{1.2254}{\frac{t}{t_m}}\{1 - \exp\left[-2.3367(\frac{t}{t_m})^2\right]\}^2 \text{ ……………………………………………….(8)}$$

Fig. 3.10(b) and (c) represent the fitting of experimental data with that obtained from equation 7 and 8 (zone-II, t >10 s). Near to the peak maximum in the reduced current-time curve, the deposition can be described well by equation (7) and at this time CdSe deposition occurs instantaneously perhaps with hemispherical growth. However, during the short-time regime (zone-I, t <10 s) there is a strong competition between progressive and instantaneous nucleation although instantaneous mechanism is more pronounced.

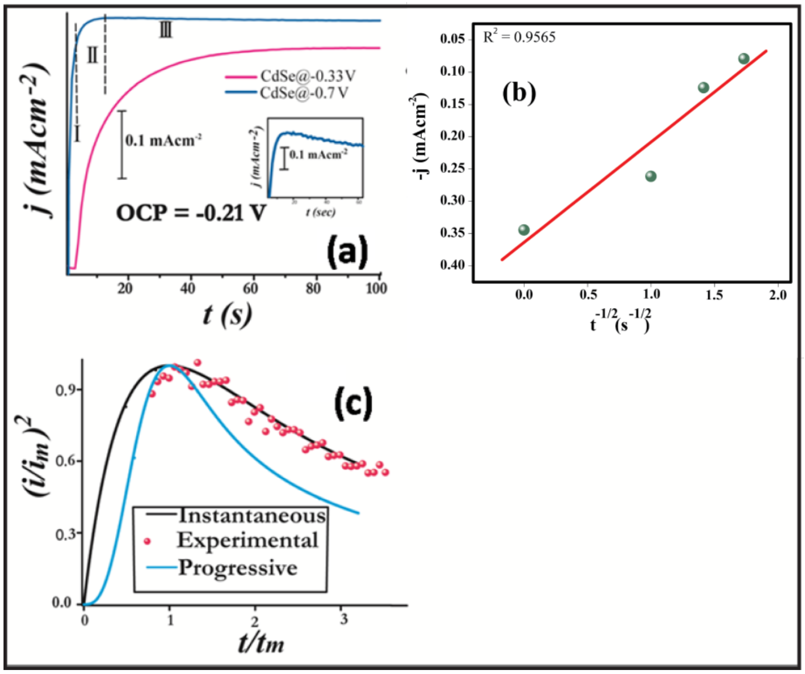

**Figure 3.10.** (a) i-t transients during the electrodeposition of CdSe at -0.33 and -0.7 V respectively, (b) current density *vs* $t^{-1/2}$ during the initial stage of deposition and (c) dimensionless *i-t* transient for nucleation of CdSe on GNRs and corresponding theoretical curves for instantaneous and progressive nucleation.

### 3.4.7. Powder XRD (PXRD)

Fig.3.11 shows the X-ray diffraction pattern of unzipped SWCNT-CdSe composite (denoted as un-SWCNT-CdSe) which confirms the formation of CdSe nanoparticles on unzipped nanotubes. The main diffraction peak is observed at 23° (broad) corresponding well to the (100) reflection of primitive hexagonal CdSe reported previously(JCPDS 77-

0046).[21] Other broad peaks (at 36.5°, 42.8°, 49.4° and 56.3°) also match very well with the same crystal structure of CdSe. The (002) peak of SWCNT/graphitic structure is overlapped with the (100) peak of CdSe and hence is not clearly visible. In fact, the appearance of so many peaks proves the polycrystalline nature of CdSe particles and the broadening of the XRD peaks reveals that the particles are in the nanometer range.

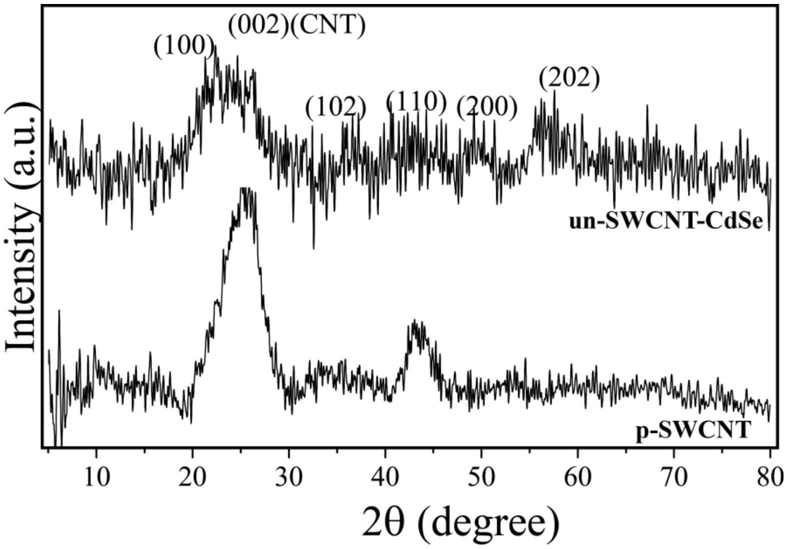

**Figure 3.11.** Powder X-ray diffractograms of the CdSe-unzipped SWCNT composite prepared *in situ*. Diffraction peaks of un-SWCNT-CdSe match with the primitive hexagonal phase of CdSe and thus confirms the formation of CdSe.

### 3.4.8. Contact angle measurement

A detailed contact angle study has been carried out in order to understand the surface properties of CNTs, i.e., surface energy changes due to adsorption, which is very useful in designing new functionalization strategy as well as processability. Acetonitrile ($CH_3CN$) and dichloromethane ($CH_2Cl_2$) have been chosen as model molecules for the study as these two molecules differ in physical (viz. dipole moment, surface tension, viscosity etc.), molecular and electronic properties. More significantly, these results can be used to compare with that of the CdSe QDs-CNT interactions, because QD is also thought of as a giant artificial atom (it shows atom like properties). Accordingly, wetting behavior of acetonitrile and dichloromethane on MWCNT surfaces has been depicted in fig.3.12 along with that of water for comparison. Surface roughness is a critical contributing factor in explaining the results of these experiments. Hence, macroscopic surface roughness has been tried to keep at its minimum by pressing each CNT paper (bucky paper) sample between two glass-plates in an identical fashion although it is difficult to control the microscopic roughness all the time. Fig.3.12 shows that water does not wet the surface of both pristine as well as ozonized MWCNT and the contact angle values are invariant with time, although oz-MWCNT shows super-hydrophobicity with contact angles ~158°-160°unlike 112°-114° for p-MWCNTs. This super-hydrophobicity has been attributed in part to the more compact nature of the oz-CNT paper with very small pore sizes and also due to the generation of hydrophobic ester groups which repel the water and causes it to bounce back from the oz-CNT surface.[22] High surface tension of water (72 mNm$^{-1}$ at 20°C) is another factor for this contact angle variation. Water is a highly polar liquid (μ = 6.2 Debye) and exists as a network of water molecules through H-bonding and not as discrete water molecules. Naturally, it has a very low value of dispersive component and that is why it cannot penetrate through the inter-tubular gaps of CNT bundles (both p-and oz-MWCNT) resulting in non-wetting situation. The ester group derived from the ozonolysis further restricts the penetration of water molecules and causes super-hydrophobicity.

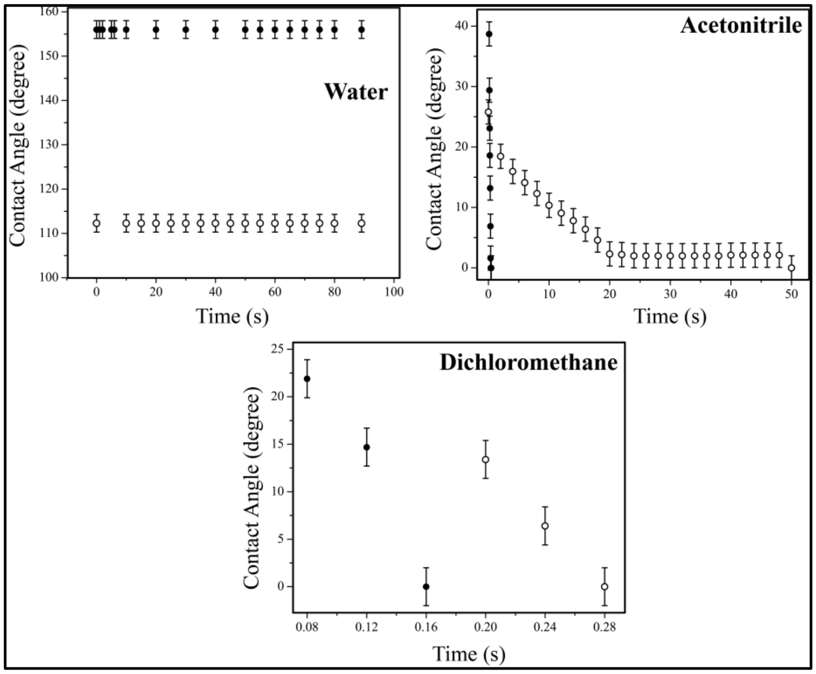

**Figure 3.12.** Wetting behavior of water ($H_2O$), acetonitrile ($CH_3CN$) and dichloromethane ($CH_2Cl_2$) on p-MWCNT (○) as well as oz-MWCNT (●)(Y-axis error

bar = ± 2°).

Acetonitrile ($CH_3CN$), on the other hand, completely wets the CNT surfaces. However, the wetting process shows interesting dynamics on p-and oz-MWCNT surfaces. As fig.3.12 suggests, acetonitrile shows a time dependent wetting pattern on p-MWCNT surface. More specifically, there is a gradual decrease in contact angle of acetonitrile from an initial value of ca.25.8°±2°over a period of ~50 sec in case of pristine-MWCNT (p-CNT) until it reaches 0°(Complete wetting). But contact angle of acetonitrile abruptly decreases from an initial value of 38.9°± 2° to 0° almost immediately (< 1 sec from the moment of droplet dispense of the drop) on oz-MWCNT (instantaneous wetting). Parallel but distinctly different behavior is observed also in case of wetting by dichloromethane ($CH_2Cl_2$), although the dynamics is pretty fast (< 400 ms) for both p-CNT and oz-CNT unlike the case for acetonitrile. Instantaneous contact angles in these cases are 13.4° ±2°and 21.8°±2°for p-CNT and oz-CNT respectively. Surface tension of acetonitrile (19.10 $mNm^{-1}$ at 20°C) is less than that of dichloromethane (26.50 $mNm^{-1}$ at 20°C). This means that acetonitrile should spread more rapidly than dichloromethane on CNT surface, i.e., lower contact angle than dichloromethane according to Young's equation.,

$$cos\theta_c = \frac{\gamma_{SV} - \gamma_{LS}}{\gamma_{VL}} \ldots\ldots(9)$$

Where, $\gamma_{SV}$, $\gamma_{LS}$ and $\gamma_{LV}$ are the solid-vapor, liquid-solid and liquid-vapor surface tensions respectively and $\theta_e$ is the apparent contact angle (experimental contact angle). Hence, the different wetting behavior cannot be explained solely by taking into account the surface tension and capillary effect. In practice, the solid-liquid interfacial energy ($\gamma_{LS}$) is governed by many forces like van der Waals, hydrogen-bonding and dipolar, and a resultant of all these competing interactions determines the spreading of a liquid over a surface. Actually, the interactions of the liquids with the CNTs seem to be responsible for those interesting wetting dynamics in case of dichloromethane and acetonitrile (though it is difficult to draw a molecular level picture by observing macroscopic property like apparent contact angle, a probable interpretation can be obtained by combining with other experimental data like spectroscopic evidence and so on). Dichloromethane is a relatively lesspolar liquid with a very low dipole moment of 1.60 D as compared to that of 3.92 D in case of acetonitrile. Theoretical calculations suggest the dispersive components of 17.0 and 15.3 and a polar component of 7.3 and 18.0 for dichloromethane and acetonitrile respectively. This means dispersive forces are more pronounced in dichloromethane. On the other hand, dipole-dipole interactions prevail in acetonitrile, as is revealed from X-ray diffraction and that results in a zigzag chain of acetonitrile molecules by an antiparallel dipole-dipole interaction.[23] This situation is, thus similar, although little different, to the long network of water molecules. Due to this more dispersive nature than acetonitrile, dichloromethane exists as discrete molecules which are much smaller in size than the dimension of the inter-tubular gaps and, therefore, can penetrate more easily into the inter-tubular gaps of the CNT papers and thereby results in instantaneous wetting both in case of p-CNT as well as oz-CNT unlike the situation for acetonitrile. Now, the change of the mode of wetting on two surfaces (p-CNT and oz-CNT) can be rationalized in terms of the opening of the tips of CNTs caused by the oxidation during ozonolysis in case of oz-CNT. Liquids can easily penetrate into the channels of oz-CNTs through the open tips and that probably is observed as instantaneous wetting. Somewhat higher momentary contact angle in case of oz-CNTs than p-CNTs can be understood by the momentary hindrance or hydrophobic interaction of the liquids (-$CH_3$ in case of $CH_3CN$ and -$CH_2$ for $CH_2Cl_2$) with the dangling –$COOCH_3$ groups which causes superhydrophobicity in case of water droplet.[22] The value of contact angle (instantaneous contact angle) is more for acetonitrile than for dichloromethane because –$CH_3$ group is less polarizable and hence more hydrophobic than –$CH_2$ group. This may also be due to the more compact interconnected nature of the bucky paper obtained after ozonolysis of MWCNT. The wetting behaviors have been summarized in table 3.1, which shows comparative values of contact angles for water, $CH_3CN$, $CH_2Cl_2$ (both initial and final) and thus reflects the different types of interactions.

**Table 3.1.** Variation in contact angle of water, acetonitrile and dichloromethane on Pristine and ozonized MWCNTs; surface tension values of all the solvents have been given for comparison. Before measurements, all samples are compacted under identical conditions to get smooth surface so as to minimize errors due to surface roughness.

| **Sample** | **Liquid** | **Surface Tension ($\gamma$) $mNm^{-1}$ at 20°C** | **Initial value of contact angle (°)** | **Final value of contact angle (°)** | **Time of measurement (s)** | **Time for complete spreading (s)** |
|---|---|---|---|---|---|---|
| **Pristine CNT** | Water | 72 | 114 | 114 | 90 | Does not spread |
| | Acetonitrile | 19.10 | 25.8 | 0 | 90 | 50 |
| | Dichloromethane | 26.50 | 13.4 | 0 | 90 | 0.28 |
| **Ozonized CNT** | Water | 72 | 158-160 | 158-160 | 90 | Does not spread |
| | Acetonitrile | 19.10 | 38.9 | 0 | 90 | Instantaneous |
| | Dichloromethane | 26.50 | 21.8 | 0 | 90 | 0.17 |

### 3.4.9. Micro Raman

Raman scattering is used extensively to probe the interaction of $CH_3CN$ and $CH_2Cl_2$ with CNT as well as to characterize SWCNT-SH-CdSe and GNR-CdSe hybrids. Accordingly, fig.3.13(A) shows a comparison of the Micro Raman spectra of p-CNT and oz-CNT samples. However, after the ozone treatment, G-band intensity drops down significantly ensuring the breaking of graphitic structure during ozonolysis. As a result, $I_D$ to $I_G$ ratio increases from 0.61 to 0.76 on ozonolysis indicating more defect formation (more $sp^3$ than $sp^2$ carbons as compared to that on p-MWCNT) on the side-walls of MWCNTs and thereby causes changes in its electronic structure. In comparison fig.3.13(B) represents the micro Raman spectra of p-MWCNT and oz-MWCNT after wetting experiment by acetonitrile and dichloromethane. Raman spectra show a D and G band shift of ~13 $cm^{-1}$ and 4 $cm^{-1}$ on wetting by acetonitrile and dichloromethane respectively in case of p-CNTs. Interestingly, there is no such shift in case of oz-CNTs. Moreover, acetonitrile causes upshift while dichloromethane causes downshift of the corresponding bands of p-CNTs. Indeed, D (defective) and G (graphitic) are two tangential modes of phonon vibrations in CNTs and these two modes are characteristics of $sp^3$ and $sp^2$ type of C-C bonding respectively. A shift in the positions of these bands thus, really indicates vibrational energy transfer between CNTs and the liquid molecules.

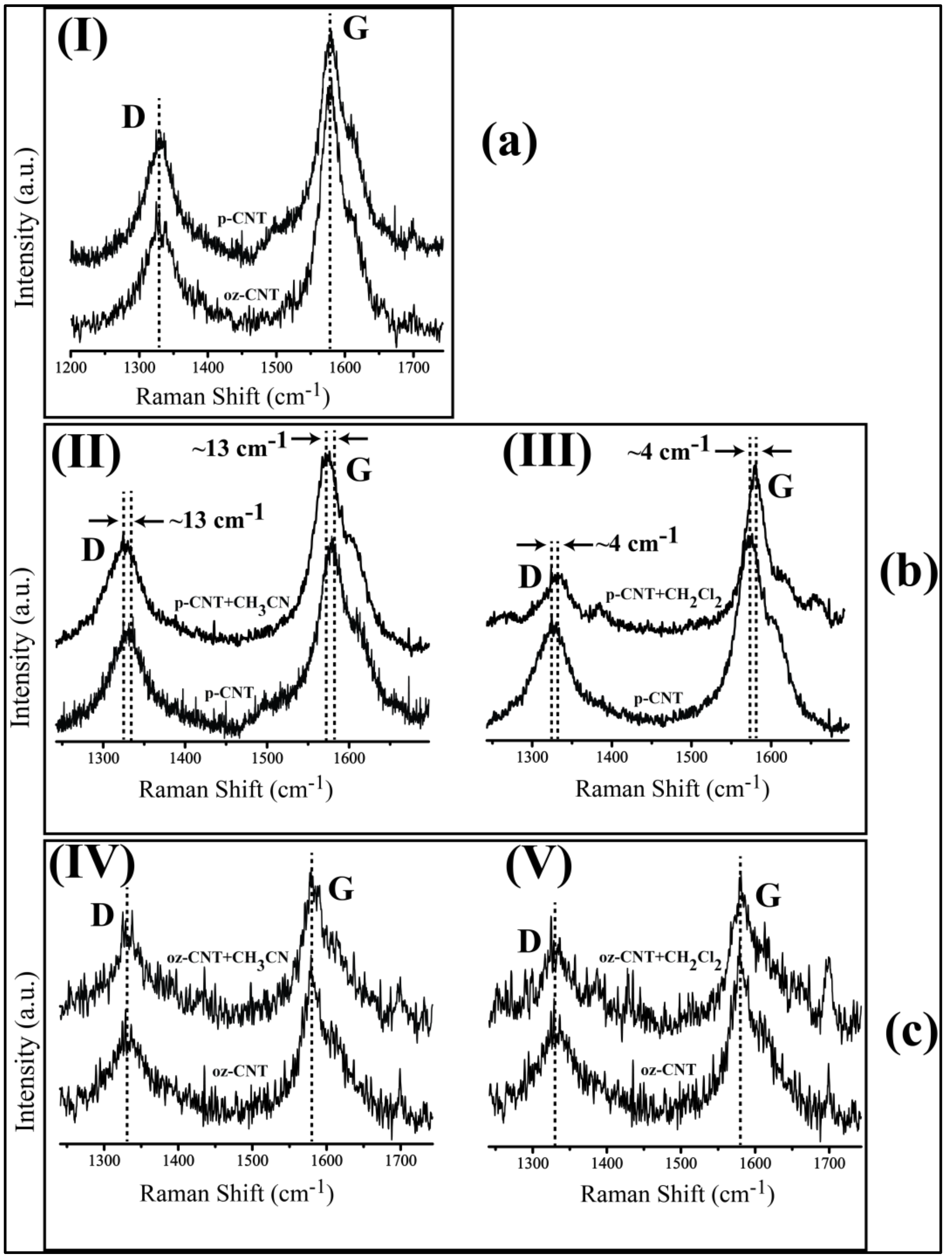

**Figure 3.13.** (a) Superimposed Micro Raman Spectra of pristine (p-MWCNT) and ozonized (oz-MWCNT) carbon nanotubes showing the rupture of the C=C backbone during ozonolysis to form $–COOCH_3$ groups; (b) and (c) Micro Raman spectra during the wetting experiments by acetonitrile and dichloromethane respectively; Acetonitrile on (I)

p-CNT (III) oz-CNT and dichloromethane on (II) p-CNT and (IV) oz-CNT measured using 632.8 nm LASER.

Many types of experimental evidences suggest a shift in Raman band positions of CNTs on charge transfer to or from the CNTs (as a result of doping).[24] In case of p-type doping, electrons are taken away from the CNT and thereby causing an upshift of the band while, similar n-type doping pushes charges on CNT causing a concomitant downshift in both D and G band. However, CNTs are a huge reservoir of mobile π-electrons and acetonitrile ($CH_3CN$) having –C≡N π bond can interact with this π-cloud through π- π interaction. The non-bonded electrons on N-atom can also be donated to the CNT and this causes n-type doping of CNTs and that is manifested in the form of red-shift in D and G frequencies from their original position in CNT on wetting by acetonitrile. This is confirmed from the value of the shift ($13\ cm^{-1} = 2$ meV) which is equivalent to the interaction energy for the weakly adsorbing acetonitrile molecules. It has been shown that binding energies for benzonitrile molecule to SWCNT and graphene surface vary from 10meV to 60meV depending upon the orientation of the benzonitrile molecule with respect to the SWCNT or grapheme surface (i.e., π-π or π-C≡N interaction).[25] Acetonitrile ($CH_3CN$) having no benzene ring for strong π-π interaction like benzonitrile (PhCN), can only interact via -C≡N π-bond or nitrogen lone pair andthat explains the less binding energy for $CH_3CN$ unlike benzonitrile. It, thus appears that acetonitrile molecules form a thin film on CNT after spreading and transfer vibrational energy electronically to the CNTs is likely affecting a change in vibrational frequency of the CNTs. Dichloromethane ($CH_2Cl_2$) molecule, however, does not have any charge transfer component to interact like $CH_3CN$ and vibrational bands (Raman bands), therefore, are not affected significantly. Interestingly, there is no change in position either of D or G band of oz-MWCNT on wetting by both of the liquids (Fig.3.13(B)). This is somewhat contradictory to what reported by Nelson *et al.*[20] where molecules inside the CNTs are more efficient in transferring vibrational energy with the CNT than the molecules around it, because afterozonolysis the shorter and open-ended CNTs can allow the solvent molecules ($CH_3CN$ and $CH_2Cl_2$) to go in. Moreover, covalent functionalization disrupts the π-clouds and the possibility of π-π interaction reduces and so there is little or almost no change in the D or G band positions in case of oz-MWCNT even with $CH_3CN$.

In order to confirm the unzipping of SWCNT and subsequent deposition of CdSe on them under electrochemical conditions, we have carried out micro Raman study at various stages of the unzipping process concomitant to the CdSe anchoring. Accordingly, fig.3.14 describes the micro Raman spectra for (i) pristine SWCNT before unzipping, (ii) SWCNT on subjecting to 0.8 V, (iii) GNRs after CdSe decoration at -0.7 V. The intensity ratio of the two phonon modes, namely D-band and G-band, is found to increase from 0.08 to 0.86 after the SWCNTs are subjected to 0.8 V for 10 h. This indicates the increase of defects after electrochemical oxidation. More striking feature of the Raman spectra is the disappearance of the so called RBM band of pristine SWCNT (258.1 $cm^{-1}$ corresponding to metallic nanotubes) on 6 h oxidation. This is in agreement with the observed report that metallic CNTs are more susceptible towards electronic attack than their semiconductor analogues.[26] Other two RBM phonon modes (due to semiconducting nanotubes) also decrease in intensity–strongly suggesting the opening of CNTs (unzipping) with the concomitant formation of graphene nanoribbons. The application of external anodic potential modulates the Fermi level of CNTs and allows oxidative unzipping. In fact, anodic bias gives rise to defect sites which thereby disrupts the symmetry of electron distribution on CNTs rendering the surrounding carbon atoms more reactive. This activation helps to propagate the defects along the tubular axis of CNT and eventually opens up the nanotubes to form graphene. However, the Raman spectrum is different after *in situ* CdSe decoration, specially in the low frequency region (Fig.3.14(iii)). The spectrum clearly shows the presence of CdSe NPs. On the low frequency region (210-300 $cm^{-1}$ inset of fig.3.14(ii)), peak corresponding to LO phonon of CdSe NPs (205 $cm^{-1}$) has been observed. Appearance of LO phonon at 205 $cm^{-1}$ as compared to that in case of bulk CdSe (210 $cm^{-1}$) suggests the formation of nanosized clusters of CdSe on GNRs.[27] Moreover, a broad two photon 2LO band for CdSe NPs is also observed at 408 $cm^{-1}$. The peak at 238 $cm^{-1}$ can be assigned to $\nu_{10}$ ($\varepsilon_3$) mode of phonon vibration of amorphous selenium conforming the presence of excess selenium during electrodeposition.[28]

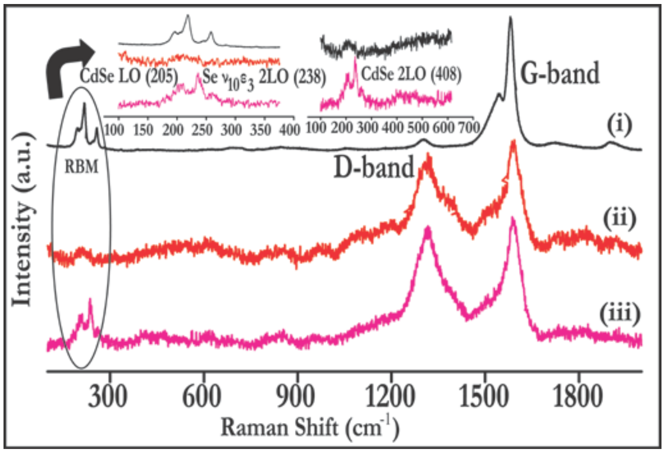

**Figure 3.14. Superimposed** Micro Raman spectra of (i) pristine SWCNT (before unzipping), (ii) SWCNT after unzipping at 0.8 V for 10 h and (iii) unzipped SWCNT after CdSe decoration at -0.7 V; All the spectra are recorded with 632.8 nm laser with 20 mW power.

On the other hand, Raman spectra of SWCNT-SH and SWCNT-SH-CdSe show (fig. 3.15) characteristic radial breathing modes of vibrations (RBM bands) in the region 100-300 $cm^{-1}$for the presence of SWCNTs other than the normal D and G bands. The RBM bands remain intact even upon functionalization and CdSe QD attachment suggesting its stability as even partial unzipping can alter this.[26] This proves that the electronic structure and morphology of SWCNTs is not affected by the functionalization or CdSe decoration. The 2D band which is the overtone of D-band (~at 2600 $cm^{-1}$) is also unaffected by functionalization. It also indirectly suggests that SWCNTs undergo longitudinal unzipping upon applying electrochemical potential for 10 h.

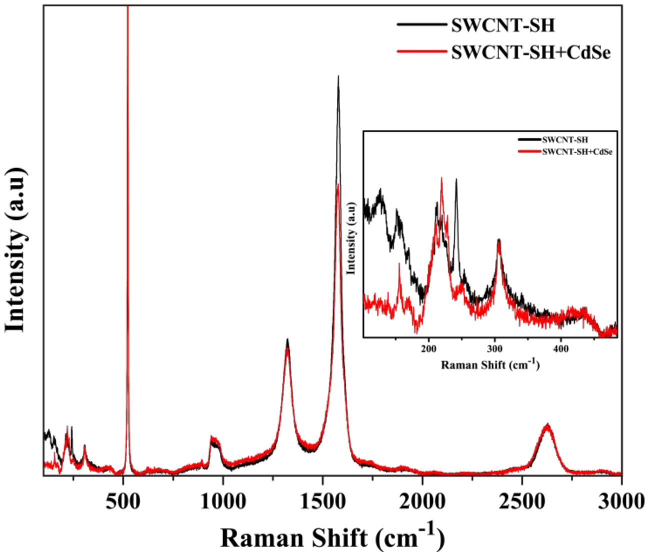

**Figure 3.15.** Micro Raman spectra of SWCNT-SH and SWCNT-SH-CdSe showing the RBM bands and 2D band along with D and G-bands; inset shows the enlarged view of RBM bands.

### 3.4.10. Transmission Electron Microscopy

Fig. 3.16 represents the TEM images of CdSe QDs attached to SWCNT-SH. A uniform decoration of CdSe QDs (fig. 3.16(c) and (d)) around the thiolated SWCNT is observed. In comparison, CdSe QDs do not get bonded easily to pristine SWCNT (p-SWCNT) and so poor distribution of QDs is observed around p-SWCNT (fig. 3.16(a) and (b)). This shows the effectiveness of thiol functionalization for CdSe QD attachment.

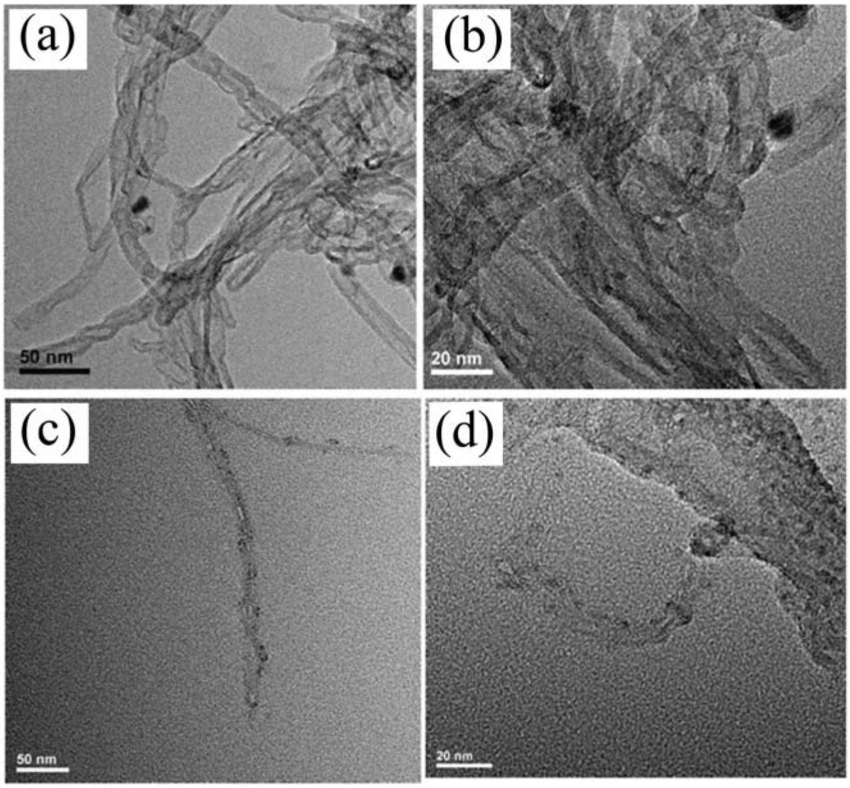

**Figure 3.16**. Representative high resolution TEM images of CdSe QDs-SWCNT hybrids (a) to (b) p-SWCNT-CdSe and (c) to (d) SWCNT-SH-CdSe; QDs are uniformly arranged around SWCNT-SH as compared to p-SWCNT.

Similarly, fig.3.17 represents the TEM images of GNRs which are generated from the unzipping of SWCNTs and the GNR-CdSe hybrids where CdSe QDs are *in situ* decorated on GNRs. The average diameter of the SWCNTs varies from 1.1 to 2 nm (fig. 3.17(a)). However, after unzipping process, the diameter increases up to 5-6 nm (as theoretically expected for opening the CNT along its length) indicating the transformation of SWCNTs in to graphene by longitudinal unzipping in presence of the electric field although it is difficult to get a single large sheet of graphene from the unzipping of SWCNTs since only at selected positions such individual sheets are observed on the TEM grid. On the other hand, fully or partially unzipped tubes are entangled together and appear as 40-50 nm wide bundled sheets in most places, linked also to sample preparation procedures. CdSe QDs obtained after 5 min is 5-6 nm in size (fig.3.17(c)). Selected area electron diffraction is shown in the inset of Fig.3.17(d) and indexing of the spots gives d-spacings which are in fair agreement with the d-spacings of primitive hexagonal CdSe, thereby further confirming the formation of hexagonal CdSe particles.

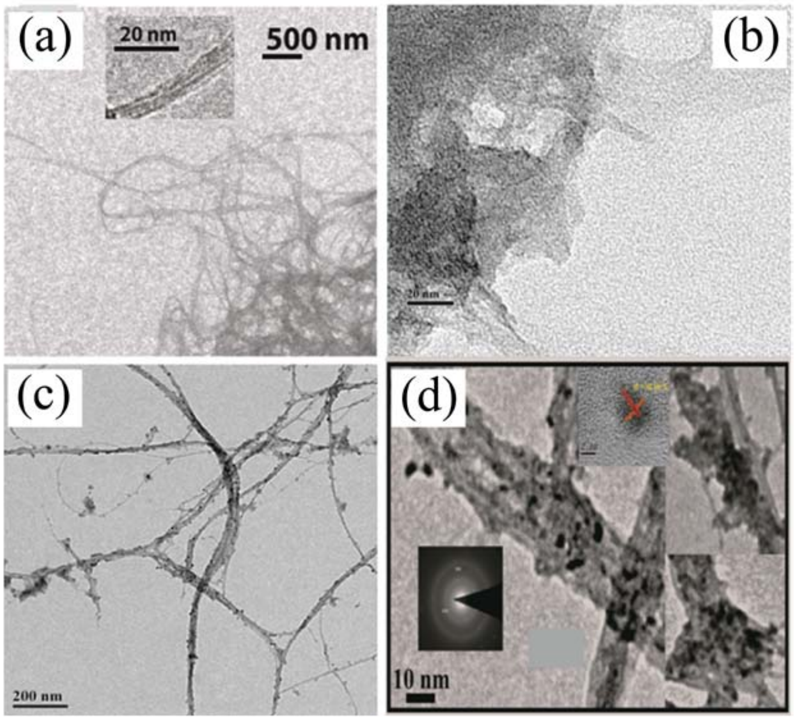

**Figure 3.17.** Representative TEM mages of (a) p-SWCNT, (b) GNRs (unzipped CNTs), (c) CdSe QDs of 5-6 nm decorated *in situ* and (d) enlarged view of 3.14 (c).

However, small particles further grow, in presence of excess precursor, with the time of deposition and eventually form large clusters, typically after 1 h. These particles are 15-20 nm after 15 min and become 40-50 nm clusters after 1 h to eventually cover the GNRs (Fig. 3.18 (a) and (b)).

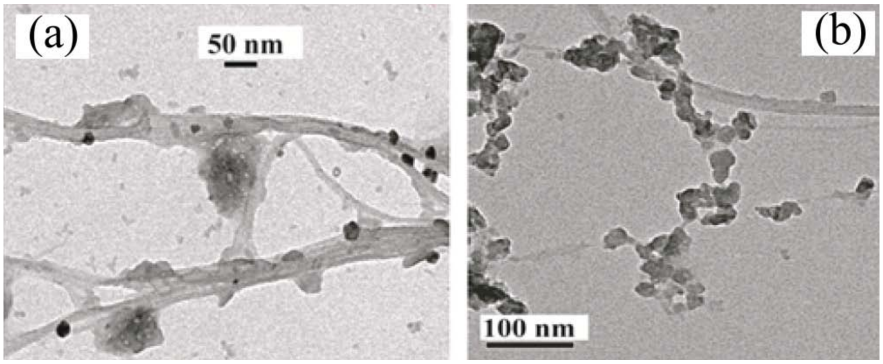

**Figure 3.18.** Representative TEM mages of GNRs during CdSe deposition, (a) deposition time 15 min (b) deposition time 1 h; CdSe particle size increases with time.

Thus TEM analysis suggests that CdSe QDs can be organized on GNR without any bifunctional linker molecule. The residual functionality in GNR most probably helps to bind the CdSe formed during electrodeposition.

### 3.4.11. UV-Vis Absorption and Photoluminescence (PL)

UV-Vis absorption and photoluminescence studies have been carried out to explore the properties of the hybrids made up of CdSe and carbon nanostructures, mainly SWCNT and un-SWCNTs (GNRs) derived from SWCNT. CdSe QDs alone show a peak corresponding to $1S_h$-$1S_e$ transition as has been discussed in the preceding chapters. On the other hand, SWCNT shows multiple small peaks (undulations) in the absorbance spectrum. These undulations are called Van Hove’s singularities which originate due to transitions within the discrete molecular type states in the band structure of SWCNTs. For example, fig. 3.19(a) shows the absorbance plots of p-SWCNTs and un-SWCNTs (GNRs) after *in situ* CdSe decoration. p-SWCNT sample shows features of Van Hove’s singularities which vanish after unzipping and a new peak emerges out at 576 nm which is the characteristic peak for CdSe QDs having size of 4-5 nm. Disappearance of the features of SWCNT suggests the change in electronic properties due to the application of electrical potential (unzipping). On the other hand, PL emission spectrum of the hybrid of

CdSe-GNR (fig. 3.19(b)) upon excitation with 480 nm wavelength does not give any peak, whereas oleic acid capped CdSe QDs having 4-5 nm diameter, show a sharp PL emission under similar conditions. In presence of GNR, therefore, quenching of CdSe PL takes place and this is due to the proper band alignment between CdSe QDs and GNRs. This clearly indicates that GNR acts as an electron acceptor in this case.

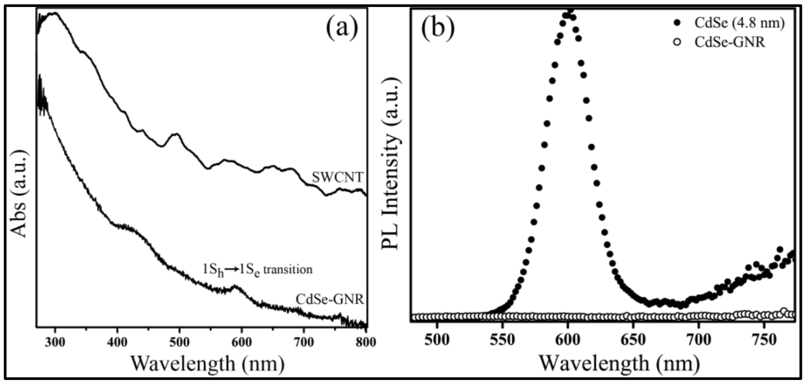

**Figure 3.19.** (a) Absorption and (b) Solid state Photoluminescence spectra of the CdSe QDs-GNR hybrids. Excitation wavelength is 480 nm for PL.

Similarly, when SWCNT-SH is gradually added to a solution of oleic acid capped CdSe QDs (4 nm size), the PL emission intensity of the latter is gradually reduced to zero (fig. 3.20(a)). This is because CdSe QDs get bonded to –SH group of SWCNT-SH via ligand exchange and thus establishes a direct link between SWCNT and QDs levels. So, charge transfer can easily occur from excited CdSe QD to SWCNT resulting in observed PL quenching. On the other hand, p-SWCNT is not much effective in quenching the PL of CdSe QD because of immiscibility of SWCNT suspension (poorly dispersed DMF suspension) and toluene solution of CdSe QDs (fig. 3.20(b)). This is more because no direct contact is possible in case of p-SWCNT-CdSe QDs unlike the SWCNT-SH case. Insulating oleic acid is responsible for hindrance to this electron transfer.

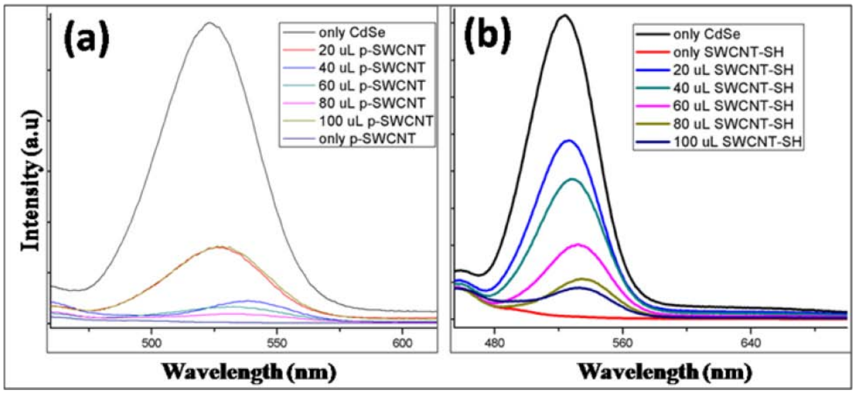

**Figure 3.20.** PL quenching experiment of CdSe QDs (4 nm) using (a) p-SWCNT and (b) SWCNT-SH; SWCNT-SH is found to be a better quencher because of the presence of –SH group which binds to CdSe QDs.

Thus it is clear from the combined results of a UV-Vis and PL study that free CdSe QDs and those bound to some carbon nanostructures behave differently. Electronic property of the QD remains unaffected as is evident from UV-Vis absorbance, but its emission property is severely affected due to charge transfer. Moreover, bound CdSe QDs are effective in transferring charge from excited QDs to the carbon nanostructures rather than the free QDs in solution in contact with carbon nanostructures. In fact, similar phenomenon has already been discussed in the preceding section (3.4.8) where only acetonitrile has been found to be strongly adsorbed on CNT surface, due to its capability of charge transfer to CNT, unlike that of dichloromethane because of its weakadsorption on CNT. The only difference between the two is that CdSe QDs can transfer charge to CNTs when activated by external photon (photo-induced charge transfer); whereas acetonitrile can do the same without activation by light. The combination of CdSe QDs and carbon nanostructure, therefore, can give rise to important hybrids for the application of various optoelectronic devices.

### 3.4.12. Photoconductivity study

In order to prove the efficiency of the hybrid materials discussed above, photoconductivity measurement has been performed. Accordingly, fig.3.21reveals the representative I-V curve for CdSe-GNR hybrid in the presence and absence of light (AM1.5 solar simulated light). The plot shows Ohmic behavior at very low voltage range (±0.2 V), although subsequently this changes to Schottky type at voltages more than ±0.2

V. Photocurrent enhancement is found to be almost double than that under the dark current. It can thus be concluded that these hybrids would be promising candidates for various optoelectronic applications like solar cells and photodetectors.

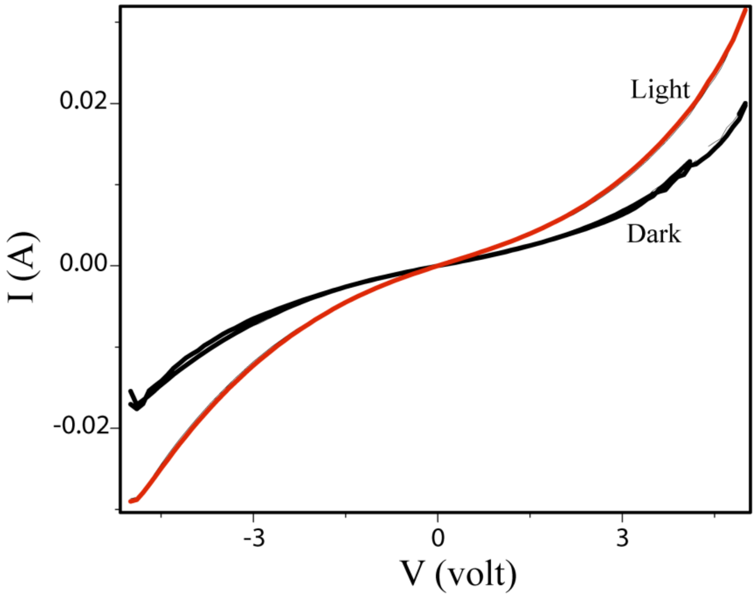

**Figure 3.21.** I-V characteristics of CdSe-GNR hybrid in dark and in presence of AM 1.5 solar simulated light. The device area is 1 $cm^2$.

Thus a combined analysis of all results unambiguously indicatesthat CdSe QDs behave differently in presence of carbon nanostructures, especially CNT and GNRs and these reasons for this have been explored. More specifically, excited state deactivation of QD occurs in contact with CNT and GNRs and hence those carbon nanostructures act as electron acceptors as well as transparent conductors.

## 3.5. Conclusion

Synthesis, characterization and probable applications of the hybrids of CdSe QDs and carbon nanostructures are discussed in this chapter with special emphasis on CdSe-SWCNT and CdSe-GNR structures. QDs, regarded as giant artificial atoms, are compared with small probe molecules like acetonitrile in having ability to transfer charge to CNTs. Charge transfer induced competitive wetting behavior of CNT with acetonitrile and dichloromethane has also been discussed and compared with that of water. Diazonium functionalization has been shown to be a very effective method of functionalizing CNT surface for anchoring CdSe QDs. On the other hand, SWCNTs have been unzipped to produce graphene nanoribbons and CdSe QDs are generated *in situ* to make CdSe-GNR hybrids. All these hybrids show efficient PL quenching and perhaps a good photoresponse indicating their ability to serve as next generation optoelectronic materials.

### 3.6. References

1. (a) Reimann, S. M.; Manninen, M. *Rev. mod. phys.* **2002**, *74*, 1283. (b) Brus, L. *J. Phys. Chem.* **1986**, *90*, 2555.
2. Nozik, A. J. *Chem. Phys. Lett.* **2008**, *457(1)*, 3-11.
3. (a) Konstantatos, G.; Howard, I.; Fischer, A.; Hoogland, S.; Clifford, J.; Klem, E.; Levina, L.; Sargent, E. H. *Nature* **2006** *442(7099)*, 180. (b) Oertel, D. C.; Bawendi, M. G.; Arango, A. C.; Bulović, V. *Appl. Phys. Lett.* **2005,** *87(21)*, 213505. (c) Kim, J. Y.; Voznyy, O.; Zhitomirsky, D.; Sargent, E. H. *Adv. Mater.* **2013**, *25*, 4986. (d) Tang, A. W.; Teng, F.; Hou, Y. B.; Xiong, S.; Feng, B.; Qian, L.; Wang, Y. S. *J. Nanosci. Nanotechno.* **2008**, *8*, 1330. (e) Zhao, L. J.; Hu, L. F. *Pure Appl. Chem.* **2012**, *84*, 2549.
4. (a) Lu, L. L.; Hou, W. J.; Sun, J.; Wang, J. J.; Qin, C. X.; Dai, L. X. *J. Mat. Sci.* **2014**, *49*, 3322. (b) Wei, H.; Li, Z. Q.; Xiong, D. B.; Tan, Z. Q.; Fan, G. L.; Qin, Z.; Zhang, D. *Scripta Mater.***2014**, *75*, 30. (c) Lee, C.; Wei, X.; Kysar, J. W.; Hone, J. *Science* **2008**, *321*, 385. (d) Han, J.; Ryu, S.; Sohn, D.; Im, S. *Carbon* **2014**, *68*, 250. (e) Shokrieh, M. M.; Esmkhani, M.; Vahedi, F.; Shahverdi, H. R. *Ira. Pol. J.* **2013**, *22*, 721. (f) Zhu, K. K.; Sun, J. M.; Zhang, H.; Liu, J.; Wang, Y. *J. Nat. Gas Chem.* **2012**, *21*, 215.
5. (a) Schlogl, R.: Carbon in Catalysis. In *Advances in Catalysis, Vol 56*; Gates, B. C., Jentoft, F. C., Eds.; Elsevier Academic Press Inc: San Diego, 2013; Vol. 56; pp 103. (b) Choi, H. J.; Jung, S. M.; Seo, J. M.; Chang, D. W.; Dai, L. M.; Baek, J. B. *Nano Energy* **2012**, *1*, 534. (c) Wan, X. J.; Huang, Y.; Chen, Y. S. *Acc. Chem. Res.* **2012**, *45*, 598. (d) Singh, V.; Joung, D.; Zhai, L.; Das, S.; Khondaker, S. I.; Seal, S. *Prog. Mater Sci.* **2011**, *56*, 1178. (e) Falcao, E. H. L.; Wudl, F. *J. Chem. Technol. Biotechnol.* **2007**, *82*, 524.
6. (a) Wang, Q. H.; Bellisario, D. O.; Drahushuk, L. W.; Jain, R. M.; Kruss, S.; Landry, M. P.; Mahajan, S. G.; Shimizu, S. F. E.; Ulissi, Z. W.; Strano, M. S. *Chem. Mater.*

**2014**, *26*, 172. (b) Wang, Q.; Arash, B. *Comput. Mat. Science* **2014**, *82*, 350. (c) Berman, D.; Erdemir, A.; Sumant, A. V. *Mater. Today* **2014**, *17*, 31. (d) Tovee, P. D.; Pumarol, M. E.; Rosamond, M. C.; Jones, R.; Petty, M. C.; Zeze, D. A.; Kolosov, O. V. *Phys. Chem. Chem. Phys.* **2014**, *16*, 1174. (e) Wang, F.; Zhao, J. B.; Gong, J. M.; Wen, L. L.; Zhou, L.; Li, D. F. *Chem. Eur. J.* **2012**, *18*, 11804.

7. Kakade, B. A.; Pillai, V. K. *Appl. Surf. Sci.* **2008**, *254*, 4936.
8. (a) Shinde, D. B.; Debgupta, J.; Kushwaha, A.; Aslam, M.; Pillai, V. K.: *J. Am. Chem. Soc.* **2011**, *133*, 4168. (b) Debgupta, J.; Shinde, D. B.; Pillai, V. K. *Chem. Commun.* **2012**, *48*, 3088.
9. Kakade, B. A; Allouche, H.; Mahima, S.; Sathe, B. R.; Pillai, V. K. *Carbon* **2008**, *46*, 567.
10. Sbai, K.; Rahmani, A.; Chadli, H.; Bantignies, J. L.; Hermet, P.; Sauvajol, J. L. *J. Phys. Chem. B,* **2006**, *110*, 12388.
11. (a) Shirley, D. A. *Phys. Rev. B* **1972**, *5*, 4709 (b) Oberlin, A.; Endo M.; Koyama, T. *J. Crystal. Growth* **1976**, *32*, 335.
12. (a) Mawhinney, D. B.; Naumenko, V.; Kuznetsova, A.; Yates Jr. J. T.; Liuand, J.; Smalley, R. E. *J. Am. Chem. Soc.* **2000**, *122*, 2383. (b) Skakalova, S. V.; Kaiser, A. B.; Weglikowska, D. U.; Hrncarikova, K.; Roth, S. *J. Phys. Chem. B* **2005,** *109*, 7174.
13. (a) Natarajan, C.; Sharon, M.; Levyclement, C.; Neumannspallart, M. *Thin Solid Films* **1994**, *237*, 118. (b) Majidi, H.; Baxter, J. B. *Electrochim. Acta* **2011**, *56*, 2703.
14. Kressin, A. M.; Doan, V. V.; Klein, J. D.; Sailor, M. J. *Chem. Mater.* **1991**, *3*, 1015.
15. Schaff, Jason E.; Jeffrey T. Roberts. *Surf. sci.* **1999**, 426.3, 384.
16. Kannan, R.; Bipinlal, U.; Kurungot, S.; Pillai, V. K.; *Phys. Chem. Chem. Phys.,* **2011**, *13*, 10312.
17. Shinde, D. B.; Debgupta, J.; Kushwaha, A.; Aslam, M.; Pillai, V. K. *J. Am. Chem. Soc.* **2011**, *133*, 4168.
18. (a) Rashwan, S. M.; Abd El-Wahab, S. M.; Mohamed, M. M. *J. Mat. Sci.Mat. Electron.* **2007**, *18*, 575. (b) Bouroushian, Mirtat. *Electrochemistry of metal chalcogenides*. Springer, **2010**. (c) Chandramohan, R.; Sanjeeviraja, C.; Mahalingam, T. *Physica Status Solidi a-Appl. Res.* **1997**, *163*, R11-R12.

19. Paunovic M.; Mordechay, S.; "Fundamentals of electrochemical deposition." *John Wiley & Sons, Hoboken* **2006**, 144.
20. Scharifker, B.; Hills, G. *Electrochim. Acta* **1983**, *28*, 879.
21. Debgupta, J.; Shinde, D. B.; Pillai, V. K. *Chem. Commun.* **2012**, *48*, 3088.
22. Kakade, B. A.; Mehta, R.; Durge, A.; Kulkarni, S.; Pillai, V. K. *Nano Lett.* **2008**, *8*, 2693.
23. Takamuku, T.; Tabata, M.; Yamaguchi, A.; Nishimoto, J.; Kumamoto, M.; Wakita, H.; Yamaguchi, T. *J. Phys. Chem. B* **1998**. *102(44)*, 8880.
24. (a) Chandra, B.; Afzali, A.; Khare, N.; El-Ashry, M. M.; Tulevski, G. S. *Chem. Mater.* **2010**, *22*, 5179. (b) Aguiar, A.; Fagan, S.; Silva, L. *J. Phys. Chem. C* **2010**, *114*, 10790.
25. Nelson, R. T.; Chaban, V. V.; Kalugin, O. N.; Prezhdo, O. V. *J. Phy. Chem. B* **2010**, **114**, 4609.
26. (a) Dyke, C. A.; Tour, J. M. *J. Phys. Chem. A* **2004** *108(51)*, 11151. (b) John, R.; Shinde, D. B.; Liu, L.; Ding, F.; Xu, Z.; Vijayan, C.; Pillai, V. K.; Pradeep, T. *ACS Nano* **2013**, *8*, 234.
27. Trallero-Giner, C.; Debernardi, A.; Cardona, M.; Menendez-Proupin, E.; Ekimov, A. *Phys. Rev. B* **1998**, *57*, 4664.
28. (a) Ohta, N.; Scheuermann, W.; Nakamoto, K. *Solid State Commun.***1978**, *27*, 1325. (b) Lucovsky, G.; Mooradian, A.; Taylor, W.; Wright, G.; Keezer, R. *Solid State Commun.* **1967**, *5*, 113. Shaikh, P. A.; Thakare, V. P.; Late, D. J.; Ogale, S. *Nanoscale* **2014**, *6*, 3550.

# CHAPTER 4

# Anchoring of CdSe QDs on Graphene through molecular linkers

This chapter deals with the effective organization of small CdSe quantum dots on graphene sheets achieved by a simple solution exchange with thiol terminated graphene prepared by diazonium salt chemistry. Excitation dynamics study has been carried out on CdSe QD-graphene(-SH) hybrids in order to design animproved solar light harvesting system and other optoelectronic devices. This chapter also shows the improved rate of electron transfer from excited state CdSe QDs to the Fermi level of grapheme which has been prefunctionalized with 4-aminothiophenol (4-ATP) to get thiol modified graphene. Electron transfer rate (measured as non-radiative decay rate) on such thiol-modified graphene has been found to be as high as 12.8x10$^{8}$ s$^{-1}$. The rate has also been shown to depend on the relative size as well as quantum yield of the CdSe QDs. Micro Raman study carried out on these hybrids also complements the electron transfer features. Moreover, the prototype photovoltaic cells made out of these hybrids show good photoresponse in presence of 1.5 AM solar simulated light and this suggests them as promising materials for various light conversion devices. This generic methodology of a QD attachment to graphene surface has remarkable implications in designing hybrid heterostructures.

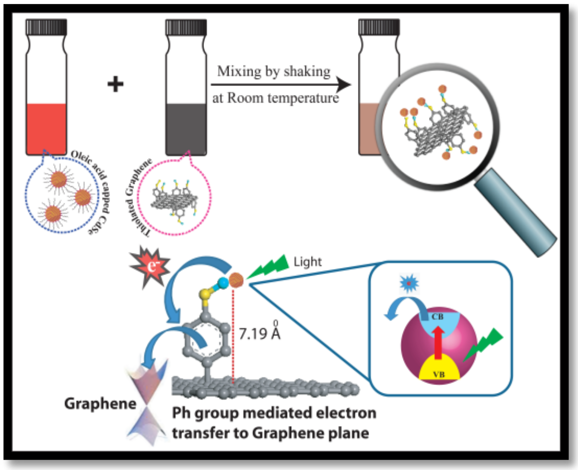

---

*Part of the works discussed in this chapter has been published in: (a) *Nanoscale* **2013**, *5*, 3615-3619. (b) *RSC Adv*. **2014**, *4*, 13788-13795.

## 4.1. Introduction

Graphene, the celebrated 2-D allotrope of carbon is regarded widely as the mother of all types of carbon allotropes.[1] It essentially consists of $sp^2$ carbon arranged in a 2-D honeycomb lattice exhibiting several unique properties. For example, it is considered as a semimetal which is well known for its exceptional properties like quantum Hall effect at room temperature, ballistic transport behavior due to the availability of particles like Dirac fermions[2] and excellent tensile strength (1 TPa)[3]. Ideal, single layer graphene possesses extremely high mobility of charge carriers (electrons or holes) but absorbs only ~2% of the visible light so that it is considered as a transparent semimetal.[1], [4]These properties make graphene a promising candidate for use in ultrafast photodetector,[5] chemical sensing,[6]thermal management,[7]high-speed electronics,[8] and solar cells.[9], [10]One of the key factors which determines the use of graphene in electronics or solar cells, is the efficient manipulation of its electronic properties with accurate control to obviate its zero bandgap. For example, graphene surface has been successfully tuned to make electron or hole rich by applying a suitable gate voltage.[11] The presence of metal ions or adsorbed molecules has also been found to be very effective in causing a shift of graphene Fermi level with precise control.[6], [12]

On the other hand, zero-dimensional semiconductors like CdSe quantum dots (QDs) are becoming increasingly important because of their broad and size tunable absorption[13] and multi-exciton generation[14] facilitating higher theoretical efficiencies than that prescribed by the Schockley Quiesser limit.[15] However, challenge lies in the efficient use of CdSe quantum dots (QDs) in optoelectronic applications because the film, composed of neat CdSe QDs, is known to have poor carrier transport properties. In CdSe QD films, photoexcitation can also lead to slow photocorrosion. Moreover, the hot electrons, generated during the process of photoexcitation, can be absorbed by surface defects on QDs leading to poor performance of the optoelectronic devices made out of QDs. Hence, the key to successful utilization of the optical properties of CdSe QDs requires them to be in intimate contact with a conducting medium which can give rise to proper band alignment with the CdSe QDs.[16]Graphene, a transparent, 2D semimetal, is, therefore, an obvious choice for this because its Fermi level (ranging from -4.42 to -4.5

eV) lies well below the conduction band of CdSe QDs (-3.5 to -4 eV), facilitating effective electron injection into the graphene Fermi level. Graphene-CdSe QD hybrids are, therefore, promising candidates for sensitized solar cells where graphene acts as highly conducting, flexible and transparent medium.[17]

Although, there are few reports on the attachment of CdSe QDs on graphene surface,[18] the real challenge lies in the controlled attachment of QDs onto the graphene surface with pre-defined areal density. This is a result of the fact that the surface of graphene, obtained from graphene oxide by complete reduction, contains very less number of functional groups to anchor the QDs. Polymer wrapping of graphene sheets, hydrothermal method and *in situ* generation of QDs on graphene[19] are few limited methods available so far for the decoration of QDs on 2D graphene sheets. One major limitation of such methods is that monodispersed QDs can hardly be achieved. Moreover, in some cases, the interaction between QDs and graphene is purely by physical adsorption causing extensive reorganization. These limitations can be avoided by a rational and controlled functionalization of graphene sheets before attaching CdSe quantum dots. Among many functionalization strategies, diazonium-salt functionalization of graphene[20] has been proved to be one of the most easiest and effective method of graphene surface modification which has the potential to chemically tailor graphene surface with desired functionality (by using suitable precursors) to allow further modification. This also provides sufficient solubility of graphene in various solvents to ease the fabrication of hybrid materials. Furthermore, this strategy has an additional benefit that areal density can be enhanced by a layer-by-layer approach to create multidimensional hybrid structures of CdSe and graphene with accurate dimensional control.[21]

In the previous chapter (chapter 3), we have discussed the synthesis, characterization and applications of the hybrids of CdSe QDs to carbon nanotubes (CNTs) and graphene nanoribbons. A unique diazonium functionalization strategy has also been developed to make thiol (-SH) functionalized CNTs in order to attach CdSe QDs to CNTs. In the present chapter we have adopted the same methodology (fig. 4.1) to selectively make thiol (-SH) terminated graphene sheets by reacting graphene with diazonium salt of 4-aminothiophenol (4-ATP) followed by building-up of CdSe QDs. Since –SH group has strong affinity towards CdSe QDs (both –SH and CdSe are soft), oleic acid capped CdSe

QDs with pre-defined sizes have been effectively exchanged with these thiolated graphene by mixing in solution, to orchestrate CdSe-Graphene hybrids. These hybrids are characterized using FTIR, UV-VIS, Photoluminescence (PL), TEM and cyclic voltammetry.

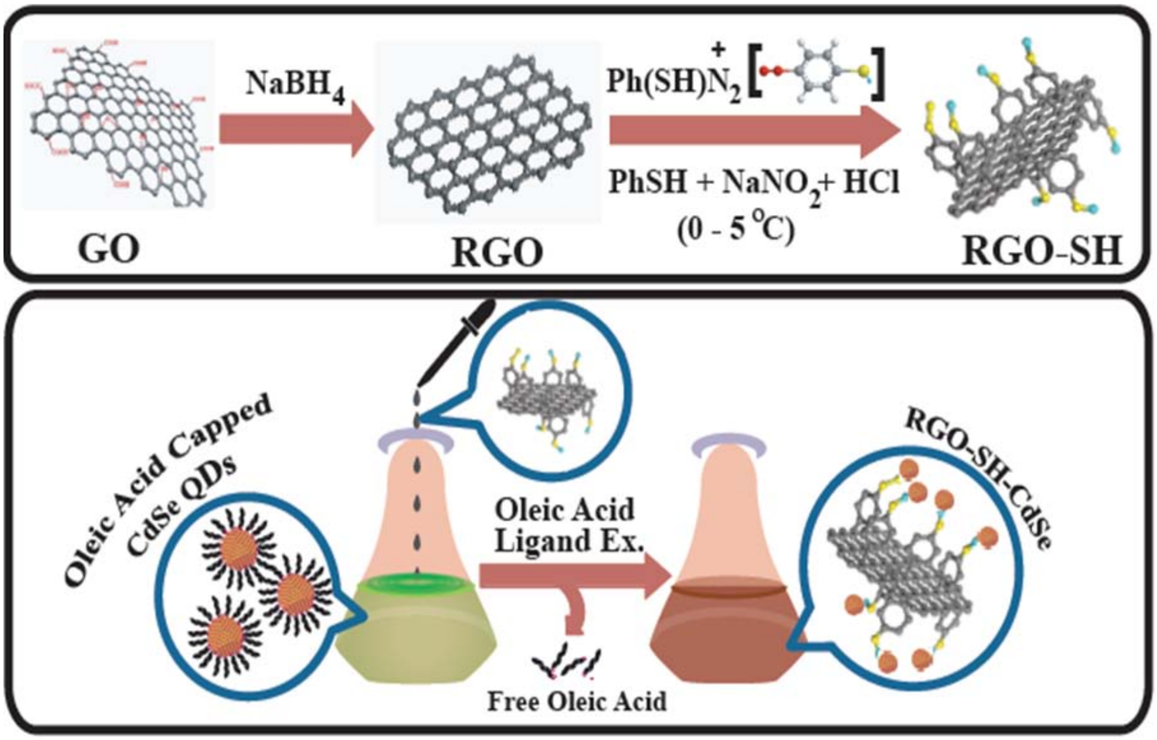

**Figure 4.1.** A schematic representation of the synthetic strategy of RGO and –SH terminated RGO followed by CdSe attachment through chemical exchange with oleic acid.

On the other hand, in spite of several reports on graphene-CdSe QD hybrids,[17], [22] the basic understanding of relaxation of excited CdSe QDs in presence of graphene is not clear. Similarly, how the "edge effect" of graphene impacts the carriers in CdSe QDs or *vice versa*, also remains a question. Brus*et al.*[23] have reported that the excited CdSe QDs decays by energy transfer (by the celebrated "Förster Resonant Energy Transfer mechanism") to pristine graphene and also have explored the possibility of electron transfer. According to them electron transfer can predominate over energy transfer when there is a strong chemical interaction between CdSe QDs and graphene. But, unfortunately there has been no experimental report to date which can prove this important hypothesis. A closely related report by Bang *et al.* shows an interesting thiol modification of $C_{60}$, which is a structural analogue of graphene ($C_{60}$ is topologically linked with graphene) explaining both its ability to anchor CdSe QDs effectively and also the higher efficiency of exciton generation.[24] Accordingly, in this chapter steady state and time resolved photoluminescence (PL) measurements have been employed to confirm the electron transfer process in CdSe-RGO-SH hybrid systems and this is also supported by Raman analysis of the CdSe-RGO-SH hybrids. The rate of charge transfer has been shown to increase with increase in particle size. Photoconductivity properties of the graphene-QD device under illumination have also been examined and it is to be noted that 2-3 fold increase in the photocurrent is found in this composite device in presence of 1.5 AM solar simulated light. The enhancement of photocurrent in this hybrid device is found to be suitable for potential applications in optoelectronic and solar cell systems. The results of the present study are relevant for the effective utilization of the hybrids for solar cells and other photon energy harvesting systems because the understanding of fundamental charge transfer process to graphene is directly related to the photon to current conversion efficiency of such devices. More significantly, a fundamental understanding of the size dependent efficiency of QDs in transferring electrons to graphene is extremely valuable for designing better solar cells employing colloidal QDs and graphene or its derivatives.

## 4.2. Experimental Section

### 4.2.1. Materials

Graphite powder, Sodium dodecylsulphonate (SDS), $NaBH_4$ and 4-aminothiophenol were purchased from Aldrich and used as received. $H_2SO_4$ (98%), $HNO_3$ (63%), HCl (38%), $NaNO_2$, $H_2O_2$ were received from Thomas Baker and used without any further purification. PTFE filter paper was obtained from Rankem. MilliQ water (DI water) was used for all purposes unless otherwise stated. Spectroscopic grade toluene and DMF were obtained from MERCK. Cadmium oxide (CdO), trioctyl phosphine (TOP) and 1-octadecene were purchased from Aldrich and used as received. Se powder, hexane and ethanol (99.9%) of analytical reagent grade were purchased from Thomas Baker. Oleic acid was purchased from Rankem and used without further purification.

### 4.2.2. Reduction of surfactant wrapped graphene oxide (GO) using $NaBH_4$

GO was prepared separately from powder graphite adopting the Hummers and Offman method. [25-26] 0.1g Graphene Oxide (GO) was suspended in water using sonication for 15 min followed by reduction with $NaBH_4$ (1:3 wt. ratio) for 12 h to obtain chemically converted graphene (CCG) or reduced graphene oxide (RGO).

### 4.2.3. Preparation of thiol (-SH) functionalized graphene (RGO-SH)

A diazonium salt of 4-aminothiophenol (4-ATP) was prepared by mixing 70 mg 4-ATP with 200 mg $NaNO_2$ in 40 mL distilled water at 0-5°C followed by the addition of 3 mL 6 M HCl solution (ice cold) slowly to the above mixture. A gradual change of the solution color (transparent) to pale yellow indicated the formation of diazonium salt. The mixture was then slowly (and with constant stirring) added to the RGO suspension (at 0-5°C) and allowed to stir for 2 h at 0-5°C and another 2 h at room temperature (30°C). Subsequently, the reaction mixture was filtered, washed with DI water and re-suspended in DMF to remove the SDS surfactant and excess unreacted 4-ATP molecules. The suspension was finally filtered and washed to get –Ph-SH functionalized RGO -SH.

### 4.2.4. Exchange of oleic acid capped CdSe QDs with RGO-SH)

Oleic acid capped CdSe NPs (CdSe-OA, Chapter 2, section 2.2) (concentration of CdSe suspension was maintained by fixing the first excitonic peak intensity at 0.1 optical density throughout all our experiments) were exchanged by mixing the DMF suspension of RGO-SH (12.7 mg $ml^{-1}$) with toluene soluble CdSe-OA.

## 4.3. Structural and Morphological Characterization

### 4.3.1. UV-Vis absorption

Optical absorption spectra were taken at room temperature by a UV-Vis spectrophotometer (SHIMADZU).

### 4.3.2. Photoluminescence Spectroscopy

Room temperature steady state photoluminescence spectra were recorded by a Fluoromax-P (HORIBA JOBIN YVON) spectrophotometer. Photoluminescence quantum yields (QY) for CdSe QDs were obtained by comparison with reference dye (rhodamine 6G in water), using the following equation:

$$QY_s = (F_s \times A_r \times n_s^2 \times QY_r) / (F_r \times A_s \times n_r^2) \ldots\ldots\ldots\ldots\ldots\ldots\ldots\ldots\ldots\ldots (1)$$

where $F_s$ and $F_r$ are the integrated fluorescence emission of the sample and the reference respectively. $A_s$ and $A_r$ are the absorbance at the excitation wavelength of the sample and the reference and $QY_s$ and $QY_r$ are the quantum yields of the sample and the reference ($QY_r$ = 95%).[27] The refractive indices of the solvents used for the preparation of the sample (in toluene) and reference (in water) are given by $n_s$ (1.49) and $n_r$ (1.33) respectively. The values of $F_s$ and $F_r$ were determined from the photoluminescence spectra corrected for the instrumental response, by integrating the emission intensity over the desired spectral range. Only the band edge luminescence peak was integrated (any other luminescence bands, such as defect associated luminescence or solvent fluorescence were discarded as background).

### 4.3.3. Time correlated single photon counting (TCSPC) measurement

For the time correlated single photon counting (TCSPC) measurements, the samples were excited at 375 nm using a nano-second diode laser (IBH Nanoled) in an IBH Fluorocube apparatus. The typical full width at half-maximum (FWHM) of the system response using a liquid scatter was about 300 ps. The repetition rate was 1 MHz.The fluorescence decays were analyzed using IBH DAS6 software. The following equation was used to analyze the experimental time resolved fluorescence decays,[28] $P(t)$

$$P(t) = b + \sum_{i}^{n} \alpha_i \exp(-\frac{t}{\tau_i}) \dots\dots\dots\dots\dots\dots\dots (2)$$

here, $n$ is a number of discrete emissive species, $b$ is a baseline correction (“dc” offset), and $\alpha_i$ and $\tau_i$ are pre-exponential factors and excited-state fluorescence lifetimes associated with the $i^{\text{th}}$ component, respectively. For multi-exponential decays the average lifetime, $\langle\tau\rangle$, was calculated from the following equation,[29]

$$< \tau >= \sum_{i=1}^{n} a_i \tau_i \dots\dots\dots\dots\dots\dots\dots\dots (3)$$

Where $a_i = \alpha_i / \sum \alpha_i$ and $a_i$ is contribution of the decay component.

Other characterization details like FTIR, SEM, EDAX, XPS, Contact angle measurement, TGA and electrochemical techniques have already been discussed in Chapter 2 (section 2.2) and Chapter 3 (section 3.2)

## 4.4. Results and Discussion

### 4.4.1. FTIR analysis

FTIR spectra were recorded in order to confirm the successful grafting of –PhSH group. Accordingly, fig. 4.2 shows comparative FTIR spectra of reduced Graphene oxide (RGO), 4-aminothiophenol (4-ATP) and thiol modified graphene. Less intense characteristic peak for –SH group (~2530 $cm^{-1}$) is observed in thiol modified graphene. The same peak appears at 2569 $cm^{-1}$ (very weak at 2569 $cm^{-1}$) in case of 4-ATP molecule. However, the peak for thiol is rather broad. This is in accordance with the information available in literature that the –SH peak is very difficult to be observed in FTIR and moreover, vibrational peaks of graphene (specially remaining –COOH group) are so strong that those can mask the actual –SH peak. The presence of –SH group hence confirms the successful grafting of –PhSH group on graphene surface. It also proves that –SH group exists mostly as –SH moiety and not any other form. The spectrum for 4-ATP molecule however shows, (other than –SH peak) several peaks corresponding to =C-H deformation of benzene ring (825 $cm^{-1}$), C=C in plane vibration (1625, 1497 $cm^{-1}$), aromatic =C-H stretching (3026 $cm^{-1}$) and finally the N-H stretching (3375 $cm^{-1}$) of charged aromatic amine group.[30] The absence of N-H stretching peak as well as the presence of both S-H and C-H stretching peaks ensure proper functionalization, presumably with the loss of $–NH_2$ group as molecular $N_2$ during aromatic electrophilic reaction (C-C bond formation) on the graphene surface.

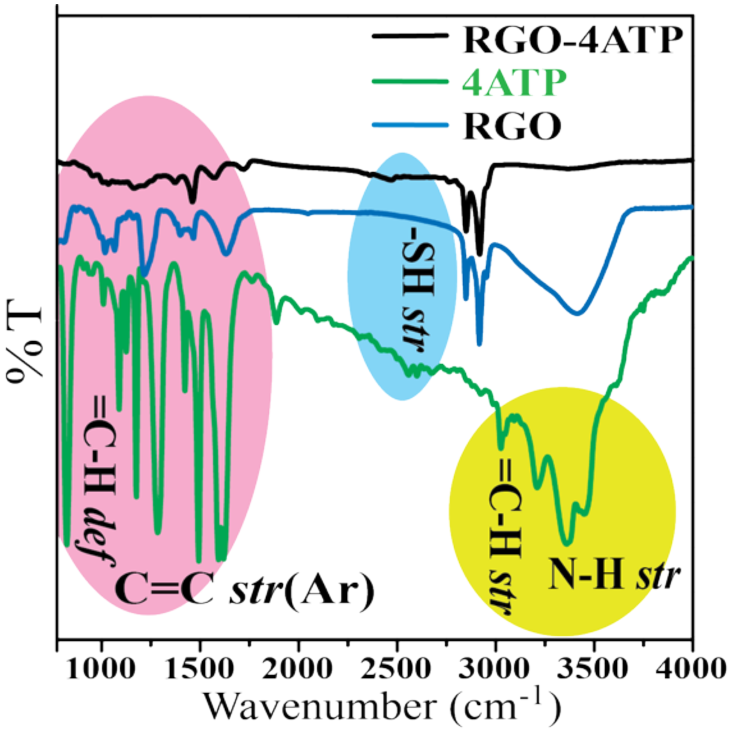

**Figure 4.2.** Superimposed FTIR spectra of RGO (RGO), -SH grafted RGO (RGO-SH) and 4-ATP; Stretching peak of –SH group is seen at 2530 $cm^{-1}$ for RGO-SH and at 2569 $cm^{-1}$ for 4-ATP molecule (sky blue region); N-H stretching vibration disappears after diazotization (yellow region).

### 4.4.2. Scanning Electron Microscopy and EDAX mapping

After confirming the presence of –SH group on RGO surface, SEM elemental mapping (EDAX) has been employed in order to see the distribution or the grafting density of –SH groups in RGO-SH. Accordingly, fig. 4.3 shows the elemental mapping of the thiolated graphene revealing an almost complete coverage of S (or –SH group). From the quantitative analysis of EDAX, ~4 wt% sulphur (S) has been estimated for the case of 1:1 wt% of graphene to 4-ATP. This approximately indicates about ~$10^{18}$ to$10^{20}$ number of –SH units per gram of graphene surface.

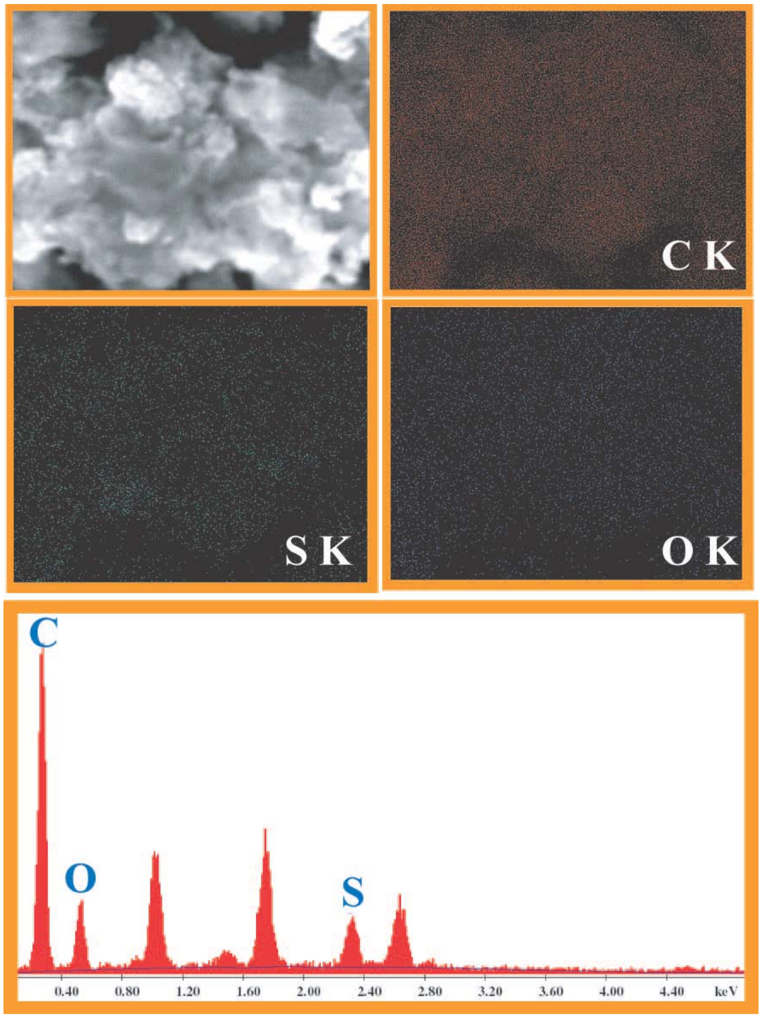

**Figure 4.3.** SEM image of a portion of RGO-SH and the EDAX maps of C, S, O elements in the hybrid material; S-shows a uniform distribution over the material indicating similar functionalization throughout the RGO surface; below is the EDAX plot of RGO-SH showing the presence of S.

### 4.4.3. TGA analysis

In order to further confirm the chemical bonding between –PhSH group and RGO surface, several thermogravimetric experiments have been carried out. Accordingly, fig. 4.4 shows a comparison of the thermograms of pure RGO, pure 4-ATP molecule, RGO-SH (chemically functionalized RGO) and a physical mixture of RGO and 4-ATP (RGO+4-ATP) in nitrogen. It can be observed from the thermograms that the physical mixture shows same decomposition profile as that of pure 4-ATP molecule except the remaining mass at 900 °C. The higher residual mass in case of the physical mixture as compared to that of pure 4-ATP is due to the presence of graphene. This clearly suggests that no chemical adsorption occurs when RGO and 4-ATP are physically mixed. The situation is, however, different in case of RGO-SH. The decomposition profile is entirely different than that of the physical mixture. This undoubtedly proves that chemical interaction occurs between 4-ATP and RGO during diazotization. Presence of functional groups other than oxygen functionalities in RGO-SH is also confirmed from the observation that RGO-SH shows higher decomposition than pure RGO at 900 °C. FTIR, EDAX and TGA analysis thus ostensibly confirms the successful grafting of –SH group in RGO.

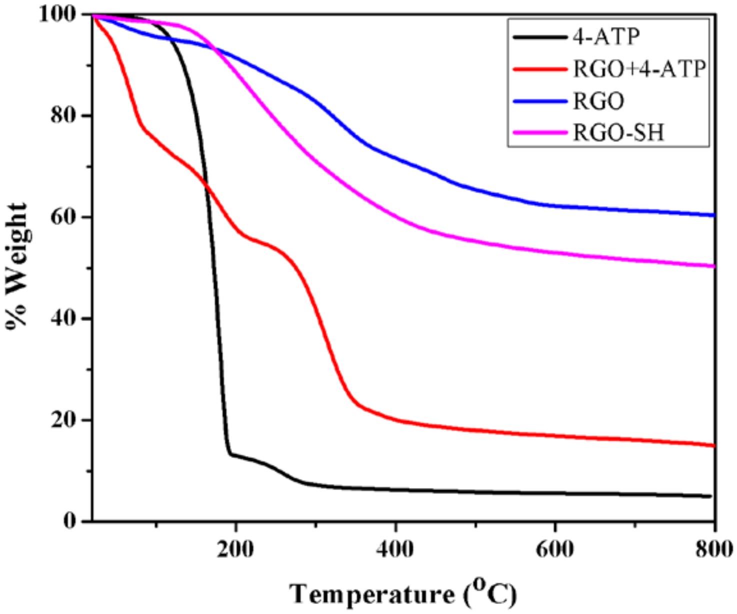

**Figure 4.4.** Decomposition profile of 4-ATP, RGO+4-ATP, RGO-SH and pure RGO in nitrogen atmosphere; mismatch of the profile of RGO-SH and that of the physical mixture confirms the chemical interaction between –PhSH moiety and RGO surface.

### 4.4.4. XPS analysis

XPS of RGO-SH-CdSe (4.7 nm) has been carried out in order to validate the presence of thiol group as well as its binding to CdSe QDs (4.7 nm) mainly by analyzing the Carbon (C 1s), Sulphur (S 2p) as well as Cadmium (Cd 3d) signals using this RGO-SH-CdSe (4.7 nm) hybrid. Accordingly, fig. 4.5 (a), (b) and (c) show typical core level XP spectra of carbon, cadmium and sulphur of the hybrid. Cadmium (in the form of CdSe) (Fig. 4.5 (b)) signal can be fitted quite well with a single spin-orbit pair at 405.3 eV ($3d_{5/2}$) and 412 eV ($3d_{3/2}$). These values are in good agreement with that reported for TOPO capped CdSe QDs.[31] Similarly, S2p core level spectrum (Fig. 4.5(c)) can be deconvoluted to two peaks at 163.4 eV and 166.7 eV respectively. The first peak (163.4 eV) corresponds to the S atoms of –PhSH groups, bonded to CdSe QDs while the peak at higher binding energy (166.7 eV) is associated with the presence of some amount of S-atoms at higher oxidation state ($S^{6+}$), formed during the sample preparation and exposure to X-rays as has been observed previously.[32] Binding to CdSe renders the S-atom (of –SH group) more electronegative and hence the consequent blue shift of the binding energy of sulphur as compared to S in normal –SH group (161-162 eV). This value of binding energy (B.E) (for CdSe-thiol bonding) is in excellent agreement with the reported B.E value for S 2p signal in case of self-assembled monolayers of alkanethiols, aromatic thiols as well as alkanethiol capped silver nanoparticles.[33-35] It reveals that in the homogeneous mixture of CdSe QDs (in toluene) and RGO-SH (in DMF), and CdSe QDs are chemically bonded to RGO-SH surface due to ligand exchange between thiol group and oleic acid. As no peak for carbon-sulphur binding (164 eV according to literature [36]) is observed in the spectrum, 4-ATP molecule is expected to be bonded through C-C linkage to graphene and not through C-S bond. C1s (Fig.4.5 (a)) signal also corroborates well with this explanation. C1s signal can be de-convoluted to 4 different peaks. The low B.E peak at 284.1 eV corresponds to $sp^2$ carbons from the graphene (RGO-SH) surface and the peak at 284.9 eV is due to $sp^3$ carbons resulting from covalent functionalization on graphene surface. Higher B.E peaks at 286 eV and 288 eV indicate the attachment of carbons to more electronegative elements like oxygen and sulphur. However, the intensity and the area of this high B.E peak are very small as compared to rest of the peaks which suggests that the amount of higher oxidation sulphur species ($S^{6+}$) is very small.

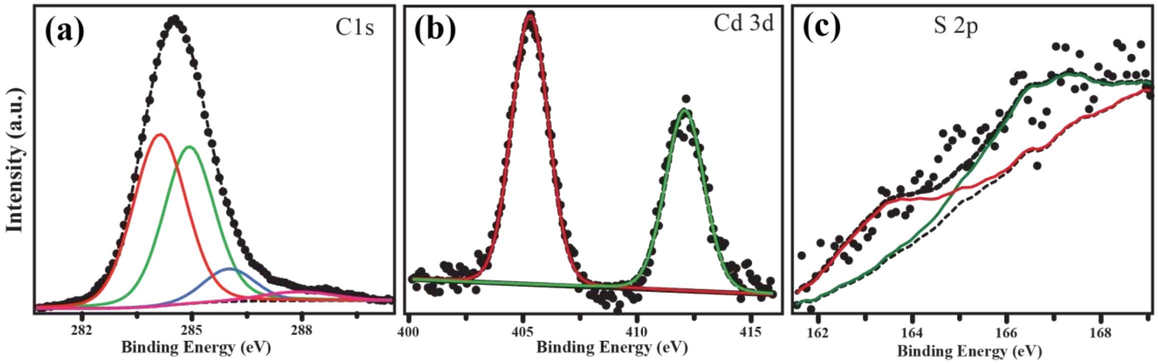

**Figure 4.5.** Core level XPspectra of (a) Carbon (C1s), (b) Cadmium (Cd 3d) and (c) Sulphur (S-2p) from RGO-SH-CdSe (4.7 nm) hybrid.

### 4.4.5. Cyclic voltammetry

Cyclic voltammetry has been employed to characterize the RGO before and after –SH grafting. Ferrocene methanol has been used as a redox probe to understand the conductivity property of RGO before and after –SH grafting. Accordingly, distinct redox peaks, for the oxidation and reduction of ferrocene methanol (fig. 4.6), are observed in case of RGO which is a good electron carrier. Interestingly, when the same coating is subjected to thiol functionalization for 2 h, the current for the redox peaks are found to decrease. This is because the surface of the RGO gets modified with –Ph-SH groups, which in turn hinders the diffusion of ferrocene methanol molecules towards the RGO surface and as a result the current drops. Integrating the area of the oxidation peak gives ~$10^{-7}$ $molcm^{-2}$ surface coverage of –PhSH group on the surface of RGO.

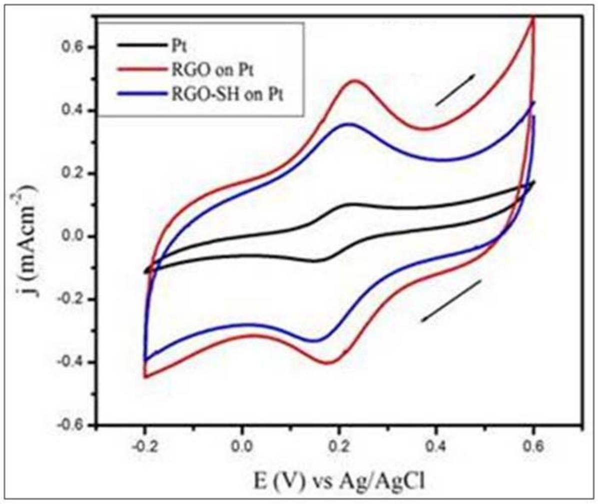

**Figure 4.6.** Cyclic voltammogram of RGO coated on Pt electrode (2 mm dia) in 0.5 mM ferrocenemethanol containing 0.1 M KCl aqueous solution, Ag/AgCl was used as

reference electrode and Pt-foil as counter electrode, Scan rate was 10 mVs$^{-1}$; For comparison CV of Pt disk also has been shown.

### 4.4.6. Impedance measurement

Impedance measurement has been carried out to support the result obtained from cyclic voltammetry. Accordingly, fig. 4.7 (a) shows Nyquist plotsof RGO and RGO-SH under similar conditions of CV using ferrocenemethanol as the redox probe. The diameter of the high frequency semicircle which is a measure of charge transfer resistance is found to increase after –SH grafting. Moreover, diffusion coefficient of ferrocene methanol, obtained from the low frequency straight line portion (by plotting modulus of Z vs. $\omega^{-1/2}$in Fig. 4.7 (b)), suggests the poor diffusion of the molecules to the electrode surface (RGO here) due to the presence of thiolgroup (pinning). The thiol groups impede the incoming flux of ferrocene methanol molecules to the RGO surface and thereby results in the higher charge transfer resistance.[37]

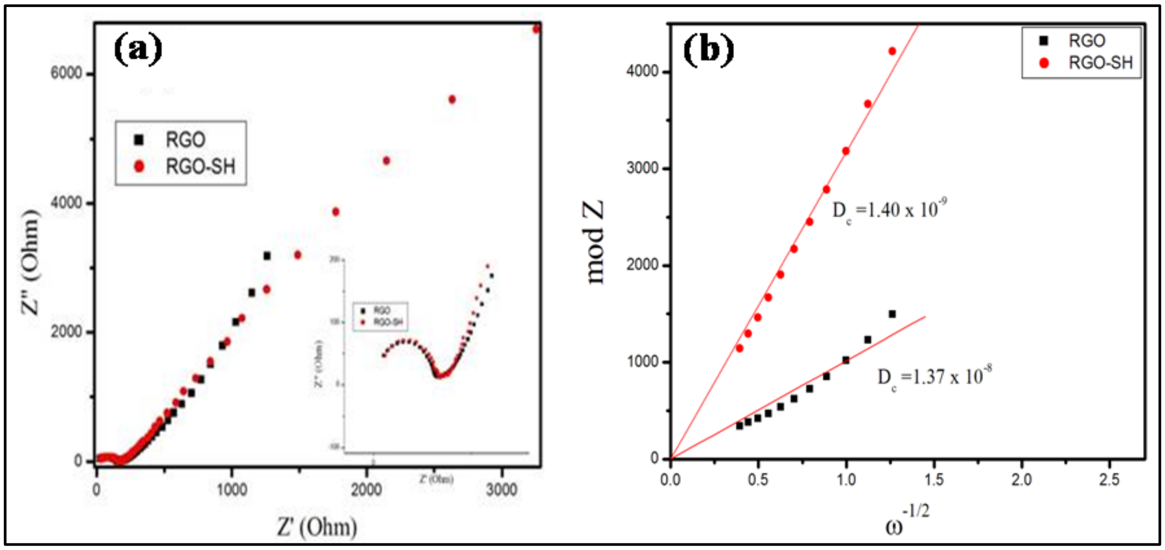

**Figure 4.7.** (a) Nyquist plot for the same system before and after –SH functionalization; The $R_{ct}$ increases after functionalization, (c) $\omega^{-1/2}$ vs mod. Z plot from the low frequency part of the Nyquist plot for the calculation of diffusion coefficient of the ferrocene methanol.

### 4.4.7. Contact angle measurement

Contact angle of any liquid on any substrate is an important parameter which is very sensitive to surface functionality provided that the microstructure remains same. Hence, a systematic analysis of the water contact angle change has been carried out on RGO and RGO-SH surfaces in order to understand the change due to –SH grafting. Accordingly, substrate change from pristine graphene to RGO-SH shows (fig. 4.8) increased hydrophobic character due to –PhSH grafting (water contact angle increases from 82° to 91° after functionalization). Surface energy of RGO has been calculated, before and after –PhSH grafting, using Ownes-Wendt method suggesting an increase in surface energy from 33.1 to 40.3 mJm$^{-2}$) after functionalization.[38] However, the polar or non-dispersive component of the surface energy decreases (5.5 to 0.6 mJm$^{-2}$) after functionalization with a concomitant increase in dispersive or non-polar component (27.6 to 39.8 mJm$^{-2}$).

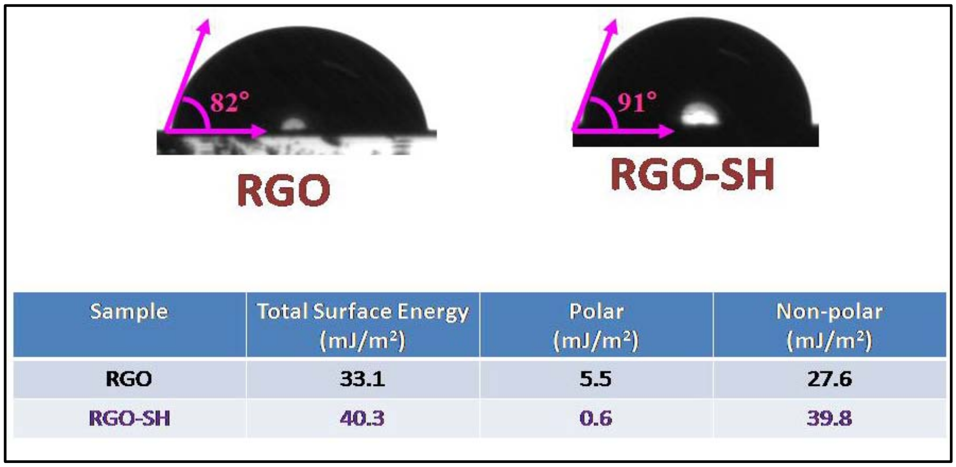

| Sample | Total Surface Energy (mJ/m²) | Polar (mJ/m²) | Non-polar (mJ/m²) |
|---|---|---|---|
| RGO | 33.1 | 5.5 | 27.6 |
| RGO-SH | 40.3 | 0.6 | 39.8 |

**Figure 4.8.** Water contact angle on RGO and RGO-SH surface; film of each sample was made by electrophoretic deposition (solvent N-methyl pyrrolidone for RGO and Dimethylformamide for RGO-SH) on clean FTO plates and dried at 100°C under vacuum for 8 h to get a smooth surface so as to minimize errors due to surface roughness.

### 4.4.8. Micro Raman

Raman mapping (fig. 4.9) has been used extensively to characterize the functionalized RGO and the hybrids. More specifically, three different sizes of CdSe QDs have been chosen, (namely 3.8 nm, 4 nm and 4.9 nm) and their capping agents were exchanged with the –SH functionalized graphene (RGO-SH) hybrid. As has been indicated in fig. 4.9(a), all the three hybrids show two characteristics phonon modes of vibrations on excitation-one at 1333.1 cm$^{-1}$ and another at 1582.8 cm$^{-1}$. The first one is identified as the D-band or defect induced band which appears due to in plane longitudinal phonon vibration or breathing mode of k-point phonons of $A_{1g}$ symmetry and the later one is the G-band or graphitic band arising due to $E_{2g}$ phonon mode for sp$^2$ carbon network of graphene plane. However, when compared with pristine RGO without any thiol functionalization and CdSe QDs decoration, there is ~13 cm$^{-1}$ shift of both D as well as G- bands towards lower wavenumber or energy (fig. 4.9(b)).This red shift (equivalent to 1.6 meV) implies softening of phonons of RGO due to electron enrichment on graphene because of charge transfer to graphene.[39] A similar effect has been observed in case of molecular doping in graphene in presence of an electron donor like tetrathiafulvalene (TTF)[32] where a shift of ~10 $cm^{-1}$ has led to a doping (electron) concentration of ~$10^{12}$ $cm^{-2}$ for 0.1 M TTF in graphene.

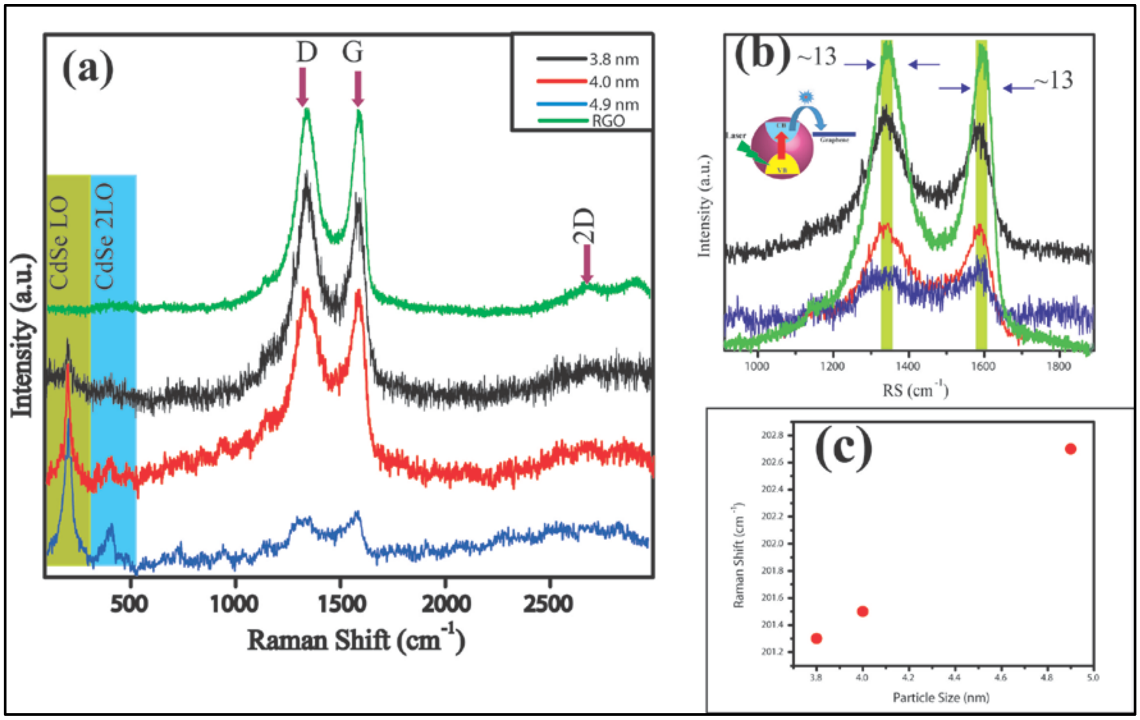

**Figure 4.9.** (a)Micro Raman spectra of CdSe-RGO-SH hybrids with 514 nm $Ar^+$ laser using 50x objective, (b) enlarged portion of D and G bands of RGO showing charge transfer from CdSe to RGO, (c) variation of peak position of CdSe QDs with particle size.

The excitation source 514 nm laser has sufficient energy (2.41 eV) to excite the valence band electrons of CdSe QDs, the work function of graphene (-4.5 eV) being favorable with the conduction band positions of these QDs (-4.17 to -4.38 eV for 3.8 nm to 4.9 nm particles), excited electrons can be transferred to graphene and thereby rendering the graphene surface electron rich. This consequently results in a red shift in the D and G-band positions of the graphene. Interestingly, $I_D$ to $I_G$ ratio (1.01 in this case) remains the same both for pristine RGO as well as for functionalized and CdSe decorated RGO confirming that the nature and amount of defect remains the same before and after the functionalization. On the other hand, the appearance of 2D band, which is the overtone band of D-band, in all samples, indicates that the number of layers is not disturbed significantly due to functionalization.[20] A typical crystallite size of ~16.6 nm has been estimated from the $I_D/I_G$ ratio, which basically represents the distance between two successive defect points. Other than the D-and G-bands, the Raman spectra of the hybrid materials also bear the feature of CdSe QDs in the 100 – 500 $cm^{-1}$ region. The peak at 201-202 $cm^{-1}$ is attributed to the longitudinal optical (LO) phonon mode of CdSe and that at 400-405 $cm^{-1}$ is the overtone of LO mode which is termed as CdSe 2LO. As Fig.4.9(c) suggests, the LO peak shows a slow red shift with the decrease in particle size, in accordance with the previous report.[40] the appearance of LO peak within 201-202 $cm^{-1}$ as compared to 210 $cm^{-1}$ for bulk CdSe, suggests the invariance of the size and shape for the attached QDs.[40]

### 4.4.9. Transmission Electron Microscopy

TEM analysis has been carried out in order to see the distribution and particle size of QDs on RGO-SH surface. Accordingly, fig. 4.10(a-d) displays low and high resolution (HRTEM) images of f-RGO and RGO-SH-CdSe QD (4.7 nm) hybrids respectively. Images for the hybrids were taken of the samples containing 0.268 mg/mL of RGO-SH. Interestingly, low magnification image shows complete coverage of the QDs on RGO-SH (fig.4.10(b)) as compared to only RGO-SH (fig.4.10(a)) in which case no CdSe QD is visible. After the exchange with the thiol groups on RGO, CdSe QDs interestingly form an almost complete monolayer on RGO at this concentration of RGO-SH. The FFT in the inset of fig. 4.10(d) indicates the formation of cubic CdSe and more significantly, the d-spacing (2.9 Å) matches well with that of literature report (zinc blende phase, JCPDS card no.19-0191).

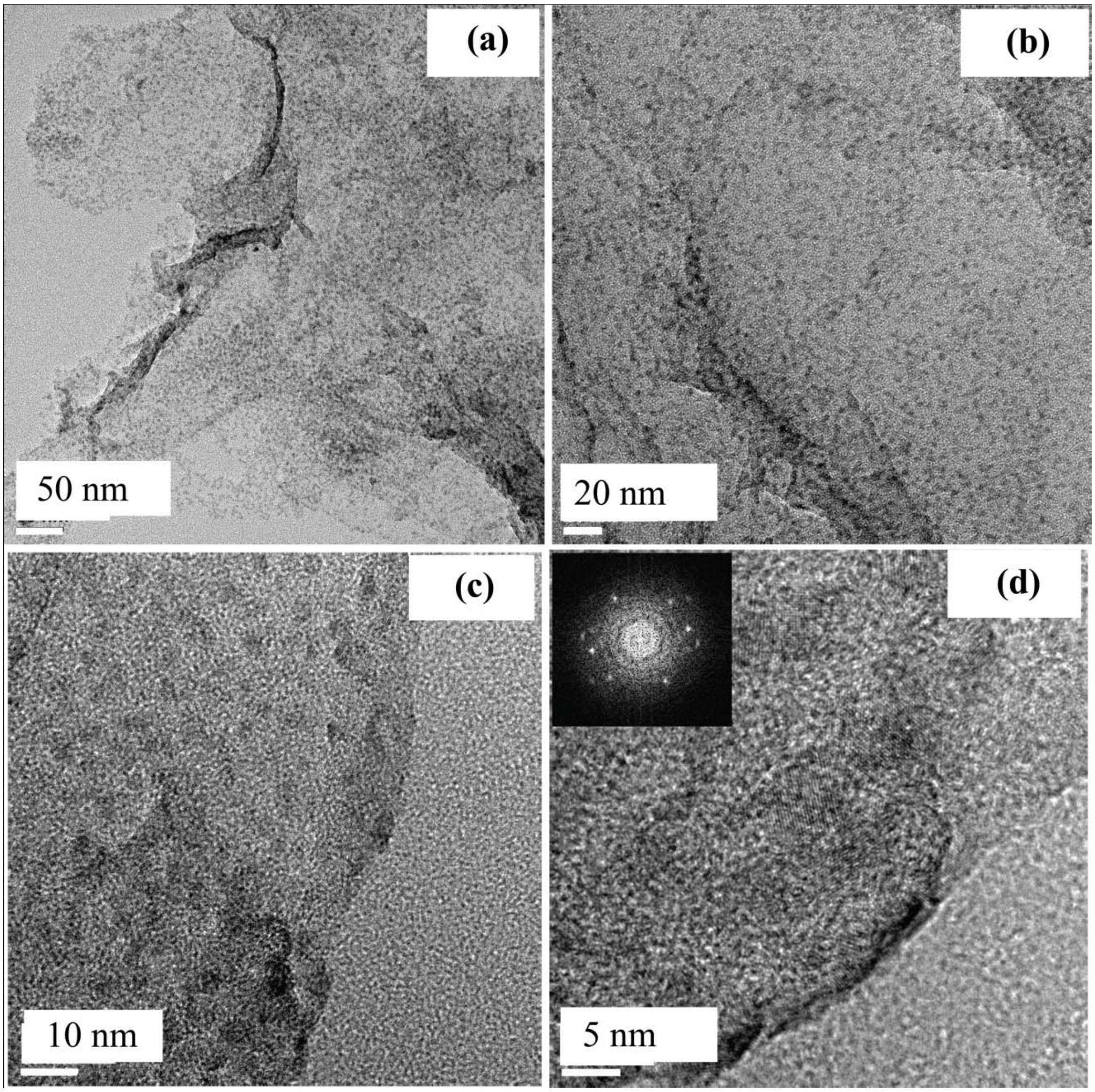

**Figure 4.10**. High resolution TEM images of RGO-SH and RGO-SH (0.268 mg/mL)-CdSe QDs (4.7 nm); (a) only RGO-SH and (b) RGO-SH-CdSe hybrids at low magnification, (c) and (d) high magnification images of RGO-SH-CdSe hybrids; Inset of (d) shows the reduced FFT pattern of QDs.

### 4.4.10. UV-Vis Absorption and Photoluminescence

Fig. 4.11(a) shows a comparison of the absorption spectra of three different sizes (3.03 nm, 3.8 nm and 4.7 nm) of oleic acid capped CdSe QDs. The position of the first electronic transition is shifted to higher photon energies (blue shift) with decreasing the particle size which is consistent with that of previous results.[40-41] Fig. 4.11(b) shows the photoluminescence (PL) emission spectra of the corresponding CdSe QDs. Furthermore, the quantum yields (QYs) of the CdSe QDs have been calculated to be 8.80%, 14.93%

and 11.52% for 3.03, 3.8 and 4.7 nm CdSe QD, respectively. It is noted that QY of 3.8 nm size CdSe QD is found to be higher. The variation of QY here (QY of 3.8 nm > QY of 4.7 nm) can be due to variation in surface defects which increases the nonradiative recombination rates and thereby decreasing QY. Smaller particles generally have larger defect states and hence QY is also less.[42]

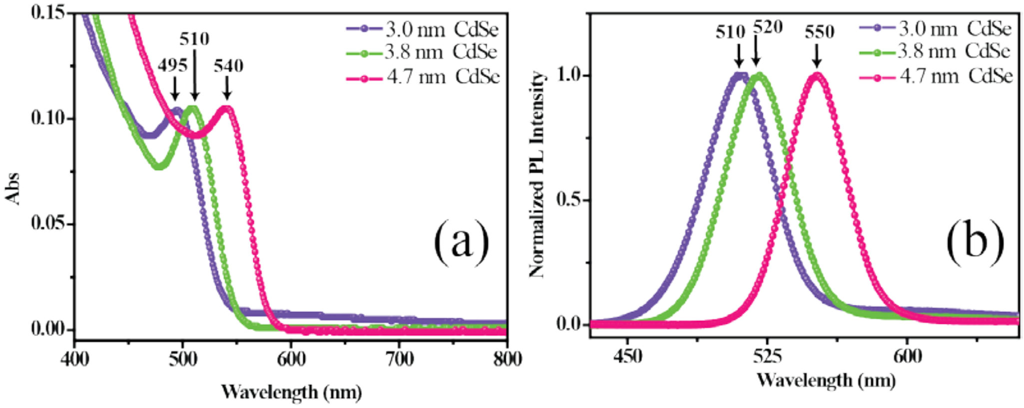

**Figure 4.11.** (A) Absorption and (B) Photoluminescence spectra of the CdSe QDs capped with oleic acid in toluene.

### 4.4.11. Steady state and Time resolved Spectroscopic study

Time resolved spectroscopic study along with steady state photoluminescence gives valuable information about the charge/energy transfer between donor and acceptor. Consequently, this tool has been used to understand the process of deactivation of excited CdSe QDs chemically attached to graphene surface. Accordingly, fig. 4.12 (a) shows the steady state photoluminescence spectra of 3.03 nm CdSe before and after the attachment. Photoluminescence intensity of CdSe is effectively quenched by RGO-SH and the PL intensity decreases with increasing RGO-SH concentration. The calculated PL quenching efficiency increases from 14.35% to 82.26% with increasing the RGO-SH concentration from 0.036 to 0.268mg/ml. In case of 3.80 nm and 4.70 nm CdSe QDs, the PL quenching efficiencies are 84.25% and 82.00% for the RGO-SH concentration of 0.268mg/ml. The photoluminescence spectra of 3.8 nm and 4.7 nm CdSe QDs-RGO-SH are also given in the fig. 4.12(b) and (c). All the spectra follow similar trend, i.e., the steady state PL decreases systematically with increasing concentration of RGO-SH. The photoluminescence quenching of CdSe QDs is indicative of strong electronic interactions between the excited state of CdSe and RGO-SH.

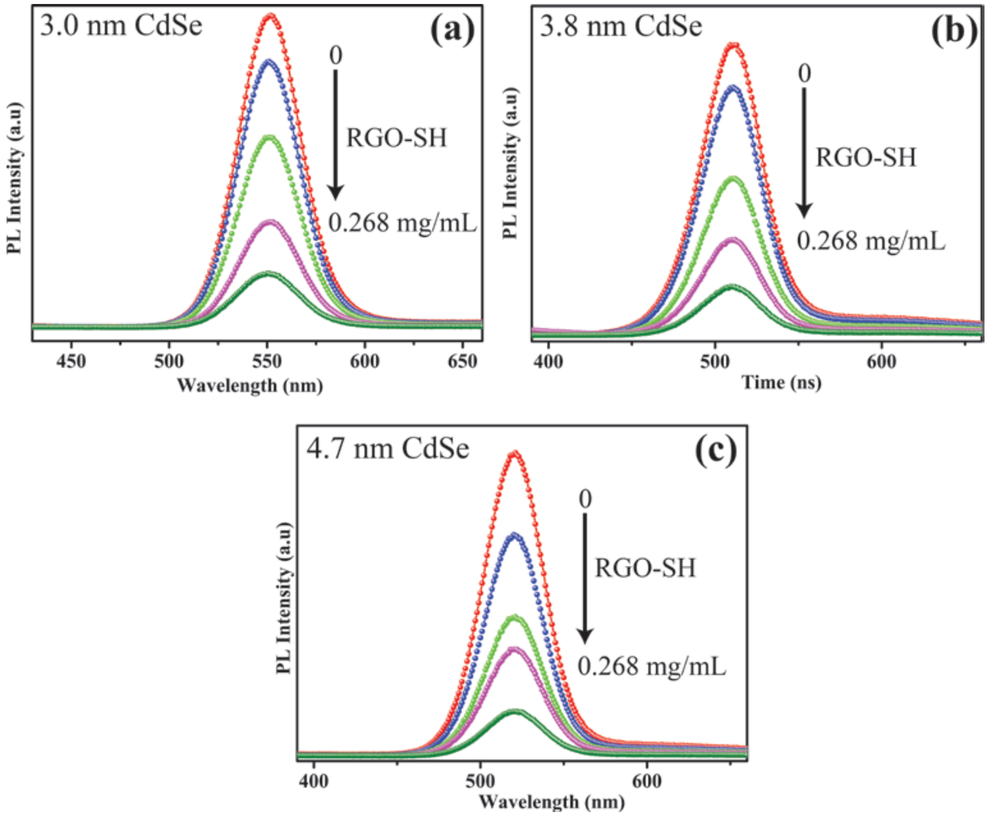

**Figure 4.12.** Steady state photoluminescence quenching with incremental amount of RGO-SH; (a) CdSe QDs of 3.0 nm, (b) CdSe QDs of 3.8 nm and (c) CdSe QDs of 4.7 nm.

To confirm the energy/electron transfer process from QD to graphene, a time resolved fluorescence study has further been performed which is indeed, more sensitive than PL quenching. Accordingly, fig. 4.13(a) shows the photoluminescence decay curves of 3.03 nm CdSe as a function of increasing concentration of RGO-SH at the excitation and emission wavelength of 375 nm and 510 nm, respectively. All the decay curves are fitted with tri-exponential functions. The decay components of the pure 3.03 nm CdSe QD are 0.76 ns (58.4%), 7.70 ns (27.4%) and 39.29 ns (14.2%) and the average decay time is 8.13 ns according to eq.3. In presence of highest concentration of RGO-SH (0.268 mg/ml), the corresponding components are 0.57 ns (74.5%), 6.48 ns (18.2%) and 38.49 ns (7.3%) and the average decay time is 4.41 ns. The fluorescence decay time of CdSe QDs decreases with the increasing concentration of RGO-SH which is consistent with the fluorescence results. With increasing the RGO-SH concentration, the fast component ($\tau_1$) decreases from 0.76 ns to 0.57 ns over the RGO-SH concentration range of 0.036-0.268

mg/ml but slow components ($\tau_2$ and $\tau_3$) decrease negligibly small (Table 4.1). The contribution of the fast component increases from 58.8% to 74.5% respectively while the contribution of slow components decreases from 27.7% to 18.2% and 14.2% to 7.3% only.

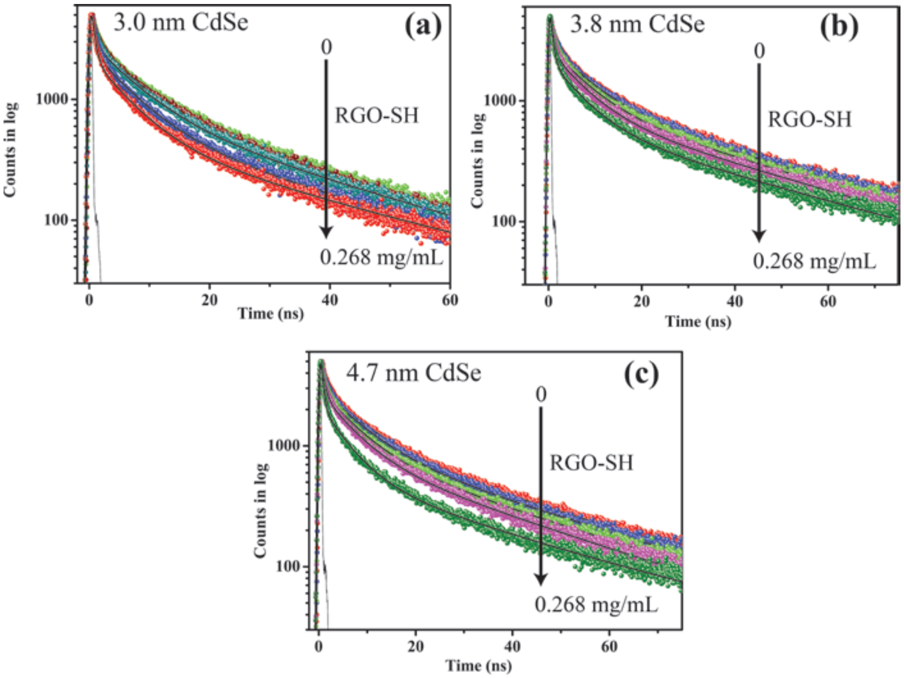

**Figure 4.13.** Time resolve spectra of CdSe and CdSe- RGO-SH at the excitation wavelength of 375 nm; (a) 3.0 nm CdSe QDs, (b) 3.8 nm CdSe QDs and (c) 4.7 nm CdSe QDs.

Actually, the fast component is responsible for the photo-excited electron transfer[22] and the slow component mainly arises from the free CdSe in the solution. With the increase of RGO-SH concentration, the number of free CdSe QDs is expected to diminish in the solution and as a result, the contribution of the slow decay components decreases. For the other two QDs, 3.8 nm and 4.7 nm CdSe, similar results are observed. The corresponding decay profiles and decay parameters are given in fig. 4.13(b), (c) and Table 4.2 and 4.3 respectively. The fast components decrease from 0.91ns to 0.42 ns and 0.77 ns to 0.49 ns for the 3.80 nm and 4.70 nm CdSe QDs, respectively. Therefore, the decrease of fast component and increase of fast decay component contribution in CdSe-RGO-SH hybrid implies the photoluminescence quenching of CdSe QDs by RGO-SH through photo-excited electron transfer from CdSe QDs to RGO-SH. We have calculated the rate of non-radiative decay due to electron transfer, $k_{NRD}$ of three different sized CdSe QDs by using equation 4.

$$k_{NRD} = \frac{1}{\tau_{1(CdSe-RGO-SH)}} - \frac{1}{\tau_{1(CdSe)}} \text{......................(4)}$$

Where, $\tau_1$ represents the fast decay component.[22] The calculated $k_{NRD}$ values are found to be 4.38 x$10^8$, 12.80 x$10^8$ and 7.42 x$10^8$ $s^{-1}$ for the 3.0 nm, 3.80 nm and 4.70 nm CdSe QDs, respectively.

**Table 4.1.** Decay parameters of 3.0 nm CdSe and CdSe-RGO-SH at the excitation and emission wavelength of 375 and 510 nm, respectively.

| **System** | **$\tau_1$ (ns)<br>($a_1$)** | **$\tau_2$ (ns)<br>($a_2$)** | **$\tau_3$ (ns)<br>($a_3$)** | **<τ>(ns)** |
|---|---|---|---|---|
| **Pure CdSe** | 0.76<br>(0.584) | 7.70<br>(0.274) | 39.29<br>(0.142) | 8.13 |
| **CdSe+0.036mg/ml RGO-SH** | 0.69<br>(0.581) | 7.52<br>(0.273) | 38.30<br>(0.017) | 8.05 |
| **CdSe+0.107mg/ml RGO-SH** | 0.65<br>(0.630) | 7.32<br>(0.252) | 38.80<br>(0.118) | 6.83 |
| **CdSe+0.178mg/ml RGO-SH** | 0.62<br>(0.674) | 6.76<br>(0.225) | 38.23<br>(0.101) | 5.80 |
| **CdSe+0.178mg/ml RGO-SH** | 0.57<br>(0.745) | 6.48<br>(0.182) | 38.49<br>(0.073) | 4.41 |

**Table 4.2.** Decay parameters of 3.8 nm CdSe and CdSe-RGO-SH at the excitation and emission wavelength of 375 and 520 nm, respectively.

| **System** | **$\tau_1$ (ns)<br>($a_1$)** | **$\tau_2$ (ns)<br>($a_2$)** | **$\tau_3$ (ns)<br>($a_3$)** | **<τ> (ns)** |
|---|---|---|---|---|
| **Pure CdSe** | 0.91<br>(0.538) | 8.21<br>(0.302) | 36.54<br>(0.160) | 8.81 |
| **CdSe+0.036mg/ml RGO-SH** | 0.77<br>(0.568) | 7.68<br>(0.288) | 35.59<br>(0.144) | 7.77 |

| | | | | |
|---|---|---|---|---|
| **CdSe+0.107mg/ml RGO-SH** | 0.65<br>(0.618) | 6.86<br>(0.260) | 33.9<br>(0.122) | 6.27 |
| **CdSe+0.178mg/ml RGO-SH** | 0.63<br>(0.645) | 6.39<br>(0.250) | 32.46<br>(0.105) | 5.41 |
| **CdSe+0.268mg/ml RGO-SH** | 0.42<br>(0.780) | 5.37<br>(0.163) | 32.31<br>(0.057) | 3.04 |

**Table 4.3.** Decay parameters of 4.7 nm CdSe and CdSe-RGO-SH at the excitation and emission wavelength of 375 and 550 nm, respectively.

| **System** | **$\tau_1$ (ns)<br>($a_1$)** | **$\tau_2$ (ns)<br>($a_2$)** | **$\tau_3$ (ns)<br>($a_3$)** | **<$\tau$> (ns)** |
|---|---|---|---|---|
| **Pure CdSe** | 0.77<br>(0.585) | 7.73<br>(0.297) | 30.85<br>(0.118) | 6.39 |
| **CdSe+0.036mg/ml RGO-SH** | 0.67<br>(0.568) | 7.16<br>(0.288) | 29.57<br>(0.144) | 5.63 |
| **CdSe+0.107mg/ml RGO-SH** | 0.60<br>(0.640) | 6.72<br>(0.262) | 29.19<br>(0.098) | 5.00 |
| **CdSe+0.178mg/ml RGO-SH** | 0.58<br>(0.698) | 6.17<br>(0.229) | 28.49<br>(0.073) | 3.89 |
| **CdSe+0.268mg/ml RGO-SH** | 0.49<br>(0.764) | 5.69<br>(0.184) | 29.20<br>(0.052) | 2.94 |

This nonradiative decay rate is due to electron transfer process. It is found that 3.80 nm CdSe QD exhibits highest electron transfer rate, which may be due to the higher QY (less number of non-emissive trap states favors the electron transfer rate) and better electronic interaction with the RGO-SH (the energy gap between conduction band of 3.8 nm CdSe QD [-3.3 eV] and the Fermi level of graphene [-4.5 eV]). Table 4.4 clearly shows that the non-radiative rate constant, is for the electron transfer from CdSe to RGO-SH.

**Table 4.4.** Rate constant of electron transfer from CdSe QDs to RGO-SH as a function of QD size.

| CdSe QD | $\tau_{1(\text{RGO-SH-CdSe})}$ | $\tau_{1(\text{CdSe})}$ | Rate constant ($ns^{-1}$) |
|---|---|---|---|
| **3.0 nm** | 0.42 | 0.76 | 0.438 |
| **3.8 nm** | 0.57 | 0.91 | 1.280 |
| **4.7 nm** | 0.49 | 0.71 | 0.742 |

**Table 4.5.** Energy band positions of CdSe QDs with respect to vacuum.

| Size of CdSe QD (nm) | HOMO (eV) vs vacuum | LUMO (eV) vs vacuum |
|---|---|---|
| **3.0** | -6.24 | -3.48 |
| **3.8** | -6.15 | -3.30 |
| **4.7** | -5.95 | -3.40 |

It is also predicted that the enhancement of the electron transfer (and not energy transfer) is observed due to direct electronic interaction between CdSe QDs and graphene, i.e., if the QDs are chemically bonded to the graphene surface. It is reported that the efficiency of exciton generation increases when CdSe QDs are attached with $C_{60}$ by a thiol linker.[43] Functionalization of $C_{60}$ allows binding of ~110-150 $C_{60}$ units to one CdSe QDs and that leads to enhanced quenching of CdSe photoluminescence, thereby yielding more efficient exciton generation. For example, Chaban *et al.*[43] also have reported that thiol functionalization of $C_{60}$ can effectively bind the CdSe QDs to accelerate the electron transfer process from CdSe QDs to $C_{60}$ LUMO level by employing the phonon vibrations of the molecular bridge containing thiol group. In the present study, the graphene has –SH (-PhSH group) terminated group which will replace the oleic acid ligand on the surface of QDs and a chemical coupling occurs between CdSe and graphene. Removal of some of the oleic acid ligand with the short thiol group (-PhSH group) thus establishes direct linking to RGO-SH through –PhSH unit which facilitates the electron transfer process. Moreover, the conduction band of these QDs (Table 4.5) is well aligned with the Fermi level of graphene (-4.5 eV) to enhance the electron transfer from QDs to graphene upon photoexcitation. Moreover, the rate constant for the non-radiative decay is in good agreement with that reported recently by both Kamat*et* al[22] and Brus *et al*.[23] The distance between QDs and graphene surface is ~7 Å (calculated using MATERIALS STUDIO package) which is in favorable position for electron transfer from excited CdSe to graphene surface. The phenyl group of –PhSH can also help in electron transfer most probably through its π-electrons. Molecular vibration of this linker also assists this electron transfer. Above all, thiol group is well known to improve photoluminescence by suppressing the defect sites, which can change the band structure of CdTe QDs.[44] Binding of CdSe QDs to graphene surface via short molecular linker (-PhSH) thus improves the electron transfer rate from excited CdSe to graphene Fermi level. Table 4.5 represents the absolute band positions of the CdSe QDs studied and these values are in excellent agreement with that reported elsewhere.[45] The variation in rate of electron transfer for different QD sizes can be understood from the difference in the energy gap between conduction band of CdSe and the Fermi level of graphene (-4.5 eV). The difference in energy between the conduction band of CdSe and the Fermi level of graphene is maximum for 3.8 nm QDs (Table 4.5). This can also be understood by considering that the electrochemical techniques probe mostly the surface of QDs. Defect states lying on the surface of QDs, can thus alter the position of peak position in CV or DPV and this results in shifts in band positions.

### 4.4.12. Photovoltaic study

A bulk heterojunction type of device has been fabricated as a proof-of-concept of the above study. Accordingly, fig.4.14 shows the dark and photocurrent of the device prepared by graphene-CdSe-3.03 nm QD composite system. Intrinsic graphene does not show any photocurrent under visible light exposure. However, the asymmetric shape of I-V curves is observed in both dark and in visible light. This could be explained since CdSe generates excitons (electron-hole pair) on illumination and these excited electrons are readily transferred to RGO-SH from CdSe QD because of the favorable band alignment between the conduction band of CdSe and the Fermi level of RGO-SH so that the hole migrates to PEDOT:PSS (p-type material). This consequently, leads to the enhancement in photocurrent in CdSe-RGO-SH hybrids. The observed $I_{light}/I_{dark}$ is ~2.2 at 0.6 V for 3.03 nm CdSe while for the other two QDs, the ratio is 2.7 (for 3.8 nm) and 1.54 (4.7 nm) respectively under similar condition (fig. 4.14(a) and (b)). Indeed, the increment in photocurrent is in accordance with the observed rate of electron transfer. A similar trend has also been recently observed for CdTe-Graphene oxide system.[46] Thus, these hybrids of CdSe QDs and f-RGO-SH may act as potential candidates with unique advantages for optoelectronic devices due to high photon to current conversion. Although further investigation is required for a detailed understanding of this hybrid system for device applications, the design of such graphene-QD functional materials open up new avenue in solar energy conversion.

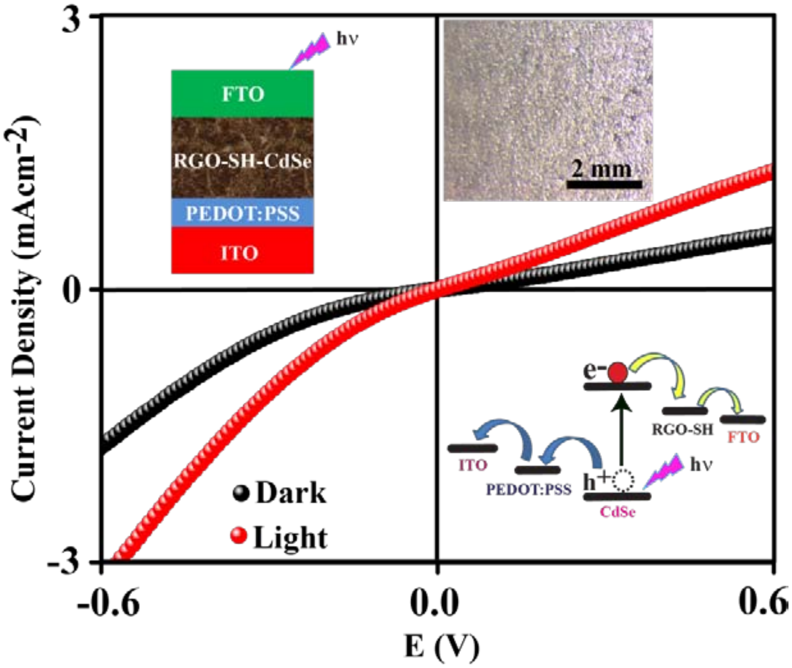

**Figure 4.14.** Room temperature Photoconductivity of device comprising of CdSe (3.0 nm)-RGO-SH hybrid on FTO coated glass; The device structure and the band alignments (not to scale) of the individual component are shown in the inset; the inset optical image corresponds to the spray coated film of RGO-SH-CdSe on FTO coated glass plate; Device area is 0.56 $cm^{-2}$, Bias is applied to FTO with respect to ITO.

Thus from the above discussion, it is clear that anchoring of CdSe QDs chemically to conducting graphene surface not only provides a mean to homogeneously decorate the graphene, but gives a new type of hybrid material with promising applications also. Chemical bonding enhances the rate of charge transfer from excited CdSe QD to graphene as compared to the competing process of energy transfer. However, the mechanism of charge transfer *via* the molecular linker is still unclear and it requires additional sophisticated tools to explore the same. Moreover, there is always the probability of restacking due to the tendency of H-bonding among –SH groups of one RGO sheet with that of the other, which can be alleviated by proper sonication procedures.

## 4.5. Conclusion

This chapter deals with the synthesis of a unique CdSe-graphene hetero structure revealing synergistic optical properties by employing a novel methodology of functionalizing chemically converted graphene using diazonium salt of 4-aminothiophenol. Robust CdSe QD decoration has been achieved by a simple solution exchange procedure, which has a remarkable potential to control both the size of the QD on RGO as well as the graphene quality. Structural changes due to attachment have been elucidated by Raman and XPS studies while steady state and time resolved spectroscopic data have been used to understand the electronic interaction between QD and graphene sheets. It is demonstrated that the efficient electron transfer process occurs from photoexcited QD to graphene with electron transfer rates as $4.38\text{x}10^8$, $12.80\text{x}10^8$ and $7.42\text{x}10^8$ $s^{-1}$ for the 3.03, 3.8 and 4.7 nm CdSe QDs, respectively. A prototype device shows 2-3 fold increase in photocurrent in graphene-QD composite under visible light which suggests a strong potential for solar cell and optoelectronic applications. Thiol terminated graphene can also be used for 3-D hetero structure (CdSe-Graphene) formation using a layer-by-layer strategy, especially for photosensitive device. This type of novel hybrid device configuration is expected to perform well also as next generation sensitized solar cells, solar water electrolyzers and photodetectors especially since the presence of graphene can provide much sought-after flexibility (stretchable electronic devices).

## 4.6. References

1. (a) Novoselov, K. S.; Jiang, Z.; Zhang, Y.; Morozov, S. V.; Stormer, H. L.; Zeitler, U.; Maan, J. C.; Boebinger, G. S.; Kim, P.; Geim, A. K. *Science* **2007**, *315*, 1379. (b) Haddon, R. C. *Acc. Chem. Res.* **2013**, *46*, 2191.
2. (a) Rao, C. N. R.; Sood, A. K.; Voggu, R.; Subrahmanyam, K. S. *J. Phys. Chem. Lett.* **2010**, *1*, 572. (b) Novoselov, K. S.; Geim, A. K.; Morozov, S.V.; Jiang, D.; Katsnelson, M. I.; Grigorieva, I. V.; Dubonos, S.V.; Firsov, A. A. *Nature* **2005**, *438*, 197.
3. Lee, C.; Wei, X.; Kysar, J. W.; Hone, J. *Science* **2008**, *321*, 385.
4. Mak, K. F.; Sfeir, M. Y.; Wu, Y.; Lui, C. H.; Misewich, J. A.; Heinz, T. F. *Phys. Rev. Lett.* **2008**, *101*, 196405/1_4.
5. Xia, F. N.; Mueller, T.; Lin, Y. M.; Garcia, A. V.; Avouris, P. *Nat. Nanotech.* **2009**, *4*, 839.
6. Schedin, F.; Geim, A. K.; Morozov, S. V.; Hill, E. W.; Blake, P.; Katsnelson, M. I.; Novoselov, K. S. *Nature Materials* **2007**, *6*, 652.
7. (a) Ghosh, S.; Calizo, I.; Teweldebrhan, D.; Pokatilov, E. P.; Nika, D. L.; Balandin, A. A.; Bao, W.; Miao, F.; Lau, C. N. *App. Phys. Lett.* **2008,** 92,151911. (b) Ghosh, S.; Bao, W. Z.; Nika, D. L.; Subrina,S.; Pokatilov, E. P.; Lau, C. N.; Balandin, A. A. *Nature Materials* **2010**, *9*, 555.
8. Lin, Y. M.; Dimitrakopoulos, C.; Jenkins, K. A.; Farmer, D. B.; Chiu, H. Y.; Grill, A.; Avouris, P *Science* **2010**, *327*, 662.
9. Zhang, D. W.; Li, X. D.; Li, H. B.; Chen, S.; Sun, Z.; Yin, X. J.; Huang, S. M., *Carbon* **2011**, *49*, 5382.
10. Wang, X.; Zhi, L. J.; Mullen, K. *Nano Lett.* **2008**, *8*, 323.
11. Novoselov, K. S.; Geim, A. K.; Morozov, S. V.; Jiang, D.; Zhang, Y.; Dubonos, S. V.; Grigorieva, I. V.; Firsov, A. A. *Science* **2004**, *306*, 666.

12. Chen, J. H.; Jang, C.; Adam, S.; Fuhrer, M. S.; Williams, E. D.; Ishigami, M. *Nat. Phys.* **2008**, *4*, 377.

13. Brus, L. *J. Phys. Chem.* **1986**, *90*, 2555.
14. Nozik, A. *J. Chem. Phys. Let.* **2008**, *457~~(1)~~*, 3.

15. Shockley, W.; Queisser, H. J. *J. App. Phys.* **1961**, *32*, 510.

16. Robel, I., Kuno, M., Kamat, P. V. *J. Am. Chem. Soc.* **2007**, *129*, 4136.
17. Sun, S; Gao, L; Liu, Y; Sun, J. *Appl. Phys. Lett.* **2011**, *98*, 93112.

18. (a) Lin, Y.; Zhang, K.; Chen, W.; Liu, Y.; Geng, Z.; Zeng, J.; Pan, N.; Yan, L.; Wang, S.; Hou, J. G. *ACS Nano* **2010**, *6*, 3033. (b) Wang, Y.; Yao, H. B.; Wangand, X. H.; Yu, S. H. *J. Mater. Chem.* **2010**, *21*, 562. (c) Kim, Y. T.; Han, H. J.; Hong, B. H.; Kwon, Y. U. *Adv. Mater.* **2010**, *22*, 515. (d) Park, W. I.; Lee, C. H.; Lee, J. M.; Kim, N. J.; Yi, G. C. *Nanoscale* **2011**, *3*, 3522.
19. (a) Yan, J.; Ye, Q.; Wang, X.; Yu, B.; Zhou, F. *Nanoscale* **2012**, *4*, 2109. (b) Lin, Y.; Zhang, K.; Chen, W.; Liu, Y.; Geng, Z.; Zeng, J.; Hou, J. G. *ACS nano* **2010**, ***4***, 3033.(c) Li, Q., Guo, B., Yu, J., Ran, J., Zhang, B., Yan, H., & Gong, J. R., *J. Am. Chem. Soc.* **2011,** *133*, 10878.(d) Xiang, Q.; Yu, J.; Jaroniec, M. *Nanoscale*, **2011**, ***3***, 3670. (e) Wang, W.; Yu, J.; Xiang, Q.; Cheng, B. *App.Cat. B: Env.* **2012**, *119*, 109. (f) Xiang, Q.; Yu, J.; Jaroniec, M. *Chem. Soc. Rev.* **2012**, *41*, 782.
20. (a) Fang, M.; Wang, K.; Lu, H.; Yang, Y.; Nutt, S. *J. Mater. Chem.* **2009**, *19*, 7098. (b) Lomeda, J. R.; Doyle, C. D.; Kosynkin, D. V.; Hwang, W. F.; Tour, J. M. *J. Am. Chem. Soc.* **2008**, *130*, 16201.
21. Alazemi, M.; Dutta, I.; Wang, F.; Blunk, R. H.; Angelopoulos, A. P. *Carbon* **2010**, *48*, 4063.
22. Lightcap, I. V.; Kamat, P. V.*-J. Am. Chem. Soc.* **2012**, *134*, 7109.

23. Chen, Z.; Berciaud, S.; Nuckolls, C.; Heinz, T. F.; Brus, L. E. *ACS Nano* **2010**, *4*, 2964.

24. Bang, J. H.; Kamat, P. V. *ACS Nano* **2011**, 5, 9421.

25. Huang, Z.; Geyer, N.; Werner, P.; Boor, J. Gösele, U. *Adv. Mater.* **2011**, *23*, 285.

26. Hummers, W. S.; Offeman, R. E. *J. Am. Chem. Soc.* **1958**, *80*, 1339.
27. (a) Shirley, D. A. *Phys. Rev. B* **1972**, *5*, 4709. (b) Oberlin, A.; Endo. M.; Koyama, T. *J. Crystal. Growth* **1976**, *32*, 335.
28. Kubin, R. F.; Fletcher, A. N. *J. Lumin.* **1982**, *27*, 455.
29. Lakowicz, J. R. *Principles of Fluorescence Spectroscopy*, 3rd ed.; Kluwer Academic/Plenum Publishers: New York, **1999**, 496.
30. Mandal, S.; Bhattacharyya, S.; Borovkov. V.; Patra, A.; *J. Phys. Chem. C* **2012**, *116*, 11401.
31. (a) Sharma, J.; Chaki, N. K.; Mahima, S.; Gonnade, R. G.; Mulla, I. S.; Vijayamohanan, K. *J. Mater. Chem.* **2004**,14, 970. (b) Silverstein, R. M.; Webster, F. X.; Kiemle, D. J., *Spectrometric Identification of Organic Compounds*, 7th Ed., John Wiley & Sons.
32. Katari, J. B.; Colvin. V. L.; Alivisatos, A. P. *J. Phys.Chem.* **1994**, *98*, 4109.
33. Choudhury, D.; Das, B.; Sarma, D. D.; Rao, C. N. R. *Chem.Phys.Let.* **2010**, *497*, 66.
34. Laibinis, E. Paul; Whitesides, G. M. *J.Am.Chem. Soc.*, **1992**, *114*, 1990.
35. Bandyopadhyay, K.; Mayya, K. S.; Vijayamohanan K.; Sastry, M.; *J. Electron Spec. and Rel. Phen.* **1997**, *87*, 101.
36. Patil, V.; Sastry, M.; *Langmuir* **1998**, *14*, 2707.
37. Labib, M. E.; Thomas, J. H.; Embert, D. D. *Carbon* **1984**, *22*, 445.
38. (a) Bao, L.; Sun, L.; Zhang, Z. L.; Jiang, P.; Wise, F. W.; Abruña, H. D.; Pang, D. W. *J. Phys. Chem. C* **2011**, ***115***, 18822. (b) Ramesha, G. K.; Sampath, S. *J. Phys. Chem. C* **2009**, *113*, 7985.
39. (a) Fowkes, F. M.; *J. Phys. Chem.* **1980**, *84*, 510. (b) Debgupta, J.; Kakade, B. A.; Pillai, V. K. *Phys. Chem. Chem. Phys.***2011**, *13*, 14668.
40. Casiraghi, C.; Robertson, J.; Ferrari, A. C.; *Materials Today* **2007**, *10*, 44.
41. Reimann, S.M.; Manninen, M. *Rev. Mod. Phys.* **2002**, *74*, 1283.
42. Sapra, S.; Shanthi, N.; Sarma, D. D. *Phys. Rev. B* **2002**, *66*, 205202.
43. Chaban, V. V.; Prezhdo, V. V.; Prezhdo, V. O. *J. Phys. Chem. Lett.* **2013**, *4*, 1.

44. Sarkar, P.; Sarkar, S.; Saha S.; Pal, S. *J. Phys. Chem. C.* **2012**, *116*, 21601.
45. Inamdar, S.N.; Ingole, P.P.; Haram, S.K. *Chem. Phys. Chem.* **2008**, *9*, 2574.
46. Kundu, S.; Sadhu, S.; Bera, R.; Pramanik, B.; Patra, A. *J. Phys. Chem. C* **2013**, *117*, 23987.

# CHAPTER 5

# Vertically Aligned CdSe Nanotubes and Their Applications in p-n Hetero-junction Diodes

This chapter describes the growth and characterization of vertically aligned, hollow nanotubes of CdSe on fluorine doped tin oxide (FTO) coated glass substrates. For this, first aligned ZnO nanowires have been grown as a template on FTO by a hydrothermal method before electrodeposition of CdSe followed by selective removal of ZnO core using $NH_4OH$.Detailed mechanisms of nucleation and anisotropic growth kinetics during electrode position have been studied by a combination of tools such as Chronoamperometry, SEM and TEM. Interestingly, “as grown” CdSe nanotubes (CdSe NTs) on Fluorine doped tin oxide (FTO) coated glass behave as n-type semiconductors exhibiting excellent photo-response. A prototype diode fabricated using CdSe NTs in contact with p-type $Cu_2O$ (grown separately on another FTO plate) generates a photocurrent density as high as 470 $\mu Acm^{-2}$ perhaps due to the formation of n-p heterojunction (type II). This photo-current is three times higher than that of similar devices prepared with electrodeposited CdSe film and $Cu_2O$ on FTO. This has been attributed to the hollow 1-D nature of CdSe NTs, which provides enhanced inner and outer surface area for better absorption of light and also for higher mobility which assists facile transport of photogenerated charge carriers.

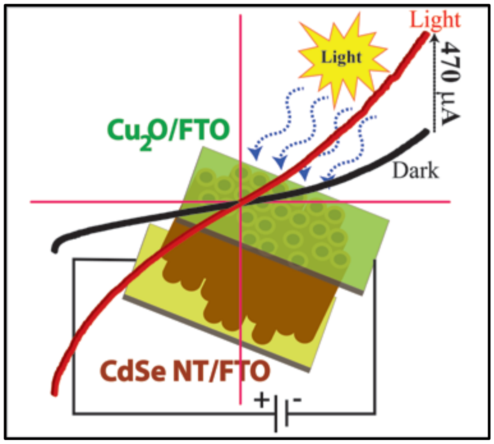

---

*A part of the work discussed here has been published in *Nanoscale (2014)*

## 5.1. Introduction

One dimensional (1D) nanostructures have attracted a great deal of interest recently due to their unique size and shape dependent optical and electronic properties.[1] For example, ballistic transport,[2] density of state singularities, spin-charge separation (Luttinger liquid)[3-5] are some of the notable unusual properties of such nanostructures. The remarkable discovery of carbon nanotubes (CNTs) [6] has caused a paradigm shift in the field of 1-D nanostructures because of their high surface-to-volume ratio as well as high conductivity, flexibility and tuneable electronic structure which allow chemical modifications for specific applications. In this respect, semiconducting nanotubes are more interesting because of a perfect blend of properties like tuneable band gap, stability and process control by surface functionalization as well as the intrinsic advantage of tubular morphology. This makes them promising candidates for certain applications such as solar cells, catalysts, gas sensors and photo-detectors. [7-8] However, the properties and applications of semiconducting nanotubes depend strongly on the synthetic methods employed as this decides the aspect ratio. Solution chemical synthesis, for example, can produce nanotubes with uniform size and shape, but further processing is difficult and often challenging from the application perspective. It also requires the use of many costly and toxic solvents. On the other hand, gas phase techniques employ high temperature and sophisticated instrumentations to precisely control the structure and morphology of the resultant materials. Moreover, the yield of materials is generally less in both the cases and a slight variation in synthetic condition brings about appreciable changes in the end product specifications. Compared to all these, electrochemical deposition is rather a simple, and cost effective technique which can be used to make large-area cells and more significantly, the morphology and thickness can be precisely controlled by fine-tuning the deposition potential. Although CdSe nanotubes (CdSe NTs) have been synthesized so far by various methods such as hot injection synthesis, [9] sono-electrochemical synthesis [10] or hydrothermal method,[11] only very few reports are available on electrochemical synthesis. For example, template assisted electrochemical preparation of vertically aligned CdSe NTs is reported by Zhou *et al*. [12] Similarly, a more recent work describes a method to grow template-free 1-D CdSe nanowires through electrodeposition on FTO coated glass substrate. [13] The sparse use of electrodeposition for the preparation of 1-D nanostructure of CdSe can be justified by considering the crystal structure of CdSe and growth kinetics of its planes. The three fastest growing directions of CdSe , namely <0001>, $\langle 01\bar{1}0\rangle$, $\langle 2\bar{1}\bar{1}0\rangle$ and ±(0001) are polar surfaces and CdSe grows relatively faster along these directions under the applied potential tending to form particles on conducting substrates rather than on the 1-D structure during template-free electrodeposition.[13] The latter process of making CdSe NTs is, thus, a better choice and more significantly the electrodeposition process can be carried out at room temperature to get more stable phases compared to many phases obtained by the template less process (95°C, DMF solvent).[13] ZnO core can be easily removed with $NH_4OH$ giving hollow CdSe NTs.[12] Unfortunately, despite being an important material with promising optoelectronic applications, these CdSe NTs have not been further explored for practical optoelectronic applications. Moreover, no further attempt has been made to understand the electrochemistry of deposition process, as well as the mechanism of nucleation during deposition.

The preceding chapters have shown many interesting features of CdSe QDs such as low band-gap (1.7 eV for bulk CdSe), high absorption cross section of visible light ($C_{abs} = 5.501 \times 10^5 a^3$ $cm^{-1}$ for absorption at 350 nm, where $a$ is the particle radius in cm)[14] and its tuneable and unmatched optical properties with size and shape.[15-16] The interesting electronic, electric and optical properties of CdSe QDs and their hybrids with various carbon nanostructures have also been discussed. More specifically, the previous chapter (chapter 4) has shown selective decoration of CdSe QDs on graphene through molecular linkers and its effect on the rate of charge transfer from excited CdSe to graphene. Possible applications of those hybrid nanostructures have also been shown. However, the importance of 1D nanostructure of CdSe and its applications have not been discussed. In this chapter, we address these concerns after a cursory description of the synthesis and characterization of nanotubes of CdSe grown vertically on FTO coated glass substrate via ZnO nanowires template by electrodeposition at room temperature and at nearly neutral pH (pH 7.5). Cadmium acetate ($Cd(OAc)_2$), nitrilotriacetic acid (NTA) and sodium selenite ($Na_2SeO_3$) have been employed for electrodeposition due to their well known roles.[17a] A detailed analysis of nucleation has been carried out by electrochemical methods and the NTs have been further characterized by SEM, TEM, AFM, Raman, UV-

VIS and Photoluminescence (PL). An n-p heterojunction diode has been fabricated by combining the CdSe NTs (on FTO glass) with electrodeposited $Cu_2O$ (on separate FTO glass) with a favourable band alignment (type II) with CdSe energy bands. This device configuration (n-CdSe/p-$Cu_2O$ heterojunction) in presence of AM 1.5 solar simulated light (100 $mWcm^{-2}$) interestingly shows ~470 $\mu A/cm^2$ current density enhancement upon illumination. This photo-response is indeed considerably larger (~3 times) than that of analogous measurements with electrodeposited CdSe nanoparticles without ZnO templates indicating its promise for improvement.

## 5.2. Experimental Section

### 5.3.1. Materials

Cadmium acetate dihydrate [$Cd(OAc)_2.2H_2O$] (98%), Sodium selenite [$Na_2SeO_3$] (99%) Nitrilotriacetic acid [NTA] (99%) and ammonium hydroxide ($NH_4OH$) were purchased from Thomas Baker (AR grade). Sodium hydroxide [NaOH] was procured from Rankem. Zinc nitrate hexahydrate [$Zn(NO_3)_2 \cdot 6H_2O$], hexamine and polyethylenimine ($M_w$: 800) were obtained from Aldrich and used as received. Cupric sulphate pentahydrate [$CuSO_4.$ $5H_2O$] (99.5%) and lactic acid (99%) were purchased from Rankem and Aldrich respectively. MilliQ water (deionized water, 18 MΩ resistance) was used for the preparation of all solutions.

### 5.3.2. Preparation of ZnO nanoparticles (seed solution) in Ethanol

ZnO seeds (~50 nm size) were prepared as follows,

Solution A: 6.38 mg NaOH (0.16mmol) was dissolved in 28 mL ethanol by constant stirring and sonication.

Solution B: 22.12 mg of $Zn(OAc)_2.2H_2O$ (0.1 mmol) was dissolved in 40 mL ethanol.

Solution A was subsequently added drop-wise into solution B with vigorous stirring till solution B changed from transparent to slightly whitish.

### 5.3.3. Preparation of vertically aligned ZnO nanowires (ZnO NWs) on FTO coated glass substrate

ZnO NW arrays were synthesized on FTO coated glass (7 $\Omega cm^{-2}$ sheet resistance), initially cleaned by sonication in acetone, 2-propanol, and methanol and subsequently rinsed with water, and finally dried in a nitrogen stream. The FTO coated glass plates were coated with the ZnO seed particles by drop-casting followed by annealing at 300°C for 20 min in air. In order to grow vertically aligned ZnO nanorods the ZnO seed particles coated FTO glass plates were kept in a glass vial containing the solution comprising of 25 mM $Zn(NO_3)_2$, 12.5 mM hexamine, 2 mM polyethylenimine ($M_w$: 800) and 0.35 M $NH_4OH$ at 90°C for 3 h. The resulting nanowire arrays were rinsed with water and sintered at 450°C in an inert atmosphere for 30 min in order to increase crystallinity.

### 5.3.4. Electrodeposition of CdSe on ZnO NWs and CdSe Nanotube formation

CdSe was electrodeposited on the FTO coated glass substrate containing ZnO NWs from an aqueous solution containing 10 mM $Cd(OAc)_2$, 5 mM $Na_2SeO_3$ and 50 mM NTA. The pH of the solution was adjusted to 7.5 with a drop-wise addition of saturated aq. NaOH solution so that the overall volume does not change. A three electrode system was used for electrodeposition with FTO coated glass containing ZnO NWs as the working electrode, Hg/HgO (0.1 M KOH) and a platinum foil as reference and counter electrodes respectively. A constant potential of -1.2 V (*vs* Hg/HgO) was applied for 15 min on the working electrode for electrodeposition to get a good quality film of desired thickness. After electrodeposition, the ZnO NWs were selectively removed by dipping them in 25% $NH_4OH$ solution for 1 h. Subsequently, the FTO coated glass plate containing CdSe nanotubes (CdSe NTs) was annealed at 300°C for 30 min in $N_2$ atmosphere to increase the crystallinity. For controlled experiments, CdSe was electrodeposited on FTO coated glass plate under identical conditions.

### 5.3.5. Electrodeposition of Cuprous Oxide ($Cu_2O$) on FTO coated glass:

$Cu_2O$ nanoparticles were electrodeposited on FTO coated glass from a mixture of 20 mM $CuSO_4$ and 1 M lactic acid aq. solution.[17b] The pH of the solution was adjusted to 9 by the drop-wise addition of saturated NaOH solution. A similar set up (except the working electrode which is clean FTO coated glass plate) was used for $Cu_2O$ deposition using a constant potential of -0.55 V (*vs* Hg/HgO) for 2 min. The deposit was subsequently annealed at 150°C in an inert atmosphere. The overall process of CdSe NT formation is shown in fig. 5.1.

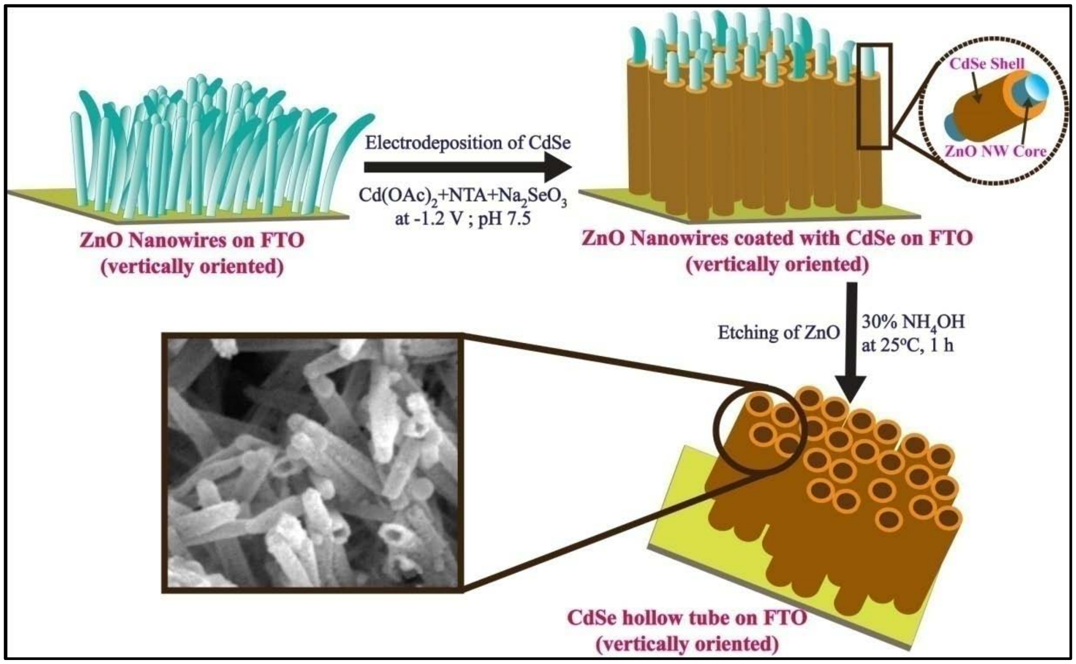

**Figure 5.1.** Controlled electrochemical synthesis of vertically aligned, CdSe NTs on FTO-glass by ZnO NWs as template and subsequent ZnO core dissolution with ammonium hydroxide.

**Table-5.1.** Experimental parameters for the electrodeposition of CdSe and $Cu_2O$

| **Material** | **Substrate** | **Source of Cd/Cu** | **Source of Se/O** | **pH** | **Temperature (K)** | **Potential** |
|---|---|---|---|---|---|---|
| CdSe | FTO coated glass | $Cd(OAc)_2$. $2H_2O$(as NTA complex) | $Na_2SeO_3$ | 7.5 | 303 | -1.2 V (*vs* Hg/HgO) |
| $Cu_2O$ | FTO coated glass | $CuSO_4.5H_2O$ | Alkaline $H_2O$ | 9 | 303 | -0.55 V (*vs* Hg/HgO) |

## 5.3. Results and Discussion

### 5.3.1. Cyclic Voltammetry

Cyclic voltammetry is a versatile method to understand various steps of electrodeposition and also to find out optimum conditions like suitable potential, concentration, nature and quantity of additives. Accordingly, cyclic voltammograms have been recorded in a solution of 10 mM $Cd(OAc)_2$, 5 mM $Na_2SeO_3$ and 50 mM NTA before electrodeposition. Plausible reactions for CdSe formation can be summarized as follows,

$SeO_3^{2-} + 3H_2O + 4e^- = Se^0 + 6OH^-, E^0 = -0.36\,V vs\,NHE$.................................. (1)

$Se^0 + 2e^- = Se^{2-}, E^0 = -0.92\,V\,vs\,NHE$......................................................... (2)

$Cd^{2+} + Se^{2-} = CdSe \downarrow$............................................................................ (3)

Total cell reaction thus is,

$$SeO_3^{2-} + \mathrm{Cd}^{2+} + 3H_2O + 6e^- = CdSe \downarrow + 6OH^-$$

These reactions are similar to that reported previously for CdTe deposition.[19]But the problem associated with the use of $Na_2SeO_3$ as a source of Se is that the standard redox potential ($E^o_{\mathrm{SeO}_3^{2-}/\mathrm{Se}^{2-}}$= -0.92 V)[20] for reducing $SeO_3^{2-}$ into $Se^{2-}$ is more than the standard redox potential for $Cd^{2+}$ ($E^o_{\mathrm{Cd}^{2+}/\mathrm{Cd}}$= -0.40 V).[21] Hence, at the potential where $Se^{2-}$ is generated, a significant amount of elemental Cd gets deposited along with the formation of CdSe. This competing reaction, therefore, changes the composition of the electrodeposited CdSe and results in poor quality of the resulting material. One way to overcome this problem is to shift the formal reduction potential of $Cd^{2+}$, by means of complexation, [21] to such an extent that it cannot get reduced within the potential window employed for the electro generation of $Se^{2-}$. Nitrilotriacetic acid (NTA, an aminopolycarboxylic acid ($[N(CH_2CO_2H)_3]$)) is employed for this purpose. NTA forms a stable chelate (pK = 9.78) with $Cd^{2+}$ion[22] and its formal potential is, therefore, shifted significantly far negative so that $Cd^{2+}$ does not get reduced prior to the reduction of $SeO_3^{2-}$. Eventually, the electrogenerated $Se^{2-}$ combines with the chelated $Cd^{2+}$ to form CdSe which then gets deposited on the substrate (FTO coated glass or ZnO NWs grown on FTO coated glass). The above mechanism seems to be especially valid when we consider all the features of the cyclic voltammograms (CVs) in fig. 5.2. Accordingly, fig. 5.2(a) shows a typical voltammogram in a solution of $Cd(OAc)_2$ and NTA with FTO coated glass as the working electrode. The voltammogram shows mostly capacitive current and interestingly, no diffusion limited peak is clearly observed. The situation is, however, different in the case of $Na_2SeO_3$ as evident from fig. 5.2(b). In contrast, this voltammogram shows two clear reduction peaks (C1 and C2) with formal potentials -0.71 V and -1.16 V respectively as well as one oxidation peak A1 (with formal potential -0.89 V when FTO is used as the working electrode. C1 and C2 peaks are attributed to the successive reduction of $SeO_3^{2-}$ to $Se^0$ and $Se^{2-}$ according to equations 1 and 2 respectively. Similar reduction peaks are also seen in the voltammogram of a mixture containing $Cd(OAc)_2$, $Na_2SeO_3$ and NTA. The absence of similar reduction peaks in case of Cd-NTA complex and the presence of the same in the mixture of Cd-NTA and $Na_2SeO_3$ clearly show that $SeO_3^{2-}$ reduction takes place first with the formation of $Se^{2-}$ which is subsequently consumed for CdSe formation. Similar peaks are observed when ZnO NW coated FTO plates are used instead of normal FTO plates. This suggests that similar mechanism is operative in case of ZnO NWs coated electrodes in comparison to that on FTO electrode.

In this deposition process, pH plays a crucial role and accordingly, we have found pH 7.5 to be optimum for a smooth deposition. Interestingly, either above or below this pH, no deposition occurs and instead, ZnO NWs dissolve out. This might be due to the fact that the point of zero charge (PZC)/isoelectric point of ZnO is 7.5 to 9.8.[23] This might also be explained due to the pH sensitivity of the $SeO_3^{2-}$ reduction in alkaline medium where $OH^-$ is generated during the reduction to selenium (equation 1). Although temperature has also a profound effect on the rate of deposition, we have carried out all the deposition only at room temperature (303 K) for brevity. CdSe deposition has also been observed below -1.2 V (upto -0.96 V *vs* Hg/HgO, i.e., the onset of the second reduction peak C2 in the voltammogram) although the rate and quality of deposition is poor than that observed at -1.2 V. With an increase in deposition time, the outer diameter of CdSe NTs increases significantly as has been reported previously, [15] despite no enhancement of length.

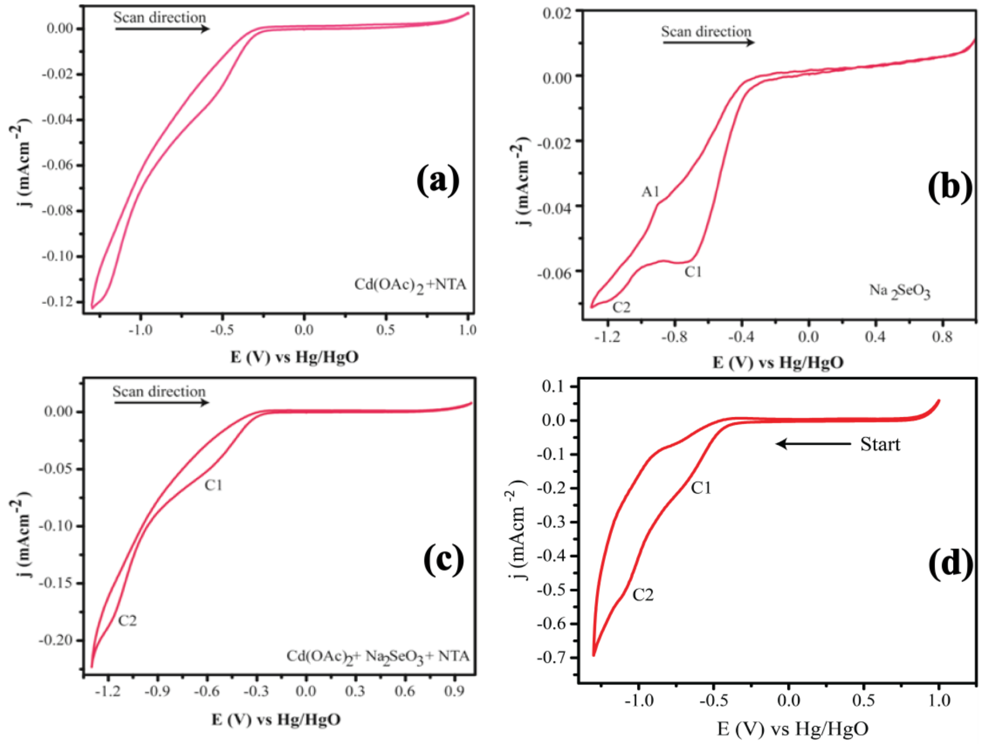

**Figure 5.2.** A comparison of Cyclic voltammograms of solutions containing (a) 10 mM $Cd(OAc)_2$ and 50 mM Nitrilotriacetic acid (NTA), (b) only 5 mM $Na_2SeO_3$ with no NTA, (c) 10 mM $Cd(OAc)_2$, 5 mM NTA and 50 mM $Na_2SeO_3$ and (d) same as (c) but using ZnO NWs grown FTO coated glass plate as working electrode; FTO coated glass plate is used as a working electrode in all cases from (a) to (c) except for (d) where ZnO NWs grown on FTO coated glass is the working electrode; Hg/HgO (0.1 M KOH) is used as reference and a platinum foil is used as counter electrode. Saturated NaOH is added to maintain the pH value of 7.5 in all cases and all measurements were done at 303 K.

### 5.3.2. Chronoamperometry

Chronoamperometry, i.e. study of current as a function of time at a constant potential, is an important electrochemical technique, which gives valuable information about the electrochemical process like electrodeposition, dissolution and other redox processes occurring at the electrode surface. In the present study, this technique has been employed to understand the mechanism of nucleation at the initial stage of deposition. Accordingly, fig.5.3 shows representative chronoamperograms taken during the electrodeposition of CdSe on plain FTO coated glass plate and also on ZnO NWs grown FTO coated glass plates. Both the chronoamperograms show similar features, i.e., initial sharp increase in current followed by a maximum current region at very short time scale (<50 s) and then the maximum current decreases to a steady state at higher time scale (>50 s). However, the current density obtained in case of plain FTO coated glass plates is even with respect to time (i.e., does not show ups and downs with time), whereas the current density for the deposition on ZnO NWs shows small asperities as time progresses. These asperities may originate due to roughness of ZnO NWs as compared to that on much less rough FTO coated glass plates. This fact is reflected also in the total charge (Q, blue line) passed during electrodeposition. Initial increase in current in the chronoamperograms is due to nucleation, i.e., formation of nuclei on the substrate used on the application of potential (the increment can be due to both the increase in total number of nuclei as well as the growth of the initially formed nuclei). These nuclei then grow and ultimately coalesce and form a continuous film on the substrate as has been predicted by the Volmer-Weber growth model (because strong cohesive force between the nuclei surpasses the nuclei-substrate adhesive interaction).[24] Coalescence of nuclei is reflected as a peak in the chronoamperograms. After the maximum, the current density decreases to a steady state value because of linear diffusion-limited growth and a planar film is formed, the roughness of which does not change with time.[25,26] Thus Chronoamperometry is useful in studying nucleation process during electrodeposition.

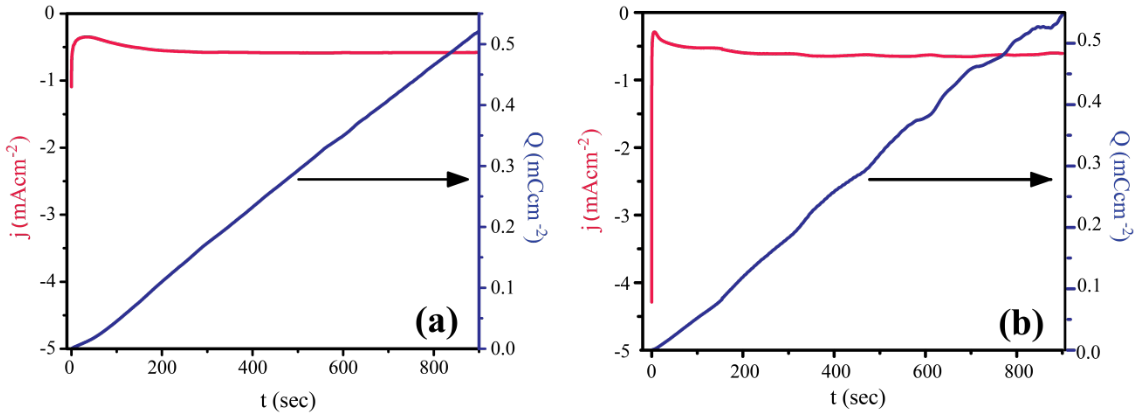

**Figure 5.3.** Chronoamperogram (pink line) during CdSe electrodeposition on (a) a plain FTO coated glass and (b) ZnO NW coated glass substrate; Blue line indicates total charge passed during electrodeposition; Chronoamperometry experiments were carried out with the same set-up used for cyclic voltammetry and the potential of the working electrode (FTO or ZnO NWs grown FTO coated glass plates) was held constant at -1.2 V *vs* Hg/HgO electrode for 15 min at (303 K).

According to the classical theory of nucleation, two fundamental categories of nucleation processes can occur. [27] One of them is known as Instantaneous nucleation where all the nuclei are formed at the same time upon the application of potential followed by their collective subsequent growth.[27] The other category is the progressive nucleation in which nuclei are formed one after another, (i.e., progressive formation of nuclei). Scharifker and Hills proposed a quantitative treatment for this three-dimensional multiple nucleation with diffusion controlled growth. [28] According to their treatment, the nuclei are thought of hemispherical in shape and those nuclei grow in size due to spherical diffusion at short time scale, but at higher time the diffusion field of individual nucleus merge together and finally growth occurs due to linear diffusion. Fig. 5.4 shows schematically the diffusion field around each nucleus.

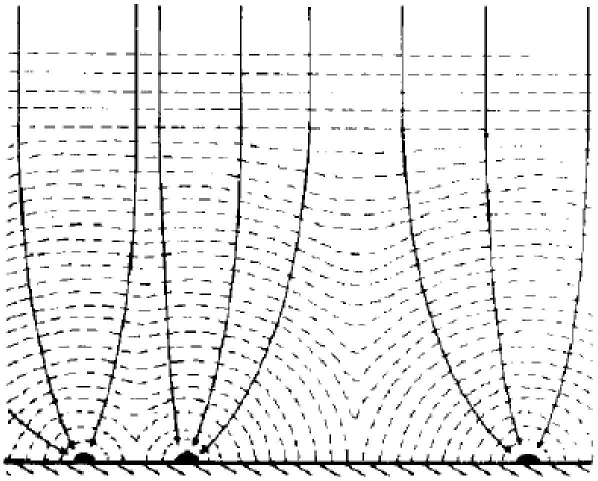

**Figure 5.4.** Schematic representation of the diffusion zones of individual nuclei and their eventual merging at higher time scale. [28]

They proposed two equations to describe the current transients obtained for the two different modes of nucleation as follows:

$$(\frac{i}{i_m})^2 = \frac{1.9542}{\frac{t}{t_m}}\{1 - \exp[-1.2564\left(\frac{t}{t_m}\right)]\}^2 \text{.........................................................} (3)$$

$$(\frac{i}{i_m})^2 = \frac{1.2254}{\frac{t}{t_m}}\{1 - \exp\left[-2.3367(\frac{t}{t_m})^2\right]\}^2 \dots\dots\dots\dots\dots\dots\dots\dots\dots\dots\dots\dots\dots\dots\dots.. (4)$$

where, *i* is the observed current, *i*$_{m,}$ the maximum current in the current-time transient (chronoamperogram), and $t_m$ corresponds to the time for the maximum current.

Equation 3 describes the case of instantaneous nucleation whereas; equation 4 is for progressive nucleation. These two equations are often regarded as diagnostic criteria for the two different types of nucleation. A general observation for potentiostatic current-time transient during electrodeposition is that the current maximum shifts towards lower time as the applied potential becomes more and more negative. This also happens in the present case as has been observed in fig. 5.5(a).

In order to understand the type of nucleation mechanism during the electrodeposition of CdSe on ZnO NWs grown on FTO coated glass plate, the current-time transients (chronoamperogram) can be further subdivided into three distinct regions (fig. 5.5(b)):

Region-I: Very short time region where the current is inversely proportional to the square root of time [fig. 5.5(d)]and thus indicates that the process is under diffusion controlled. Such a dependency is in accordance with the Cottrell behaviour and is indicative of instantaneous nucleation where all the nuclei form at the same time. [28]

Region-II: Intermediate time region where the current reaches its maximum value and then decays according to the Cottrell relation. So formed nuclei in region-I, start to coalesce near to the peak maximum and at the peak maximum all the nuclei merge together to form a continuous film.

Region-III: This is the region where there is continuous film growth governed by the linear diffusion.

To further confirm the mode of nucleation, dimensionless current-time plot ($i^2/i_m^2$ vs $t/t_m$) has been constructed according to the equations 3 and 4. Fig. 5.5(c) is a comparison of the dimensionless current-time plots obtained from the experimental data to the plots obtained from equation 3 and 4. In the present case the normalized current-time relationship follows the behaviour known for instantaneous nucleation mechanism. It is clearly observed that in the short-time region the kinetics of nucleation follows the instantaneous pathway rather than the progressive one although it deviates when $t$ is increasingly greater than $t_m$.

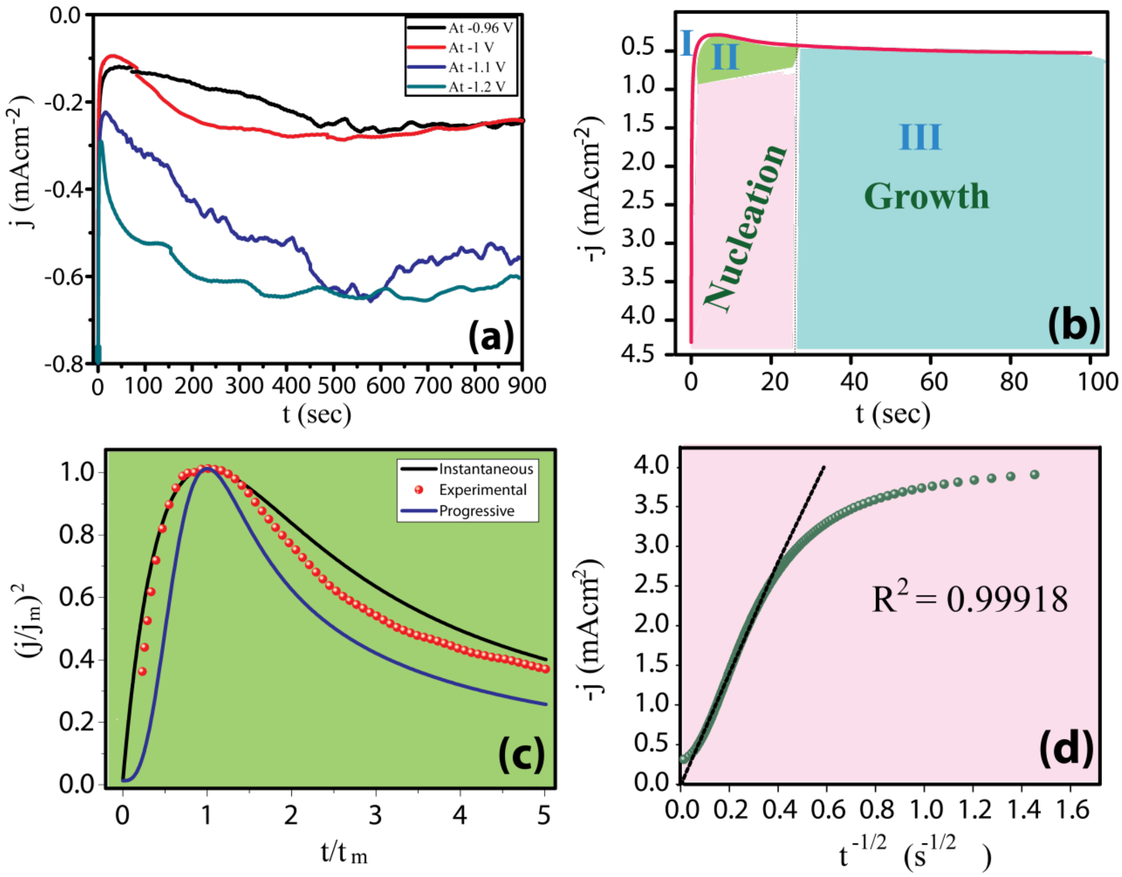

**Figure 5.4.** (a) Current density-time transients (chronoamperograms) at various potentials for the electrodeposition of CdSe on ZnO NWs grown FTO coated glass plates; Maximum current occurs at lesser time as the potential becomes more negative; (b) Current density-time profile for electrodeposition at -1.2 V *vs* Hg/HgO; Nucleation and growth zones are highlighted with different colors; (c) Dimensionless $(j/j_m)^2$ *vs* $t/t_m$ plot for the data in (b); Red dots are the experimental points and solid lines are obtained from eqn.3 and 4; (d) Current density *vs* $t^{-1/2}$ plot obtained from very short time regime (4-5 s); Linear behavior of $j$ with the inverse of square root of t proves the Cottrell type diffusion and thereby proves instantaneous nucleation.

### 5.3.3. Scanning Electron Microscopy (SEM) and EDAX

Scanning electron micrographs of ZnO NWs as well as CdSe NTs on FTO coated glass plates are shown in fig. 5.5(a) and 5.5(b) respectively. All ZnO NWs are ~2.5 µm long having ~170-200 nm diameter and reveal nearly vertical alignment with respect to the substrate (FTO coated glass) plane and the approximate density of the as-grown nanowires is ~3 x $10^9$ $cm^{-2}$. However, after CdSe deposition, the diameter of each NW increases and more significantly, the surface becomes rough (fig. 5.5(c) and 5.5(d)) indicating the successful deposition on the walls of ZnO NWs. In comparison, after

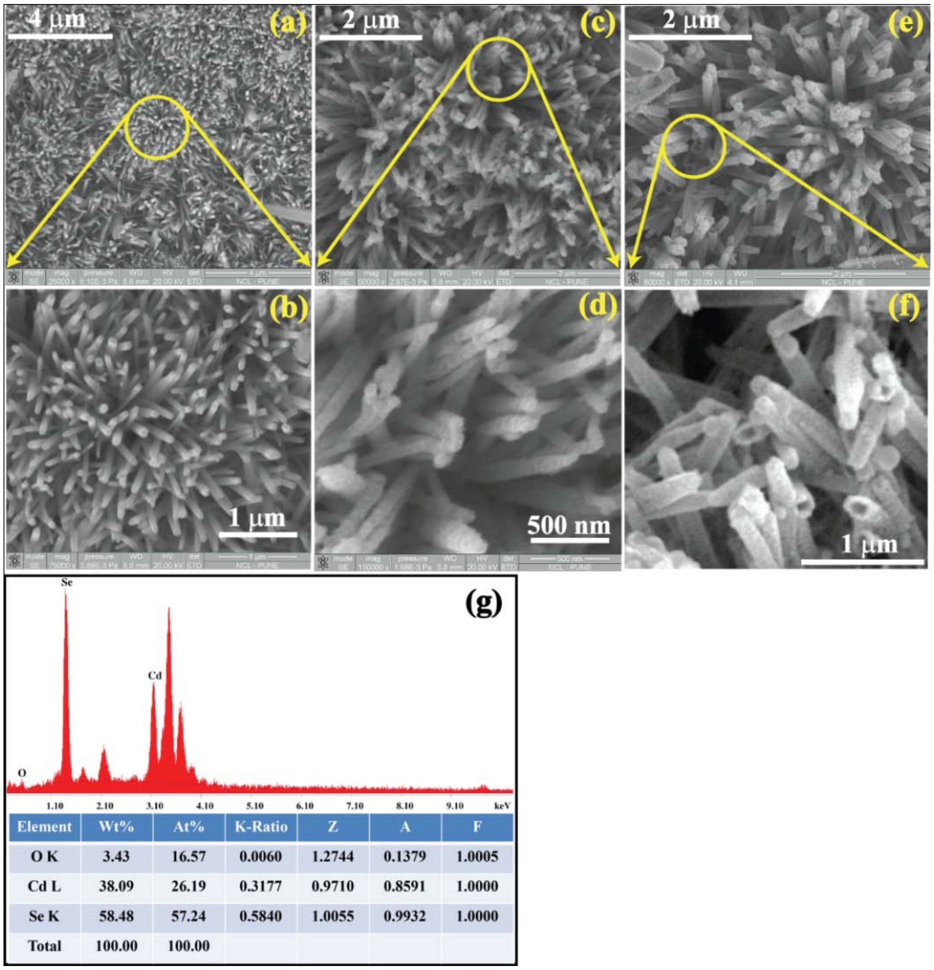

| Element | Wt% | At% | K-Ratio | Z | A | F |
|---|---|---|---|---|---|---|
| O K | 3.43 | 16.57 | 0.0060 | 1.2744 | 0.1379 | 1.0005 |
| Cd L | 38.09 | 26.19 | 0.3177 | 0.9710 | 0.8591 | 1.0000 |
| Se K | 58.48 | 57.24 | 0.5840 | 1.0055 | 0.9932 | 1.0000 |
| Total | 100.00 | 100.00 | | | | |

**Figure 5.5.** A comparison of Scanning Electron Micrographs of (a) Top view of ZnO NWs; (b) ZnO NWs with enlarged portion; (c) ZnO NWs covered with electrodeposited CdSe (top view); (d) enlarged view of ZnO NWs covered with CdSe; (e) CdSe nanotubes (CdSe NTs) after leaching out the ZnO NW core (top view); (f) enlarged view of the CdSe nanotubes and (g) EDAX of CdSe NTs after leaching out ZnO NW core.

leaching the ZnO NW core with 25% $NH_4OH$ for 1 h, images clearly reveal the presence of CdSe hollow tubes as displayed in (fig. 5.5(e) and 5.5(f) respectively). These tubes reveal the same length as that of the ZnO NWs and EDAX analysis confirms the presence of only CdSe (1:1.5 ratio). More important is the conspicuous absence of ZnO thus ensuring perhaps the near-complete removal of ZnO core. A closer look at the tips of so formed CdSe NTs reveals their hexagonal morphology, which is similar to that seen in the case of ZnO NW tips. This observation thus implies that the growth of CdSe occurs along the walls of ZnO NWs and hence the morphology is retained even after the removal of template ZnO. The ZnO NWs look thicker and rougher after CdSe electrodeposition (fig. 4(d)) than that of the pristine NWs. Tip of CdSe NTs retains the hexagonal shape (170-200 nm diameter and 2.5 μm in length) of ZnO NW tip and thereby gives further evidence for nanowire templating. In order to further confirm the role of ZnO NWs as template, we have carried out deposition on plain FTO without having any ZnO NWs grown on it. Accordingly, fig. 5.6(c) and (d) show images of the electrodeposited CdSe on plain FTO coated glass substrate. It does not show any specific morphology and the thin film (~300 nm thick) consists of only particles of CdSe. Fig. 5.6(a) shows vertical cross section of CdSe nanotubes supported on FTO base coated on glass plate and fig. 5.6(b) is the enlarged view for the same. This clearly demonstrates the importance of ZnO NWs as template. Fig. 5.6(d) is the representative SEM image of electrodeposited $Cu_2O$ on FTO coated glass. The film appears to be uniform throughout the FTO coated glass surface with no characteristic morphology.

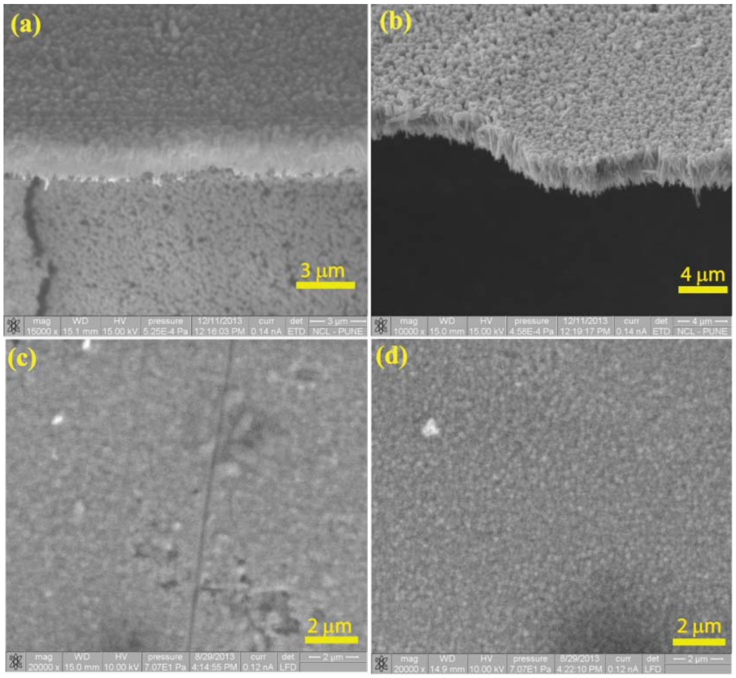

**Figure 5.6.** Scanning Electron micrographs of (a) CdSe NTs on FTO coated glass substrates showing vertical cross section where CdSe nanotubes are seen standing vertically on FTO coated glass; (b) enlarged view of the vertical cross section; (c) Thin film of electrodeposited CdSe on plain FTO coated glass without ZnO NW coating (top view) and (d) top view of electrodeposited $Cu_2O$ film on FTO coated glass plate; Uniform coating is observed throughout the substrate.

### 5.3.4. Transmission Electron Microscopy (TEM)

In order to get more insight into the microstructure, we have carried out TEM analysis of the CdSe NTs. Accordingly, fig. 5.7 depicts the high resolution TEM images of as grown ZnO NWs and annealed CdSe NTs.

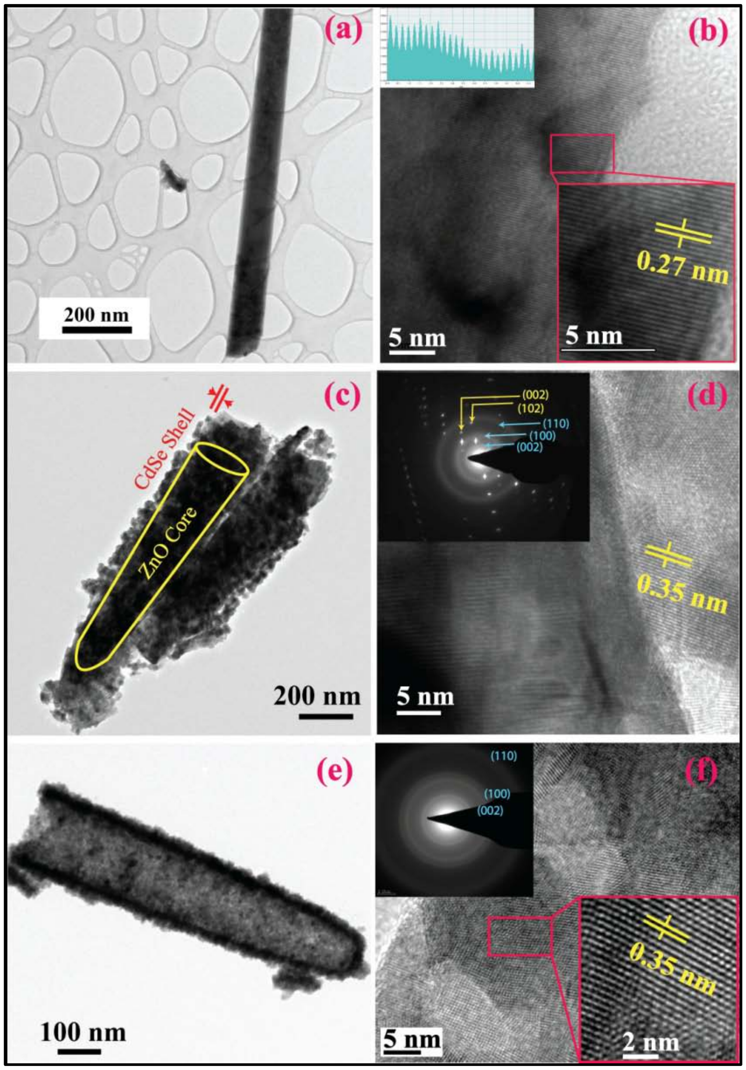

**Figure 5.7.** High resolution transmission electron micrographs of CdSe NTs grown vertically by electrochemical deposition using ZnO NW as template;(a) A single ZnO nanowire and (b) its high magnification image revealing its atomic planes (inset is the inverse FFT pattern); (c) ZnO NW core and CdSe shell (before leaching); (d) its high resolution image showing atomic planes of both CdSe and ZnO; inset shows selected area diffraction (SAED) pattern; (e) a single CdSe NT showing the absence of ZnO core and (f) high resolution CdSe NTs showing atomic planes; Selected area diffraction pattern (SAED) of the CdSe NT showing (002) and (110) planes to be exposed preferentially and

lattice planes with a d-spacing of 0.35 Å indicating primitive hexagonal crystal structure of the nanotubes.

The diameter of a single ZnO NWs is ~60-70 nm (fig. 5.7(a)), but the diameter is found to increase (~242 nm) after electrodeposition of CdSe on ZnO NWs as is clear from fig. 5.7(c). On the other hand, the diameter of CdSe shell does not change after the dissolution of ZnO NW core (fig. 5.7(e)). Moreover, a comparative study of high resolution images of ZnO NW, CdSe deposited ZnO NWs and CdSe NTs (fig. 5.7(b), 5.7(d) and (f) respectively) reveals the presence of CdSe shell on ZnO core, mainly because the lattice fringe patterns are different in three different cases. Indexing of the diffraction spots for ZnO reveals (002) and (102) planes are mostly exposed. For example, in fig. 5.7(b), the outer wall of the nanowires shows a characteristic d-spacing of 2.7 Å for ZnO, whereas fig. 5.7(d) shows two different types of d-spacing values-the outer portion (edge) mainly comprises of CdSe (3.5 Å) while the centre region has two types of lattice fringes due to the presence of both CdSe and ZnO. Thus TEM analysis proves the critical role of ZnO NWs as template for the growth of hollow CdSe NTs. As can be seen from fig. 5.7(e) and 5.7(f), the surface of each CdSe NT is granular and consists of CdSe nanoparticles of size 8-10 nm (fig. 5.7(f)) as illustrated in the enlarged view of fig. 5.7(e). These nanoparticles are deposited on the walls of ZnO NWs and linked together to form a tubular morphology. These particles are interconnected by strong cohesive forces as they do not get separated easily even upon ultrasonication, which is especially relevant for the sample after annealing at 300°C in $N_2$ atmosphere. Fig. 5.7(f) is a representative selected area electron diffraction pattern (SAED) of the CdSe NTs.

The sharp nature of the diffraction rings is indicative of polycrystalline nature of the CdSe NTs and an assignment of the rings shows that (002) plane is more intense than the (110) plane. This, thus implies that the growth of CdSe NTs is mainly along the <002> direction (c-axis). The d-spacing values obtained both from SAED as well as lattice fringes (3.5 Å) is in good confirmation with the primitive hexagonal phase formation (JCPDS card no. 77-0046) and matches well with that obtained previously.[29] The core-shell nature of ZnO NW-CdSe is also evident from the SAED. Its high magnification image (fig. 5(d)), revealing its atomic planes, shows ZnO NW core and

CdSe shell (before leaching) and the inset shows selected area electron diffraction (SAED) pattern for the same. Fig. 5.7(e) is the representative TEM image of a single CdSe NTs showing the absence of ZnO core while fig. 5.7(f) is the high resolution image of CdSe NTs showing atomic planes. SAED of the CdSe NT shows (002) and (110) planes to be exposed preferentially. Lattice plane with a d-spacing of 3.5 Å, indicates primitive hexagonal crystal structure of the nanotubes. SAED patterns of ZnO NWs and CdSe/ZnO NWs hybrids as well as CdSe NTs are shown in the inset of fig. 5.7(b), 5.7(d) and 5.7(f) respectively. For ZnO/CdSe system (before leaching the ZnO), two different types of SAED spots are observed (fig. 5.7(d)), whereas in case of CdSe NTs (fig. 5.7(f)), only ring pattern is observed. This is because of the presence of both ZnO and CdSe particles after electrodeposition, again confirming the core-shell nature of the hybrids. However, after leaching out the core ZnO, the characteristic dot SAED pattern disappears and only ring patterns of CdSe is observed. This is also an indication of complete removal of ZnO.

### 5.3.5. Micro Raman

Fig. 5.8 shows the micro Raman spectrum of CdSe NTs, recorded using a 632.8 nm laser line with a 50x objective lens. For comparison, the Raman spectrum of electrodeposited CdSe nanoparticles (CdSe NPs on FTO coated glass without any ZnO NW template) is also displayed along with that of CdSe NTs. Both the spectra show characteristic longitudinal optical phonon (LO) modes arising due to Se-Cd-Se symmetric vibration [30] at 205 cm$^{-1}$ for CdSe NPs and at 208 cm$^{-1}$ for CdSe NTs. The appearance of a peak below 210 cm$^{-1}$ confirms that CdSe is in the nanosize range because the same peak comes at 210 cm$^{-1}$ for bulk CdSe.

The second order bands (2LO) also appear in the spectra at 408 cm$^{-1}$ for CdSe NPs and at 415 cm$^{-1}$ in case of CdSe NTs. This band originates due to a double resonance process during the Raman scattering. Interestingly, both positions of LO and 2LO peaks of CdSe NT are shifted to a higher wave number (or higher energy) by 3 and 7 cm$^{-1}$ respectively than that of CdSe NPs. Interestingly, FWHM of LO peak also decreases slightly in the case of CdSe NTs than that of CdSe NPs. This ostensibly suggests quantum confinement effect, since both the LO and 2LO peak frequencies show a blue shift. However, a careful inspection of the TEM images suggests that the nanoparticles consisting the NTs, are of 8-10 nm in size which is far beyond the strong confinement region for CdSe (exciton Bohr radius is 5.4 nm for bulk CdSe).[31] Hence quantum confinement is not expected to explicitly contribute to the shift of the phonon peaks. A more appropriate explanation for the shift might be the presence of surface traps. It is well known that CdSe nanoparticles (NPs) have surface defects (or traps) due to more surface-to-volume ratio and the extent of defect increases when the nanoparticles assemble into a quasi 1D structure like nanotubes.[32] So the net surface defect content is significantly higher in case of CdSe NTs than that for CdSe NPs. This higher defect content may be responsible for shifting the fundamental phonon modes of CdSe NPs to higher energy. [32] Interestingly, no peak is observed for selenium (Se) and this cancels out the possibility of the presence of excess Se on the surface of CdSe during electrodeposition.

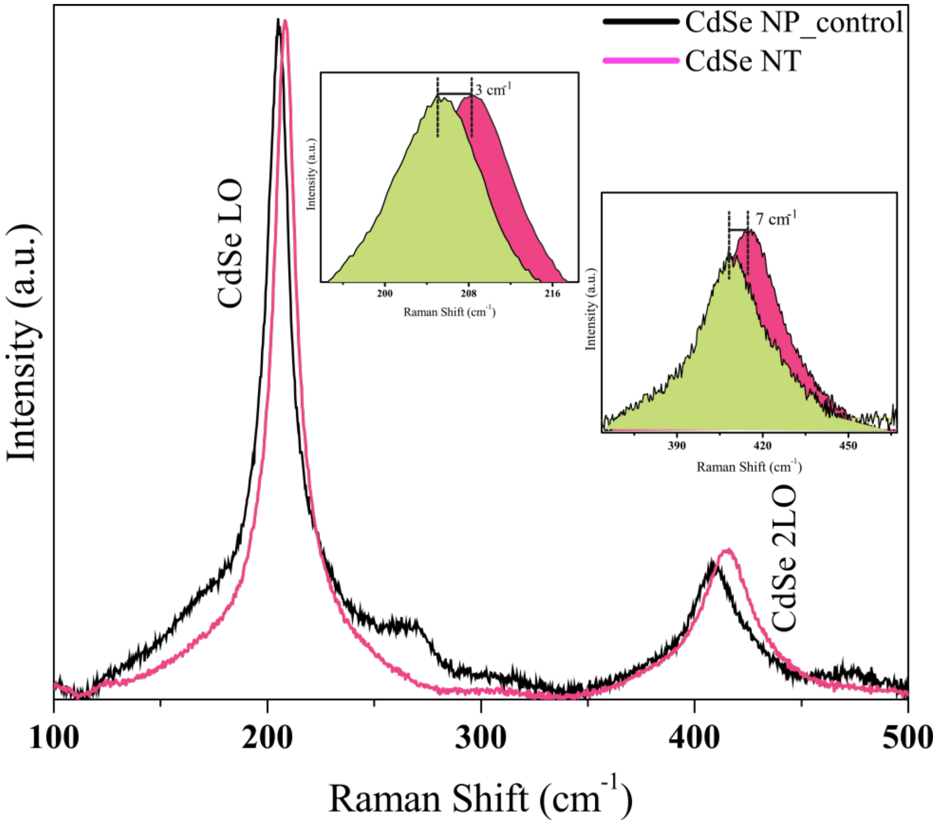

**Figure 5.8.** A comparison of the Micro Raman spectra of CdSe nanoparticles (black line) with that of CdSe nanotubes (red line); All the measurements were taken using 632.8 nm He-Ne laser line (20 mW source energy) with 50x objective lens; No density filter was used for the measurement; Insets are the enlarged portion of the LO (200-214 cm$^{-1}$) and 2LO (360-450 cm$^{-1}$) bands respectively; Both the bands shift bathochromically in case of nanotubes, although the amount of shift is more for 2LO band.

### 5.3.6. Powder X-ray Diffraction (PXRD)

Fig. 5.9 is a comparison of the powder XRD patterns of ZnO NWs and CdSe NTs without ZnO in it. The presence of multiple peaks suggests that all the materials are polycrystalline in nature. PXRD pattern of ZnO NWs (fig. 5.9 (a)) suggests that the ZnO has a hexagonal wurzite structure with strong diffraction patterns at 31.8°, 34.5° and 36.4° with cell constants comparable to that in the reported data (JCPDS card no.00-005-0664).[33] A strong diffraction peak of ZnO along the (002) plane is observed in ZnO nanorods on FTO coated glass plate; it indicates that the ZnO preferentially grows in the (002) plane on FTO coated glass plate. CdSe NTs, on the other hand, form primitive hexagonal phase (JCPDS card no. 77-0046)[29] as revealed from careful observation of the PXRD of CdSe NTs (fig. 5.9 (b)). This matches well with that observed in SAED pattern in HRTEM. Moreover, the peak corresponding to (001) plane of CdSe is more intense than that of the other peaks. This indicates that the CdSe NTs are c-axis oriented and thus proves their vertical alignment with respect to basal FTO coated glass plate. Moreover, the absence of any ZnO reflection in CdSe NTs indicates near-complete removal of ZnO during the leaching with $NH_4OH$.

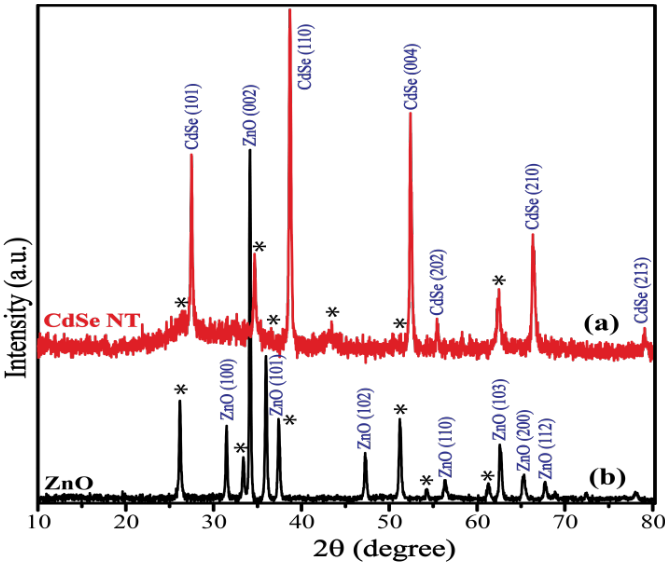

**Figure 5.9.** Powder X-ray diffraction pattern of ZnO NWs and CdSe NTs grown on FTO coated glass ; No ZnO diffraction is observed after removal of ZnO core; (*) indicates peaks from FTO coated glass substrate.

Similarly, fig. 5.10 shows the PXRD pattern of electrodeposited film of $Cu_2O$ on FTO coated glass. The peaks obtained in the pattern matche exactly with the pattern of JCPDS-05-667 (space group $Pn\bar{3}m, a = 4.2682$ Å) and also with that reported by Switzer *et al*.[34] The particles which constitute the $Cu_2O$ film have mostly their (111) plane exposed. Average crystallite size according to Scherrer formula (equation 5) is found to be ~24 nm (based on (111) reflection).

$$D_p = \frac{0.94\lambda}{\beta_{1/2}cos\theta} \ldots\ldots\ldots\ldots\ldots\ldots\ldots\ldots (5)$$

Where, $D_p$ = crystallite size, $\lambda$ = wavelength of X-ray used (here $CuK_\alpha$ =1.54 Å), $\beta_{1/2}$ = full width at half maximum (FWHM) of the peak concerned and $\theta$ = Bragg's angle for diffraction.

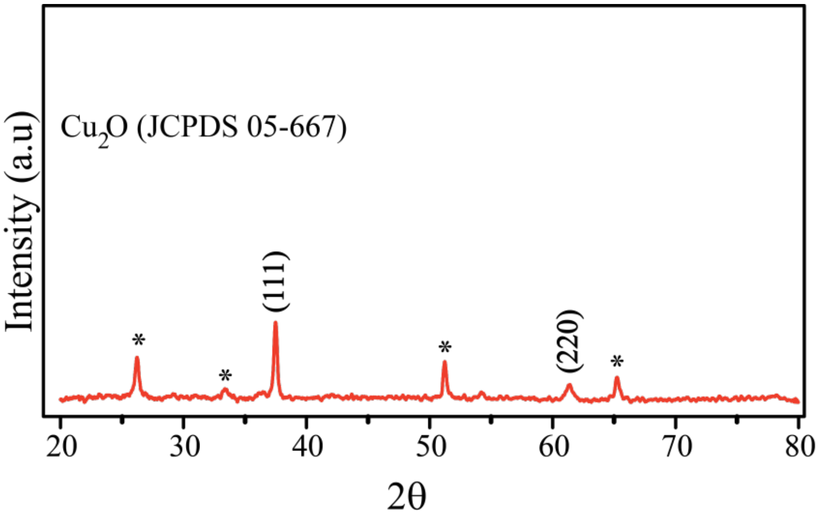

**Figure 5.10.** Powder X-ray diffraction pattern of $Cu_2O$ film electrodeposited on FTO coated glass;(*) indicates peaks from FTO coated glass substrate; The reflections match well with JCPDS 05-667 reflections.

### 5.3.7. UV-Vis Spectroscopy:

A UV-Vis absorption study has been carried out in order to understand the subtle changes in the electronic property of the electrochemically prepared CdSe NTs and $Cu_2O$, i.e., change in band-gap which could be directly related to the light absorption of the material. In order to obtain the absorbance plot, FTO coated glass plate containing the material is kept across the path of light beam source in the spectrophotometer and the intensity of the transmitted light is measured. Accordingly, fig. 5.11 (a) shows a comparison of the absorption spectrum of CdSe NTs, where a broad hump of maximum absorption is observed at 650 nm followed by a small shoulder at 550 nm. The hump is related to the first excitonic transition (1s-1p) in CdSe [35] and the shoulder is due to the second exciton generation. After this the spectrum gradually shoots up as the wavelength decreases or energy increases. The onset of absorption is 750 nm which corresponds to a bandgap energy of 1.8 eV which is close to the bulk bandgap value of CdSe.[36] The higher bandgap value can be justified by considering that the CdSe NTs are composed of CdSe nanocrystallites while lower value enables it to absorb strongly in the visible region.

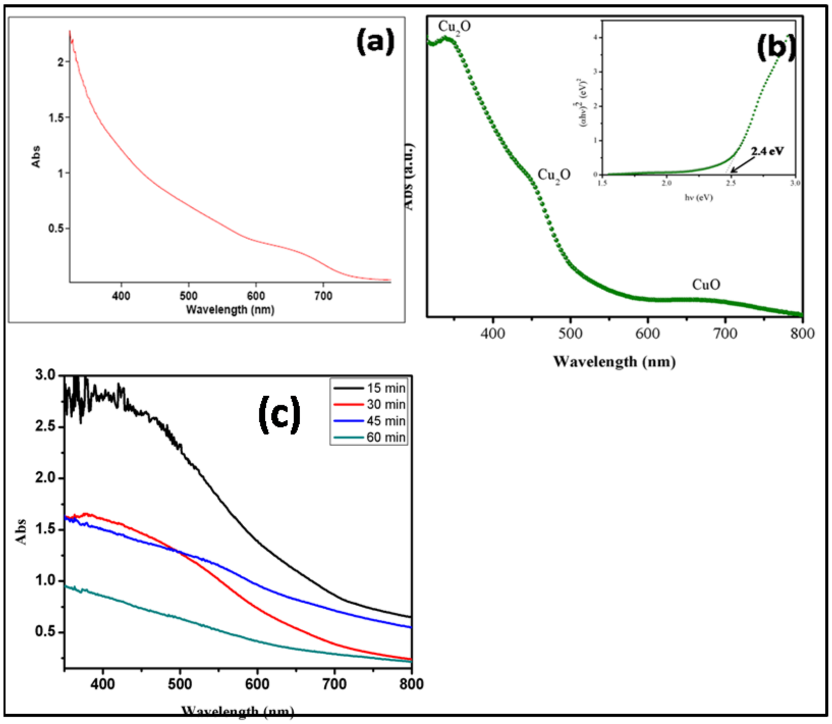

**Figure 5.11.** A comparison of the UV-Vis absorbance spectra of electrodeposited (a) CdSe NTs and (b) $Cu_2O$ on FTO coated glass; CdSe NTs show one broad peak followed by a small hump, $Cu_2O$ shows one peak and two broad humps;Inset of (b) shows the corresponding Tauc plot showing the direct band gap transition for the material ($Cu_2O$);(c) UV-Vis absorption spectra of ZnO NWs-CdSe at different time of leaching ZnO NWs with 25% $NH_4OH$ solution; plateau within the range 550-350 nm corresponds to ZnO absorption and is found to decrease with increase in leaching time; This indicates a gradual removal of ZnO along with the formation of CdSe nanotubes.

A similar UV-Vis absorption study has also been carried out to find out the proper time required to leach out completely the ZnO NW core using $NH_4OH$. A FTO coated glass plate containing CdSe coated ZnO NWs has been dipped in 25% $NH_4OH$ solution for etching. The plate has been taken out periodically after every 15 m, washed and absorbance has been measured. Fig. 5.11 (c) shows the absorbance plot at different etching duration. It is found that the ZnO absorption feature completely vanishes after 1 h. On the other hand, the absorption spectrum clearly shows one broad hump at 650 nm, corresponding to CuO formed during the exposure of the $Cu_2O$ sample in the atmosphere, and two peaks with $\lambda_{max}$ 452 nm and 340 nm. The peak at 452 nm corresponds to the band edge transition for p-type $Cu_2O$ and the other peak at 340 nm is due to band-to-band transition in $Cu_2O$.[37] The band gap of $Cu_2O$ turns out to be 2.4 eV as calculated from the Tauc plot. However, bulk $Cu_2O$ has a band gap of 2.2 eV. The observation of slightly higher band gap in this case can be attributed to the fact that the electrodeposited film consists of $Cu_2O$nanoparticles having average crystallite size ~24 nm (as obtained from PXRD) so that perhaps a negligible contribution comes from the higher band gap energy (i.e., quantum confinement effect).[37]

### 5.3.8. Photoluminescence

Fig. 5.12 shows a comparison of the steady state photoluminescence (emission) spectra of CdSe NTs (a) and electrodeposited film of $Cu_2O$ (b) collected by exciting the samples at their band edge energy. The photoluminescence (PL) spectrum of CdSe nanotubes is broad and centered at 662 nm when excited at 650 nm which is the transition energy for CdSe ($1S_h$-$1S_e$ transition). The Stoke's shift in this case is ~12 nm (103.3 eV) which matches well with similar values. [38] More specifically, $Cu_2O$ shows three emissions when excited with 450 nm to 531.7 nm (band edge emission), 528 nm and another at 687.6 nm.

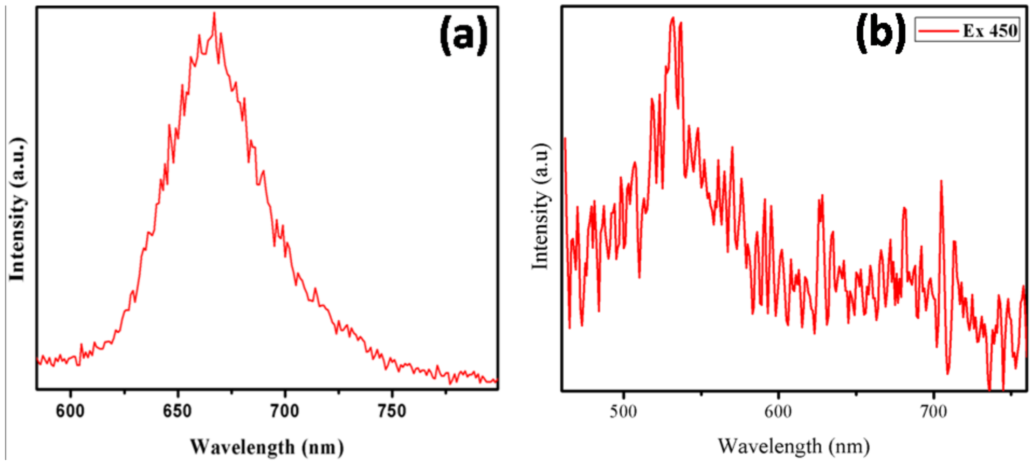

**Figure 5.12.** Photoluminescence spectra of (a) CdSe NTs and (b) electrodeposited $Cu_2O$; CdSe NT shows one broad peak centered around 662 nm (excitation wavelength is 650 nm); $Cu_2O$ shows three emission peaks (531.7 nm, 528 nm and 687.6 nm) when excited with 450 nm wavelength light.

### 5.3.9. Mott-Schottky Plot

Capacitance measurement on the electrode/electrolyte interface has been carried out to determine the flat band ($E_{fb}$) potential of the material and carrier density ($N_A$), which are important parameters to describe a semiconductor electrode/electrolyte interface. When a semiconductor comes in contact with an electrolyte solution, semiconductor Fermi level tends to align itself with the Fermi level of the electrolyte solution, until equilibrium is established. As a result, the valence and conduction bands shift upward or downward (depending on the position of the two Fermi levels before contact). $E_{fb}$ is a measure of the

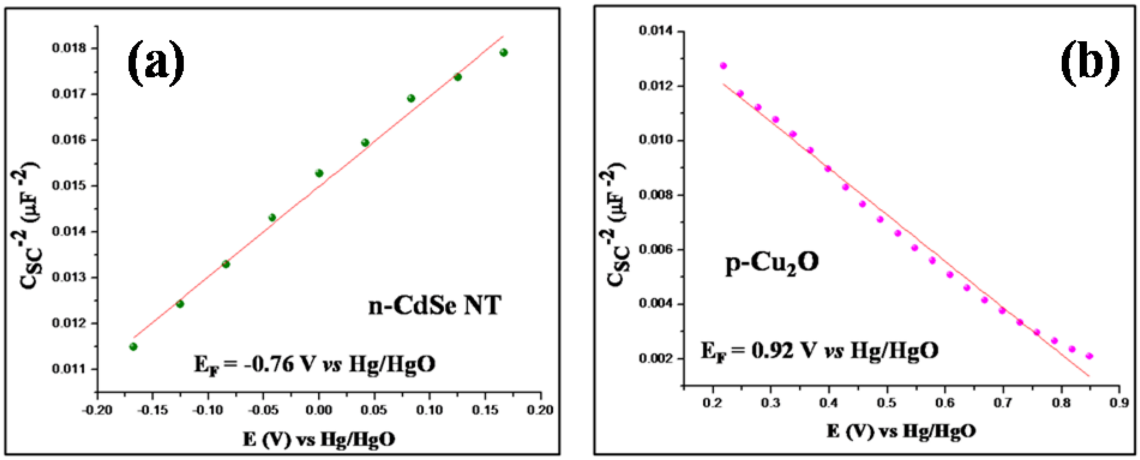

**Figure 5.13.** Mott-Schottky plot for (a) n-type CdSe NTs and (b) p-type $Cu_2O$; Impedance is carried out in $Na_2S$-$Na_2SO_3$ solution for CdSe NTs and in 0.1 M NaOAc

aq. solution for $Cu_2O$; nature of the plots suggests that CdSe NT is n-type semiconductor while the electrodeposited $Cu_2O$ is a p-type semiconductor.

extent of band bending, when a semiconductor electrode is brought in contact with an electrolyte solution. More importantly, both $E_{fb}$ and carrier density ($N_A$) can be determined from the Mott-Schottky plot, which is a plot of $1/C^2$ *vs* applied potential at a fixed frequency (where, C is the space charge capacitance of the semiconductor) of 20 kHz. The capacitance measurements are presented as per the equation (Mott-Schottky equation):[21]

$$\frac{1}{C^2} = \frac{2}{N_A \varepsilon \varepsilon_0 e}\left[\left(E - E_{fb} - \frac{kT}{e}\right)\right] \ldots\ldots\ldots\ldots\ldots (6)$$

where, C is the interfacial capacitance (i.e., capacitance of the semiconductor depletion layer), $\varepsilon$ is the dielectric constant of the material, $\varepsilon_0$ is the permittivity of free space (8.85 x $10^{-12}$ $Fm^{-1}$), $N_A$ is the number density ($cm^{-3}$) of donors/acceptors in the semiconductor (doping level), $E$ is the applied potential, $E_{fb}$ is the flat band potential, $T$ is the absolute temperature (298 K), $k$ is the Boltzmann constant (1.38 x $10^{-23}$ $JK^{-1}$) and e is the electron charge (1.6 x $10^{-19}$ C). The temperature term is generally small and can be neglected.

Fig. 5.13 accordingly shows Mott-Schottky (MS) plot for both CdSe NTs and $Cu_2O$. The nature of the plots suggests that CdSe is n-type while $Cu_2O$ is a p-type semiconductor. Moreover, the intercept of the plot on potential (E) axis (at y = 0) is the $E_{fb}$ of the material for a specific electrode /electrolyte interface. Hence, the $E_{fb}$ of CdSe NTs is -0.76 V *vs* Hg/HgO and that for $Cu_2O$ is 0.92 V *vs* Hg/HgO at room temperature (303 K). Carrier density ($N_A$) as calculated from the slope of the MS plot is found to be 7.3 x $10^{16}$ $m^{-3}$for CdSe NTs (electron is the majority carrier) and 1.09 x $10^{17}$ $m^{-3}$for $Cu_2O$ (hole is the majority carrier). These values obtained are quite similar with that reported for CdSe[39] and $Cu_2O$[40].

### 5.3.10. Properties of CdSe NTs-$Cu_2O$ flip-chip n-p Heterojunction Diode

$Cu_2O$ is a well-known p-type material (since the majority carrier is hole and not electron due to its natural propensity to form cation vacancies) with a band gap of 2.2 eV [41] and its valence and conduction bands (VB and CB respectively) are at 1.30 and -0.70 V (*vs* NHE) respectively. These bands are well aligned with the VB and CB of CdSe (1.32 and -0.59 V *vs* NHE). [42] Hence, a remarkable combination of both these two can in principle give rise to important heterojunction (fig. 5.14 (a)), which can show good optoelectronic properties. FTO coated glass plate containing CdSe NTs can be brought into intimate contact with the FTO coated glass plate containing $Cu_2O$ in order to establish the n-p hetero-junction. Here, the CdSe has a band-gap of 1.8 eV while that of $Cu_2O$ is 2.4 eV. The device shows rectifying behaviour under dark with a rectification ratio ($I_{forward}/I_{reverse}$) of 3 at a bias of 0.6 V, indicating the formation of a p-n junction diode. The “turn on” voltage is 0.13 V and the reverse leakage current value is 7 x $10^{-5}$ A at -1 V (Fig. 5.14 (b)).[43] In order to see the effect of CdSe NT/FTO and $Cu_2O$/FTO junctions on the I-V characteristic of the n-p heterojunction, I-V measurement has been carried out for the respective junctions in a similar flip-chip method. Accordingly, fig. 5.14 (c) and (d) show I-V characteristics of CdSe NT/FTO and $Cu_2O$/FTO junctions respectively. $Cu_2O$/FTO junction shows ohmic behavior at very low voltage (within ± 0.04 V), but changes to Schottky type at voltage larger than this threshold voltage. On the other hand, CdSe NT/FTO junction shows ohmic behavior upto ~0.6 V.Although absorption spectrum of electrodeposited $Cu_2O$ (fig. 5.11 (b)) shows the presence of very small amount of CuO formed due to aerial oxidation on the surface of $Cu_2O$, but the presence of CuO (a p-type Mott insulator) does not affect the electron transfer from p-type $Cu_2O$ because the valence and conduction bands of the latter are properly aligned with CdSe (fig. 5.14 (a)) so as to allow electron transfer from p-type $Cu_2O$ to n-type CdSe NTs upon external excitation. Due to the difference in Fermi energy of the n and p-type materials as well as due to the different nature of majority carriers, an intrinsic potential builds up at the interface between the two. This potential assists in separating the photo generated carriers at the interface.

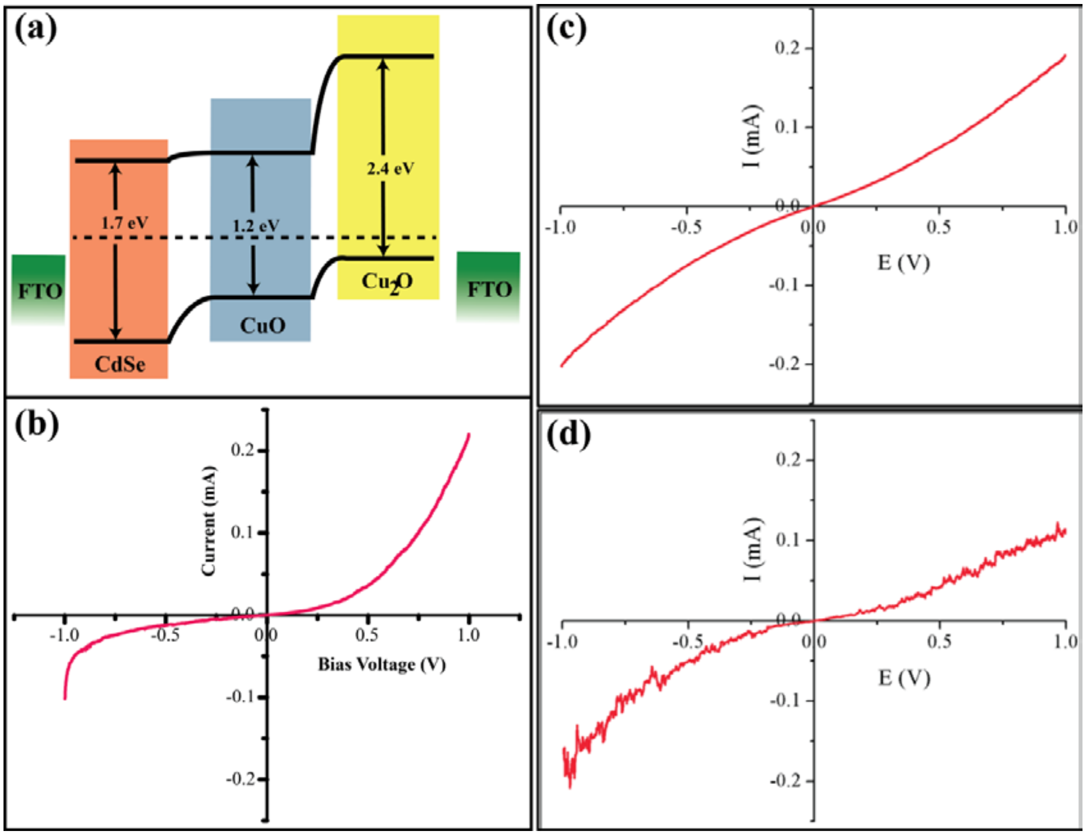

**Figure 5.14.** (a) Band alignment diagram of CdSe and Cu$_2$O. Type II band alignment is responsible for photoresponse and (b) Current-voltage (I-V) characteristic of n-p heterojuncion device comprising of CdSe NTs and Cu$_2$O (device area 1cm$^2$). The plot shows rectifying nature of the device. (c) Current-voltage characteristic of CdSe nanotube/FTO junction. CdSe NT film is flip-chipped with FTO coated glass plate, (d) Current-voltage characteristic of Cu$_2$O/FTO junction. Cu$_2$O film is flip-chipped with FTO coated glass plate.

The device shows stronger photoresponse when compared with that obtained for CdSe NPs (non-templated growth) as an n-type material. Fig. 5.15(b) and (c) show the photo-response of the so formed device in presence of AM 1.5 solar simulated light. For CdSe NTs, the increment in current on irradiation is ~470 µA whereas for a similar device with CdSe NPs gives ~149 µA increment in presence of light when applied a forward bias of 1 V. The much larger photoresponse (~3.2 times) of the device consisting of CdSe NTs obviously comes from the quasi 1D nanostructures, which efficiently generates excitons and the 1D nanostructure of CdSe provides an expressway for carrying the electrons to the FTO coated glass which act as a current collector. Thus the device can act as a promising candidate for harvesting light energy.

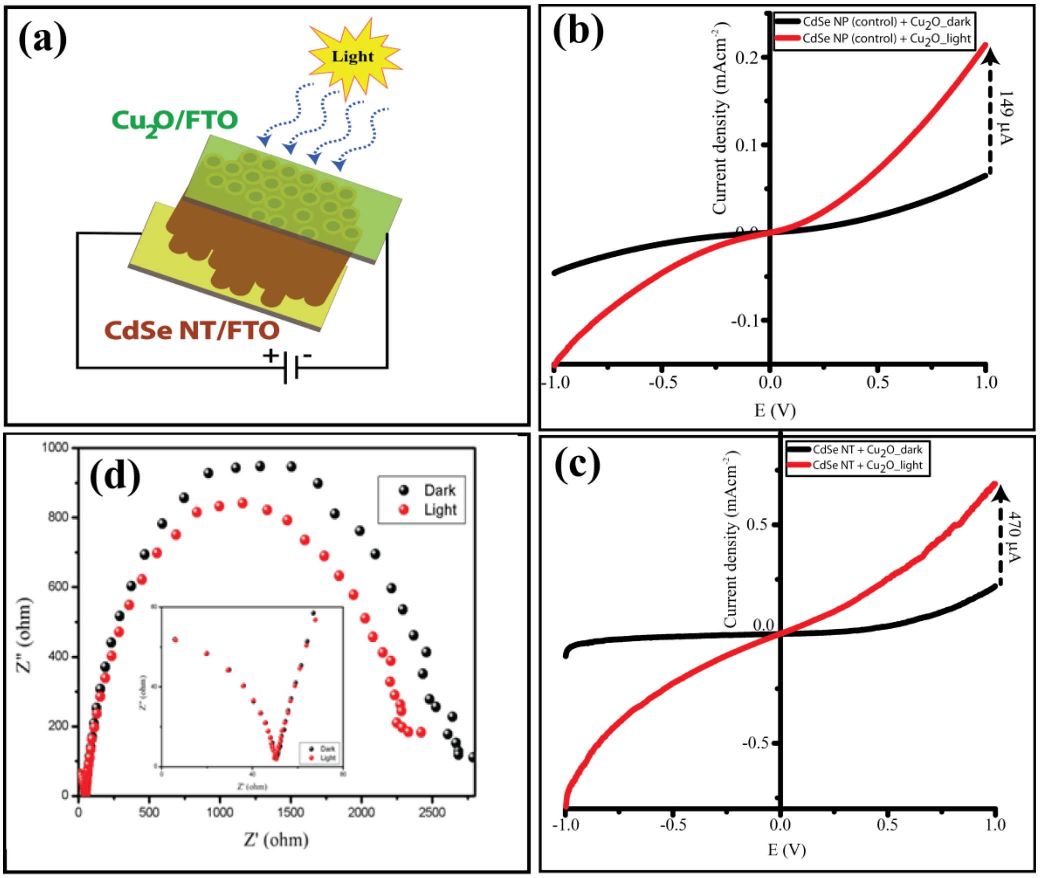

**Figure 5.15.** (a) A schematic representation of the flip-chip n-p heterojunction device fabricated. Current is measured perpendicular to the plane of the FTO plate. Current-voltage (I-V) characteristics of CdSe–$Cu_2O$ heterojunction devices (n-p junction) in dark (black) and under AM 1.5 solar simulated light (i.e., 100 $mWcm^{-2}$) (red), (b) corresponds to the device with CdSe Nanoparticles (NPs)-$Cu_2O$ and (c) with CdSe NTs-$Cu_2O$, (d) Nyquist plot for the device under dark and light; The first semicircle remains unchanged while the second one decreases upon illumination with AM 1.5 solar simulated light.

Fig. 5.15 (d) represents the Nyquist plot for the device under dark and illuminated conditions. Interestingly, the low frequency semicircle decreases (3)19upon illumination indicating probably the reduced charge transfer resistance at the interface. The valence band (VB) and conduction band (CB) of CdSe are well aligned with that of $Cu_2O$ and hence the photo-generated minority carriers (electron) in $Cu_2O$ can be easily transferred to the CB of CdSe NTs. At the same time the hole can migrate from the VB of CdSe to the $Cu_2O$ VB (fig.5.14 (a)). This thereby reduces the probability of recombination leading to a decrease in charge transfer resistance as well as an improved photocurrent generation in the case of CdSe NTs and $Cu_2O$ hetero-junction.

In order to understand the effect of different excitation on the photoresponse of the n-p heterojunction device, response of the device has been studied at various wavelengths using monochromatic light sources and the corresponding response has been calculated by dividing the photocurrent through the device with power of the incident light.[44] Accordingly, fig.5.16 shows the normalized response plot as a function of wavelength of the incident light. The plot gives a maximum at 700 nm with a small hump between 500 and 600 nm. The highest response in the near IR region can be attributed to the absorption of light by CdSe NTs ($\lambda_{max}$ = 662 nm, fig. 5.11(a)) due to low band-gap as well as higher inner and outer accessible surface area. CdSe absorbs higher amount of light and generates a large number of excitons which dissociates at the CdSe/$Cu_2O$ junction thereby giving a higher photocurrent at 700 nm. On the other hand, $Cu_2O$ absorbs in the region of 350 to 580 nm in the spectrum (fig. 5.11(b)). Hence, the photoresponse shows a small hump in the region from 500 to 600 nm indicating that $Cu_2O$ absorption predominates in generating exciton and photocurrent as a consequence. But, $Cu_2O$ film has lower surface area for absorption of light as compared to that of CdSe NTs. The response in this region is, therefore, not as high as in case of CdSe NT especially at this higher wavelength of light. Moreover, the device has been illuminated from $Cu_2O$ side which is a higher band gap (2.4 eV) material than CdSe. Lights of wavelengths less than 600 nm, therefore, cannot pass through $Cu_2O$ film to reach CdSe NTs and so CdSe NTs do not contribute much in the photoconductivity of the device below 600 nm. Similarly, the photons having a wavelength greater than 600 nm are absorbed mostly by CdSe NTs and not by $Cu_2O$ causing a higher photoresponse. Thus $Cu_2O$ in combination with CdSe NTs acts as a visible light sensitive photodetector which can work at any wavelength ranging from 400 to 800 nm.

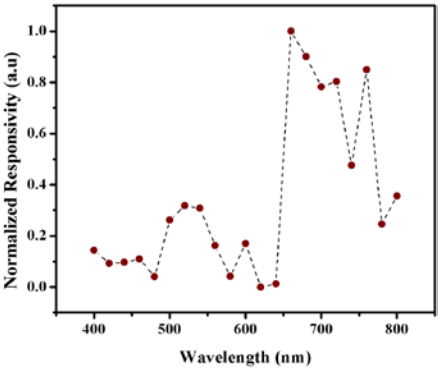

**Figure 5.16.** Normalized photo-response as a function of wavelength the device has been illuminated from $Cu_2O$ side. Newport incident photon to converted electron (IPCE) measurement setup was used for getting responsivity at various wavelengths coupled with Keithley 2400 SMU for electrical measurement *in situ*. Photoconductance was measured using LEDs of different wavelengths. All the electrical measurements were done inside a dark room under ambient conditions.

Thus from the above data we see a successful fabrication of vertically aligned, hollow CdSe NTs on conducting glass substrate (FTO coated glass) by ZnO NW templating. SEM and TEM provide distinct evidence for the hollow structure and more significantly CdSe NTs can form a proper n-p heterojunction diode with p-type $Cu_2O$ deposited electrochemically, in a current perpendicular to the plane (CPP) geometry. The diode shows good photo-response as compared to that of devices made out of electrodeposited films of CdSe NPs without ZnO NWs template. Nevertheless, the present study is carried out only with electrodeposited $Cu_2O$ and no shape and size selective activity has been investigated. Moreover, temperature has profound effect on the performance of n-p diodes because thermal energy also promotes diffusion of charge carriers across the interface. Light intensity as well as the interface structure also affects the photoconductivity of such devices and more quantitative studies are needed to understand these influences.

## 5.4. Conclusion

This chapter describes the growth of vertically aligned quasi 1-D CdSe NTs with hollow inner core grown on transparent conducting glass (FTO-glass) substrates by electrochemical deposition. Zinc oxide nanowires, grown on FTO-glass, act as structure directing template for the growth of these nanotubes. The deposition has been found to dependent strongly on pH, concentration of species, deposition potential and also temperature and the Nucleation mechanism of CdSe deposition has been shown to follow the instantaneous pathway. Moreover, these nanotubes are found to form rectifying n-p heterojunction diode with p-type $Cu_2O$ deposited electrochemically. The heterojunction shows a strong photoresponse (~470 $\mu Acm^{-2}$ current density increment with 100 $mWcm^{-2}$ light) and the photosensitivity is better (~3 times more) than that in case of electrodeposited CdSe nanoparticles film. Thus, the results presented in this chapter is expected to provide a general NW platform for the fabrication of solar cells, photodetectors and other optoelectronic devices.

### 5.5. References

1. Ciraci, S.; Buldum, A.; Batra, I. P. *J. Phys.: Condens. Matter* **2001**, *13,* R537.
2. Link, S.; El-Sayed, M. A. *J. Phys. Chem. B* **1999**, *103*, 8410.
3. Voit, J. *Rep. Prog. Phys.***1995**, *58*, 977.
4. Kane, C.; Balents, L.; Fisher, M. P. *Phys. Rev. Lett.***1997**, *79*, 5086.
5. Lieber, C. M. *Solid State Commun.***1998**, *107*, 607.
6. Iijima, S. *nature* **1991**, *354*, 56.
7. Rao, C.; Govindaraj, A.; *RSC Nanosc. and Nanotech. Series RSC Publishing: Cambridge, UK*, **2005**.
8. a) Zhu, K.; Neale, N. R.; Miedaner A.; Frank, A. J. *Nano Lett.* **2007**, *7,* 69 b) Shankar, K.; Mor, G. K.; Prakasam, H. E.; Yoriya, S.; Paulose, M.; Varghese, O. K. Grimes, C. A. *Nanotechnol.* **2007**, *18*, 065707 c) Roy, P.; Kim, D.; Lee, K.; Spiecker, E.; Schmuki, P. *Nanoscale* **2010**, *2*, 45 d) Martinson, A. B.; Goes, M. S.; Fabregat-Santiago, F.; Bisquert, J.; Pellin, M. J.; Hupp, J. T. *J. Phys. Chem. A* **2009**, *113*, 4015 e) Zhang, Q.; Dandeneau, C. S.; Zhou, X.; Cao, G. *Adv. Mater.* **2009**, *21*, 4087.
9. Rao, C.; Govindaraj, A.; Deepak, F. L.; Gunari. N.; Nath, M. *Appl. Phys. Lett.* **2001**, *78*, 1853.
10. Shen, Q.; Jiang, L.; Miao, J.; Hou W.; Zhu, J.-J. *Chem. Commun.* **2008**, ***14***, 1683.
11. Nagaraju, G.; Chandrappa, G. T. *J. Mater. Sci. Technol.* **2012**, *28*, 495.
12. a) Zhou, M.; Zhu, H.; Wang, X.; Xu, Y.; Tao, Y.; Hark, S.; Xiao, X.; Li, Q. *Chem. Mater.* **2009**, *22*, 64. b) Zhu, H.; Li, Q. *Nanoscale res. Lett.* **2013**, *8*, 1.
13. Feng, Z.; Zhang, Q.; Lin, L.; Guo, H.; Zhou, J.; Lin, Z. *Chem. Mater.* **2010**, *22*, 2705.
14. Leatherdale, C.; Woo, W.-K.; Mikulec, F.; Bawendi, M. *J. Phys. Chem. B*, **2002**, *106*, 7619.
15. a) Norris, D.; Bawendi, M. *Phys. Rev. B* **1996**, *53*, 16338. b) Leutwyler, W. K.; Bürgi, S. L.; Burgl, H. *Science* **1996**, *271*, 933.

16. a) Li, L.-s.; Hu, J.; Yang W.; Alivisatos, A. P. *NanoLett.* **2001**, ***1***, 349. b) Mohamed, M. B.; Burda, C.; El-Sayed, M. A. *NanoLett.* **2001**, ***1***, 589.
17. (a) Bouroushian, M. *Electrochemistry of metal chalcogenides*. Springer **2010**. (b) Joseph, S.; Kamath, P. V. *J. Electrochem. Soc.* **2007**, *154*, E102.
18. Suryanarayana, C.; Norton, M. G. *X-Ray Diffraction: A Practical Approach*
19. Wang, X.; Zhu, H.; Xu, Y.; Wang, H.; Tao, Y.; Hark, S.; Xiao, X.; Li, Q. *ACS nano* **2010**, *4*, 3302.
20. Bouroushian, M. *Electrochemistry of metal chalcogenides*. Springer **2010**.
21. Bard, A. J.; Faulkner, L. R. *Electrochemical methods: fundamentals and applications*. Vol. 2. New York: Wiley, **1980**.
22. (a) Itabashi, H.; Yoshida, M.; Kawamoto, H. *Anal. Sci.* **2001**, *17*, 1301. (b) Ahlers, J.; Rösik, E.; Stadtlander, K. *Am. Soc. Test. Mat. Philadelphia* **1988**, 106.
23. Kosmulski, M. *J. Colloid Interface Sci.* **2004**, *275*, 214.
24. Hodes, G. ed. *Electrochem. nanomat*. Wiley. com, **2008**.
25. Armstrong, R. D.; Fleischmannand M.; Thirsk, H. R. *J. Electroanal. Chem.* **1966**, *11*, 208.
26. Abyaneh, M. Y. *Electrochim. Acta* **1982**, *27*, 1329.
27. Paunovic, M.; Mordechay, S. "Fundamentals of electrochemical deposition." *John Wiley & Sons, Hoboken* 144 (**2006**).
28. (a) Scharifker, B.; Hills, G. *Electrochim. Acta* **1983**, 28, 879. (b) Debgupta, J. Shinde, D. B.; Pillai, V. K. *Chem. Commun.* **2012**, *48*, 3088.
29. Talapin, D. V.; Shevchenko, E. V.; Kornowski, A.; Gaponik, N.; Haase, M.; Rogach, A. L.; Weller, H. *Adv. Mater.* **2001**, *13*, 1868.
30. a) Ingale, A.; Rustagi, K. *Phys. Rev. B* **1998**, *58*, 7197. b) Trallero-Giner, C. *Phys. Status Solidi B* **2004**, *241*, 572.
31. Norris, D.; Efros, A. L.; Rosen, M.; Bawendi, M. *Phys. Rev. B* **1996**, *53*, 16347.
32. a) Venugopal, R.; Lin, P.-I.; Liu C.-C.; Chen, Y.-T. *J. Am. Chem. Soc.* **2005**, *127*, 11262. b) Lange, H.; Artemyev, M.; Woggon, U.; Thomsen, C. *Nanotechnol.* **2009**, *20*, 045705.
33. Devarapalli, R. R.; Shinde, D. R.; Barka-Bouaifel, F.; Yenchalwar, S. G.; Boukherroub, R.; More, M. A.; Shelke, M. V. *J. Mater. Chem.* **2012**, *22*, 22922.

34. Golden, T. D.; Shumsky, M. G.; Zhou, Y.; VanderWerf, R. A.; Van Leeuwen, R. A.; Switzer, J. A. *Chem. Mater.* **1996**, *8,* 2499.

35. .Troparevsky, M. C; Kronik, L.; Chelikowsky, J. R. *J. Chem. Phys.* **2003**, *119,* 2284.
36. Parson, R. B.; Wardzynski, W.; Yoffe, A. D.; Parsons, R. B.; *Pro. Royal Soc. London. Series A. Mathematical and Physical Sciences* **1961**, *262*8, 120.

37. Yin, M.; Wu, C. K.; Lou, Y.; Burda, C.; Koberstein, J. T.; Zhu, Y.; O'Brien, S. *J. Am. Chem. Soc.* **2005**, *127(26)*, 9506.
38. Laidoudi, S.; Bioud, A.; Azizi, A.; Schmerber, G.; Bartringer, J.; Barre, S.; Dinia, A. *Semicond. Sci. Technol.* **2013**, *28*, 115005.
39. Zhou, M.; Zhu, H.; Wang, X.; Xu, Y.; Tao, Y.; Hark, S.; Li, Q. *Chem. Mater.* **2009,** *22*, 64.
40. Kondo, J. *Chem. Commun.***1998**, ***3***, 357.
41. Chen, S.; Wang, L.-W. *Chem. Mater.***2012**, *24*, 3659.
42. Deo, M.; Mujawar, S.; Game, O.; Yengantiwar, A.; Banpurkar, A.; Kulkarni, S.; Jog, J.; Ogale, S. *Nanoscale* **2011**, *3*, 4706.

43. a) Konstantatos, G.; Sargent, E. H. *Nature nanotech.* **2010**, *5*, 391. b) Mandal, L.; Chaudhari ,N. S.; Ogale, S. *ACS appl. Mater. interfaces* **2013**, *5*, 9141.

# CHAPTER 6

# Conclusions and Future Prospects

This chapter deals with significant conclusions of the present study with respect to the controlled synthesis of size-selective CdSe QDs, heterostructures with carbon nanotubes and graphene along with their structure-property relationship. Related promising developments and daunting challenges in this broad area are also discussed in order to map the device applications of these fascinating nanomaterials in view of their fundamental as well as technological interests. This chapter also outlines some of the limitations of the present study. Finally, some of the future prospects and precautions for processing CdSe QDs and related hybrids are also explained within the broad perspective of nanotechnology and its societal impacts for various applications.

Cadmium selenide (CdSe) is an important and well known semiconductor for a multitude of applications due to its low band-gap and high absorption cross section for photons. These intriguing properties make CdSe, especially in its reduced dimensions (CdSe QDs), an ideal material in the field of sensitized solar cells, water splitting, photodetectors, biological imaging etc. Size -dependent photoluminescence of CdSe QDs is an important advantage for those optical and optoelectronic applications. Consequnetly, it is hardly surprising to see from recent developments that the field of application of CdSe QDs is ever expanding. Indeed, hybrids of CdSe QDs with suitable materials such as carbon nanotubes (CNT) and graphene are even more important, because CNT and graphene not only help channelize the photogenerated carriers of CdSe QDs in the corresponding devices, but also provide stability of CdSe QDs against photo corrosion. Significant amount of effort has, therefore, been devoted in recent times in the synthesis and applications of these hybrid materials in recent years.[1] However, despite the immense knowledge in this area, the synthesis of these nanostructures possesses a number of challenges such as availability of simple and cost effective methods of preparation, lack of selectivity and uniformity in size distribution, difficulty of scale-up etc. These issues remain to be addressed before these materials find viable applications. Moreover, a thorough understanding of the electron transfer processes in these hybrid materials under external excitation (heat, light, electric field etc.) is an essential prerequisite to understand the mechanism, which is of particular significance both for the creation of new hybrid materials as well as for the fabrication of devices using these materials.[2] The main objectives of the present investigation have been formulated to address some of these important challenges related to the synthesis, characterization and possible applications (especially in photoelectronic devices) of CdSe based nanostructures (QDs, nanotubes) and their hybrids with various carbonaceous nanomaterials (particularly CNT and graphene).

Accordingly, chapter-1 demonstrates a critical review of the synthesis, properties and potential applications of CdSe QDs and their hybrid materials. Various synthetic routes such as physical, chemical as well as electrochemical methods for CdSe QDs and their hybrids have been discussed in this chapter. Elegant features of these hybrids have been elaborated on the basis of their structure property relationships. While dealing with these aspects, it is found that in spite of so many existing methods available for the synthesis and applications of CdSe QDs and their hybrids,[3] several daunting challenges of these materials such as development of low cost, synthetic methods, scale up synthesis as well as ease of fabrication of devices requires breakthrough results for the sake of technology. These facts have motivated greatly in formulating the aims of the present thesis. Further designing any hybrid material employing QDs requires prior knowledge of the electronic band structure, especially the relative positions of valence and conduction band edges of both QDs and the host material. This is important because that determines the type of hetero-junction (type-I, II or III) to be formed and thereby decides the ultimate function of the hybrids.[4] Techniques such as photoelectron spectroscopy gives very accurate information about the band edge position but suffers from a major limitation that it is difficult to perform in real situation like in solution. Electrochemical techniques like cyclic voltammetry has been proven to be very useful in determining band positions of QDs.[5] Hence, chapter-2 describes the electrochemistry of CdSe QDs in order to get the band edges (HOMO-LUMO positions) with varying particle size in solution. Differential pulse voltammetry (DPV) and cyclic voltammetry (CV) are used for this purpose. It is found that DPV gives better resolution than CV especially in low concentration of the QDs (~µM) because of the reduced effect of background current. The difference in HOMO-LUMO positions gives the electrochemical band-gap which matches closely with the optical band-gap of these QDs. Moreover, electrochemical impedance technique is also employed in order to estimate the heterogeneous electron transfer rate constant between QDs in solution and electrode. The kinetics of electron transfer has been found to be much faster in smaller QDs presumably because of the less viscoelastic drag than the larger one in similar solutions.

Considerable amount of effort has been devoted in the last few years for the development of synthetic methods for the preparation of CdSe QDs-graphene hybrids.[6] But most of them employ costly chemicals, high temperature, long insulating bi-functional molecules for the synthesis of the hybrids and in many cases the stability lasts only for few days. Simple, cost effective and easily scalable methods are, therefore highly desirable.

Chapter-3 describes a simple, all electrochemical method for the synthesis of CdSe QD decorated graphene nanoribbons (GNRs). GNRs are graphene ribbons with finite length and narrow width thereby having special band structures depending on the aspect ratio.[7] In the present case, GNRs are obtained by electrochemical unzipping of SWCNT with more or less similar length.[8] The process is easy and can be scaled up easily by increasing the size of the electrodes and moreover the width of the GNRs can be fine tuned by simply adjusting the potential and time. All these novel hybrids have been characterized well by various tools such as UV-Vis, PL, FTIR, Raman, CV and I-V measurements. The hybrids also show very good photoconductivity and are promising for thin photovoltaic devices. Again, CdSe QDs have been attached to pristine CNTs by means of diazonium salt chemistry in order to study the behavior of CdSe QDs on different carbon nanostructures. Moreover, wetting studies on CNTs suggest that small polar molecule like acetonitrile can transfer charge to CNTs. This is compared with the charge transfer from excited QDs to CNTs and GNRs, because QDs are regarded as giant artificial atoms.[9]

CdSe QDs on graphene is a promising material for optoelectronic applications, but before implementing them in actual use it is imperative to know the nature of energy or charge transfer processes between them and also similarly the kinetics of the processes. Chapter-4 is, therefore, designed to provide details of the kinetics of charge transfer from excited CdSe QDs to graphene. CdSe QDs are connected to graphene by thiol linkers which are generated on graphene by a simple diazonium salt reaction employing 4-aminothiphenol and reduced graphene oxide (RGO). The process of thiol functionalization to generate thiolated RGO is discussed in detail in this chapter. Thiol functionalization results in uniform and almost monolayer coverage of CdSe QDs on RGO surface. Photoluminescence lifetime measurements show that the thiol functionalization enhances the rate of charge transfer (as high as $12.8 \times 10^{8}$ $s^{-1}$) while subsequently reducing the rate of energy transfer from excited QDs to RGO. Charge transfer process is also supported by Raman measurements. Finally, a prototype bulk heterojunction device is fabricated with this hybrid employing PEDOT:PSS as hole conductor and 2-3 times enhancement in photocurrent is observed in such a device under AM 1.5 solar simulated light illumination suggesting the utility.

1D nanostructures are very useful in optoelectronic devices because of their higher aspect ratio and unique band structures as compared to 0-D nanostructures.[10] This results in higher absorption and generates more charge carriers, with enhanced mobility. Accordingly, chapter-5 describes the ZnO nanowire templated electrochemical synthesis of vertically aligned CdSe nanotubes and their detailed characterization using various electrochemical and spectroscopic tools. Higher inner as well as outer surface area of these nanotubes allows far better absorption of light and also higher mobility of generated light carriers. A prototype diode fabricated using CdSe NTs (n-type) in contact with electrodeposited film of $Cu_2O$ (p-type) has been shown to generate a photocurrent density as high as 470 $\mu Acm^{-2}$. This value is ~3 times higher than that of similar device consisting of CdSe nanoparticles and $Cu_2O$ thereby proving the utility of 1D hollow nanostructure.

Thus the main results of this thesis unravel few contemporary issues in the field of CdSe QDs, their hybrids with various carbon nanostructures (CNT, graphene) as well as 1D nanostructures of CdSe with particular emphasis on their novel chemical and electrochemical synthesis for specific applications. A unique blend of optical, electrical, electronic, thermal and mechanical properties of these hybrid nanostructures is expected to facilitate the prospect of these materials for many more tangible applications in the foreseeable future. Although several methods are reported for the preparation of such materials, designing a simple, precise, cost effective, scalable, commercially viable methods of synthesis, uniform distribution of QDs on graphene surface, ease of processability, their environmental effects are some of the daunting challenges which still exist and demand breakthrough results in order to completely utilize their technological and social benefits in the area of electronics, energy and so on. In addition, several existing lacunae in our understanding need to be filled by urgent investigations such as atomic level manipulation of these materials, method for obtaining QDs that fluoresce in the deep blue region, improvement of the junction characteristics of QDs and other materials, reducing the number of surface traps on QDs and thereby minimizing the recombination loss in the resulting devices and so on.[11]

Thus the major accomplishments of the present investigations can be summarized as follows-

- Preparation of oleic acid capped CdSe QDs with a narrow distribution using hot injection method.
- Investigation of the HOMO-LUMO positions of the CdSe QDs of different sizes using differential pulse and cyclic voltammetry. Impedance technique is employed in this context to find out the heterogeneous electron transfer rate constant during the redox processes of QDs in suitable solutions.
- Attachment of CdSe QDs to SWCNT to form hybrids by using thiol linkers and a study of their optical properties.
- Development of a one step electrochemical method to generate *in situ* CdSe QDs on graphene nanoribbons (GNRs), during the electrochemical unzipping of SWCNT. The hybrid material is characterized by various electrochemical and spectroscopic tools to illustrate their superior optoelectronic properties for suitable applications.
- Development of a new, simple methodology for the uniform decoration of monodispersed CdSe QDs on graphene surface by employing thiol functionalization of graphene through diazonium salt chemistry.
- Study of the relaxation dynamics of CdSe QDs attached to thiolated graphene using time correlated single photon counting experiments.
- Preliminary photovoltaic study of the CdSe QDs-thiolated graphene hybrids.
- Preparation of vertically aligned hollow, CdSe nanotubes by electrodeposition using ZnO nanowires template.
- Fabrication of a prototype n-p hetero-junction diode using n-type CdSe NTs and p-type $Cu_2O$ (electrodeposited) and study of the I-V characteristics of the device under AM 1.5 light illumination.

In a nutshell, the present study is devoted mainly to the novel synthesis and characterizations of CdSe QD and its hybrids and to test them for optoelectronic applications to harvest energy from sunlight. These methods offer an unprecedented opportunity to obviate many limitations of the currently employed synthetic routes for these fascinating materials. However, the study has the following limitations which need to be kept in mind before their commercial exploitation.

- It is difficult to study the electrochemistry of QDs having size below 2 nm or even lesser than that because of the difficulty in preparation and poor reproducibility arising perhaps from the contribution of surface states (surface to volume ratio increases with increase in size).
- A simple equivalent circuit is used to explain the impedance plots at different bias potentials, but in practice the situation is complicated by the presence of surface states and hence a more complex model based on this would be better to describe the experimental results.[12]
- Although the one step electrochemical approach for the preparation of CdSe QD-GNR hybrids has several advantages in terms of unzipping CNT to form GNRs and quality control of the product, it is limited by the poor yield. Moreover, the naked QDs on GNRs are prone to get easily oxidized in absence of suitable capping agent and thereby reducing the quantum yield.
- Ultrafast dynamic technique such as that used here, gives a reasonably good estimate of the rate of electron transfer processes from QDs to graphene, but more sophisticated techniques employing single molecule fluorescence, transient absorption or femtosecond laser would have given better insights.
- In fabricating the n-p heterojunction diode employing vertically aligned CdSe NTs, excess pressure destroys the morphology and hence the device performance drops down significantly.
- Cadmium is toxic and hence proper precautions should be taken prior to handle cadmium compounds. Moreover, the long term effect of these hybrid materials on the environment is still unknown.[13]

Nevertheless, the present study offers enough scope to design novel optical as well as optoelectronic materials involving easier, low cost methods in order to achieve better efficiency, recyclability and simplified functionalization chemistry in the foreseeable future.

## References:

1. (a) Chen, M. L.; Meng, Z. D.; Zhu, L.; Park, C. Y.; Choi, J. G.; Ghosh, T.; Cho, K. Y.; Oh, W. C. *J. Nanomat.* **2012**, *2012*, 21. (b) Zedan, A. F.; Sappal, S.; Moussa, S.; El-Shall, M. S. *J. Phys. Chem. C* **2010**, *114(47)*, 19920. (c) Kamat, P. V. *J. Phys. Chem. Lett.* **2011**, *2*, 242. (d) Wang, Y.; Yao, H. B.; Wang, X. H.; Yu, S. H. *J. Mater. Chem.* **2011**, *21*, 562.
2. (a) Jain, V. K.; Verma, A. *Physics of Semiconductor Devices: 17th International Workshop on the Physics of Semiconductor Devices* **2013**, Springer. (b) Jun, H. K.; Careem, M. A.; Arof, A. K.; *Renew. Sust. Energy Rev.* **2013**, *22*, 148.
3. Debgupta, J.; Shinde, D. B.; Pillai, V. K. *Chem. Comm.* **2012**, *48(25)*, 3088.
4. Sze, S. M.; Ng, K. K. *Physics of semiconductor devices* **2006**, John Wiley & Sons.
5. Amelia, M.; Lincheneau, C.; Silvi, S.; Credi, A. *Chem. Soc. Rev.* **2012**, *41(17)*, 5728.
6. (a) Krishnamurthy, S.; Kamat, P. *Abstracts of Papers of the American Chemical Society* **2013**, *246*. (b) Wei, D. *Nanomat.* **2013**, *3(3)*, 325. (c) Ghosh, T.; Lee, J. H.; Meng, Z. D.; Ullah, K.; Park, C. Y.; Nikam, V.; Oh, W. C. *Mater. Res. Bull.* **2013**, *48(3)*, 1268. (d) Kim, Y. T.; Shin, H. W.; Ko, Y. S.; Ahn, T. K.; Kwon, Y. U. *Nanoscale* **2013**, *5(4)*, 1483.
7. (a) Son, Y. W.; Cohen, M. L.; Louie, S. G. *Phys. Rev. Lett* **2006**, *97(21)*, 216803. (b) Brey, L.; Fertig, H. A. *Phys. Rev. B* **2006**, *73(23)*, 235411.
8. (a) Shinde, D. B.; Debgupta, J.; Kushwaha, A.; Aslam, M.; Pillai, V. K. *J. Am. Chem. Soc.* **2011**, *133(12)*, 4168. (b) Shinde, D. B.; Pillai, V. K. *Chem. Eur. J.* **2012**, *18(39)*, 12522.
9. Hawrylak, P. *Phys. Rev. B* **1999**, *60(8)*, 5597.
10. (a) Kongkanand, A.; Tvrdy, K.; Takechi, K.; Kuno, M.; Kamat, P. V. *J. Am. Chem. Soc.* **2008**, *130(12)*, 4007. (b) Huynh, W. U.; Dittmer, J. J.; Alivisatos, A. P. *science* **2002**, *295(5564)*, 2425.
11. Tian, J.; Guozhong, C. *Nano reviews* **2013**, 4.
12. (a) Vanmaekelbergh, D. *Electrochim. Acta* **1997**, *42(7)*, 1135. (b) Parthasarathy, M.; Ramgir, N. S.; Sathe, B. R.; Mulla, I. S.; Pillai, V. K. *J. Phys. Chem. C* **2007**, *111(35)*, 13092.
13. Neathery, M. W.; Miller, W. J. *J. dairy Sci.* **1975**, *58(12)*, 1767.

# List of Publications

1. “Carbonnanotube-modified sodiumdodecylsulfate polyacrylamidegel electrophoresis for molecular weight determination of proteins” Meera Parthasarathy, **Joyashish Debgupta**, Bhalchandra Kakade, Abu A. Ansary, M. Islam Khan, Vijayamohanan K.Pillai, *Anal. Biochem.* **2010**, *409*, 230.
2. “Competitive wetting of acetonitrile and dichloromethane in comparison to that of water on functionalized carbon nanotube surfaces” **Joyashish Debgupta**, Bhalchandra A. Kakade and Vijayamohanan K. Pillai, *Phys. Chem. Chem. Phys.* **2011**, *13*, 14668.
3. “Electrochemical Unzipping of Multi-walled Carbon Nanotubes for Facile Synthesis of High-Quality Graphene Nanoribbons” Dhanraj B. Shinde, **Joyashish Debgupta**, Ajay Kushwaha, Mohammed Aslam and Vijayamohanan K. Pillai, *J. Am. Chem. Soc.* **2011**, *133*, 4168.
4. “SHI irradiation induced effects in functionalized MWCNTs” V. Saikiran, A. P. Pathak, N. S. Rao, G. Devaraju, **Joyashish Debgupta**, I. Kyriakou and D. Emfietzoglou, *Radiation Effects and Defects in Solids* **2012**, *167*, 569.
5. “*In situ* Electrochemical Organization of CdSe nanoclusters on Graphene during Unzipping of Carbon Nanotubes” **Joyashish Debgupta**, D. B. Shinde and Vijayamohanan K. Pillai, *Chem. Comm.* **2012**, *48*, 3088.
6. “Laser synthesized super-hydrophobic conducting carbon with broccoli-type morphology as a counter-electrode for dye sensitized solar cells” Rohan R. Gokhale, S. A. Agarkar, **Joyashish Debgupta**, D. B. Shinde, B. Lefez, A. Banerjee, J. Jyog, M. More, B. Hannoyer and Satishchandra Ogale, *Nanoscale* **2012**, *4*, 6730.
7. “Thiolated Graphene-a new platform for hybrid heterostructures” **Joyashish Debgupta** and Vijayamohanan K. Pillai, *Nanoscale* **2013**, *5*, 3615.
8. “Photophysical and Photoconductivity Properties of Thiol Functionalized Graphene-CdSe QD Composites” **Joyashish Debgupta**, Sadananda Mandal, Hemen Kalita, Mohammed Aslam, Amitava Patra and Vijayamohanan Pillai, *RSC Advances* **2014**, *4*, 13788.
9. “Effect of Self Assembly on Triiodide Diffusion in Water based Polymer Gel Electrolytes: An Application in Dye Solar Cell” Kishan Fadadu, Rohit Vekariya, **Joyashish Debgupta**, K D Patel, Alain Gibaud, Vinod Aswal and Saurabh Sureshchandra Soni, *J. Colloid Interface Sci.* **2014**, *425*, 110.
10. “C@SiNW/TiO2 Core-Shell Nanoarrays with Sandwiched Carbon Passivation Layer as High Efficiency Photoelectrode for Water Splitting” Rami Reddy Devarapalli, **Joyashish Debgupta**, Vijayamohanan K. Pillai and Manjusha V. Shelke, *Scientific Reports* **2014**, *4*, DOI: 10.1038/srep04897.
11. “Electrochemical Preparation of Vertically aligned, Hollow CdSe Nanotubes and its p-n junction Hybrid with Electrodeposited $Cu_2O$” **Joyashish Debgupta**, Ramireddy Devarapally, Shakeelur Rahman, Manjusha V. Shelke and Vijayamohanan K. Pillai, *Nanoscale* (Just Accepted, **2014**), Manuscript ID: NR-ART-12-2013-006917.R2.

**List of Patent:**

“An electrochemical process for water splitting using porous $Co_3O_4$ nanorods” WO 2013160915 A1.

A. J. Pattayil, V. K. Pillai, R. M. Ramsundar, **J. Debgupta**, Google Patents, **2013**.

# Erratum